



ATLAS Note

GROUP-2017-XX



25th March 2021

Draft version 0.1

1

2 **A Deep Learning Approach to Differential**
3 **Measurements of Higgs - Top Interactions in**
4 **Multilepton Final States**

5

The ATLAS Collaboration

6 Several theories Beyond the Standard Model modify the momentum spectrum of the Higgs
7 Boson, without significantly altering the overall rate of Higgs produced from top quark pairs.
8 A differential measurement of the Higgs transverse momentum provides a way to search for
9 these effects at the LHC. Because of the challenges inherent to reconstructing the Higgs in
10 multilepton final states, a deep learning approach is used to predict the momentum spectrum
11 of the Higgs for events where the Higgs Boson is produced from top quark pairs and decays
12 to final states that include multiple leptons. The regressed Higgs p_T is fit to data for events
13 with two or three leptons in the final state, and estimates of the sensitivity to variations in the
14 Higgs p_T spectrum are given.

© 2021 CERN for the benefit of the ATLAS Collaboration.

15 Reproduction of this article or parts of it is allowed as specified in the CC-BY-4.0 license.

16 **Contents**

17	I Introduction	7
18	1 Introduction	7
19	II Theoretical Motivation	10
20	2 The Standard Model and the Higgs Boson	10
21	2.1 The Forces and Particles of the Standard Model	10
22	2.2 The Higgs Mechanism	13
23	2.2.1 The Higgs Field	13
24	2.2.2 Electroweak Symmetry Breaking	15
25	2.3 $t\bar{t}H$ Production	18
26	2.4 Extensions to the Standard Model	20
27	III The LHC and the ATLAS Detector	23
28	3 The LHC	23
29	4 The ATLAS Detector	26
30	4.1 Inner Detector	28
31	4.2 Calorimeters	29
32	4.3 Muon Spectrometer	30
33	4.4 Trigger System	31
34	IV Measurement of WZ + Heavy Flavor	32
35	5 Introduction	32
36	6 Data and Monte Carlo Samples	34
37	6.1 Data Samples	34
38	6.2 Monte Carlo Samples	35
39	7 Object Reconstruction	37
40	7.1 Trigger	38
41	7.2 Light leptons	38
42	7.3 Jets	40
43	7.4 B-tagged Jets	40
44	7.5 Missing transverse energy	42
45	7.6 Overlap removal	42

46	8 Event Selection and Signal Region Definitions	43
47	8.1 Event Preselection	43
48	8.2 Fit Regions	48
49	8.3 Non-Prompt Lepton Estimation	65
50	8.3.1 $t\bar{t}$ Validation	65
51	8.3.2 Z+jets Validation	71
52	9 tZ Interference Studies and Separation Multivariate Analysis	76
53	9.1 Top Mass Reconstruction	76
54	9.2 tZ BDT	78
55	10 Data and Monte Carlo Samples	82
56	10.1 Data Samples	83
57	10.2 Monte Carlo Samples	84
58	11 Object Reconstruction	86
59	11.1 Trigger	87
60	11.2 Light leptons	87
61	11.3 Jets	89
62	11.4 B-tagged Jets	89
63	11.5 Missing transverse energy	91
64	11.6 Overlap removal	91
65	12 Event Selection and Signal Region Definitions	92
66	12.1 Event Preselection	92
67	12.2 Fit Regions	97
68	12.3 Non-Prompt Lepton Estimation	114
69	12.3.1 $t\bar{t}$ Validation	114
70	12.3.2 Z+jets Validation	120
71	13 tZ Interference Studies and Separation Multivariate Analysis	125
72	13.1 Top Mass Reconstruction	125
73	13.2 tZ BDT	127
74	14 Systematic Uncertainties	131
75	15 Results	140
76	15.1 1-jet Fit Results	141
77	15.2 2-jet Fit Results	150
78	V Differential Studies of $t\bar{t}H$ Multilepton	159
79	16 Data and Monte Carlo Samples	159
80	16.1 Data Samples	160

81	16.2 Monte Carlo Samples	160
82	17 Object Reconstruction	161
83	17.1 Trigger Requirements	161
84	17.2 Light Leptons	162
85	17.3 Jets	163
86	17.4 Missing Transverse Energy	163
87	18 Higgs Momentum Reconstruction	164
88	18.1 Decay Candidate Reconstruction	165
89	18.2 b-jet Identification	166
90	18.2.1 2lSS Channel	167
91	18.2.2 3l Channel	171
92	18.3 Higgs Reconstruction	174
93	18.3.1 2lSS Channel	175
94	18.3.2 3l Semi-leptonic Channel	179
95	18.3.3 3l Fully-leptonic Channel	183
96	18.4 p_T Prediction	186
97	18.4.1 2lSS Channel	188
98	18.4.2 3l Semi-leptonic Channel	191
99	18.4.3 3l Fully-leptonic Channel	193
100	18.5 3l Decay Mode	197
101	19 Signal Region Definitions	199
102	19.1 Pre-MVA Event Selection	200
103	19.2 Event MVA	205
104	19.3 Signal Region Definitions	211
105	20 Background Rejection MVA	215
106	20.1 Pre-MVA Event Selection	216
107	20.2 Event MVA	217
108	20.3 Signal Region Definitions	223
109	20.3.1 2lSS	226
110	20.3.2 3l – Semi – leptonic	226
111	20.3.3 3l – Fully – leptonic	226
112	21 Systematic Uncertainties	226
113	22 Results	228
114	22.1 Results - 80 fb^{-1}	228
115	22.2 Projected Results - 140 fb^{-1}	231

116	VI Conclusion	233
-----	----------------------	------------

117	Appendices	235
118	.1 Non-prompt lepton MVA	235
119	.2 Non-prompt CR Modelling	239
120	.3 tZ Interference Studies	244
121	.4 Alternate tZ Inclusive Fit	248
122	.5 DSID list	253
123	A Machine Learning Models	276
124	A.1 Higgs Reconstruction Models	276
125	A.1.1 b-jet Identification Features - 2ISS	276
126	A.1.2 b-jet Identification Features - 3l	280
127	A.1.3 Higgs Reconstruction Features - 2ISS	285
128	A.1.4 Higgs Reconstruction Features - 3IS	290
129	A.1.5 Higgs Reconstruction Features - 3IF	295
130	A.2 Background Rejection MVAs	299
131	A.2.1 Background Rejection MVA Features - 2ISS	299
132	A.2.2 Background Rejection MVA Features - 3l	303
133	A.3 Alternate b-jet Identification Algorithm	308
134	A.4 Binary Classification of the Higgs p_T	308
135	A.5 Impact of Alternative Jet Selection	310

Part I**Introduction****1 Introduction**

139 Particle physics is an attempt to describe the fundamental building blocks of the universe and
140 their interactions. The Standard Model (SM) - our best current theory of fundamental particle
141 physics - does a remarkable job of that. All known fundamental particles and (almost) all of the
142 forces underlying their interactions can be explained by the SM, and the predictions from this
143 theory agree with experiment to an incredibly precise degree. This is especially true since the
144 Higgs Boson, the last piece of the SM predicted decades before, was finally discovered at the
145 Large Hadron Collider (LHC) in 2012.

146 Despite the success of the SM, there remains significant work to be done. For one, the
147 SM is incomplete: it fails to provide a description of gravity, to give an explanation for the
148 observation of Dark Matter, or to provide a mechanism for neutrinos to gain mass. Further, a
149 Higgs Boson with a mass of around 125 GeV, as observed at the LHC, gives rise to what is
150 known a hierarchy problem - such a low mass Higgs requires a seemingly unnatural level of “fine
151 tuning” that is unexplained by the SM.

152 A promising avenue for addressing these problems is to study the properties of the Higgs
153 Boson and the way it interacts with other particles, in part simply because these interactions

154 have not been measured before. Its interactions with the Top Quark are a particularly promising
155 place to look. Because the Higgs Field is responsible for allowing particle to acquire mass, the
156 strength of a particle's interaction with the Higgs Boson is proportional to its mass. As the most
157 massive of the fundamental particles, the Top Quark has the strongest coupling to the Higgs
158 Boson, meaning any new physics in the Higgs sector is likely to present itself most prominently
159 in its interaction with the Top Quark.

160 These interactions can be measured by directly by studying the production of a Higgs
161 Boson in association with a pair of Top Quarks ($t\bar{t}H$). While studies have been done measuring
162 the overall rate of $t\bar{t}H$ production, there are several theories of physics Beyond the Standard
163 Model (BSM) that would affect the kinematics of $t\bar{t}H$ production without altering its overall
164 rate. This dissertation attempts to make a differential measurement of the kinematics of the
165 Higgs Boson in $t\bar{t}H$ events in order to search for these BSM effects.

166 The proton-proton collision data collected by the ATLAS detector at the LHC from 2015-
167 2018 provides the opportunity to make this measurement for the first time. The unprecedented
168 energy achieved by the LHC during this period greatly increase the rate at which $t\bar{t}H$ events are
169 produced, and the large amount of data collected provides the necessary statistics for a differential
170 measurement to be performed.

171 A study of $t\bar{t}H$ events with multiple leptons in the final state is performed, using 139 fb^{-1}
172 of data from proton-proton collisions at an energy $\sqrt{s} = 13 \text{ TeV}$ collected by the ATLAS detector
173 from 2015-2018. Events are separated into channels based on the number of light leptons in the

174 final state - either two same-sign leptons, or three leptons. A deep neural network is used to
175 reconstruct the momentum of the Higgs Boson in each event. This momentum spectrum is fit to
176 data for each analysis channel, the result of which is used to place limits on BSM effects.

177 An additional study of WZ produced in association with a heavy flavor jet (including both
178 b-jets and charm jets) is also included. This process mimics the final state of $t\bar{t}H$ multilpjeton
179 events, making it an important background for that analysis. However, this process is poorly
180 understood, and difficult to simulate accurately, introducing large systematic uncertainties for
181 analyses that include it as a background. Therefore, a measurement of WZ + heavy flavor in the
182 fully leptonic decay mode is performed.

183 This dissertation begins with a brief explanation of the SM, its limitations, and the theor-
184 etical motivation behind this work in Part II. This is followed by a description of the LHC and
185 the ATLAS detector in Part III. Part IV details a measurement of WZ + heavy flavor. Studies
186 of differential measurements of $t\bar{t}H$ are then described in Part V, and preliminary results are
187 presented. Finally, the results of these studies are summarized in the conclusion, Part VI.

Part II**Theoretical Motivation****2 The Standard Model and the Higgs Boson**

The Standard Model of particle physics (SM) is a Quantum Field Theory (QFT) describing the known fundamental particles and their interactions. It accounts for three of the four known fundamental force - electromagnetism, the weak nuclear force, and the strong nuclear force, but not gravity. Further, the SM describes a mechanism for combining the weak and electromagnetic forces into a singular interaction, known as the electroweak force. It is a non-Abelian gauge theory, invariant under the Lie Group $SU(3)_C \otimes SU(2)_L \otimes U(1)_Y$, where C refers to color charge, L, the helicity of the particle, and Y, the hypercharge.

2.1 The Forces and Particles of the Standard Model

The SM particles, summarized in figure 2.1, can be classified into two general categories based on their spin: fermions, and bosons.

Standard Model of Elementary Particles

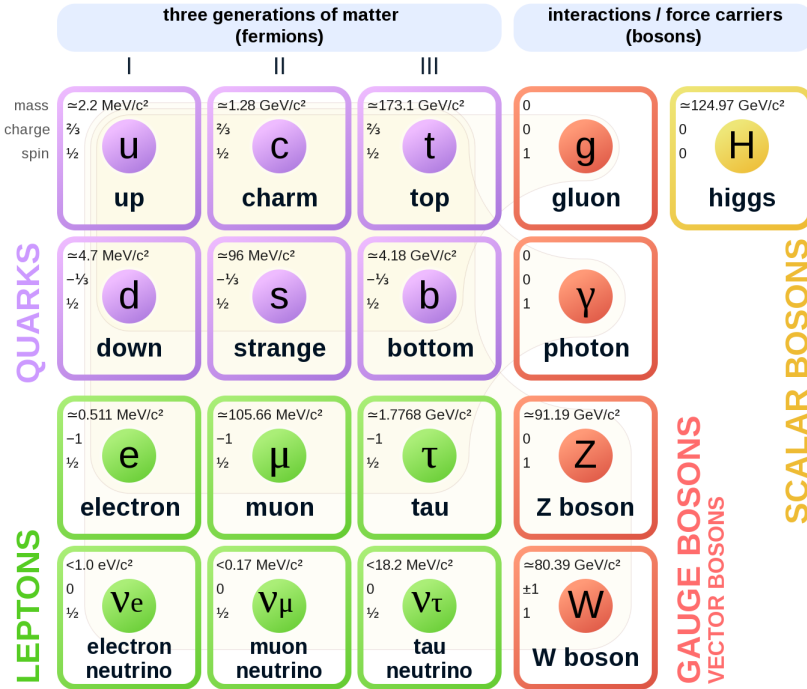


Figure 2.1: A summary of the particles of the Standard Model, including their mass, charge and spin, with the fermions listed on the left, and the bosons on the right. []

201 Fermions are particles with $\frac{1}{2}$ -integer spin, which according to the spin-statistics theorem,
 202 causes them to comply with the Pauli-exclusion principle []. They can be separated into two
 203 groups, leptons and quarks, each of which consist of three generations of particles with increasing
 204 mass.

205 Leptons are fermions interact via the electroweak force, but not the strong force. The three
 206 generation of leptons consist of the electron and electron neutrino, the muon and muon neutrino,
 207 the tau and tau neutrino. The quarks, which do interact via the strong force - which is to say they
 208 have color charge - in addition to the electroweak force. The three generations include the up

209 and down quarks, the strange and charm quarks, and the top and bottom quarks. Each of these
 210 generations form left-handed doublets invariant under SU(2) transformations. For the leptons
 211 these doublets are:

$$\begin{pmatrix} e^- \\ \nu_e \end{pmatrix}_L, \begin{pmatrix} \mu^- \\ \nu_\mu \end{pmatrix}_L, \begin{pmatrix} \tau^- \\ \nu_\tau \end{pmatrix}_L \quad (2.1)$$

212 And for the quarks:

$$\begin{pmatrix} u \\ d \end{pmatrix}_L, \begin{pmatrix} s \\ c \end{pmatrix}_L, \begin{pmatrix} t \\ b \end{pmatrix}_L \quad (2.2)$$

213 For both leptons and quarks, the heavier generations can decay into the lighter generation
 214 of particles, while the first generation does not decay. Hence, ordinary matter generally consists
 215 of this first generation of fermions - electrons, up quarks, and down quarks. Each of these
 216 fermions has a corresponding anti-particle, which has an equal mass as its partner but opposite
 217 charge. The fermions acquire their mass via the Higgs Mechanism, except for the neutrinos,
 218 whose mass has been experimentally confirmed but is not accounted for in the SM.

219 Bosons, by contrast, have integer spin, and are therefore unconstrained by the Pauli-
 220 exclusion principle. The SM includes two kinds of bosons: Gauge bosons, which are spin-1
 221 particles that mediate the interactions between the fermions, and a single scalar, i.e. spin-0,
 222 particle - the Higgs Boson. Of the gauge bosons, the W^+ , W^- and Z bosons - which are the

223 mass eigenstates of the electroweak bosons - mediate the weak interaction, while the photon

224 mediates the electric force, and the gluon mediates the strong force.

225 **2.2 The Higgs Mechanism**

226 A key feature of the SM is the gauge invariance of its Lagrangian. However, any terms added to

227 the Lagrangian giving mass to the the gauge bosons would violate the underlying symmetry of

228 the theory. This presents a clear problem with the theory: The experimental observation that the

229 W and Z bosons have mass seems to contradict the basic structure of the SM.

230 Rather than abandoning gauge invariance, an alternative way for particles to acquire mass

231 beyond adding a simple mass term to the Lagrangian was theorized by Higgs, Englert and Brout

232 in 1964 []. This procedure for introducing masses for the gauge bosons while preserving local

233 gauge invariance, known as the Higgs mechanism, was incorporated into the electroweak theory

234 by Weinberg in 1967 [].

235 **2.2.1 The Higgs Field**

236 The Higgs mechanism introduces a complex scalar SU(2) doublet, Φ , with the form:

$$\Phi = \begin{pmatrix} \phi^+ \\ \phi^0 \end{pmatrix}_L \quad (2.3)$$

237 This field introduces a scalar potential to the Lagrangian of the form:

$$V(\Phi) = \mu^2 |\Phi^\dagger \Phi| + \lambda (|\Phi^\dagger \Phi|)^2 \quad (2.4)$$

238 Where μ and λ are free parameters of the new field. This represents the most general
239 potential allowed while preserving $SU(2)_L$ invariance and renormalizability. In the case that
240 $\mu^2 < 0$, this potential takes the form shown in figure 2.2.

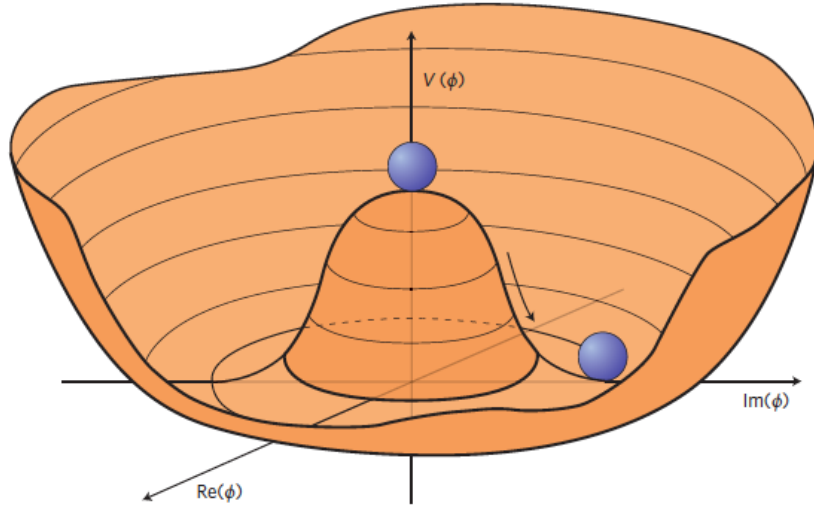


Figure 2.2: The value of the Higgs potential, $V(\Phi)$ as a function of Φ , for the case that $\mu^2 < 0$ [].

241 The significant feature of this potential is that its minimum does not occur for a value of
242 $\Phi = 0$. Instead, it is minimized when $|\Phi^\dagger \Phi| = -\mu^2/\lambda$. This means that in its ground state, the
243 Higgs field takes on a non-zero value - referred to as a vacuum expectation value (VEV). So while
244 the Higgs potential is globally symmetric, about the minimum this symmetry is broken. Since

²⁴⁵ the minimum is determined only by $\Phi^\dagger \Phi$, there is some ambiguity in the particular definition of

²⁴⁶ the VEV, but it is generally represented as

$$\langle \Phi \rangle = \frac{1}{\sqrt{2}} \begin{pmatrix} 0 \\ v \end{pmatrix} \quad (2.5)$$

²⁴⁷ The full value of Φ can be written as

$$\langle \Phi \rangle = \frac{1}{\sqrt{2}} \begin{pmatrix} 0 \\ v + H/\sqrt{2} \end{pmatrix} \quad (2.6)$$

²⁴⁸ with v being the value of the VEV, and H being the real value of the scalar field.

²⁴⁹ 2.2.2 Electroweak Symmetry Breaking

²⁵⁰ The Electroweak (EWK) interaction is described in the SM by a $SU(2)_L \otimes U(1)_Y$ gauge theory.

²⁵¹ This theory predicts three $SU(2)_L$ gauge boson, $W_\mu^1, W_\mu^2, W_\mu^3$, and a single $U(1)_Y$ gauge boson,

²⁵² B_μ . The couplings of these bosons to the Higgs field show up in the kinetic terms of the scalar

²⁵³ field Φ in the Lagrangian:

$$(D_\mu \Phi)^\dagger (D^\mu \Phi) = |(\partial_\mu - \frac{i g}{2} W_\mu^a \sigma^a - \frac{i g'}{2} B_\mu Y) \phi|^2 \quad (2.7)$$

254 Here D_μ represents the covariant derivative required to preserve gauge invariance, g and
 255 g' represent coupling constant of the gauge bosons, σ^a denotes the Pauli matrices of $SU(2)$,
 256 and Y represents the hypercharge of $U(1)$. The terms in this interaction which contribute to the
 257 masses of the gauge bosons can be written as:

$$\frac{1}{2}(0, v) \left(\frac{g}{2} W_\mu^a \sigma^a - \frac{g'}{2} B_\mu \right)^2 \begin{pmatrix} 0 \\ v \end{pmatrix} \quad (2.8)$$

258 Expanding these terms into the mass eigenstates of the electroweak interaction yields four
 259 physical gauge bosons, two charged and two neutral, which are linear combinations of the fields
 260 W_μ^1 , W_μ^2 , W_μ^3 , and B_μ :

$$\begin{aligned} W_\mu^\pm &= \frac{1}{\sqrt{2}} (W_\mu^1 \pm i W_\mu^2) \\ Z^\mu &= \frac{1}{\sqrt{(g^2 + g'^2)}} (-g' B_\mu + g W_\mu^3) \\ A^\mu &= \frac{1}{\sqrt{(g^2 + g'^2)}} (g B_\mu + g' W_\mu^3) \end{aligned} \quad (2.9)$$

261 And the masses of these fields are given by:

$$\begin{aligned} M_W^2 &= \frac{1}{4} g^2 v^2 \\ M_Z^2 &= \frac{1}{4} (g^2 + g'^2) v^2 \\ M_A^2 &= 0 \end{aligned} \quad (2.10)$$

262 This produces exactly the particles we observe - three massive gauge bosons and a single
 263 massless photon. The massless photon represents the portion of the gauge symmetry, a single
 264 $U(1)$ of the electromagnetic force, that remains unbroken by the VEV.

265 Interactions with the Higgs field also lead to the generation of the fermion masses, which
 266 in the Lagrangian take the form:

$$-\lambda_\psi(\bar{\psi}_L \phi \psi_R + \bar{\psi}_R \phi^\dagger \psi_L) \quad (2.11)$$

267 After symmetry breaking has occurred and ϕ has taken on the value of the VEV as written
 268 in equation 2.5, the mass terms of the fermions become $\lambda_\psi v$. Written this way, the fermion
 269 masses are proportional to their Yukawa coupling to the VEV, λ_ψ .

270 Based on the equation 2.6, an additional mass term, $\mu^2 H^2$ arises from the potential $V(\Phi)$.
 271 This term can be understood as an excitation of the Higgs field, a scalar boson with mass $M_H = \mu$.
 272 This is the Higgs boson, which comes about as a natural prediction of electroweak symmetry
 273 breaking.

274 The fermion's Yukawa coupling to the VEV take the same form as the fermion's coupling
 275 to the Higgs boson - λ_ψ . Therefore, the strength of a fermion's interaction with the Higgs is
 276 directly proportional to its mass. We now have a model that predicts a Higgs boson with mass
 277 $M_H = \mu$, which interacts with the fermions with coupling strength λ_ψ . Because μ and λ_ψ are

²⁷⁸ free parameters of the theory, the mass of the Higgs boson and its interactions with the fermions

²⁷⁹ must be measured experimentally.

²⁸⁰ **2.3 $t\bar{t}H$ Production**

²⁸¹ The strength of a particles interaction with the Higgs, given by its Yukawa coupling, is propor-
²⁸² tionate to its mass. The top quark - as the heaviest known particle - has the strongest interaction,
²⁸³ making this interaction particularly interesting to study. While several processes involve interac-
²⁸⁴ tions between the Higgs and the top, some Higgs production modes include the top interaction
²⁸⁵ only as a part of a loop diagram, such as the gluon-gluon fusion diagram shown in Figure 2.3.

²⁸⁶ This process therefore only allows for an indirect probe of the Higgs-top Yukawa coupling, as
²⁸⁷ the flavor of the quark in this diagram is not unique.

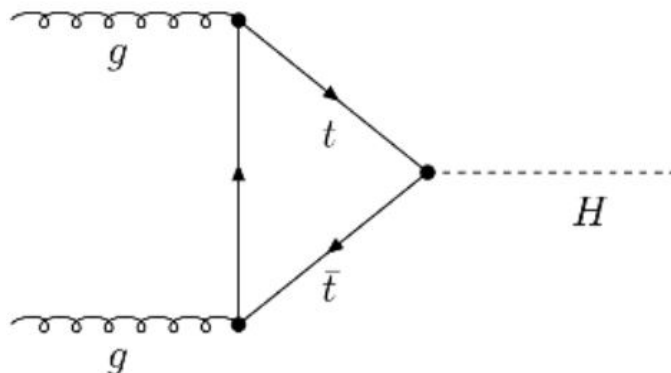


Figure 2.3: Diagram of a Higgs boson produced via gluon-gluon fusion.

²⁸⁸ Studying the Higgs produced in association with top quark pairs, $t\bar{t}H$, allows this interac-
²⁸⁹ tion to be measured directly. This process, as shown in Figure 2.4, involves a unique coupling

²⁹⁰ between the Higgs and the top, which can be identified by the top quark pair in the final state.

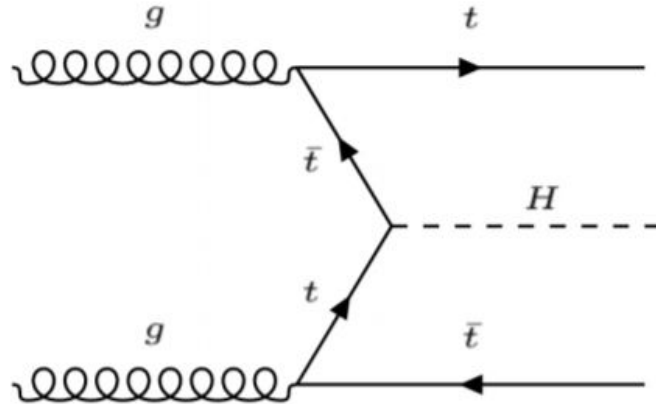


Figure 2.4: Diagram of a Higgs boson produced in association with a pair of top quarks.

²⁹¹ The Higgs boson, as well as the top quarks, have very short lifetimes - on the order of
²⁹² 10^{-22} s and 10^{-25} s respectively - meaning they can only be observed via their decay products.
²⁹³ This thesis focuses on $t\bar{t}H$ events with multiple leptons in the final state, $t\bar{t}H - ML$. This
²⁹⁴ includes $H \rightarrow W^+W^-$ events, where at least one of the W bosons decays leptonically.

²⁹⁵ While the branching ratio of $H \rightarrow W^+W^-$ is smaller than $H \rightarrow b\bar{b}$, it produces a clearer
²⁹⁶ signal. On the other hand, $H \rightarrow \gamma\gamma$ produces the most easily identifiable signal, but has a much
²⁹⁷ smaller branching ratio than $H \rightarrow W^+W^-$. Therefore, compared with other final state, the
²⁹⁸ $t\bar{t}H - ML$ channel is an attractive candidate for study, as it involves a good balance between
²⁹⁹ statistical power and identifiability.

300 **2.4 Extensions to the Standard Model**

301 While the SM has been tested to great precision, particularly at the LHC, it is generally accepted
302 that it is only valid up to a certain energy scale. It is assumed that above a certain energy, at the
303 scale where something like a Grand Unified Theory (GUT) or quantum gravity become relevant,
304 the SM will not be applicable. Further, there are several experimental observations that the SM
305 fails to explain. For example, the SM predicts neutrinos to be massless, despite experimental
306 observation to the contrary, and fails to explain the observation of dark matter and dark energy.

307 Another example, relevant to the Higgs sector, is known as the hierarchy problem: large
308 quantum corrections to the Higgs mass from loop diagrams, such as those shown in Figure 2.5,
309 are many orders of magnitude larger than the Higgs mass itself. The observed value of the Higgs
310 mass therefore requires extremely precise cancellation between these corrections and the bare
311 mass of the Higgs, a cancellation which seems unnatural and suggests something missing in our
312 theoretical picture.

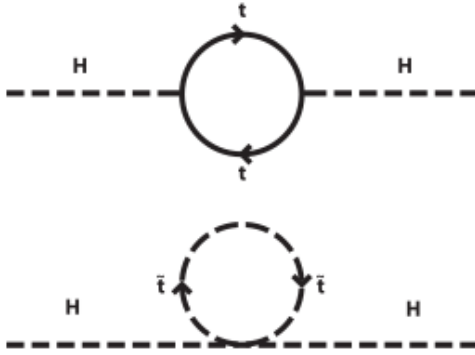


Figure 2.5: Above diagram is the leading order correction to the Higgs mass via a top quark loop, and below is the stop squark loop, coming from a supersymmetric extension of the SM, that provides a potential cancellation of the top diagram [].

313 Because so many of the properties of the Higgs boson have not yet been studied, its
 314 interactions are a promising place to search for new physics that could resolve some of the
 315 limitations of the SM. As explained above, the interactions of the Higgs with the top quark, as in
 316 $t\bar{t}H$ production, are particularly interesting: As the most massive particle in the Standard Model,
 317 the top quark is the most strongly interacting with the Higgs. Therefore, any new physics effects
 318 are likely to be seen most prominently in this interaction.

319 These interactions can be measured directly by studying the production of a Higgs Boson
 320 in association with a pair of Top Quarks ($t\bar{t}H$) []. While this process has been observed by both
 321 the ATLAS [] and CMS [] collaborations, these analyses have focused on measuring the overall
 322 rate of $t\bar{t}H$ production. There are several theories of physics Beyond the Standard Model (BSM),
 323 however, that would affect the kinematics of $t\bar{t}H$ production without altering its overall rate [].

324 An Effective Field Theory approach can be used to model the low energy effects of new,

325 high energy physics, by parameterizing BSM effects as higher dimensional operators. These
 326 additional operators can then be added to the SM Lagrangian to write an effective Lagrangian
 327 that accounts for the effects of these higher energy physics. The lowest order of these that could
 328 contribute to Higgs-top couplings are dimension-six, as represented in Equation 2.12.

$$\mathcal{L}_{\text{BSM}} = \mathcal{L}_{\text{SM}} + \frac{f}{\Lambda} O^6 \quad (2.12)$$

329 Here Λ represents the energy scale of the new physics, and f is a Wilson coefficient which
 330 represents the strength of the effective coupling. An experimental observation of any non-zero
 331 value of f would be a sign of BSM physics.

332 The addition of these operators can be shown to modify the transverse momentum (p_T)
 333 spectrum of the Higgs Boson in Higg-top interactions, without effecting the overall rate of $t\bar{t}H$
 334 production []. The effect of these higher order effects on the as shown in Figure 2.6.

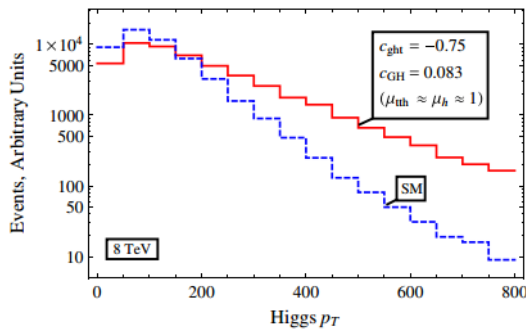


Figure 2.6: The momentum spectrum of the Higgs boson produced via top-quarks with (red) and without (blue) the presence of dimension-six operators.

335 This provides a clear, physics observable that could be used to search for BSM effect.

336 Therefore, reconstructing the momentum spectrum of the Higgs in $t\bar{t}H$ events provides a means

337 to observe new physics in the Higgs sector.

338 **Part III**

339 **The LHC and the ATLAS Detector**

340 **3 The LHC**

341 The Large Hadron Collider (LHC) is a particle accelerator consisting of a 27 km ring, designed

342 to collide protons at high energy. Located outside of Geneva, Switzerland and buried about 100

343 m underground, it consists of a ring of superconducting magnets which are used to accelerate

344 opposing beams of protons - or lead ions - which collide at the center of one of the various

345 detectors located around the LHC ring which record the result of these collisions. These

346 detectors include two general purpose detectors, ATLAS and CMS, which are designed to make

347 precision measurements of a broad range of physics phenomenon, and two more specialized

348 experiments, LHCb and ALICE, which are optimized to study b-quarks and heavy-ion physics,

349 respectively.

350 The LHC first began running in 2009 at a proton-proton center of mass energy of $\sqrt{s} = 8$

351 TeV. It operated at this energy from 2009 to 2012, known as Run 1, and data collected during

352 this period was used in discovering the Higgs Boson. The LHC began running again in 2015,
353 and collected data at an increased energy of $\sqrt{s} = 13$ TeV until 2018, a period referred to as Run
354 2.

355 The LHC consists of a chain of accelerators, which accelerate the protons to higher and
356 higher energies until they are injected into the main ring. This process is summarized in figure
357 3.1. Protons extracted from a tank of ionized hydrogen are fed into a linear accelerator, LINAC2,
358 where they reach an energy of 50 MeV. From there, they enter a series of three separate circular
359 accelerators, before being injected into the main accelerator ring at an energy of 450 GeV. Within
360 the main ring protons are separated into two separate beams moving in opposite directions,
361 and their energy is increased to their full collision energy. Radiofrequency cavities are used to
362 accelerate these particles and sort them into bunches. From 2015-2018, these bunches consisted
363 of around 100 billion protons each with an energy of 6.5 TeV per proton, which collided at a rate
364 of 40 MHz, or every 25 ns.

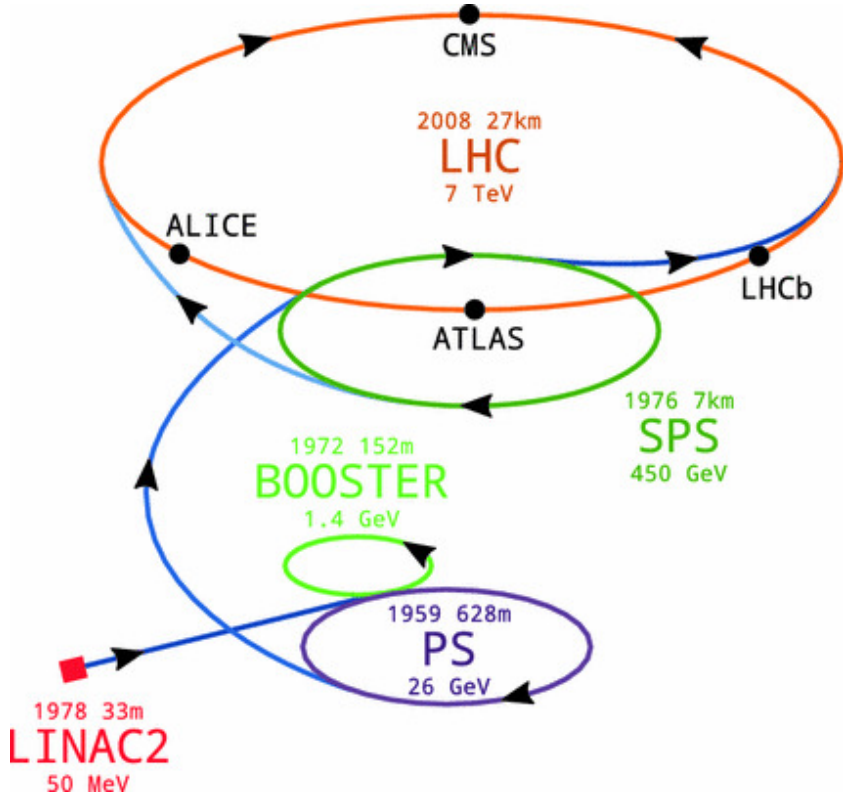


Figure 3.1: A summary of the accelerator chain used to feed protons into the LHC [].

365 Because these proton bunches consist of a large number of particles, each bunch crossing
 366 consists of not just one, but several direct proton-proton collisions. The number of interactions
 367 that occur per bunch crossing, μ , is known as pileup. During Run 2, the average pileup for bunch
 368 crossings was around $\langle \mu \rangle = 35$, with values typically ranging between 10 and 70.

369 The amount of data collected by the LHC is measured in terms of luminosity, which is the

³⁷⁰ ratio of the number of events detected per unit time, $\frac{dN}{dt}$, and the interaction cross-section, σ .

$$\mathcal{L} = \frac{1}{\sigma} \frac{dN}{dt} \quad (3.1)$$

³⁷¹ The design luminosity of the LHC is $10^{34} \text{ cm}^{-2} \text{s}^{-1}$, however the LHC has achieved a
³⁷² luminosity of over $2 \times 10^{34} \text{ cm}^{-2} \text{s}^{-1}$. The total luminosity is then this instantaneous luminosity
³⁷³ integrated over time.

$$\mathcal{L}_{\text{int}} = \int \mathcal{L} dt \quad (3.2)$$

³⁷⁴ The integrated luminosity collected by the ATLAS detector as of the end of 2018 is around
³⁷⁵ 140 fb^{-1} , exceeding the expected integrated luminosity of 100 fb^{-1} .

³⁷⁶ 4 The ATLAS Detector

³⁷⁷ ATLAS (a not terribly natural acronym for “A Toroidal LHC Apparatus”) is a general purpose
³⁷⁸ detector designed to maximize the detection efficiency of all physics objects, including leptons,
³⁷⁹ jets, and photons. This means it is capable of measuring all SM particles, with the exception of
³⁸⁰ neutrinos, the presence of which can be inferred based on missing transverse momentum. The
³⁸¹ detector measures 44 m long, and 25 m tall.

382 The ATLAS detector consists of multiple layers, each of which serves a different purpose
 383 in reconstructing collisions. At the very center of the detector is the interaction point where the
 384 proton beams of the LHC collide.

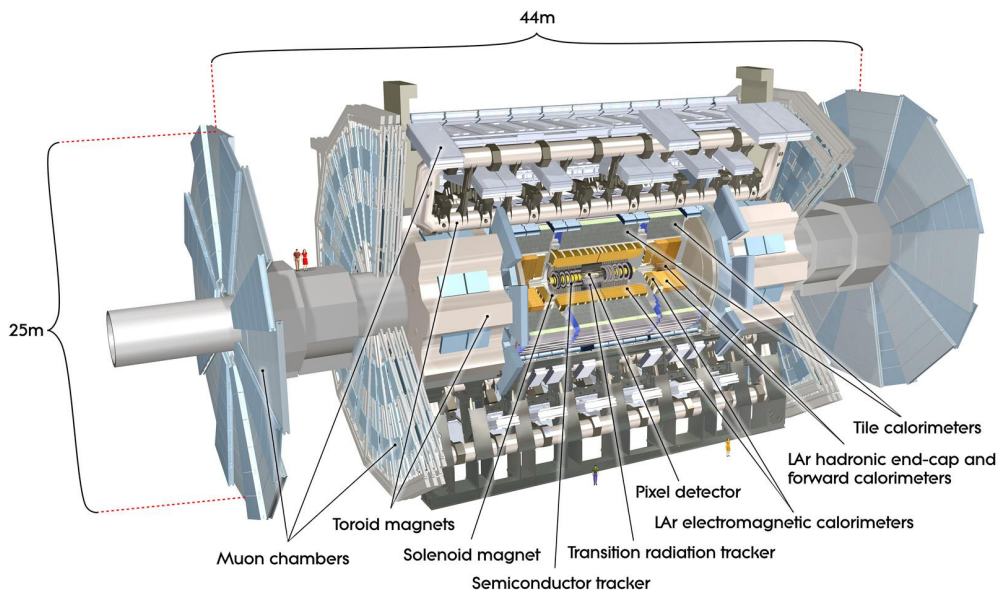


Figure 4.1: Cutaway view of the ATLAS detector, with labels of its major components [].

385 **4.1 Inner Detector**

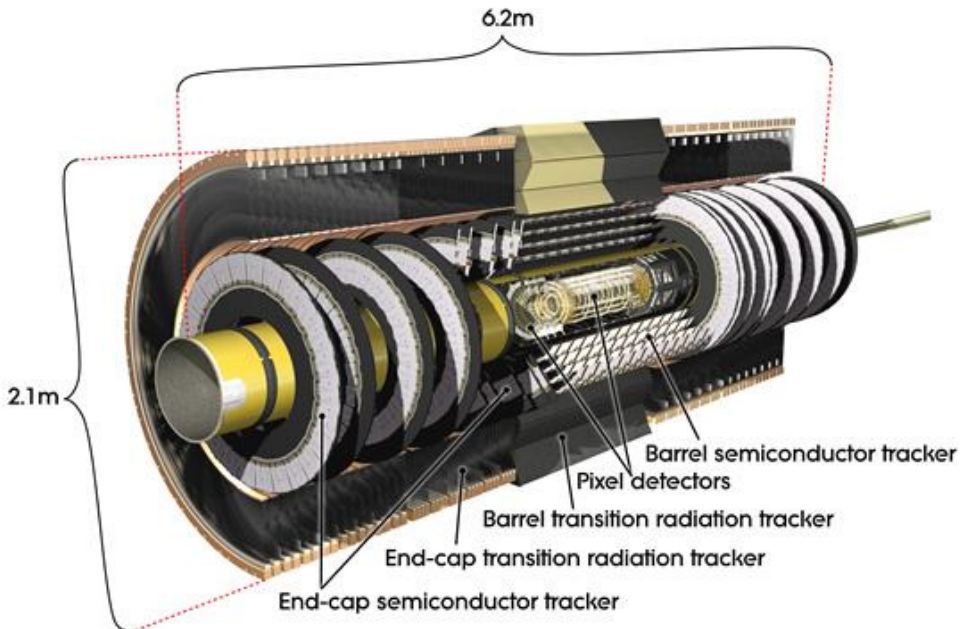


Figure 4.2: Cutaway view of the Inner Detector [].

386 Just surrounding the interaction point is the Inner Detector, designed to track the path of charged
 387 particles moving through the detector. An inner solenoid surrounding the Innder Detector is
 388 used to produces a magnetic field of 2 T. This large magnetic field causes the path of charged
 389 particles moving through the Inner Detector to bend. Because this magnetic field is uniform and
 390 well known, it can be used in conjunction with the curvature of a particles path to measure its
 391 charge and momentum.

392 The Inner Detector consists of three components - the Pixel Detector, the Semi-Conductor
 393 Tracker (SCT), and the Transition Radiation Tracker (TRT). The Pixel Detector is the innermost

394 of these, beginning just 33.25 mm away from the beam line. It consists of three silicon layers
 395 along the barrel, as well as three endcap layers, covering a range of $|\eta| < 2.5$.

396 The Semiconductor Tracker (SCT) is similar to the Pixel detector, but uses long strips
 397 rather than small pixel to cover a larger spatial area.

398 4.2 Calorimeters

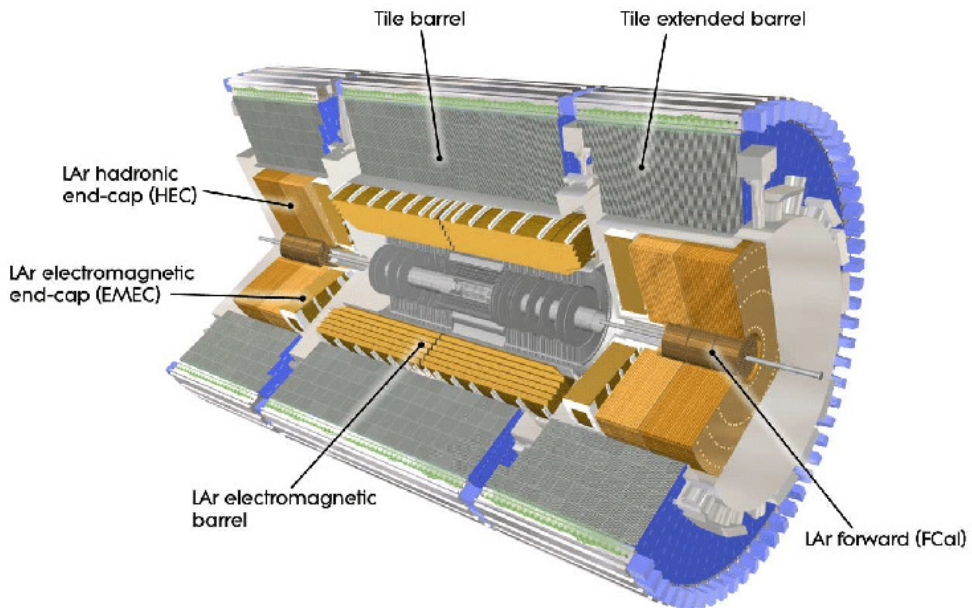


Figure 4.3: Cutaway view of the calorimeter system of the ATLAS detector [].

399 Situated outside the Inner Detector are two concentric calorimeters. The inner calorimeter uses
 400 liquid argon (LAr) to measure energy of particles that interact electromagnetically, which includes
 401 photons and any charged particle. The LAr calorimeter is made of heavy metals, primarily lead
 402 and copper, which causes electromagnetically interacting particles to shower, depositing their

403 energy in the detector. The showering of the high energy particles that pass through calorimeter
404 cause the liquid argon to ionize, and the ionized electrons are detected by electronic readouts.
405 The LAr calorimeter consists of around 180,000 readout channels.

406 The outer calorimeter measures the energy from particles that pass through the EM calor-
407 imeter, and measures the energy of particles that interact via the strong force. This is primarily
408 hadrons. It is composed of steel plates to cause hadronic showering and scintillating tiles as the
409 active material. The signals from the hadronic calorimeter are read out by photomultiplier tubes
410 (PMTs).

411 **4.3 Muon Spectrometer**

412 Because muons are heavier than electrons and photons, and do not interact via the strong force,
413 they generally pass through the detector without being stopped by the calorimeters. The outermost
414 components of the detector are designed specifically to measure the energy and momentum of
415 muons produced in the LHC. The muon spectrometer consists of tracking and triggering system.
416 It extends from the outside of the calormeter system, about a 4.25 m radius from the beam line,
417 to a radius of 11 m. This large detector system is necessary to accurately measure the momentum
418 of muons, which is essential not only for measurements involving the muons themselves, but also
419 to accurately estimate the missing energy in each event.

420 Two large toroidal magnets within the muon system generate a large magnetic field which
421 covers an area 26 m long with a radius of 10 m. Because the area covered by this magnet system

422 is so large, a uniform magnetic field like the one produced in the Inner Detector is impractical.
423 Instead, the magnetic field that exists in the muon spectrometer ranges between 2 T and 8 T, and
424 is much less uniform. The path of the muons passing through the spectrometer is bent by this
425 field, allowing their charge to be determined.

426 1200 tracking chambers are placed in the muon system in order to precisely measure the
427 tracks of muons with high spatial resolution.

428 **4.4 Trigger System**

429 Because of the high collision rate and large amount of data collected by the various subdetectors,
430 ATLAS produces far more data than can actually be stored. Each event produces around 25 Mb
431 of raw data, which multiplied by the bunch crossing rate of 40 MHz, comes out to around a
432 petabyte of data every second. The information from every event cannot practically be stored,
433 therefore a sophisticated trigger system is employed in real time to determine whether events are
434 sufficiently interesting to be worth storing.

435 The trigger system in ATLAS involves multiple levels, each of which select out which
436 events move on to the next level of scrutiny. The level-1 trigger uses hardware information from
437 the calorimeters and muon spectrometer to select events that contain candidates for particles
438 commonly used in analysis, such as energetic leptons and jets. The level-1 trigger reduces the
439 rate of events from 40 MHz to around 100 kHz.

440 Events that pass the level-1 trigger move to the High-Level Trigger (HLT). The HLT takes
441 place outside of the detector in software, and looks for properties such as a large amount of
442 missing transverse energy, well defined leptons, and multiple high energy jets. Events that pass
443 the HLT are stored and used for analysis. Because the specifics of the HLT are determined by
444 software rather than hardware, the thresholds can be changed throughout the run of the detector
445 in response to run conditions such as changes to pileup and luminosity. After the HLT is applied,
446 the event rate is reduced to around 1000 per second, which are recorded for analysis.

447 **Part IV**

448 **Measurement of WZ + Heavy Flavor**

449 **5 Introduction**

450 The production of WZ in association with a heavy flavor jet represents an important background
451 for many major analyses. This includes any process with leptons and b-jets in the final state,
452 such as $t\bar{t}H$, $t\bar{t}W$, and $t\bar{t}Z$. While precise measurements have been made of WZ production
453 [WZ_36], WZ + heavy flavor remains poorly understood. This is largely because the QCD
454 processes involved in the production of the b-jet make it difficult to simulate accurately. This
455 introduces a large uncertainty for analyses that include this process as a background.

456 Motivated by its relevance to the $t\bar{t}H$ multilepton analysis, we perform a study of the fully

457 leptonic decay mode of this channel; that is, events where both the W and Z decay leptonically.
458 Because WZ has no associated jets at leading order, while the major backgrounds for this channel
459 tend to have high jet multiplicity, events with more than two jets are rejected. This gives a final
460 state signature of three leptons and one or two jets.

461 Events that meet this selection criteria are sorted into pseudo-continuous b-tagging regions
462 based on the DL1r b-tag score of their associated jets. This is done to separate WZ + b-jet events
463 from WZ + charm and WZ + light jets. These regions are fit to data in order make a more
464 accurate estimate of the contribution of WZ + heavy-flavor, where heavy-flavor jets include
465 b-jets and charm jets. The full Run-2 dataset collected by the ATLAS detector, representing 139
466 fb^{-1} of data from pp collisions at $\sqrt{s} = 13 \text{ TeV}$, is used for this study.

467 Section 10 details the data and Monte Carlo (MC) samples used in the analysis. The
468 reconstruction of various physics objects is described in Section 11. Section 12 describes the
469 event selection applied to these samples, along the definitions of the various regions used in
470 the fit. The multivariate analysis techniques used to separate the tZ background from WZ +
471 heavy flavor are described in Section 13. Section 21 describes the various sources of systematic
472 uncertainties considered in the fit. Finally, the results of the analysis are summarized in Section
473 22, followed by a brief conclusion in Section ??.

474 **The current state of the analysis shows blinded results for the full 2018 dataset.**
475 **Regions containing >5% WZ+b events are blinded, and results are from Asimov, MC only**
476 **fits.**

477 **6 Data and Monte Carlo Samples**

478 Both data and Monte Carlo samples used in this analysis were prepared in the `xAOD` format,
 479 which was used to produce a `DxAOD` sample in the HIGG8D1 derivation framework. The HIGG8D1
 480 framework is designed for the $t\bar{t}H$ multi-lepton analysis, which targets events with multiple
 481 leptons as well as tau hadrons. This framework skims the dataset to remove unneeded variables
 482 as well as entire events. Events are removed from the derivations that do not meet the following
 483 selection:

- 484 • at least two light leptons within a range $|\eta| < 2.6$, with leading lepton $p_T > 15$ GeV and
 485 subleading lepton $p_T > 5$ GeV
- 486 • at least one light lepton with $p_T > 15$ GeV within a range $|\eta| < 2.6$, and at least two hadronic
 487 taus with $p_T > 15$ GeV.

488 Samples were then generated from these HIGG8D1 derivations with p-tag of p4134 for data
 489 and p4133 for Monte Carlo using AnalysisBase version 21.2.127 modified to include custom
 490 variables.

491 **6.1 Data Samples**

492 The study uses a sample of proton-proton collision data collected by the ATLAS detector from
 493 2015 through 2018 at an energy of $\sqrt{s} = 13$ TeV, which represents an integrated luminosity of

494 139 fb^{-1} . This data set was collected with a bunch crossing rate of 25 ns. All data used in this
495 analysis was verified by data quality checks, having been included in the following Good Run
496 Lists:

- 497 • data15_13TeV.periodAllYear_DetStatus-v79-repro20-02_DQDefects-00-02-02
498 _PHYS_StandardGRL_All_Good_25ns.xml

499 • data16_13TeV.periodAllYear_DetStatus-v88-pro20-21_DQDefects-00-02-04
500 _PHYS_StandardGRL_All_Good_25ns.xml

501 • data17_13TeV.periodAllYear_DetStatus-v97-pro21-13_Unknown_PHYS_StandardGRL
502 _All_Good_25ns_Triggerno17e33prim.xml

503 • data18_13TeV.periodAllYear_DetStatus-v102-pro22-04_Unknown_PHYS_StandardGRL
504 _All_Good_25ns_Triggerno17e33prim.xml

505 Runs included from the AllYear period containers are included.

506 **6.2 Monte Carlo Samples**

507 Several different generators were used to produce Monte Carlo simulations of the signal and
508 background processes. For all samples, the response of the ATLAS detector is simulated using
509 Geant4. The WZ signal samples are simulated using Sherpa 2.2.2 [[sherpa](#)]. Specific information

⁵¹⁰ about the Monte Carlo samples being used can be found in Table 28. A list of the specific samples
⁵¹¹ used by data set ID is shown in Table 10.

Table 1: The configurations used for event generation of signal and background processes, including the event generator, matrix element (ME) order, parton shower algorithm, and parton distribution function (PDF).

Process	Event generator	ME order	Parton Shower	PDF
WZ, VV	SHERPA 2.2.2	MEPS NLO	SHERPA	CT10
tZ	MG5_AMC	LO	PYTHIA 6	CTEQ6L1
t̄W	MG5_AMC (SHERPA 2.1.1)	NLO (LO multileg)	PYTHIA 8 (SHERPA)	NNPDF 3.0 NLO (NNPDF 3.0 NLO)
t̄t(Z/γ* → ll)	MG5_AMC	NLO	PYTHIA 8	NNPDF 3.0 NLO
t̄tH	MG5_AMC (MG5_AMC)	NLO (NLO)	PYTHIA 8 (HERWIG++)	NNPDF 3.0 NLO [Ball:2014uwa] (CT10 [ct10])
tHqb	MG5_AMC	LO	PYTHIA 8	CT10
tHW	MG5_AMC (SHERPA 2.1.1)	NLO (LO multileg)	HERWIG++ (SHERPA)	CT10 (NNPDF 3.0 NLO)
tWZ	MG5_AMC	NLO	PYTHIA 8	NNPDF 2.3 LO
t̄t, t̄tt̄	MG5_AMC	LO	PYTHIA 8	NNPDF 2.3 LO
t̄tW+W-	MG5_AMC	LO	PYTHIA 8	NNPDF 2.3 LO
t̄t	Powheg-BOX v2 [powhegtt]	NLO	PYTHIA 8	NNPDF 3.0 NLO
t̄tγ	MG5_AMC	LO	PYTHIA 8	NNPDF 2.3 LO
s-, t-channel, Wt single top	Powheg-BOX v1 [powhegstp]	NLO	PYTHIA 6	CT10
qqVV, VVV				
Z → l ⁺ l ⁻	SHERPA 2.2.1	MEPS NLO	SHERPA	NNPDF 3.0 NLO

Sample	DSID
WZ	364253, 364739-42
VV	364250, 364254, 364255, 363355-60, 364890
t̄W	410155
t̄Z	410156, 410157, 410218-20
low mass t̄Z	410276-8
Rare Top	410397, 410398, 410399
single Top	410658-9, 410644-5
three Top	304014
four Top	410080
t̄WW	410081
Z + jets	364100-41
low mass Z + jets	364198-215
W + jets	364156-97
Vγ	364500-35
tZ	410560
tW	410013-4
WtZ	410408
VVV	364242-9
VH	342284-5
WtH	341998
t̄tγ	410389
t̄t	410470
t̄tH	345873-5, 346343-5

Table 2: List of Monte Carlo samples by data set ID used in the analysis.

512 7 Object Reconstruction

513 All regions defined in this analysis share a common lepton, jet, and overall event preselection.

514 The selection applied to each physics object is detailed here; the event preselection, and the

515 selection used to define the various fit regions, is described in Section 12.

⁵¹⁶ **7.1 Trigger**

⁵¹⁷ Events are required to be selected by dilepton triggers, as summarized in Table 29.

Dilepton triggers (2015)	
$\mu\mu$ (asymm.)	HLT_mu18_mu8noL1
ee (symm.)	HLT_2e12_lhloose_L12EM10VH
$e\mu, \mu e$ (\sim symm.)	HLT_e17_lhloose_mu14
Dilepton triggers (2016)	
$\mu\mu$ (asymm.)	HLT_mu22_mu8noL1
ee (symm.)	HLT_2e17_lhvloose_nod0
$e\mu, \mu e$ (\sim symm.)	HLT_e17_lhloose_nod0_mu14
Dilepton triggers (2017)	
$\mu\mu$ (asymm.)	HLT_mu22_mu8noL1
ee (symm.)	HLT_2e24_lhvloose_nod0
$e\mu, \mu e$ (\sim symm.)	HLT_e17_lhloose_nod0_mu14
Dilepton triggers (2018)	
$\mu\mu$ (asymm.)	HLT_mu22_mu8noL1
ee (symm.)	HLT_2e24_lhvloose_nod0
$e\mu, \mu e$ (\sim symm.)	HLT_e17_lhloose_nod0_mu14

Table 3: List of lowest p_T -threshold, un-prescaled dilepton triggers used for 2015-2018 data taking.

⁵¹⁸ **7.2 Light leptons**

⁵¹⁹ Electron candidates are reconstructed from energy clusters in the electromagnetic calorimeter that

⁵²⁰ are associated with charged particle tracks reconstructed in the inner detector [**ATLAS-CONF-2016-024**].

⁵²¹ Electron candidates are required to have $p_T > 10$ GeV and $|\eta_{\text{cluster}}| < 2.47$. Muon candidates

⁵²² are reconstructed by combining inner detector tracks with track segments or full tracks in the

⁵²³ muon spectrometer [**PERF-2014-05**]. Muon candidates are required to have $p_T > 10$ GeV and

524 $|\eta| < 2.5$. Candidates in the transition region between different electromagnetic calorimeter
525 components, $1.37 < |\eta_{\text{cluster}}| < 1.52$, are rejected. A multivariate likelihood discriminant com-
526 bining shower shape and track information is used to distinguish real electrons from hadronic
527 showers (fake electrons). To further reduce the non-prompt electron contribution, the track is
528 required to be consistent with originating from the primary vertex; requirements are imposed
529 on the transverse impact parameter significance ($|d_0|/\sigma_{d_0} < 5$) and the longitudinal impact
530 parameter ($|\Delta z_0 \sin \theta_\ell| < 0.5 \text{ mm}$).

531 Muon candidates are reconstructed by combining inner detector tracks with track segments
532 or full tracks in the muon spectrometer [**PERF-2014-05**]. Muon candidates are required to have
533 $p_T > 10 \text{ GeV}$ and $|\eta| < 2.5$. The longitudinal impact parameter is the same for both electrons
534 and muons, while muons are required to pass a slightly tighter transverse impact parameter,
535 $|d_0|/\sigma_{d_0} < 3$.

536 All leptons are required to be isolated, as defined through the standard PLVLoose working
537 point supported by combined performance groups. Leptons are additionally required to pass a
538 non-prompt BDT selection developed by the $t\bar{t}H$ multilepton/ $t\bar{t}W$ analysis group. This BDT is
539 described in detail in [**ttW_140**]. Optimized working points and scale factors for this BDT are
540 taken from that analysis.

541 7.3 Jets

542 Jets are reconstructed from calibrated topological clusters built from energy deposits in the
543 calorimeters [**ATL-PHYS-PUB-2015-015**], using the anti- k_t algorithm with a radius para-
544 meter $R = 0.4$. Particle Flow, or PFlow, jets are used in the analysis. Jets with energy
545 contributions likely arising from noise or detector effects are removed from consideration
546 [**ATLAS-CONF-2015-029**], and only jets satisfying $p_T > 25$ GeV and $|\eta| < 2.5$ are used
547 in this analysis. For jets with $p_T < 60$ GeV and $|\eta| < 2.4$, a jet-track association algorithm is
548 used to confirm that the jet originates from the selected primary vertex, in order to reject jets
549 arising from pileup collisions [**PERF-2014-03**].

550 7.4 B-tagged Jets

551 In order to make a measurement of $WZ +$ heavy flavor it is necessary to distinguish these events
552 from $WZ +$ light jets. For this purpose, the DL1r b-tagging algorithm is used to distinguish
553 heavy flavor jets from lighter ones. The DL1r algorithm uses jet kinematics, particularly jet
554 vertex information, as input for a neural network which assigns each jet a score designed to
555 reflect how likely that jet is to have originated from a b-quark.

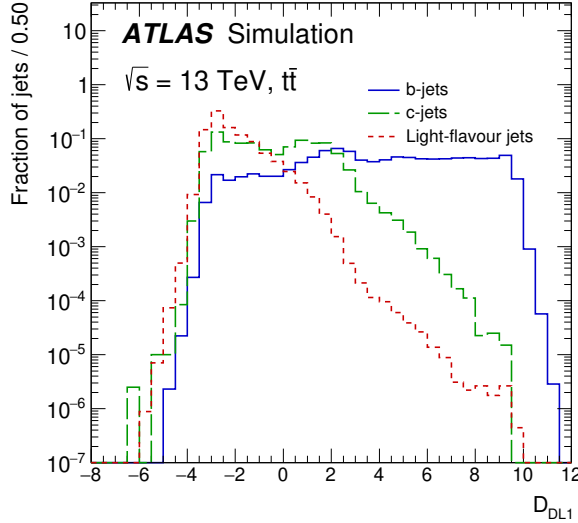


Figure 7.1: Output distribution of the DL1r algorithm for b-jets, charm jets, and light jets

556 From the output of the BDT, working points (WPs) are developed based on the efficiency
 557 of truth b-jets at particular values of the DL1r algorithm. These WPs are taken from the March
 558 2020 CDI file, 2020-21-13TeV-MC16-CDI-2020-03-11_v2.root. The working points used in
 559 this analysis are summarized in Table 12.

WP	none	loose	medium	tight	tightest
b eff.	-	85%	77%	70%	60%

Table 4: B-tagging Working Points by tightness and b-jet efficiency

560 A tighter WP will accept fewer b-jets, but reject a higher fraction of charm and light jets.
 561 Generally, analyses that include b-jets will use a fixed working point, for example, requiring that
 562 a jet pass the 70% threshold. By instead treating these working point as bins, e.g. events with
 563 jets that fall between the 85% and 77% WPs fall into one bin, while events with jets passing the

564 60% WP fall into another, and looking at the full psuedo-continuous DL1r spectrum of the jets,
565 additional information can be gained. The psuedo-continuous b-tag spectrum is used in this case
566 to separate out WZ + b, WZ + charm, and WZ + light.

567 7.5 Missing transverse energy

568 Missing transverse momentum (E_T^{miss}) is used as part of the event selection. The missing
569 transverse momentum vector is defined as the inverse of the sum of the transverse momenta of
570 all reconstructed physics objects as well as remaining unclustered energy, the latter of which is
571 estimated from low- p_T tracks associated with the primary vertex but not assigned to a hard object,
572 with object definitions taken from [ATL-PHYS-PUB-2015-027]. Light leptons considered in
573 the E_T^{miss} reconstruction are required to have $p_T > 10 \text{ GeV}$, while jets are required to have $p_T > 20$
574 GeV .

575 7.6 Overlap removal

576 To avoid double counting objects and remove leptons originating from decays of hadrons, overlap
577 removal is performed in the following order: any electron candidate within $\Delta R = 0.1$ of another
578 electron candidate with higher p_T is removed; any electron candidate within $\Delta R = 0.1$ of a muon
579 candidate is removed; any jet within $\Delta R = 0.3$ of an electron candidate is removed; if a muon
580 candidate and a jet lie within $\Delta R = \min(0.4, 0.04 + 10[\text{GeV}] / p_T(\text{muon}))$ of each other, the jet
581 is kept and the muon is removed.

582 This algorithm is applied to the preselected objects. The overlap removal procedure is
 583 summarized in Table 13.

Keep	Remove	Cone size (ΔR)
electron	electron (low p_T)	0.1
muon	electron	0.1
electron	jet	0.3
jet	muon	$\min(0.4, 0.04 + 10[\text{GeV}]/p_T(\text{muon}))$
electron	tau	0.2

Table 5: Summary of the overlap removal procedure between electrons, muons, and jets.

584 8 Event Selection and Signal Region Definitions

585 Event are required to pass a preselection described in Section 12.1 and summarized in Table 14.
 586 Those that pass this preselection are divided into various fit regions described in Section 12.2,
 587 based on the number of jets in the event, and the b-tag score of those jets.

588 8.1 Event Preselection

589 Events are required to include exactly three reconstructed light leptons passing the requirement
 590 described in 11.2, which have a total charge of ± 1 . As the opposite sign lepton is found to
 591 be prompt the vast majority of the time [ttH_paper], it is required to be loose and isolated,
 592 as defined though the standard PLVLoose working point supported by combined performance
 593 groups. The same sign leptons are required to be very tightly isolated, as per the recommended
 594 PLVTight.

595 The leptons are ordered in the analysis code as 0, 1, and 2. Lepton 0 is the lepton whose
 596 charge is opposite the other two. Lepton 1 is the lepton closest to the opposite charge lepton, i.e.
 597 the smallest ΔR , leaving lepton 2 as the lepton further from the opposite charge lepton. Lepton
 598 0 is required to have $p_T > 10 \text{ GeV}$, while the same sign leptons, 1 and 2, are required to have
 599 $p_T > 20 \text{ GeV}$ to reduce the contribution of non-prompt leptons.

600 The invariant mass of at least one pair of opposite sign, same flavor leptons is required
 601 to fall within 10 GeV of the mass of the Z boson, 91.2 GeV. Events where one of the opposite
 602 sign pairs have an invariant mass less than 12 GeV are rejected in order to suppress low mass
 603 resonances.

604 An additional requirement is placed on the missing transverse energy, $E_T^{\text{miss}} > 20 \text{ GeV}$,
 605 and the transverse mass of the W candidate, $m(E_T^{\text{miss}} + l_{\text{other}}) > 30 \text{ GeV}$, where E_T^{miss} is the
 606 missing transverse energy, and l_{other} is the lepton not included in the Z-candidate.

607 Events are required to have one or two reconstructed jets passing the selection described
 608 in Section 11.3. Events with more than two jets are rejected in order to reduce the contribution
 609 of backgrounds such as $t\bar{t}Z$ and $t\bar{t}W$, which tend to have higher jet multiplicity.

Event Selection

Exactly three leptons with charge ± 1
 Two tight Iso, tight ID same-charge leptons with $p_T > 20 \text{ GeV}$
 One loose Iso, medium ID opposite charge lepton with $p_T > 10 \text{ GeV}$
 $m(l^+l^-)$ within 10 GeV of 91.2 GeV
 Transverse mass of W-candidate, $m_T(E_T^{\text{miss}} + \text{lep}_{\text{other}}) > 30 \text{ GeV}$
 Missing transverse energy, $E_T^{\text{miss}} > 20 \text{ GeV}$
 One or two jets with $p_T > 25 \text{ GeV}$

Table 6: Summary of the selection applied to events for inclusion in the fit

610 The event yields in the preselection region for both data and Monte Carlo are summarized
 611 in Table 12.1, which shows good agreement between data and Monte Carlo, and demonstrates that
 612 this region consists primarily of WZ events. The WZ events are split into WZ + b, WZ + c, and
 613 WZ + l based on the truth flavor of the associated jet in the event. Specifically, this determination
 614 is made based on the HadronConeExclTruthLabelID of the jet, as recommended by the b-
 615 tagging working group [BtagWG]. In this ordering b-jet supersedes charm, which supersedes
 616 light. That is, WZ + l events contain no charm and no b jets at truth level, WZ + c contain at
 617 least one truth charm and no b-jets, and WZ + b contains at least one truth b-jet.

Process	Events
WZ + b	167.6 ± 6.5
WZ + c	1080 ± 40
WZ + l	7220 ± 310
Other VV	850 ± 140
t̄tW	16.8 ± 2.3
t̄tZ	115 ± 17
rare Top	2.2 ± 0.1
Single top	0.10 ± 0.45
Three top	0.01 ± 0.01
Four top	0.02 ± 0.01
t̄tWW	0.23 ± 0.05
Z + jets	600 ± 260
V + γ	37 ± 54
tZ	190 ± 70
tW	5.5 ± 1.2
WtZ	25.8 ± 1.1
VVV	26.2 ± 0.9
VH	94 ± 7
t̄t	108.68 ± 8
t̄tH	4.3 ± 0.5
Total	10600 ± 530
Data	10574

Table 7: Event yields in the preselection region at 139.0 fb^{-1}

618 Here Other VV represents diboson processes other than WZ, and consists predominantly
619 of $ZZ \rightarrow llll$ events where one of the leptons is not reconstructed.

620 Simulations are further validated by comparing the kinematic distributions of the Monte
621 Carlo with data, which are shown in Figure 12.1. Here, bins with 5% or more WZ+b are
622 blinded.

WZ Fit Region - Inclusive

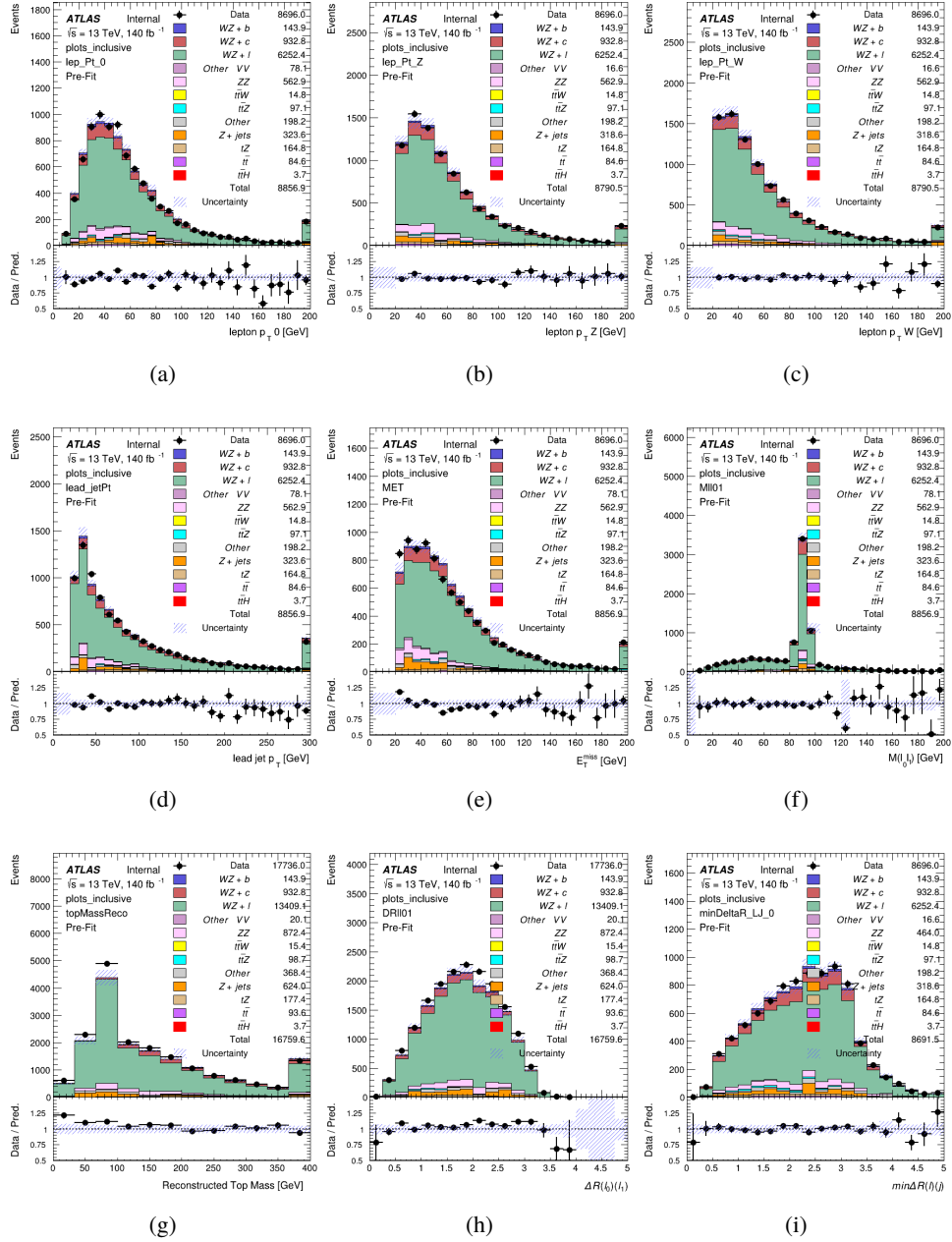


Figure 8.1: Comparisons between the data and MC distributions in the preselection region for (a) the p_T of the opposite sign lepton, (b) the p_T of the other lepton from the Z candidate, (c) the p_T of the lepton from the W candidate, (d) the leading jet p_T , (e) the E_T^{miss} , and (f) the invariant mass of leptons 0 and 1, (g) the reconstructed top mass, (h) $\Delta(R)$ between lepton 0 and 1, (i) the $\Delta(R)$ between the closest lepton and jet.

623 **8.2 Fit Regions**

624 Once preselection has been applied, the remaining events are categorized into one of twelve
 625 orthogonal regions. The regions used in the fit are summarized in Table 16.

Table 8: A list of the regions used in the fit and the selection used for each.

Region	Selection
1j, <85%	$N_{\text{jets}} = 1, n\text{Jets_DL1r_85} = 0$
1j, 85%-77%	$N_{\text{jets}} = 1, n\text{Jets_DL1r_85} = 1, n\text{Jets_DL1r_77} = 0$
1j, 77%-70%	$N_{\text{jets}} = 1, n\text{Jets_DL1r_77} = 1, n\text{Jets_DL1r_70} = 0$
1j, 70%-60%	$N_{\text{jets}} = 1, n\text{Jets_DL1r_70} = 1, n\text{Jets_DL1r_60} = 0$
1j, >60%	$N_{\text{jets}} = 1, n\text{Jets_DL1r_60} = 1, tZ \text{ BDT} > 0.725$
1j tZ CR	$N_{\text{jets}} = 1, n\text{Jets_DL1r_60} = 1, tZ \text{ BDT} < 0.725$
2j, <85%	$N_{\text{jets}} = 2, n\text{Jets_DL1r_85} = 0$
2j, 85%-77%	$N_{\text{jets}} = 2, n\text{Jets_DL1r_85} \geq 1, n\text{Jets_DL1r_77} = 0$
2j, 77%-70%	$N_{\text{jets}} = 2, n\text{Jets_DL1r_77} \geq 1, n\text{Jets_DL1r_70} = 0$
2j, 70%-60%	$N_{\text{jets}} = 2, n\text{Jets_DL1r_70} \geq 1, n\text{Jets_DL1r_60} = 0$
2j, >60%	$N_{\text{jets}} = 2, n\text{Jets_DL1r_60} \geq 1, tZ \text{ BDT} > 0.725$
2j tZ CR	$N_{\text{jets}} = 2, n\text{Jets_DL1r_60} \geq 1, tZ \text{ BDT} < 0.725$

626 The working points discussed in Section 11.4 are used to separate events into fit regions
 627 based on the highest working point reached by a jet in each event. Because the background
 628 composition differs significantly based on the number of b-jets, events are further subdivided
 629 into 1-jet and 2-jet regions in order to minimize the impact of background uncertainties.

630 An unfolding procedure is performed to account for differences in the number of recon-
 631 structed jets compared to the number of truth jets in each event. The `AntiKt4TruthDressedWZJets`
 632 truth jet collection is used to make this determination. In order to account for migration of WZ+1-
 633 jet and WZ+2-jet events between the 1-jet and 2-jet bins at reco level, the signal samples are
 634 separated based on the number of truth jets. Events with 0 jets or more than 3 jets at truth level,

yet fall within one of the categories listed in Table 16, are categorized as WZ + other, and treated as a background. The migration matrix in the number of jets at truth level versus reco level is shown in Figure 12.2. The composition of the number of truth jets in each reco jet bin is taken from MC, with uncertainties in these estimates described in detail in Section 21.

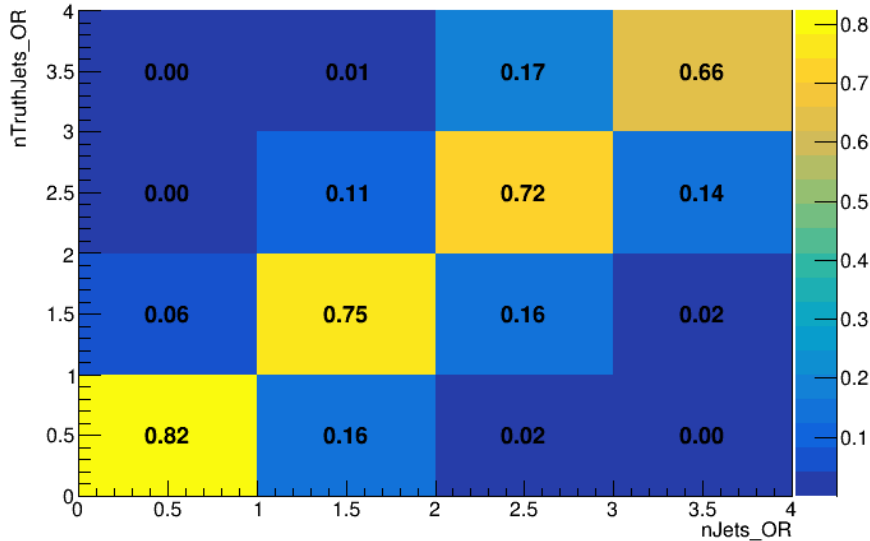


Figure 8.2: Number of truth jets compared to the number of reconstructed jets in each WZ event falling in the preselection region. Each row is normalized to unity.

An additional tZ control region is created based on the BDT described in Section 13. The region with 1-jet passing the 60% working point is split in two - a signal enriched region of events with a BDT score greater than 0.03, and a tZ control region including events with less than 0.03. This cutoff is arrived at by performing an Asimov fit with a variety of cutoffs, and selecting the value that produces the highest significance for the measurement of WZ + b.

The modeling in each region is validated by comparing data and MC predictions for

645 various kinematic distributions. These plot are shown in Figures [12.3-12.16](#).

WZ Fit Region - 1j Inclusive

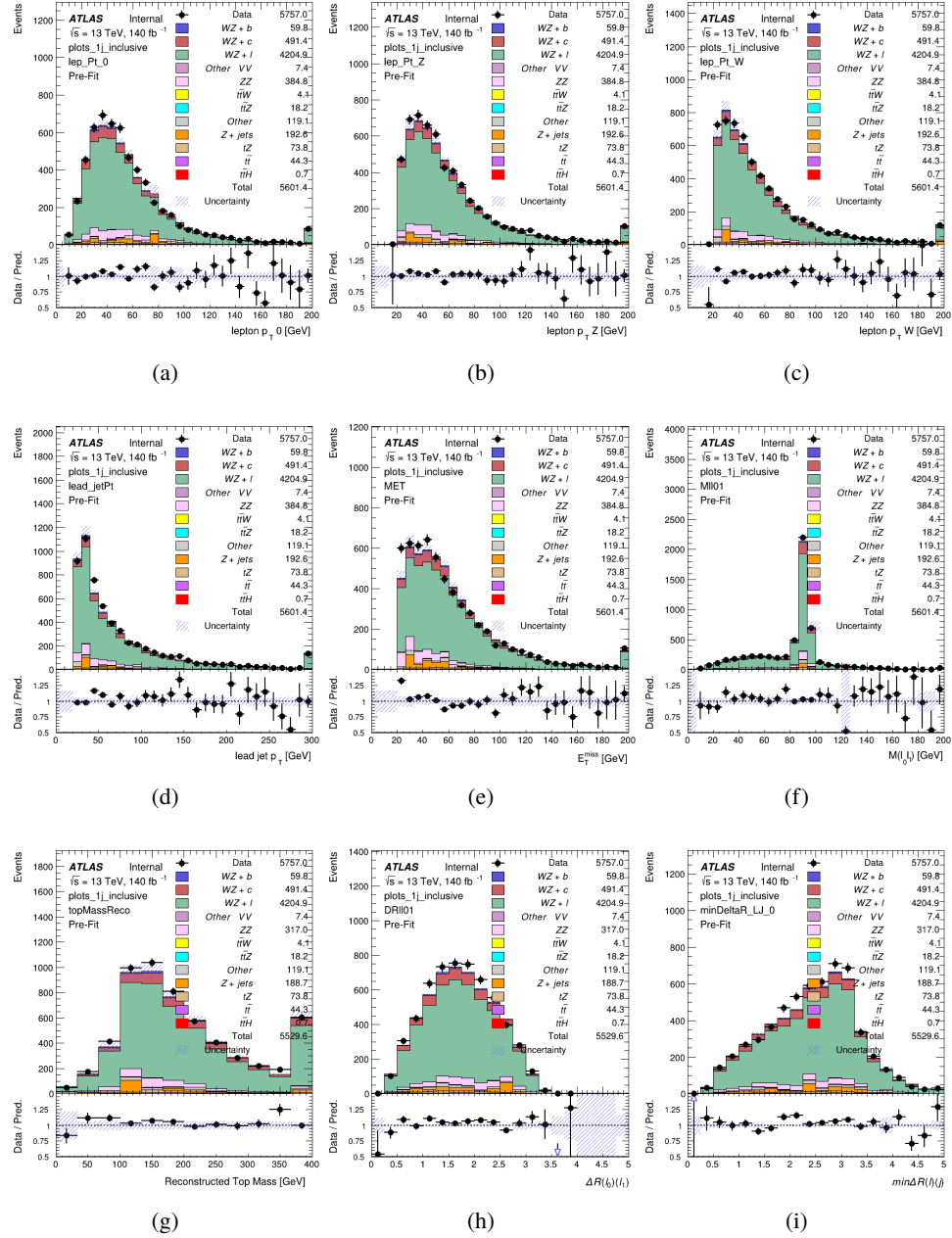


Figure 8.3: Comparisons between the data and MC distributions in the preselection region for (a) the p_T of the opposite sign lepton, (b) the p_T of the other lepton from the Z candidate, (c) the p_T of the lepton from the W candidate, (d) the leading jet p_T , (e) the E_T^{miss} , and (f) the invariant mass of leptons 0 and 1, (g) the reconstructed top mass, (h) $\Delta(R)$ between lepton 0 and 1, (i) the $\Delta(R)$ between the closest lepton and jet.

WZ Fit Region - 1j < 85% WP

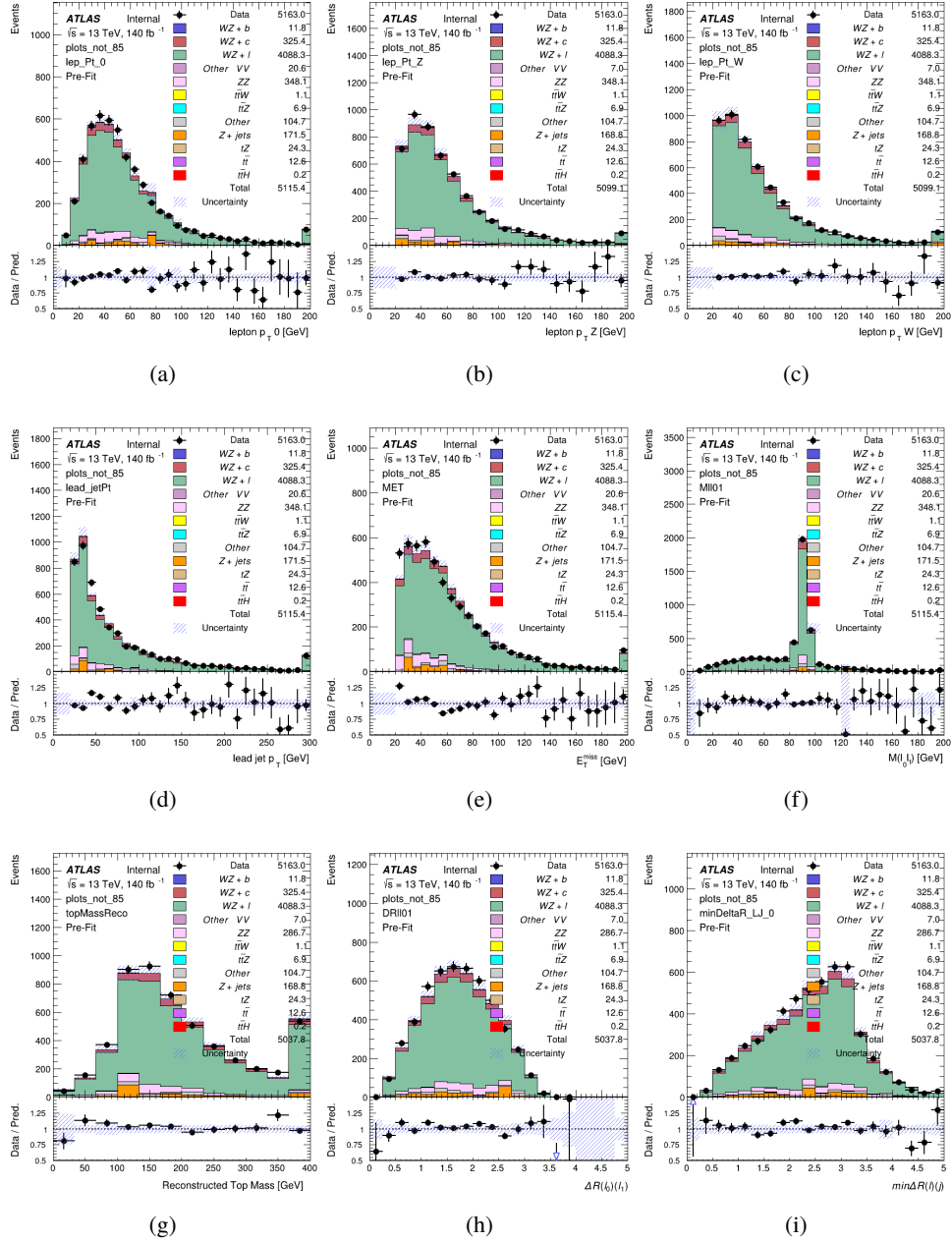


Figure 8.4: Comparisons between the data and MC distributions in the preselection region for (a) the p_T of the opposite sign lepton, (b) the p_T of the other lepton from the Z candidate, (c) the p_T of the lepton from the W candidate, (d) the leading jet p_T , (e) the E_T^{miss} , and (f) the invariant mass of leptons 0 and 1, (g) the reconstructed top mass, (h) $\Delta(R)$ between lepton 0 and 1, (i) the $\Delta(R)$ between the closest lepton and jet.

WZ Fit Region - 1j 77-85% WP

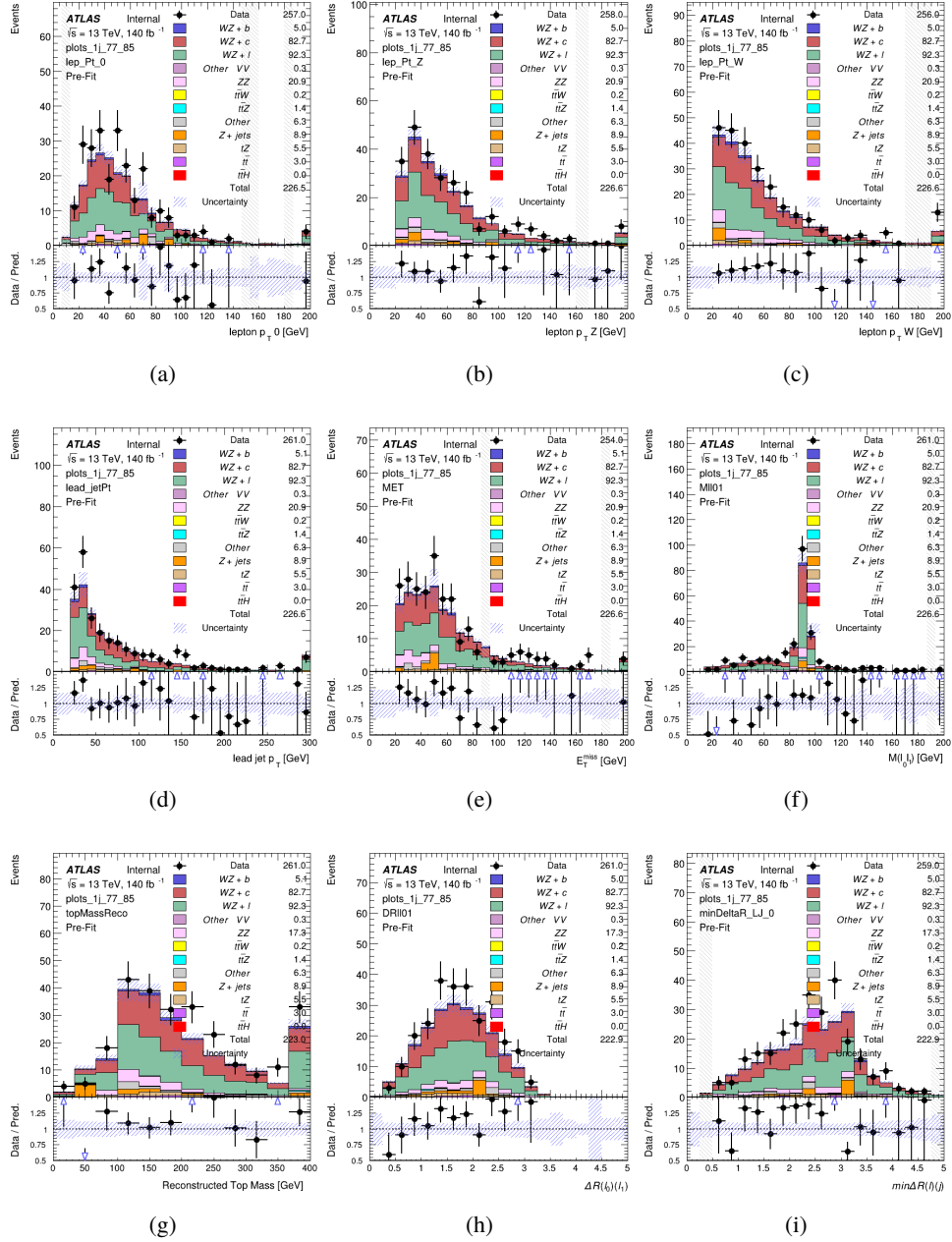


Figure 8.5: Comparisons between the data and MC distributions in the preselection region for (a) the p_T of the opposite sign lepton, (b) the p_T of the other lepton from the Z candidate, (c) the p_T of the lepton from the W candidate, (d) the leading jet p_T , (e) the E_T^{miss} , and (f) the invariant mass of leptons 0 and 1, (g) the reconstructed top mass, (h) $\Delta(R)$ between lepton 0 and 1, (i) the $\Delta(R)$ between the closest lepton and jet.

WZ Fit Region - 1j 70-77% WP

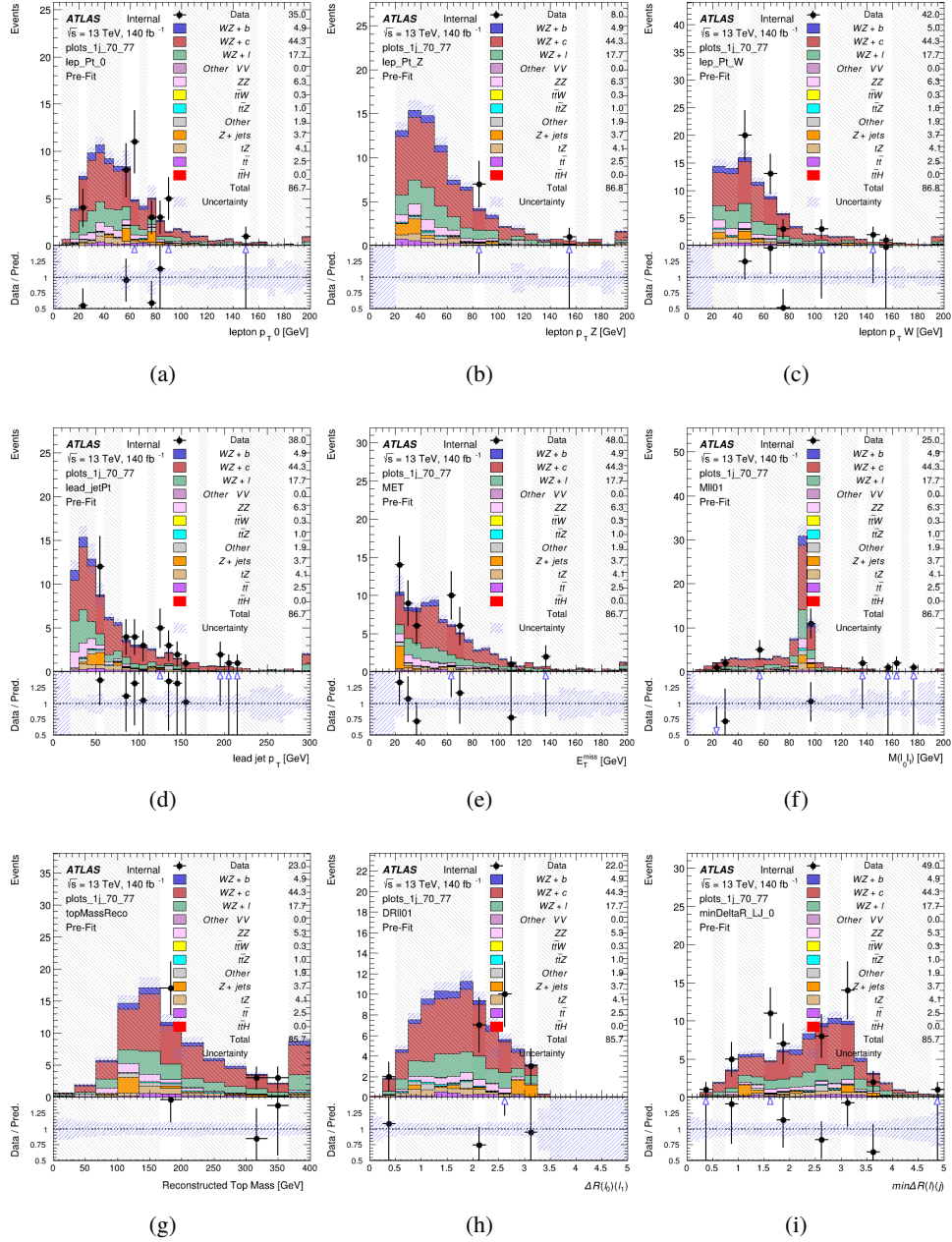


Figure 8.6: Comparisons between the data and MC distributions in the preselection region for (a) the p_T of the opposite sign lepton, (b) the p_T of the other lepton from the Z candidate, (c) the p_T of the lepton from the W candidate, (d) the leading jet p_T , (e) the E_T^{miss} , and (f) the invariant mass of leptons 0 and 1, (g) the reconstructed top mass, (h) $\Delta(R)$ between lepton 0 and 1, (i) the $\Delta(R)$ between the closest lepton and jet.

WZ Fit Region - 1j 60-70% WP

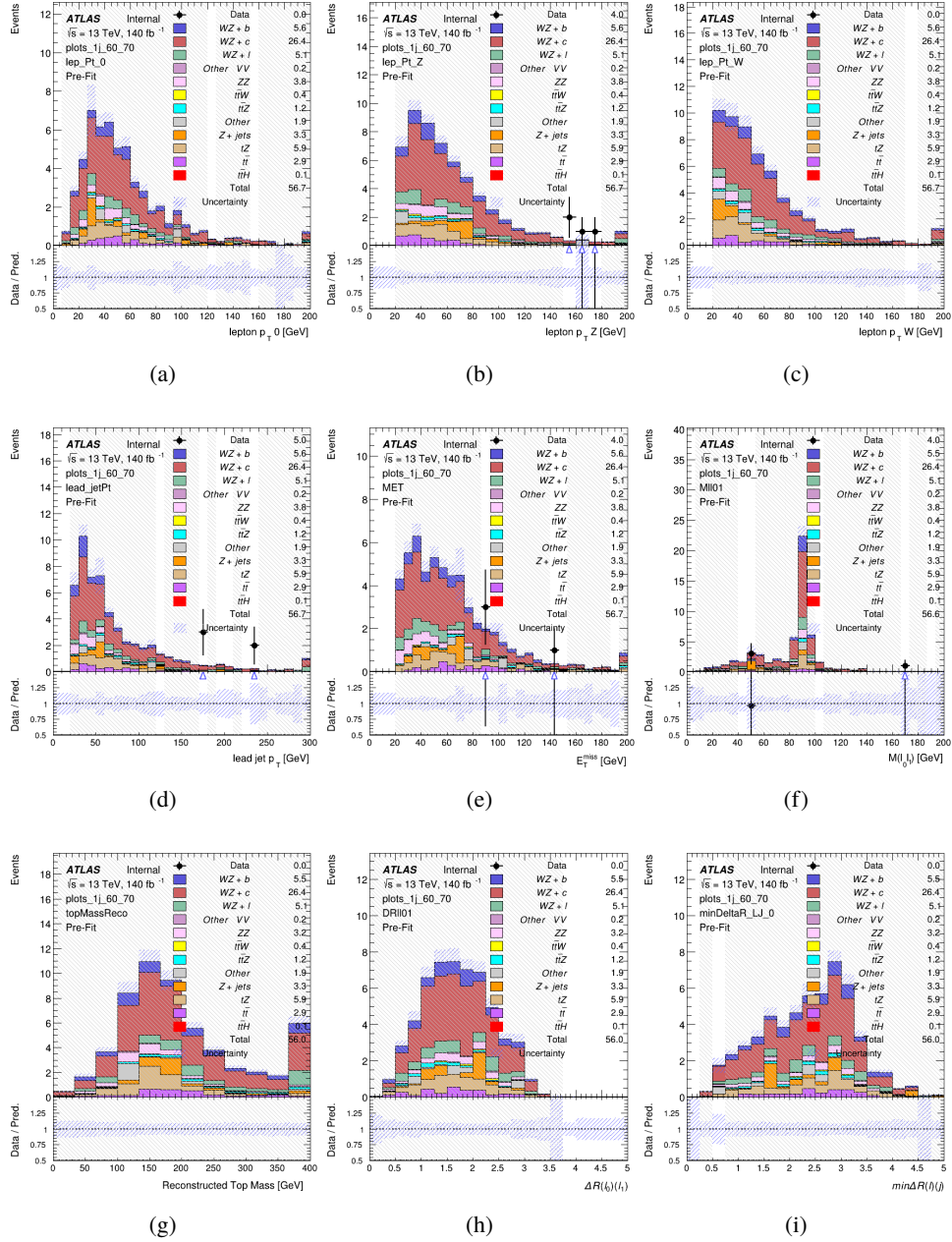


Figure 8.7: Comparisons between the data and MC distributions in the preselection region for (a) the p_T of the opposite sign lepton, (b) the p_T of the other lepton from the Z candidate, (c) the p_T of the lepton from the W candidate, (d) the leading jet p_T , (e) the E_T^{miss} , and (f) the invariant mass of leptons 0 and 1, (g) the reconstructed top mass, (h) $\Delta(R)$ between lepton 0 and 1, (i) the $\Delta(R)$ between the closest lepton and jet.

WZ Fit Region - 1j 60% WP

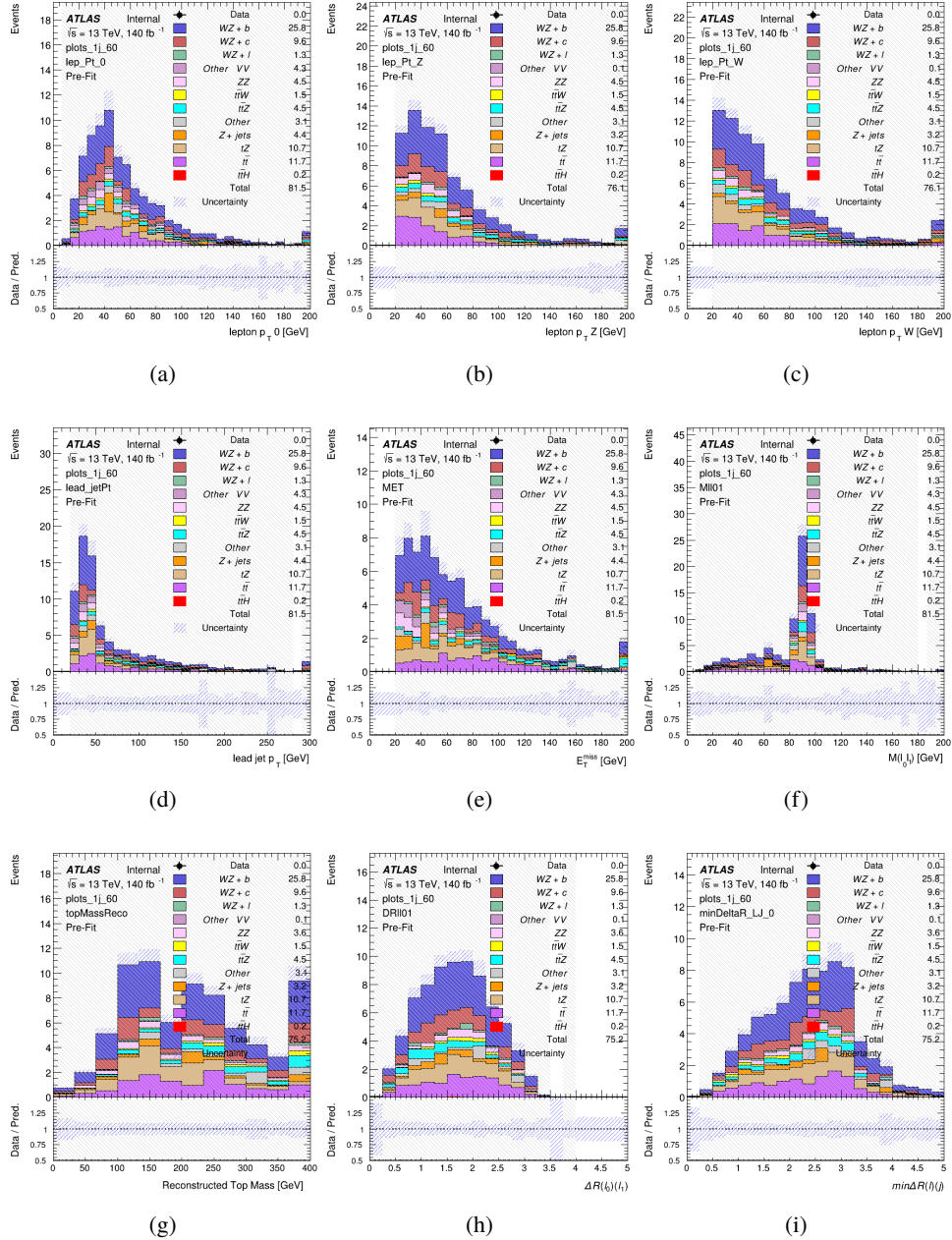


Figure 8.8: Comparisons between the data and MC distributions in the preselection region for (a) the p_T of the opposite sign lepton, (b) the p_T of the other lepton from the Z candidate, (c) the p_T of the lepton from the W candidate, (d) the leading jet p_T , (e) the E_T^{miss} , and (f) the invariant mass of leptons 0 and 1, (g) the reconstructed top mass, (h) $\Delta(R)$ between lepton 0 and 1, (i) the $\Delta(R)$ between the closest lepton and jet.

WZ Fit Region - tZ-CR

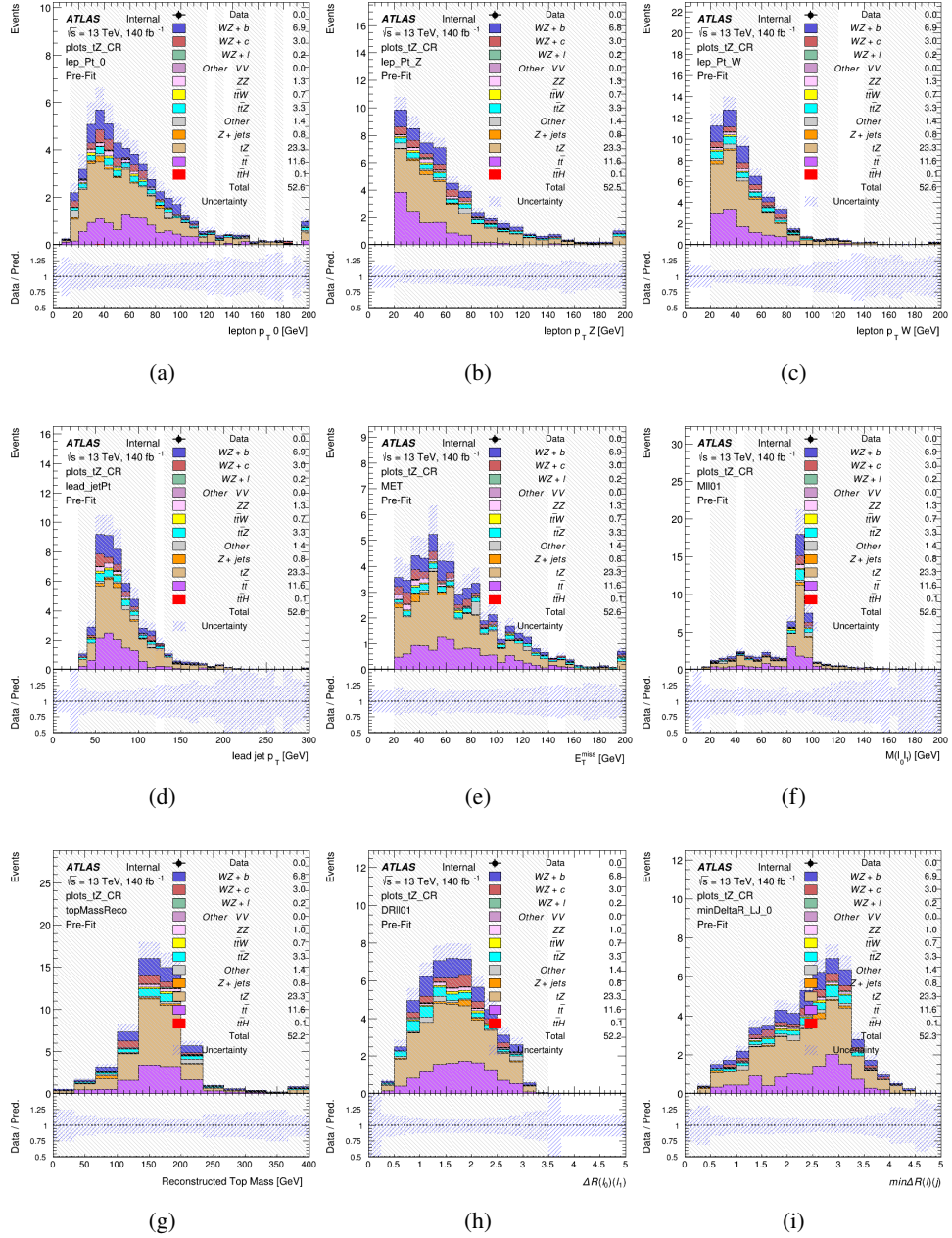


Figure 8.9: Comparisons between the data and MC distributions in the preselection region for (a) the p_T of the opposite sign lepton, (b) the p_T of the other lepton from the Z candidate, (c) the p_T of the lepton from the W candidate, (d) the leading jet p_T , (e) the E_T^{miss} , and (f) the invariant mass of leptons 0 and 1, (g) the reconstructed top mass, (h) $\Delta(R)$ between lepton 0 and 1, (i) the $\Delta(R)$ between the closest lepton and jet.

WZ Fit Region - 2j Inclusive

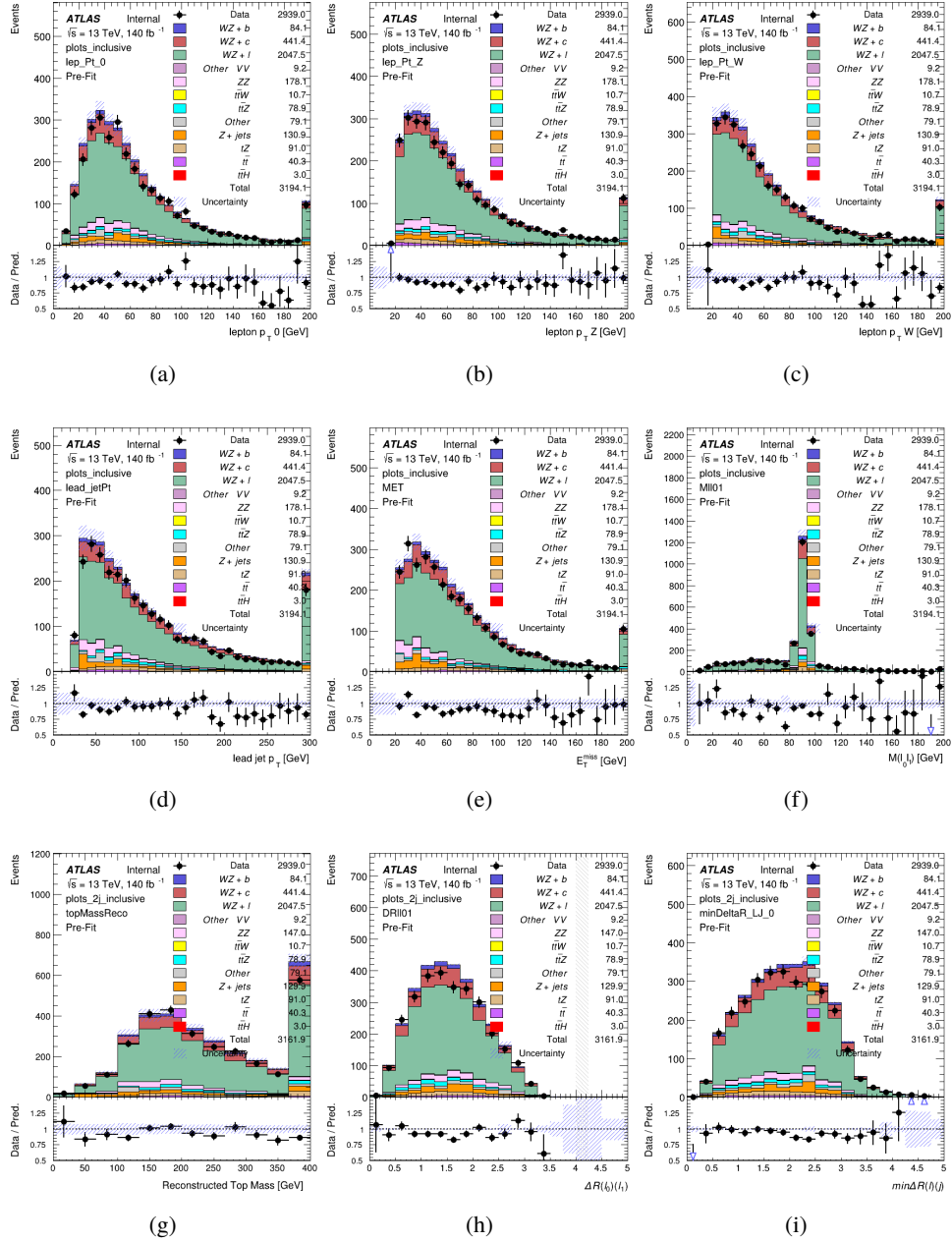


Figure 8.10: Comparisons between the data and MC distributions in the preselection region for (a) the p_T of the opposite sign lepton, (b) the p_T of the other lepton from the Z candidate, (c) the p_T of the lepton from the W candidate, (d) the leading jet p_T , (e) the E_T^{miss} , and (f) the invariant mass of leptons 0 and 1, (g) the reconstructed top mass, (h) $\Delta(R)$ between lepton 0 and 1, (i) the $\Delta(R)$ between the closest lepton and jet.

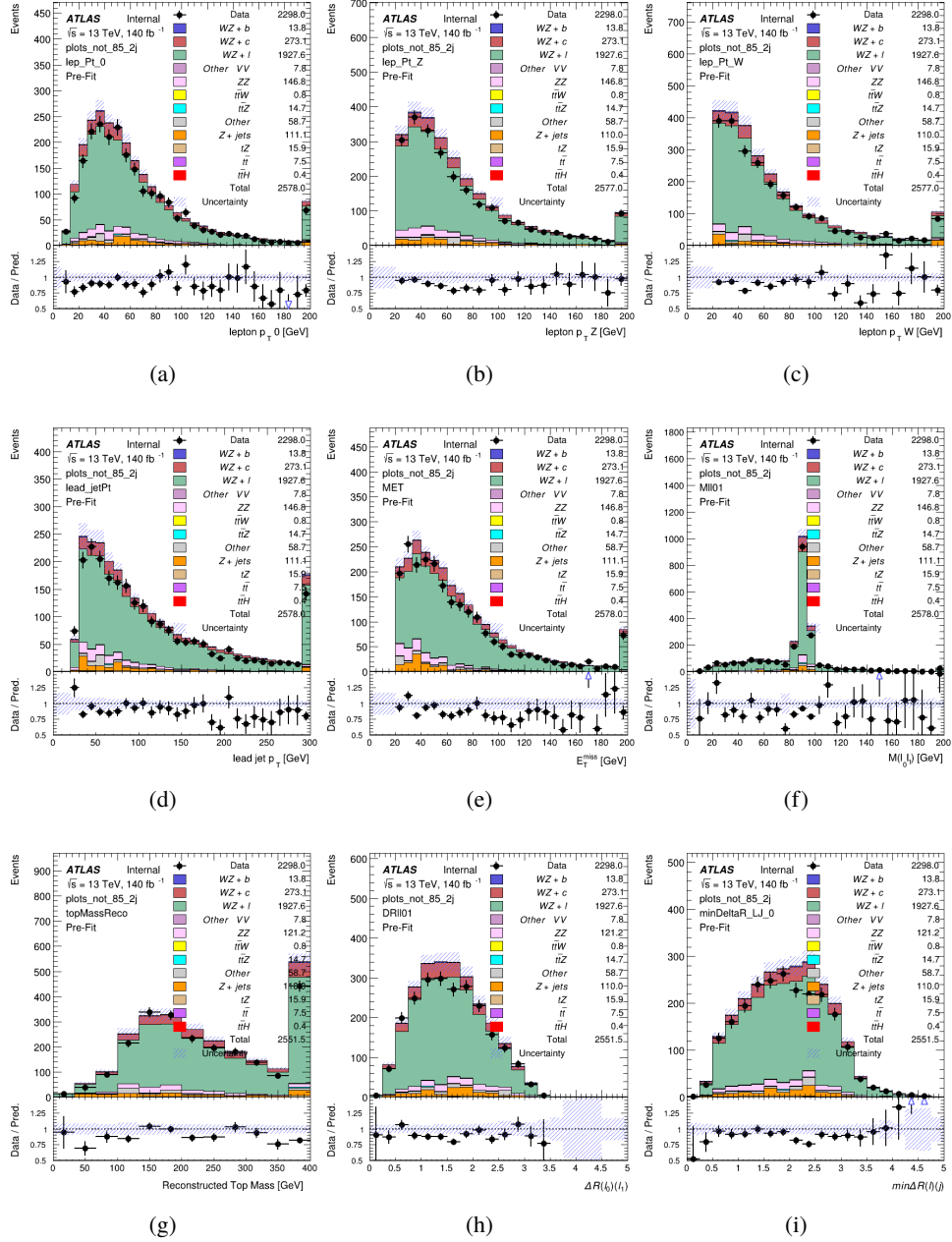
WZ Fit Region - $2j < 85\%$ WP

Figure 8.11: Comparisons between the data and MC distributions in the preselection region for (a) the p_T of the opposite sign lepton, (b) the p_T of the other lepton from the Z candidate, (c) the p_T of the lepton from the W candidate, (d) the leading jet p_T , (e) the E_T^{miss} , and (f) the invariant mass of leptons 0 and 1, (g) the reconstructed top mass, (h) $\Delta(R)$ between lepton 0 and 1, (i) the $\Delta(R)$ between the closest lepton and jet.

WZ Fit Region - 2j 77-85% WP

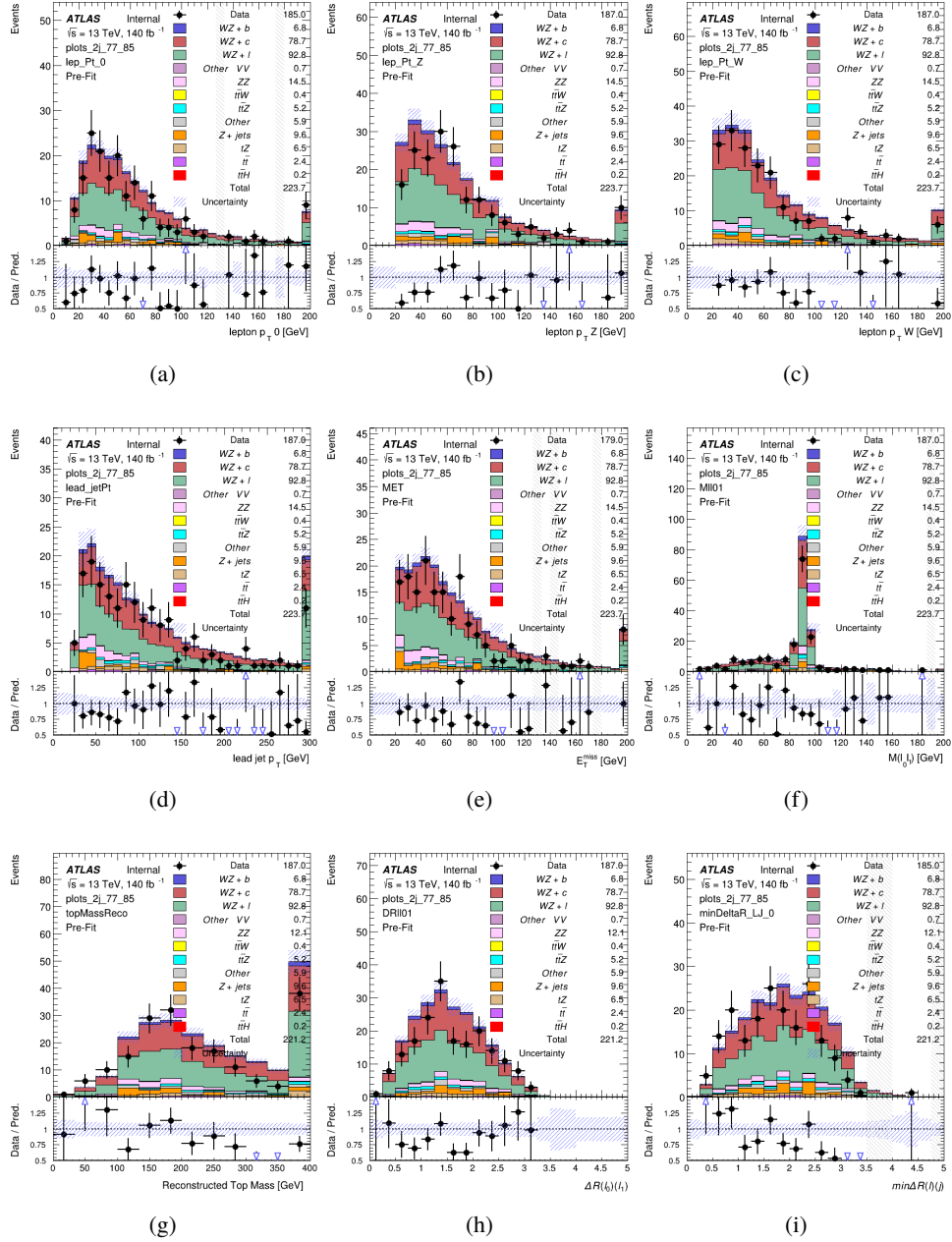


Figure 8.12: Comparisons between the data and MC distributions in the preselection region for (a) the p_T of the opposite sign lepton, (b) the p_T of the other lepton from the Z candidate, (c) the p_T of the lepton from the W candidate, (d) the leading jet p_T , (e) the E_T^{miss} , and (f) the invariant mass of leptons 0 and 1, (g) the reconstructed top mass, (h) $\Delta(R)$ between lepton 0 and 1, (i) the $\Delta(R)$ between the closest lepton and jet.

WZ Fit Region - 2j 70-77% WP

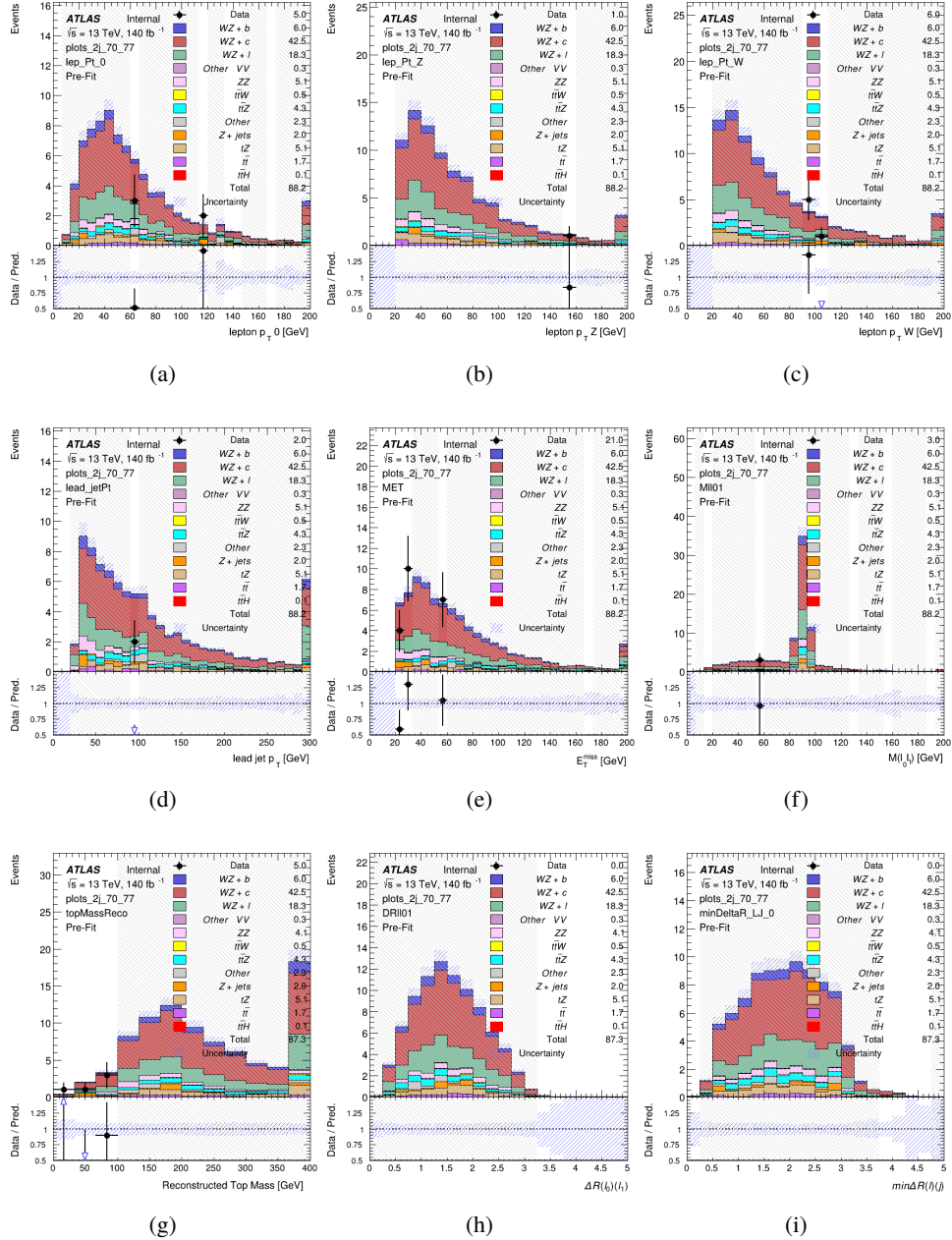


Figure 8.13: Comparisons between the data and MC distributions in the preselection region for (a) the p_T of the opposite sign lepton, (b) the p_T of the other lepton from the Z candidate, (c) the p_T of the lepton from the W candidate, (d) the leading jet p_T , (e) the E_T^{miss} , and (f) the invariant mass of leptons 0 and 1, (g) the reconstructed top mass, (h) $\Delta(R)$ between lepton 0 and 1, (i) the $\Delta(R)$ between the closest lepton and jet.

WZ Fit Region - 2j 60-70% WP

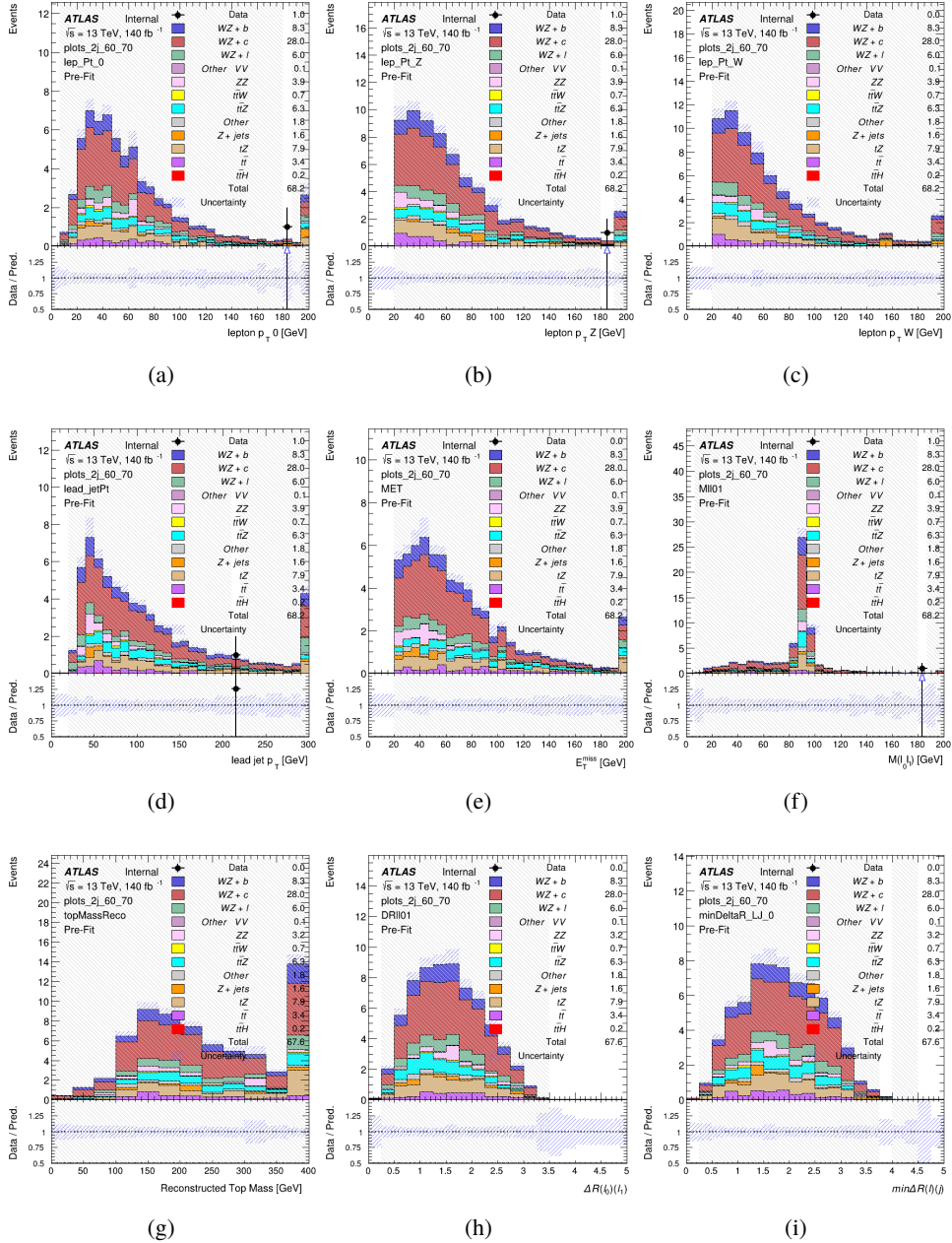


Figure 8.14: Comparisons between the data and MC distributions in the preselection region for (a) the p_T of the opposite sign lepton, (b) the p_T of the other lepton from the Z candidate, (c) the p_T of the lepton from the W candidate, (d) the leading jet p_T , (e) the E_T^{miss} , and (f) the invariant mass of leptons 0 and 1, (g) the reconstructed top mass, (h) $\Delta(R)$ between lepton 0 and 1, (i) the $\Delta(R)$ between the closest lepton and jet.

WZ Fit Region - 2j 60% WP

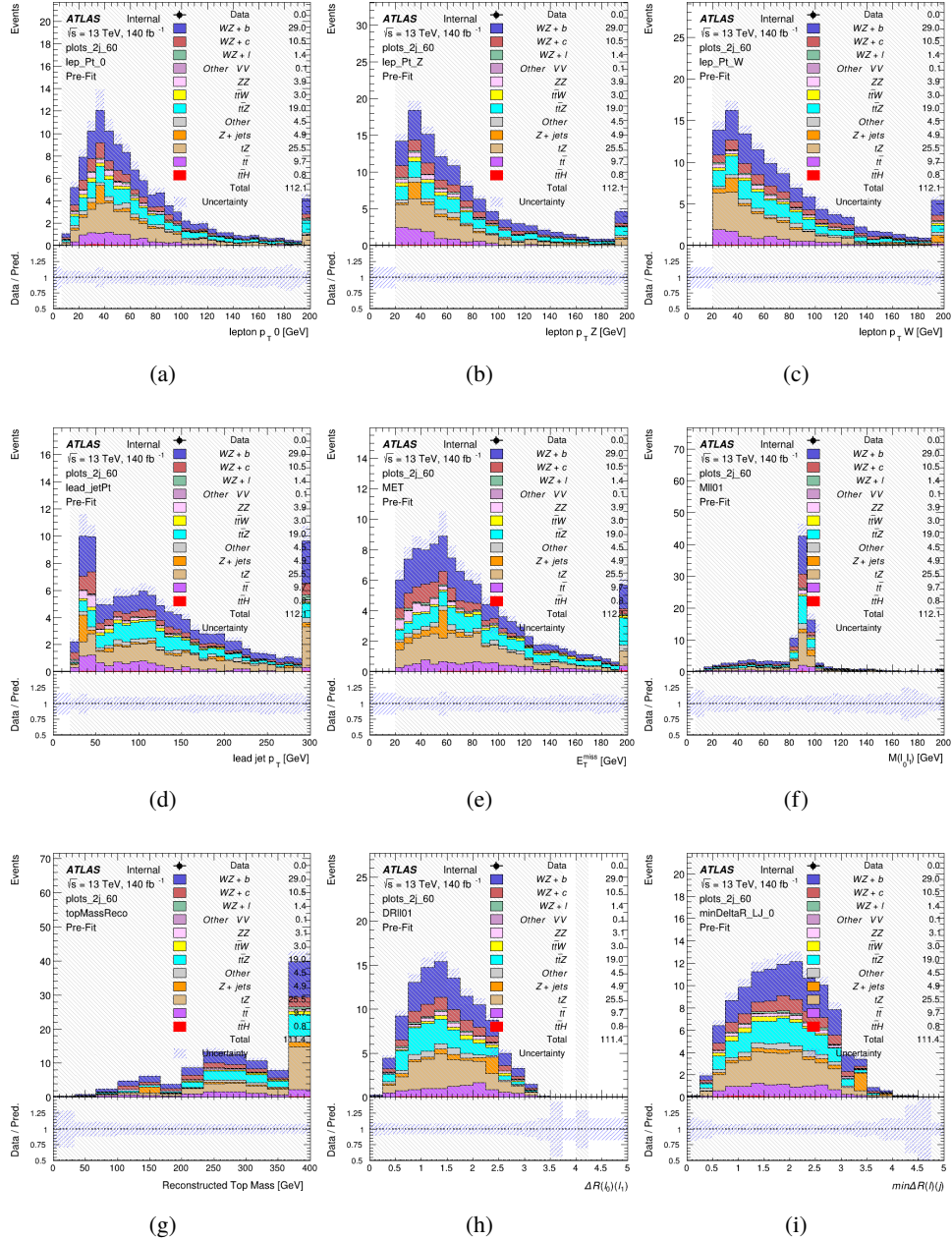


Figure 8.15: Comparisons between the data and MC distributions in the preselection region for (a) the p_T of the opposite sign lepton, (b) the p_T of the other lepton from the Z candidate, (c) the p_T of the lepton from the W candidate, (d) the leading jet p_T , (e) the E_T^{miss} , and (f) the invariant mass of leptons 0 and 1, (g) the reconstructed top mass, (h) $\Delta(R)$ between lepton 0 and 1, (i) the $\Delta(R)$ between the closest lepton and jet.

WZ Fit Region - tZ-CR-2j

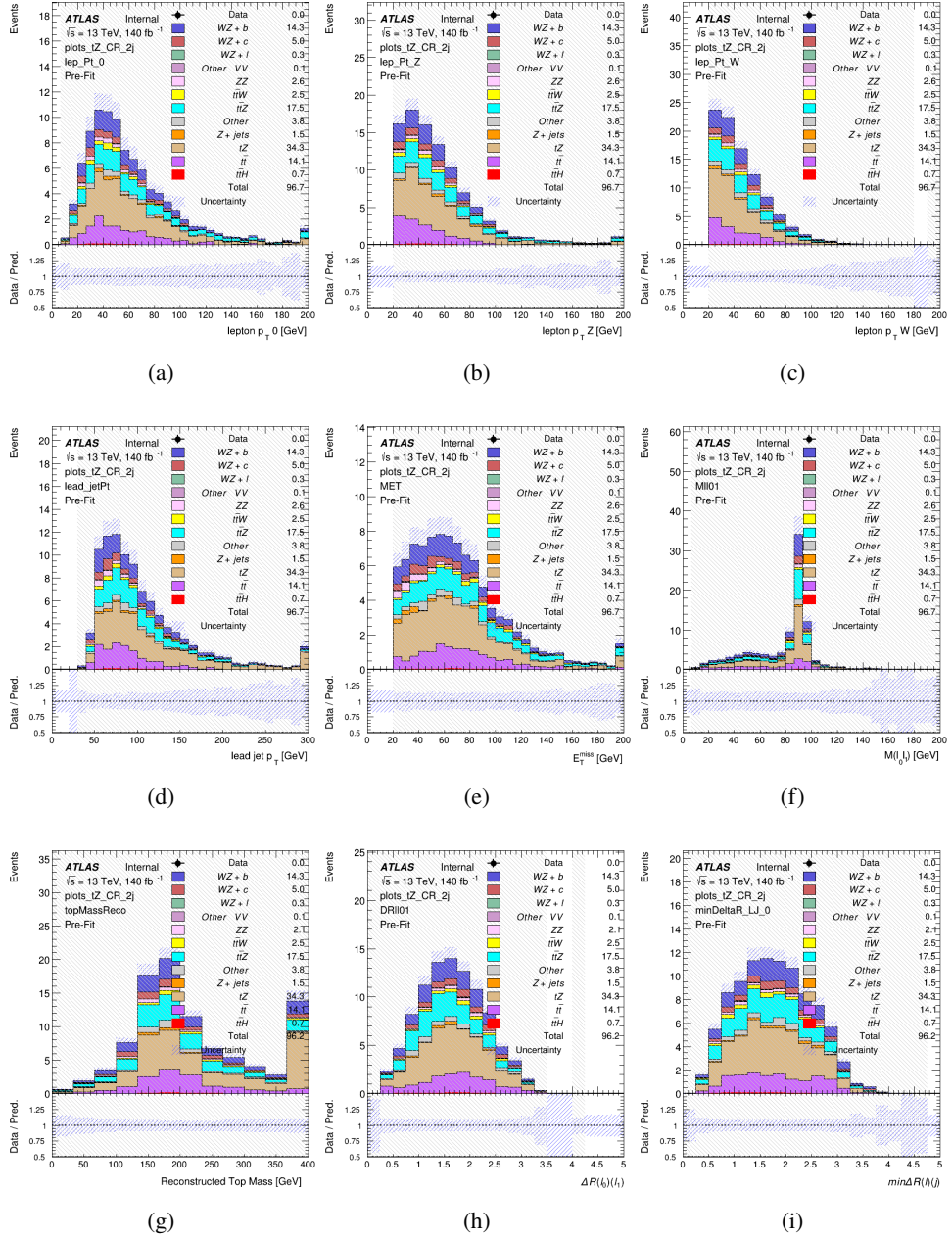


Figure 8.16: Comparisons between the data and MC distributions in the preselection region for (a) the p_T of the opposite sign lepton, (b) the p_T of the other lepton from the Z candidate, (c) the p_T of the lepton from the W candidate, (d) the leading jet p_T , (e) the E_T^{miss} , and (f) the invariant mass of leptons 0 and 1, (g) the reconstructed top mass, (h) $\Delta(R)$ between lepton 0 and 1, (i) the $\Delta(R)$ between the closest lepton and jet.

646 **8.3 Non-Prompt Lepton Estimation**

647 Two processes act as sources of non-prompt leptons appear in the analysis: $t\bar{t}$ and Z+jet
 648 production both produce two prompt leptons, and each contribute to the 31 region when an
 649 additional non-prompt lepton appears in the event. The contribution of these processes is
 650 estimated with Monte Carlo simulations, which are validated using enriched control regions.

651 **8.3.1 $t\bar{t}$ Validation**

652 $t\bar{t}$ events can produce two prompt leptons from the decay of each of the tops. These top decays
 653 produce two b-quarks, the decay of which can produce additional non-prompt leptons, which
 654 occasionally pass the event preselection. In order to validate that the Monte Carlo accurately
 655 simulates this process accurately, the MC prediction in a non-prompt $t\bar{t}$ enriched control region
 656 is compared to data.

657 The $t\bar{t}$ control region is similar to the preselection region - three leptons meeting the
 658 criteria described in Section 12 are required, and the requirements on E_T^{miss} remain the same.
 659 However, the selection requiring a lepton pair form a Z-candidate are reversed. Events where the
 660 invariant mass of any two opposite sign, same flavor leptons falls within 10 GeV of 91.2 GeV are
 661 rejected. This ensures the $t\bar{t}$ control region is orthogonal to the preselection region.

662 Further, because the jet multiplicity of $t\bar{t}$ events tends to be higher than WZ, the number
 663 of jets in each event is required to be greater than 1. As b-jets are almost invariably produced

⁶⁶⁴ from top decays, at least one b-tagged jet passing the 70% DL1r WP in each event is required.

⁶⁶⁵ Various kinematic plots of this region are shown in Figure 12.17.

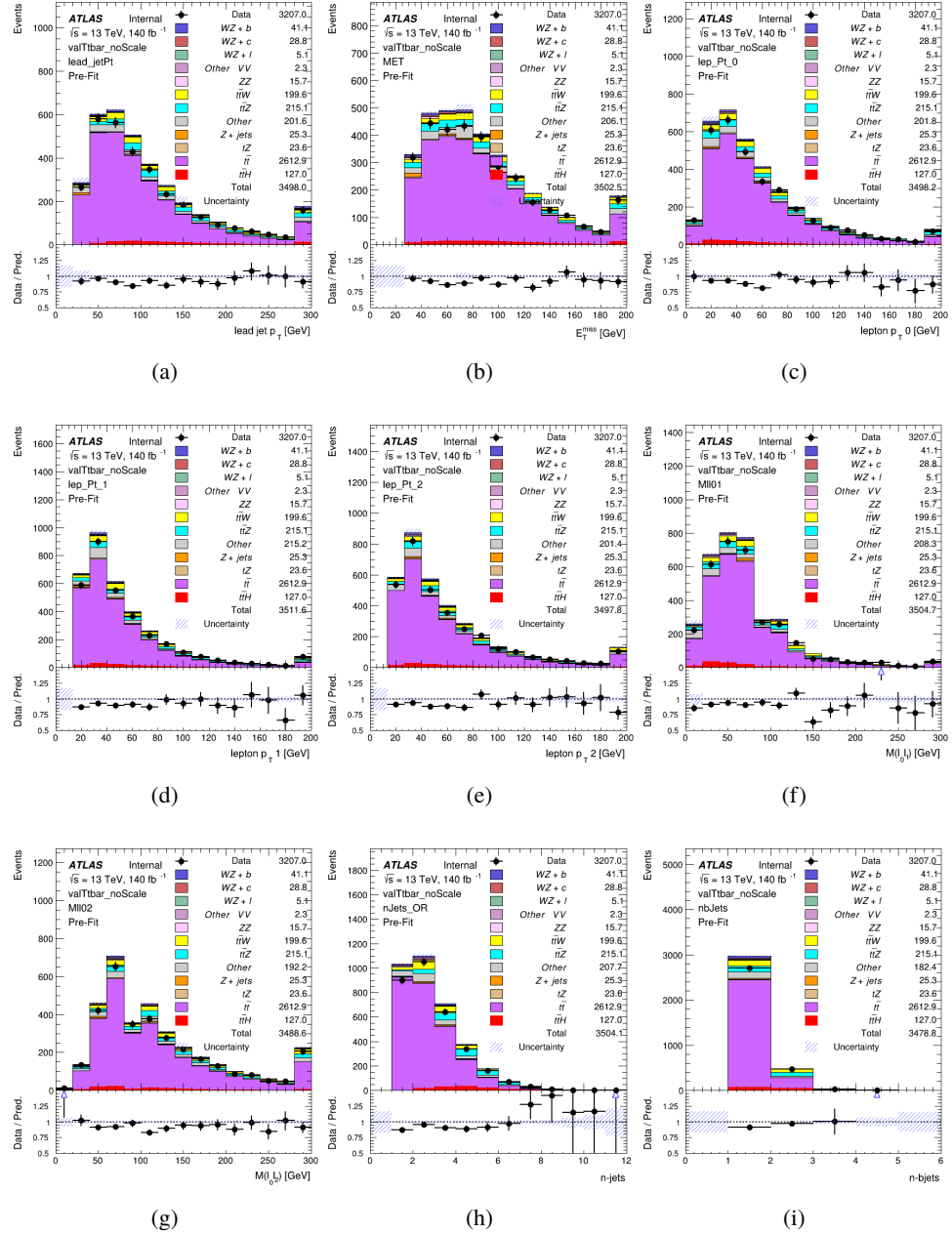


Figure 8.17: Comparisons between the data and MC distributions in the $t\bar{t}$ control region for (a) the p_T of the leading jet, (b) the missing transverse energy, (c) the p_T of lepton 0, (d) p_T of lepton 1, (e) p_T of lepton 2, (f) the invariant mass of leptons 0 and 1, (g) the invariant mass of leptons 0 and 2, (h) the number of jets, (i) the number of b-tagged jets.

666 The shape of each distribution agrees quite well between data and MC, with a constant
667 offset between the two. This is accounted for by applying a constant correction factor of 0.883
668 to the $t\bar{t}$ MC prediction. Plots showing the kinematics of the $t\bar{t}$ VR after this correction factor
669 has been applied are shown in Figure 12.18.

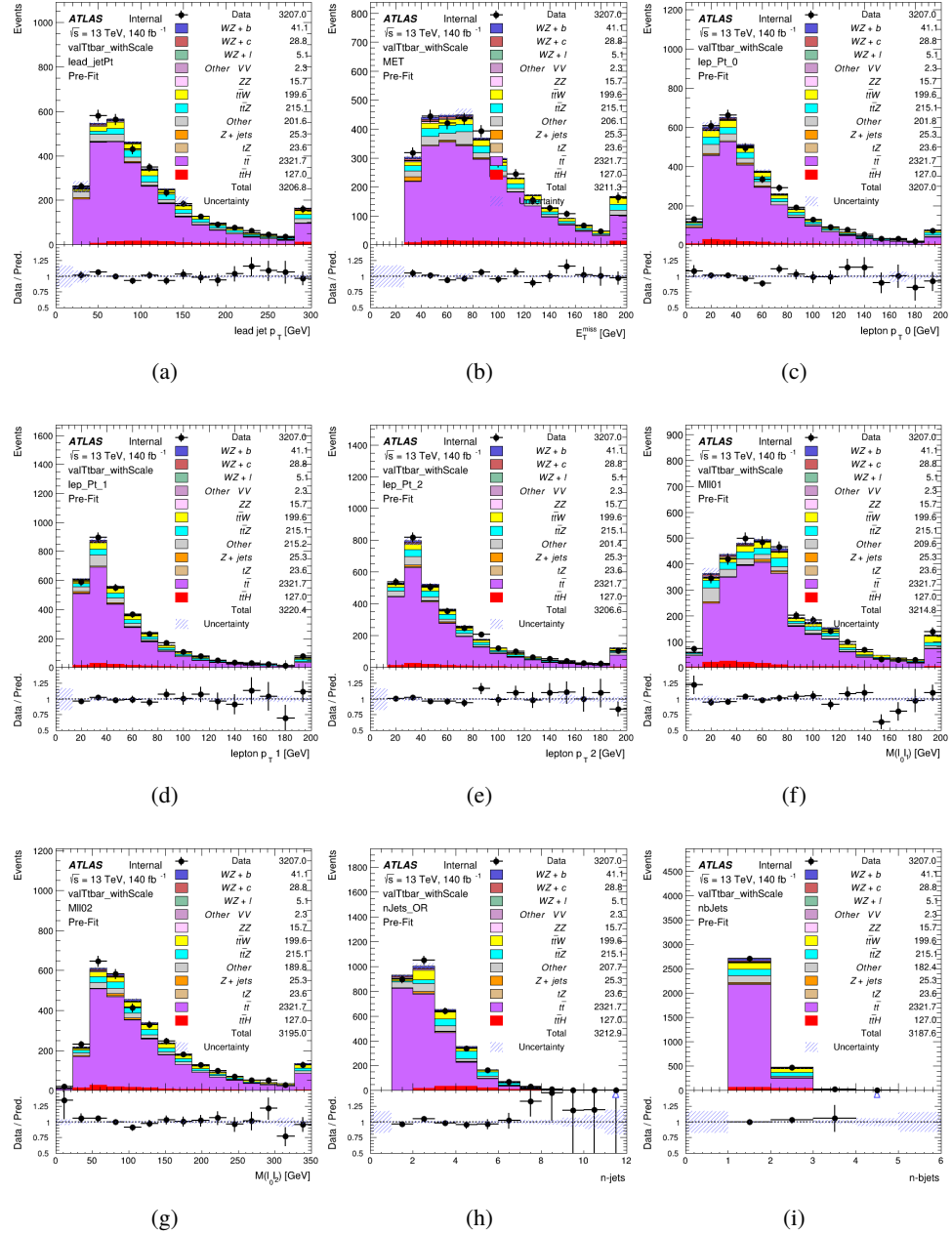


Figure 8.18: Comparisons between the data and MC distributions in the $t\bar{t}$ control region after the correction factor has been applied for (a) the p_T of the leading jet, (b) the missing transverse energy, (c) the p_T of lepton 0, (d) p_T of lepton 1, (e) p_T of lepton 2, (f) the invariant mass of leptons 0 and 1, (g) the invariant mass of leptons 0 and 2, (h) the number of jets, (i) the number of b-tagged jets.

670 The modeling is further validated by looking at the yield in the $t\bar{t}$ VR for each DL1r WP,
 671 giving a clearer correspondence to the signal regions used in the fit. Each region shown in Figure
 672 12.19 requires one or more jets pass the listed WP, with no jets passing the next highest WP.

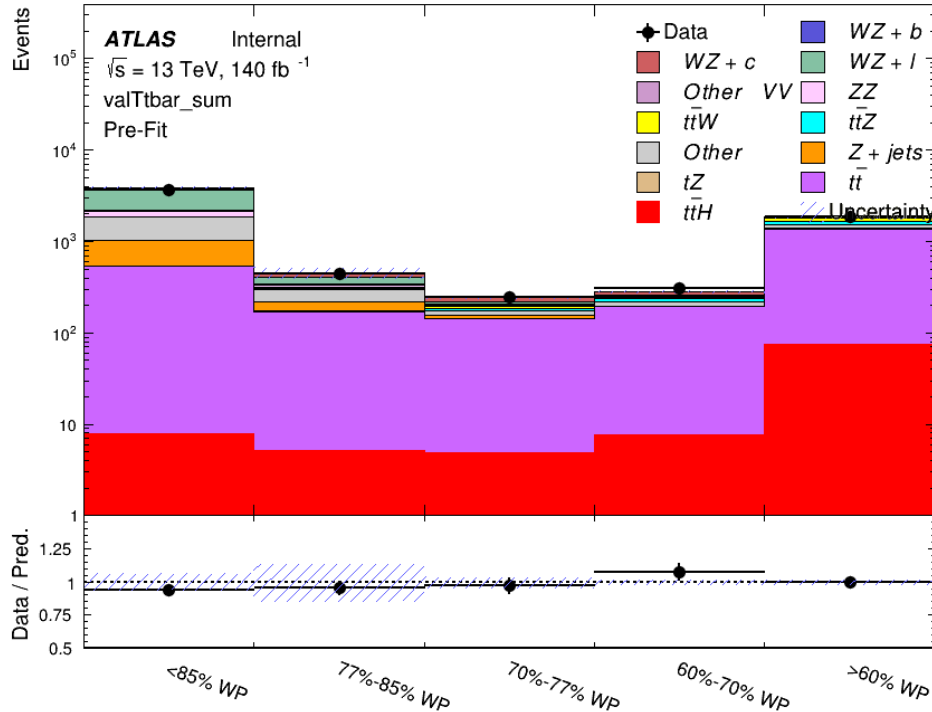


Figure 8.19: Data and MC comparisons for each DL1r WP for both 1-jet and 2-jet regions, after the $t\bar{t}$ VR selection and correction factor have been applied

673 As data and MC are found to agree within 20% for each of these working points, a 20%
 674 systematic uncertainty on the $t\bar{t}$ prediction is included for the analysis.

675 **8.3.2 Z+jets Validation**

676 Similar to $t\bar{t}$, a non-prompt Z +jets control region is produced in order to validate the MC
677 predictions. The lepton requirements remain the same as the preselection region. Because no
678 neutrinos are present for this process, the E_T^{miss} cut is reversed, requiring $E_T^{\text{miss}} < 30 \text{ GeV}$. This
679 also ensures this control region is orthogonal to the preselection region. Further, the number of
680 jets in each event is required to be greater than or equal to one. Various kinematic plots of this
681 region are shown below. The general agreement between data and MC in each of these suggests
682 that the non-prompt contribution of Z +jets is well modeled by Monte Carlo.

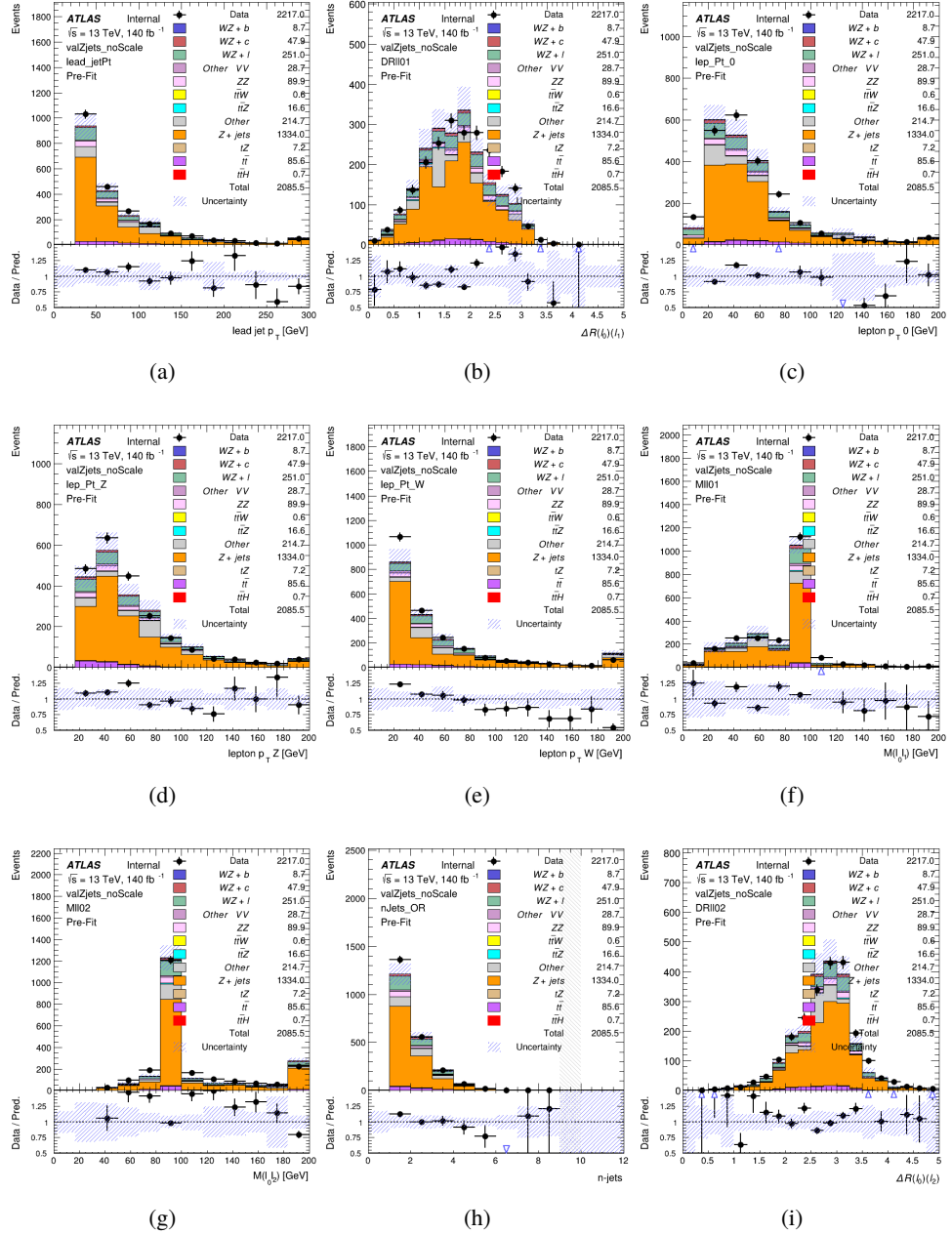


Figure 8.20: Comparisons between the data and MC distributions in the $Z + \text{jets}$ control region for (a) the p_T of the leading jet, (b) ΔR between leptons 0 and 1, (c) the p_T of lepton 0, (d) p_T of SS lepton from the Z candidate, (e) p_T of the SS lepton from the W candidate, (f) the invariant mass of leptons 0 and 1, (g) the invariant mass of leptons 0 and 2, (h) the number of jets, (i) ΔR between leptons 0 and 2. Includes only statistical uncertainties

683 While there is general agreement between data and MC within statistical uncertainty, the
684 shape of the p_T spectrum of the lepton from the W is found to differ. To account for this
685 discrepancy, a variable correction factor is applied to Z+jets. χ^2 minimization of the lepton 2 p_T
686 spectrum is performed to derive a correction factor of $1.53 - 6.6 * 10^{-6}(\text{lep}_\text{Pt}_W)$. Kinematic
687 plots of the Z + jets control region after this correction factor has been aplied are shown in Figure
688 [12.21](#).

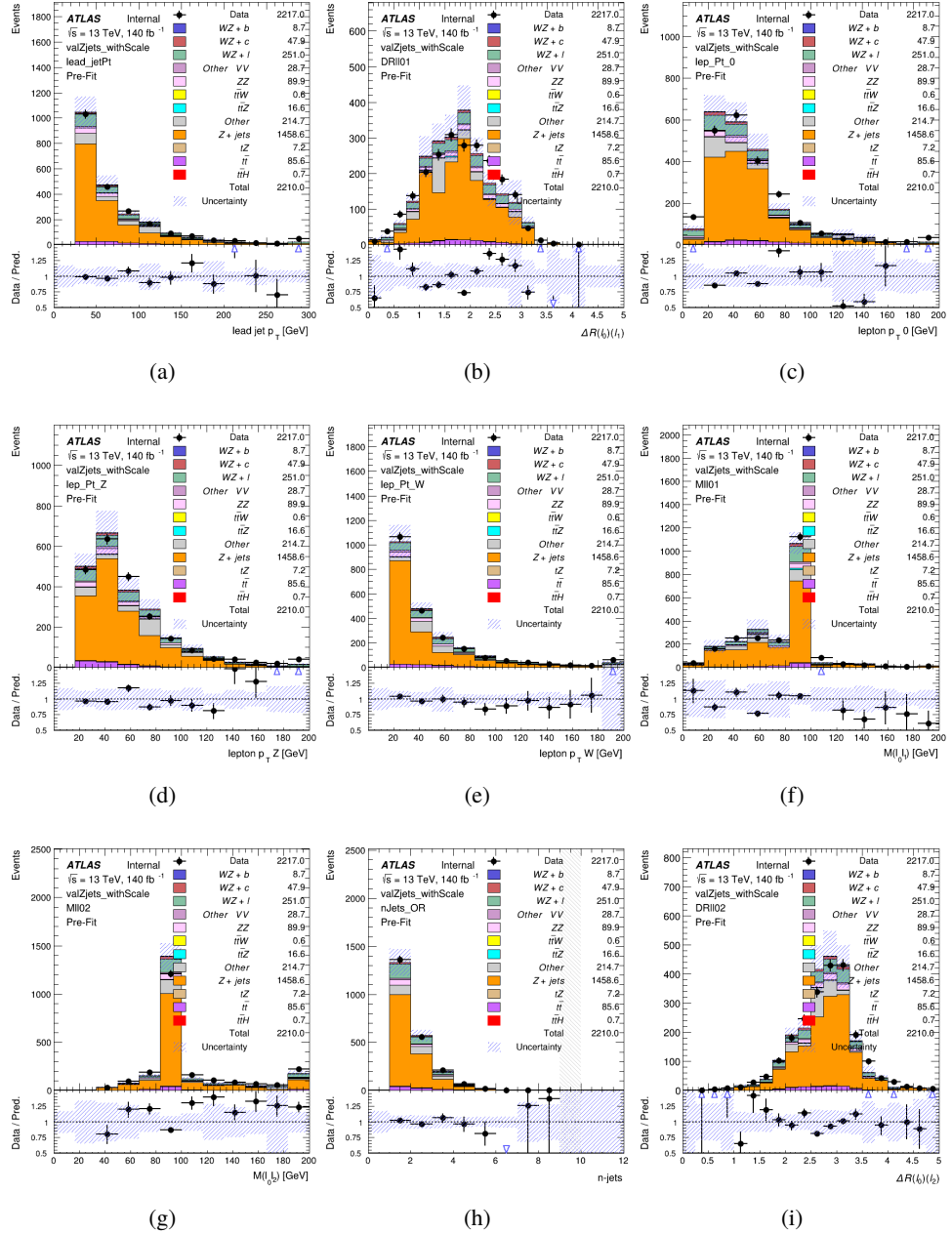


Figure 8.21: Comparisons between the data and MC distributions in the $Z + \text{jets}$ control region after the correction factor has been applied for (a) the p_T of the leading jet, (b) ΔR between leptons 0 and 1, (c) the p_T of lepton 0, (d) p_T of SS lepton from the Z candidate, (e) p_T of the SS lepton from the W candidate, (f) the invariant mass of leptons 0 and 1, (g) the invariant mass of leptons 0 and 2, (h) the number of jets, (i) ΔR between leptons 0 and 2

689 The modeling is further validated by looking at the yield in the Z+jets VR for each DL1r
 690 WP, giving a clearer correspondence to the signal regions used in the fit. Each region shown in
 691 Figure 12.22 requires one or more jets pass the listed WP, with no jets passing the next highest
 692 WP.

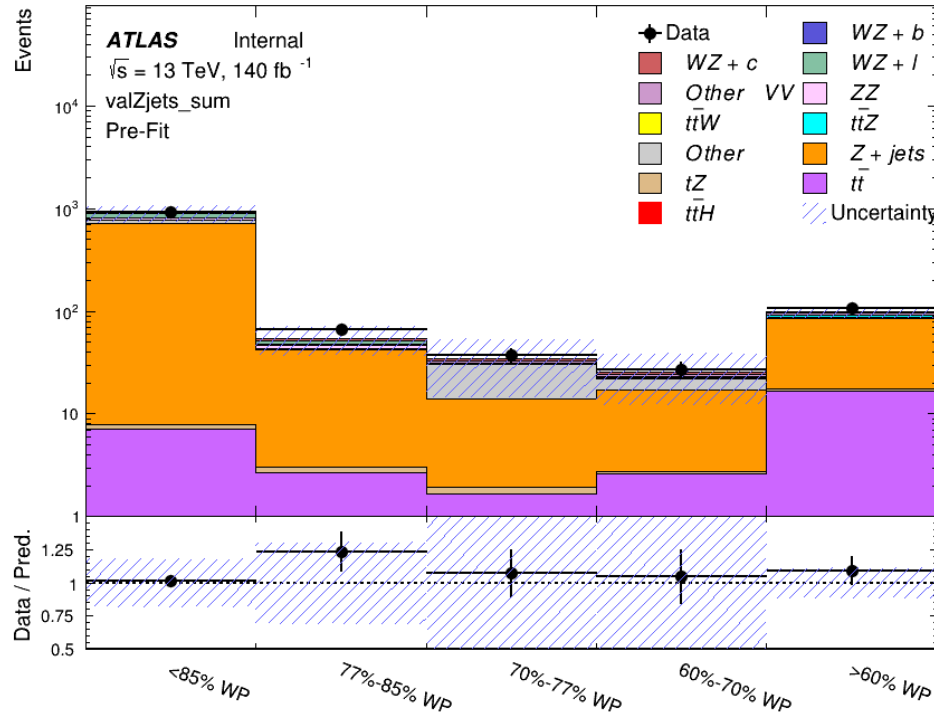


Figure 8.22: Data and MC comparisons for each DL1r WP for both 1-jet and 2-jet regions, after the Z+jets VR selection and correction factor have been applied

693 For each of the b-tagging working points considered, the data falls within 25% of the MC
 694 prediction once this correction factor has been applied. Therefore, a 25% systematic uncertainty
 695 is applied to Z + jets in the analysis.

696 9 tZ Interference Studies and Separation Multivariate Analysis

697 Because tZ produces a final state identical to signal, it represents a predominant background in
698 the most signal enriched regions. That is, the region with one jet passing the 60% DL1r WP.
699 Therefore, a boosted decision tree (BDT) algorithm is trained using TMVA [TMVA_guide] to
700 separate WZ + heavy flavor from tZ.

701 Separation between tZ and WZ + heavy flavor is achieved in part by reconstructing the
702 invariant mass of the top candidate, which clusters more closely to the top mass for tZ than WZ
703 + heavy flavor.

704 The result of this BDT is used to create a tZ enriched region in the fit, reducing its impact
705 on the measurement of WZ + heavy flavor.

706 9.1 Top Mass Reconstruction

707 The reconstruction of the top mass follows the procedure described in detail in section 6.1 of
708 [ttZ_paper]. The mass of the top quark candidate is reconstructed from the jet, the lepton not
709 included in the Z-candidate, and a reconstructed neutrino. In the case that there is one jet in the
710 event, there is only possible b-jet candidate. For events with two jets, the jet with the highest
711 DL1r score is used.

712 The neutrino from the W decay is expected to be the only source of E_T^{miss} . Therefore, the
 713 E_T and ϕ of the neutrino are taken from the E_T^{miss} measurement. This leaves the z-component
 714 of the neutrino momentum, $p_{\nu z}$ as the only unknown.

715 This unknown is solved for by taking the combined invariant mass of the lepton and
 716 neutrino to give the invariant mass of the W boson:

$$717 \quad (p_l + p_\nu)^2 = m_W^2$$

718 Expanding this out into components, this equation gives:

$$719 \quad \sqrt{p_{T\nu}^2 + p_{z\nu}^2} E_l = \frac{m_W^2 - m_l^2}{2} + p_{T\nu}(p_{lx}\cos\phi_\nu + p_{ly}\sin\phi_\nu) + p_{lz}p_{\nu z}$$

720 This equation gives two solutions for $p_{\nu z}$. For cases where only one of these solutions is
 721 real, that is taken as the value of $p_{\nu z}$. For instances with two real solutions, the one which is
 722 shown to be correct in the largest fraction of simulations is taken. For cases when no real solution
 723 is found, often because of detector effects, the value of E_T^{miss} is varied in decreasing increments
 724 of 100 MeV until a real solution is found.

725 The reconstructed top mass distribution for tZ and WZ + b can be seen in figure 13.1.

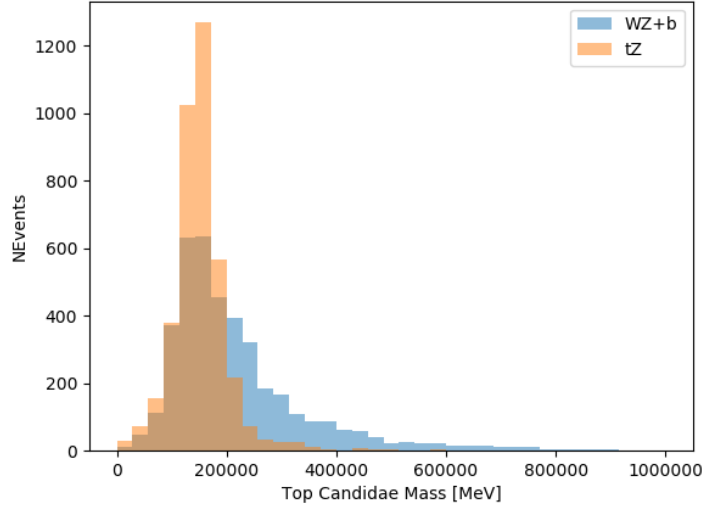


Figure 9.1: Reconstructed top mass distributions for tZ and WZ + b, measured in MeV.

726 9.2 tZ BDT

727 A Boosted Decision Tree (BDT), specifically XGBoost [xgboost_cite], is used to provide separ-
 728 ation between tZ and WZ+b. The following kinematic variables are used as inputs:

- 729 • The invariant mass of the reconstructed top candidate
- 730 • p_T of each of the leptons, jet
- 731 • The invariant mass of each combination of lepton pairs, $M(l\bar{l})$
- 732 • E_T^{miss}
- 733 • Distance between each combination of leptons, $\Delta R(l\bar{l})$

- 734 • Distance between each lepton and the jet, $\Delta R(lj)$

735 The training samples included only events meeting the requirements of the 1-jet, >60%
736 region, i.e. passing all the selection described in section 12 and having exactly one jet which
737 passes the tightest (60%) DL1r working point.

738 The distributions of a few of these features for both signal and background is shown in
739 figure 13.2.

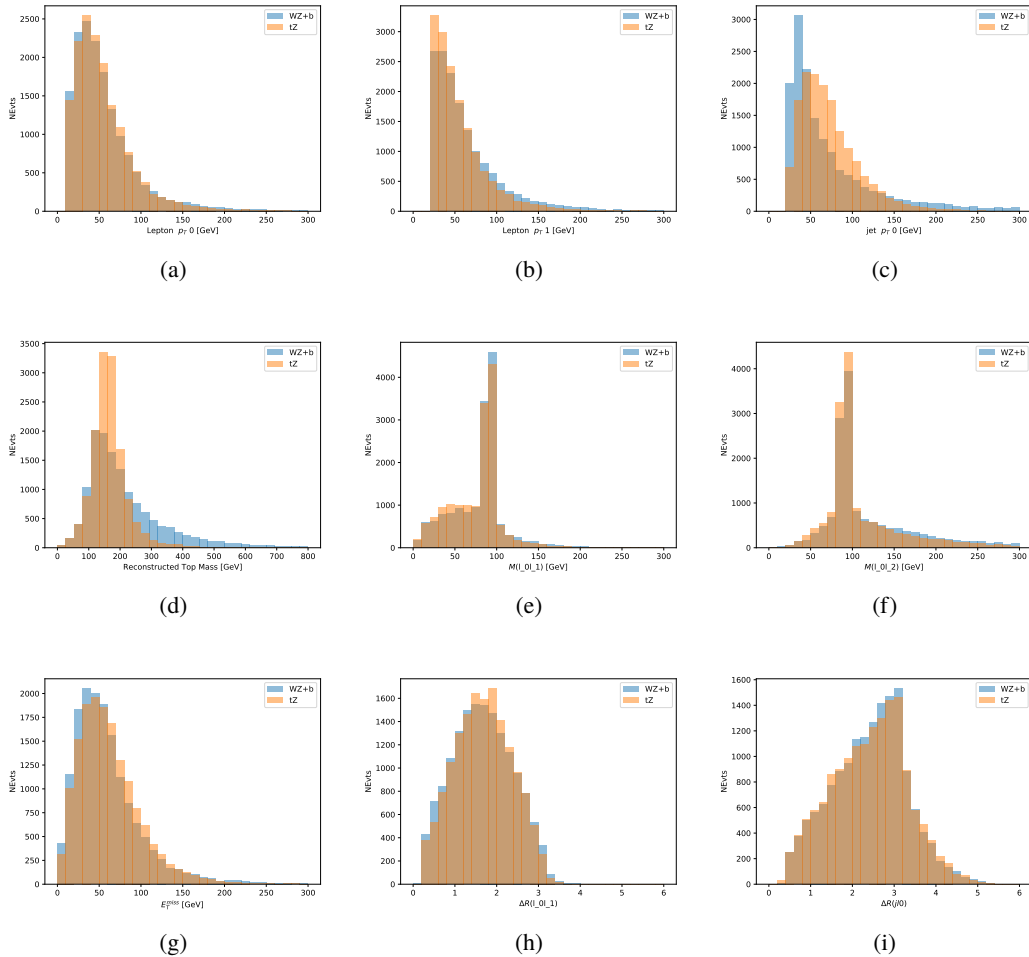


Figure 9.2: Distribution of input features of the BDT for signal (WZ) and background (tZ). Both are scaled to an equal number of events. (a), (b) and (c) show the p_T of lepton 0, lepton 1, and the jet, (d) show the reconstructed top mass, (e) and (f) show the invariant mass of leptons 0 and 1, leptons 0 and 2. (g) shows the E_T^{miss} of each event. (h) and (i) show the ΔR between lepton 0 and lepton 1, and the jet.

740 A sample of 20,000 background (tZ) and signal (WZ+b) Monte Carlo events are used to
 741 train the BDT. And additional 5,000 events are reserved for testing the model, in order to prevent
 742 over-fitting. A total of 750 decision trees with a maximum depth of 6 branches are used to build
 743 the model. These parameters are chosen empirically, by training several models with different

744 parameters and selecting the one that gave the best separation for the test sample.

745 The results of the BDT training are shown in figure 13.3. The output scores for both signal
 746 and background events is shown on the left. The right shows the receiving operating characteristic
 747 (ROC) curve that results from the MVA. The ROC curve represents the background rejection
 748 as a function of signal efficiency, where each point on the curve represents a different response
 749 score. The ROC curve of the BDT is compared to the performance of using an optimal set of flat
 750 selections on the same set of input variables.

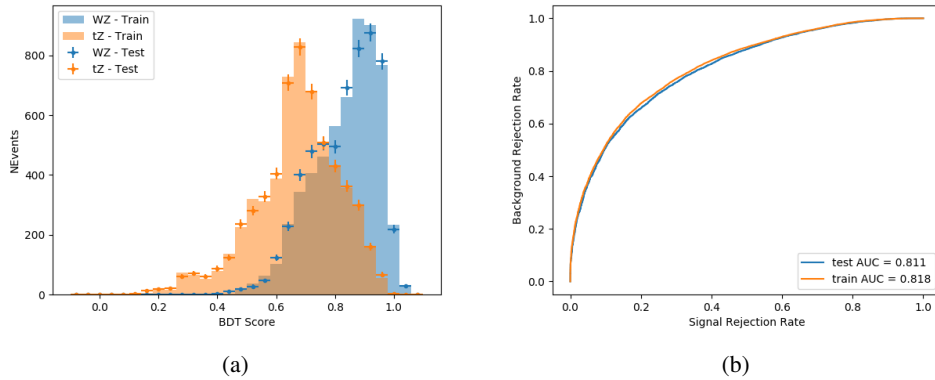


Figure 9.3: Distribution of the BDT response for signal and background events on the left, the ROC curve for the BDT on the right.

751 The relative important of each input feature in the model, measured by how often they
 752 appeared in the decision trees, is shown in figure 13.4.

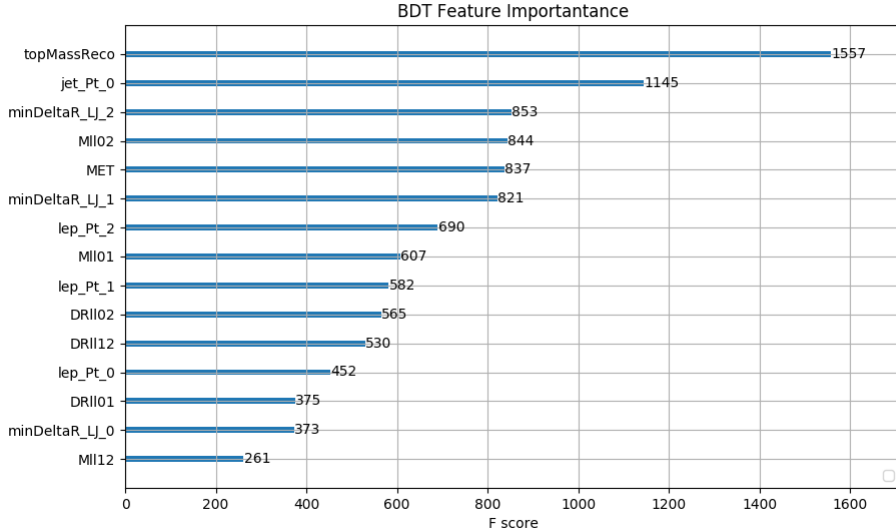


Figure 9.4: Relative importance of each input feature in the model.

753 These results suggest that some amount of separation can be achieved between these two
 754 processes, with a high BDT score selecting a set of events that is pure in $WZ + b$. A BDT score
 755 of 0.725 is selected as a cutoff, where events with scores higher than this form a signal enriched
 756 region, and events with scores lower than this form a $t\bar{Z}$ control region. This cutoff is selected by
 757 varying the value of this cutoff in stat-only Asimov fits, and selecting the value that minimizes
 758 the statistical uncertainty on $WZ + b$.

759 **10 Data and Monte Carlo Samples**

760 Both data and Monte Carlo samples used in this analysis were prepared in the xAOD format,
 761 which was used to produce a DxAOD sample in the HIGG8D1 derivation framework. The HIGG8D1

762 framework is designed for the $t\bar{t}H$ multi-lepton analysis, which targets events with multiple
763 leptons as well as tau hadrons. This framework skims the dataset to remove unneeded variables
764 as well as entire events. Events are removed from the derivations that do not meet the following
765 selection:

- 766 • at least two light leptons within a range $|\eta| < 2.6$, with leading lepton $p_T > 15$ GeV and
767 subleading lepton $p_T > 5$ GeV
- 768 • at least one light lepton with $p_T > 15$ GeV within a range $|\eta| < 2.6$, and at least two hadronic
769 taus with $p_T > 15$ GeV.

770 Samples were then generated from these HIGG8D1 derivations with p-tag of p4134 for data
771 and p4133 for Monte Carlo using AnalysisBase version 21.2.127 modified to include custom
772 variables.

773 **10.1 Data Samples**

774 The study uses a sample of proton-proton collision data collected by the ATLAS detector from
775 2015 through 2018 at an energy of $\sqrt{s} = 13$ TeV, which represents an integrated luminosity of
776 139 fb^{-1} . This data set was collected with a bunch crossing rate of 25 ns. All data used in this
777 analysis was verified by data quality checks, having been included in the following Good Run
778 Lists:

- 779 • data15_13TeV.periodAllYear_DetStatus-v79-repro20-02_DQDefects-00-02-02
780 _PHYS_StandardGRL_All_Good_25ns.xml
- 781 • data16_13TeV.periodAllYear_DetStatus-v88-pro20-21_DQDefects-00-02-04
782 _PHYS_StandardGRL_All_Good_25ns.xml
- 783 • data17_13TeV.periodAllYear_DetStatus-v97-pro21-13_Unknown_PHYS_StandardGRL
784 _All_Good_25ns_Triggerno17e33prim.xml
- 785 • data18_13TeV.periodAllYear_DetStatus-v102-pro22-04_Unknown_PHYS_StandardGRL
786 _All_Good_25ns_Triggerno17e33prim.xml
- 787 Runs included from the AllYear period containers are included.

788 **10.2 Monte Carlo Samples**

789 Several different generators were used to produce Monte Carlo simulations of the signal and
790 background processes. For all samples, the response of the ATLAS detector is simulated using
791 Geant4. The WZ signal samples are simulated using Sherpa 2.2.2 [[sherpa](#)]. Specific information
792 about the Monte Carlo samples being used can be found in Table 28. A list of the specific samples
793 used by data set ID is shown in Table 10.

Table 9: The configurations used for event generation of signal and background processes, including the event generator, matrix element (ME) order, parton shower algorithm, and parton distribution function (PDF).

Process	Event generator	ME order	Parton Shower	PDF
WZ, VV	SHERPA 2.2.2	MEPS NLO	SHERPA	CT10
tZ	MG5_AMC	LO	PYTHIA 6	CTEQ6L1
t̄W	MG5_AMC (SHERPA 2.1.1)	NLO (LO multileg)	PYTHIA 8 (SHERPA)	NNPDF 3.0 NLO (NNPDF 3.0 NLO)
t̄t(Z/γ* → ll)	MG5_AMC	NLO	PYTHIA 8	NNPDF 3.0 NLO
t̄tH	MG5_AMC (MG5_AMC)	NLO (NLO)	PYTHIA 8 (HERWIG++)	NNPDF 3.0 NLO [Ball:2014uwa] (CT10 [ct10])
tHqb	MG5_AMC	LO	PYTHIA 8	CT10
tHW	MG5_AMC (SHERPA 2.1.1)	NLO (LO multileg)	HERWIG++ (SHERPA)	CT10 (NNPDF 3.0 NLO)
tWZ	MG5_AMC	NLO	PYTHIA 8	NNPDF 2.3 LO
t̄t, t̄t̄t̄	MG5_AMC	LO	PYTHIA 8	NNPDF 2.3 LO
t̄tW+W-	MG5_AMC	LO	PYTHIA 8	NNPDF 2.3 LO
t̄t	Powheg-BOX v2 [powheggtt]	NLO	PYTHIA 8	NNPDF 3.0 NLO
t̄tγ	MG5_AMC	LO	PYTHIA 8	NNPDF 2.3 LO
s-, t-channel, Wt single top	Powheg-BOX v1 [powhegstp]	NLO	PYTHIA 6	CT10
qqVV, VVV Z → l+l-	SHERPA 2.2.1	MEPS NLO	SHERPA	NNPDF 3.0 NLO

Sample	DSID
WZ	364253, 364739-42
VV	364250, 364254, 364255, 363355-60, 364890
t <bar>t>W</bar>	410155
t <bar>t>Z</bar>	410156, 410157, 410218-20
low mass t <bar>t>Z</bar>	410276-8
Rare Top	410397, 410398, 410399
single Top	410658-9, 410644-5
three Top	304014
four Top	410080
t <bar>t>WW</bar>	410081
Z + jets	364100-41
low mass Z + jets	364198-215
W + jets	364156-97
V γ	364500-35
tZ	410560
tW	410013-4
WtZ	410408
VVV	364242-9
VH	342284-5
WtH	341998
t <bar>t>γ</bar>	410389
t <bar>t></bar>	410470
t <bar>t>H</bar>	345873-5, 346343-5

Table 10: List of Monte Carlo samples by data set ID used in the analysis.

794 11 Object Reconstruction

795 All regions defined in this analysis share a common lepton, jet, and overall event preselection.

796 The selection applied to each physics object is detailed here; the event preselection, and the

797 selection used to define the various fit regions, is described in Section 12.

798 **11.1 Trigger**

799 Events are required to be selected by dilepton triggers, as summarized in Table 29.

Dilepton triggers (2015)	
$\mu\mu$ (asymm.)	HLT_mu18_mu8noL1
ee (symm.)	HLT_2e12_lhloose_L12EM10VH
$e\mu, \mu e$ (\sim symm.)	HLT_e17_lhloose_mu14
Dilepton triggers (2016)	
$\mu\mu$ (asymm.)	HLT_mu22_mu8noL1
ee (symm.)	HLT_2e17_lhvloose_nod0
$e\mu, \mu e$ (\sim symm.)	HLT_e17_lhloose_nod0_mu14
Dilepton triggers (2017)	
$\mu\mu$ (asymm.)	HLT_mu22_mu8noL1
ee (symm.)	HLT_2e24_lhvloose_nod0
$e\mu, \mu e$ (\sim symm.)	HLT_e17_lhloose_nod0_mu14
Dilepton triggers (2018)	
$\mu\mu$ (asymm.)	HLT_mu22_mu8noL1
ee (symm.)	HLT_2e24_lhvloose_nod0
$e\mu, \mu e$ (\sim symm.)	HLT_e17_lhloose_nod0_mu14

Table 11: List of lowest p_T -threshold, un-prescaled dilepton triggers used for 2015-2018 data taking.

800 **11.2 Light leptons**

801 Electron candidates are reconstructed from energy clusters in the electromagnetic calorimeter that

802 are associated with charged particle tracks reconstructed in the inner detector [**ATLAS-CONF-2016-024**].

803 Electron candidates are required to have $p_T > 10$ GeV and $|\eta_{\text{cluster}}| < 2.47$. Muon candidates

804 are reconstructed by combining inner detector tracks with track segments or full tracks in the

805 muon spectrometer [**PERF-2014-05**]. Muon candidates are required to have $p_T > 10$ GeV and

806 $|\eta| < 2.5$. Candidates in the transition region between different electromagnetic calorimeter
807 components, $1.37 < |\eta_{\text{cluster}}| < 1.52$, are rejected. A multivariate likelihood discriminant com-
808 bining shower shape and track information is used to distinguish real electrons from hadronic
809 showers (fake electrons). To further reduce the non-prompt electron contribution, the track is
810 required to be consistent with originating from the primary vertex; requirements are imposed
811 on the transverse impact parameter significance ($|d_0|/\sigma_{d_0} < 5$) and the longitudinal impact
812 parameter ($|\Delta z_0 \sin \theta_\ell| < 0.5 \text{ mm}$).

813 Muon candidates are reconstructed by combining inner detector tracks with track segments
814 or full tracks in the muon spectrometer [**PERF-2014-05**]. Muon candidates are required to have
815 $p_T > 10 \text{ GeV}$ and $|\eta| < 2.5$. The longitudinal impact parameter is the same for both electrons
816 and muons, while muons are required to pass a slightly tighter transverse impact parameter,
817 $|d_0|/\sigma_{d_0} < 3$.

818 All leptons are required to be isolated, as defined through the standard PLVLoose working
819 point supported by combined performance groups. Leptons are additionally required to pass a
820 non-prompt BDT selection developed by the $t\bar{t}H$ multilepton/ $t\bar{t}W$ analysis group. This BDT is
821 described in detail in [**ttW_140**]. Optimized working points and scale factors for this BDT are
822 taken from that analysis.

823 **11.3 Jets**

824 Jets are reconstructed from calibrated topological clusters built from energy deposits in the
825 calorimeters [**ATL-PHYS-PUB-2015-015**], using the anti- k_t algorithm with a radius para-
826 meter $R = 0.4$. Particle Flow, or PFlow, jets are used in the analysis. Jets with energy
827 contributions likely arising from noise or detector effects are removed from consideration
828 [**ATLAS-CONF-2015-029**], and only jets satisfying $p_T > 25$ GeV and $|\eta| < 2.5$ are used
829 in this analysis. For jets with $p_T < 60$ GeV and $|\eta| < 2.4$, a jet-track association algorithm is
830 used to confirm that the jet originates from the selected primary vertex, in order to reject jets
831 arising from pileup collisions [**PERF-2014-03**].

832 **11.4 B-tagged Jets**

833 In order to make a measurement of $WZ +$ heavy flavor it is necessary to distinguish these events
834 from $WZ +$ light jets. For this purpose, the DL1r b-tagging algorithm is used to distinguish
835 heavy flavor jets from lighter ones. The DL1r algorithm uses jet kinematics, particularly jet
836 vertex information, as input for a neural network which assigns each jet a score designed to
837 reflect how likely that jet is to have originated from a b-quark.

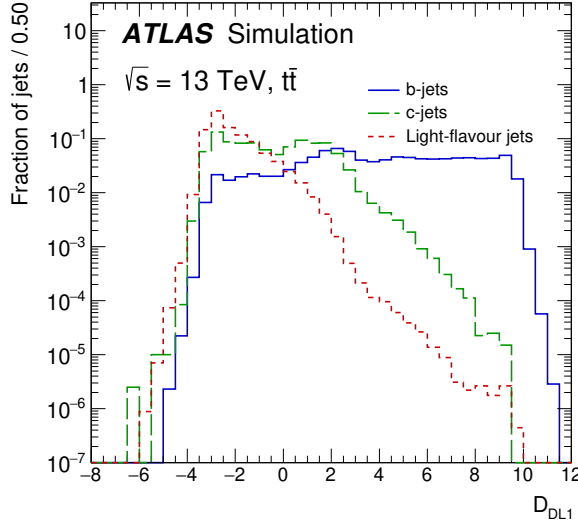


Figure 11.1: Output distribution of the DL1r algorithm for b-jets, charm jets, and light jets

838 From the output of the BDT, working points (WPs) are developed based on the efficiency
 839 of truth b-jets at particular values of the DL1r algorithm. These WPs are taken from the March
 840 2020 CDI file, 2020-21-13TeV-MC16-CDI-2020-03-11_v2.root. The working points used in
 841 this analysis are summarized in Table 12.

WP	none	loose	medium	tight	tightest
b eff.	-	85%	77%	70%	60%

Table 12: B-tagging Working Points by tightness and b-jet efficiency

842 A tighter WP will accept fewer b-jets, but reject a higher fraction of charm and light jets.
 843 Generally, analyses that include b-jets will use a fixed working point, for example, requiring that
 844 a jet pass the 70% threshold. By instead treating these working point as bins, e.g. events with
 845 jets that fall between the 85% and 77% WPs fall into one bin, while events with jets passing the

846 60% WP fall into another, and looking at the full psuedo-continuous DL1r spectrum of the jets,
847 additional information can be gained. The psuedo-continuous b-tag spectrum is used in this case
848 to separate out WZ + b, WZ + charm, and WZ + light.

849 **11.5 Missing transverse energy**

850 Missing transverse momentum (E_T^{miss}) is used as part of the event selection. The missing
851 transverse momentum vector is defined as the inverse of the sum of the transverse momenta of
852 all reconstructed physics objects as well as remaining unclustered energy, the latter of which is
853 estimated from low- p_T tracks associated with the primary vertex but not assigned to a hard object,
854 with object definitions taken from [ATL-PHYS-PUB-2015-027]. Light leptons considered in
855 the E_T^{miss} reconstruction are required to have $p_T > 10 \text{ GeV}$, while jets are required to have $p_T > 20$
856 GeV .

857 **11.6 Overlap removal**

858 To avoid double counting objects and remove leptons originating from decays of hadrons, overlap
859 removal is performed in the following order: any electron candidate within $\Delta R = 0.1$ of another
860 electron candidate with higher p_T is removed; any electron candidate within $\Delta R = 0.1$ of a muon
861 candidate is removed; any jet within $\Delta R = 0.3$ of an electron candidate is removed; if a muon
862 candidate and a jet lie within $\Delta R = \min(0.4, 0.04 + 10[\text{GeV}] / p_T(\text{muon}))$ of each other, the jet
863 is kept and the muon is removed.

864 This algorithm is applied to the preselected objects. The overlap removal procedure is
 865 summarized in Table 13.

Keep	Remove	Cone size (ΔR)
electron	electron (low p_T)	0.1
muon	electron	0.1
electron	jet	0.3
jet	muon	$\min(0.4, 0.04 + 10[\text{GeV}]/p_T(\text{muon}))$
electron	tau	0.2

Table 13: Summary of the overlap removal procedure between electrons, muons, and jets.

866 12 Event Selection and Signal Region Definitions

867 Event are required to pass a preselection described in Section 12.1 and summarized in Table 14.
 868 Those that pass this preselection are divided into various fit regions described in Section 12.2,
 869 based on the number of jets in the event, and the b-tag score of those jets.

870 12.1 Event Preselection

871 Events are required to include exactly three reconstructed light leptons passing the requirement
 872 described in 11.2, which have a total charge of ± 1 . As the opposite sign lepton is found to
 873 be prompt the vast majority of the time [ttH_paper], it is required to be loose and isolated,
 874 as defined though the standard PLVLoose working point supported by combined performance
 875 groups. The same sign leptons are required to be very tightly isolated, as per the recommended
 876 PLVTight.

877 The leptons are ordered in the analysis code as 0, 1, and 2. Lepton 0 is the lepton whose
 878 charge is opposite the other two. Lepton 1 is the lepton closest to the opposite charge lepton, i.e.
 879 the smallest ΔR , leaving lepton 2 as the lepton further from the opposite charge lepton. Lepton
 880 0 is required to have $p_T > 10 \text{ GeV}$, while the same sign leptons, 1 and 2, are required to have
 881 $p_T > 20 \text{ GeV}$ to reduce the contribution of non-prompt leptons.

882 The invariant mass of at least one pair of opposite sign, same flavor leptons is required
 883 to fall within 10 GeV of the mass of the Z boson, 91.2 GeV. Events where one of the opposite
 884 sign pairs have an invariant mass less than 12 GeV are rejected in order to suppress low mass
 885 resonances.

886 An additional requirement is placed on the missing transverse energy, $E_T^{\text{miss}} > 20 \text{ GeV}$,
 887 and the transverse mass of the W candidate, $m(E_T^{\text{miss}} + l_{\text{other}}) > 30 \text{ GeV}$, where E_T^{miss} is the
 888 missing transverse energy, and l_{other} is the lepton not included in the Z-candidate.

889 Events are required to have one or two reconstructed jets passing the selection described
 890 in Section 11.3. Events with more than two jets are rejected in order to reduce the contribution
 891 of backgrounds such as $t\bar{t}Z$ and $t\bar{t}W$, which tend to have higher jet multiplicity.

Event Selection

Exactly three leptons with charge ± 1
 Two tight Iso, tight ID same-charge leptons with $p_T > 20 \text{ GeV}$
 One loose Iso, medium ID opposite charge lepton with $p_T > 10 \text{ GeV}$
 $m(l^+l^-)$ within 10 GeV of 91.2 GeV
 Transverse mass of W-candidate, $m_T(E_T^{\text{miss}} + \text{lep}_{\text{other}}) > 30 \text{ GeV}$
 Missing transverse energy, $E_T^{\text{miss}} > 20 \text{ GeV}$
 One or two jets with $p_T > 25 \text{ GeV}$

Table 14: Summary of the selection applied to events for inclusion in the fit

892 The event yields in the preselection region for both data and Monte Carlo are summarized
 893 in Table 12.1, which shows good agreement between data and Monte Carlo, and demonstrates that
 894 this region consists primarily of WZ events. The WZ events are split into WZ + b, WZ + c, and
 895 WZ + l based on the truth flavor of the associated jet in the event. Specifically, this determination
 896 is made based on the HadronConeExclTruthLabelID of the jet, as recommended by the b-
 897 tagging working group [BtagWG]. In this ordering b-jet supersedes charm, which supersedes
 898 light. That is, WZ + l events contain no charm and no b jets at truth level, WZ + c contain at
 899 least one truth charm and no b-jets, and WZ + b contains at least one truth b-jet.

Process	Events
WZ + b	167.6 ± 6.5
WZ + c	1080 ± 40
WZ + l	7220 ± 310
Other VV	850 ± 140
t̄tW	16.8 ± 2.3
t̄tZ	115 ± 17
rare Top	2.2 ± 0.1
Single top	0.10 ± 0.45
Three top	0.01 ± 0.01
Four top	0.02 ± 0.01
t̄tWW	0.23 ± 0.05
Z + jets	600 ± 260
V + γ	37 ± 54
tZ	190 ± 70
tW	5.5 ± 1.2
WtZ	25.8 ± 1.1
VVV	26.2 ± 0.9
VH	94 ± 7
t̄t	108.68 ± 8
t̄tH	4.3 ± 0.5
Total	10600 ± 530
Data	10574

Table 15: Event yields in the preselection region at 139.0 fb^{-1}

900 Here Other VV represents diboson processes other than WZ, and consists predominantly
901 of $ZZ \rightarrow llll$ events where one of the leptons is not reconstructed.

902 Simulations are further validated by comparing the kinematic distributions of the Monte
903 Carlo with data, which are shown in Figure 12.1. Here, bins with 5% or more WZ+b are
904 blinded.

WZ Fit Region - Inclusive

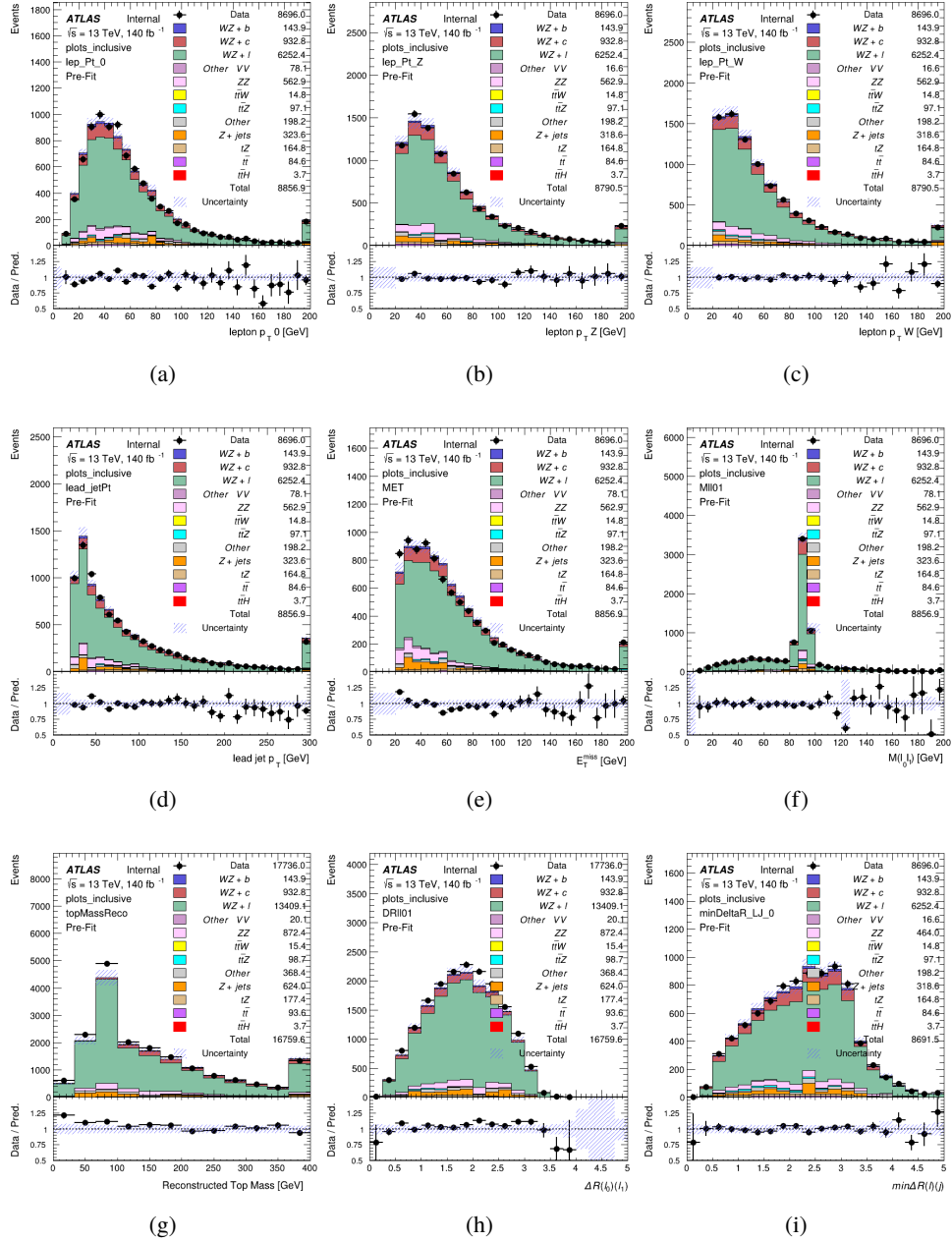


Figure 12.1: Comparisons between the data and MC distributions in the preselection region for (a) the p_T of the opposite sign lepton, (b) the p_T of the other lepton from the Z candidate, (c) the p_T of the lepton from the W candidate, (d) the leading jet p_T , (e) the E_T^{miss} , and (f) the invariant mass of leptons 0 and 1, (g) the reconstructed top mass, (h) $\Delta(R)$ between lepton 0 and 1, (i) the $\Delta(R)$ between the closest lepton and jet.

905 **12.2 Fit Regions**

906 Once preselection has been applied, the remaining events are categorized into one of twelve
 907 orthogonal regions. The regions used in the fit are summarized in Table 16.

Table 16: A list of the regions used in the fit and the selection used for each.

Region	Selection
1j, <85%	$N_{\text{jets}} = 1, n\text{Jets_DL1r_85} = 0$
1j, 85%-77%	$N_{\text{jets}} = 1, n\text{Jets_DL1r_85} = 1, n\text{Jets_DL1r_77} = 0$
1j, 77%-70%	$N_{\text{jets}} = 1, n\text{Jets_DL1r_77} = 1, n\text{Jets_DL1r_70} = 0$
1j, 70%-60%	$N_{\text{jets}} = 1, n\text{Jets_DL1r_70} = 1, n\text{Jets_DL1r_60} = 0$
1j, >60%	$N_{\text{jets}} = 1, n\text{Jets_DL1r_60} = 1, tZ \text{ BDT} > 0.725$
1j tZ CR	$N_{\text{jets}} = 1, n\text{Jets_DL1r_60} = 1, tZ \text{ BDT} < 0.725$
2j, <85%	$N_{\text{jets}} = 2, n\text{Jets_DL1r_85} = 0$
2j, 85%-77%	$N_{\text{jets}} = 2, n\text{Jets_DL1r_85} \geq 1, n\text{Jets_DL1r_77} = 0$
2j, 77%-70%	$N_{\text{jets}} = 2, n\text{Jets_DL1r_77} \geq 1, n\text{Jets_DL1r_70} = 0$
2j, 70%-60%	$N_{\text{jets}} = 2, n\text{Jets_DL1r_70} \geq 1, n\text{Jets_DL1r_60} = 0$
2j, >60%	$N_{\text{jets}} = 2, n\text{Jets_DL1r_60} \geq 1, tZ \text{ BDT} > 0.725$
2j tZ CR	$N_{\text{jets}} = 2, n\text{Jets_DL1r_60} \geq 1, tZ \text{ BDT} < 0.725$

908 The working points discussed in Section 11.4 are used to separate events into fit regions
 909 based on the highest working point reached by a jet in each event. Because the background
 910 composition differs significantly based on the number of b-jets, events are further subdivided
 911 into 1-jet and 2-jet regions in order to minimize the impact of background uncertainties.

912 An unfolding procedure is performed to account for differences in the number of recon-
 913 structed jets compared to the number of truth jets in each event. The `AntiKt4TruthDressedWZJets`
 914 truth jet collection is used to make this determination. In order to account for migration of WZ+1-
 915 jet and WZ+2-jet events between the 1-jet and 2-jet bins at reco level, the signal samples are
 916 separated based on the number of truth jets. Events with 0 jets or more than 3 jets at truth level,

yet fall within one of the categories listed in Table 16, are categorized as WZ + other, and treated as a background. The migration matrix in the number of jets at truth level versus reco level is shown in Figure 12.2. The composition of the number of truth jets in each reco jet bin is taken from MC, with uncertainties in these estimates described in detail in Section 21.

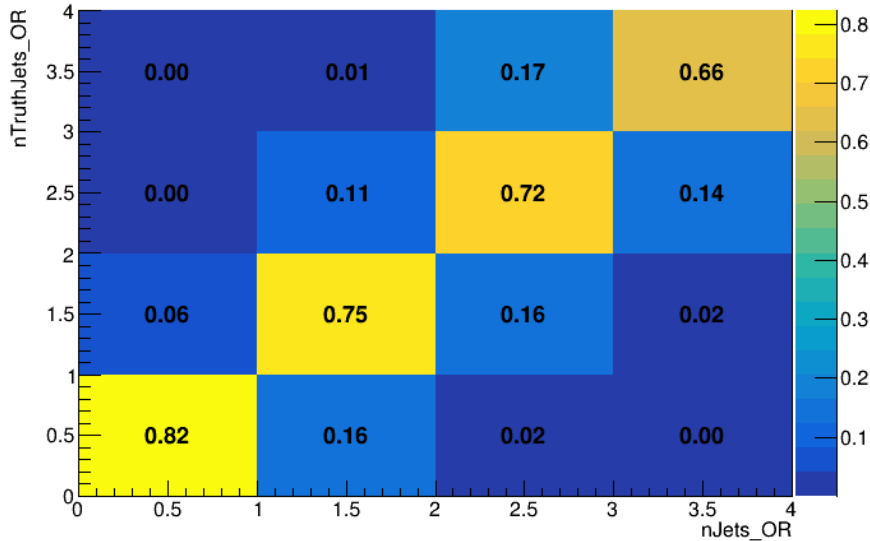


Figure 12.2: Number of truth jets compared to the number of reconstructed jets in each WZ event falling in the preselection region. Each row is normalized to unity.

An additional tZ control region is created based on the BDT described in Section 13. The region with 1-jet passing the 60% working point is split in two - a signal enriched region of events with a BDT score greater than 0.03, and a tZ control region including events with less than 0.03. This cutoff is arrived at by performing an Asimov fit with a variety of cutoffs, and selecting the value that produces the highest significance for the measurement of WZ + b.

The modeling in each region is validated by comparing data and MC predictions for

⁹²⁷ various kinematic distributions. These plot are shown in Figures [12.3-12.16](#).

WZ Fit Region - 1j Inclusive

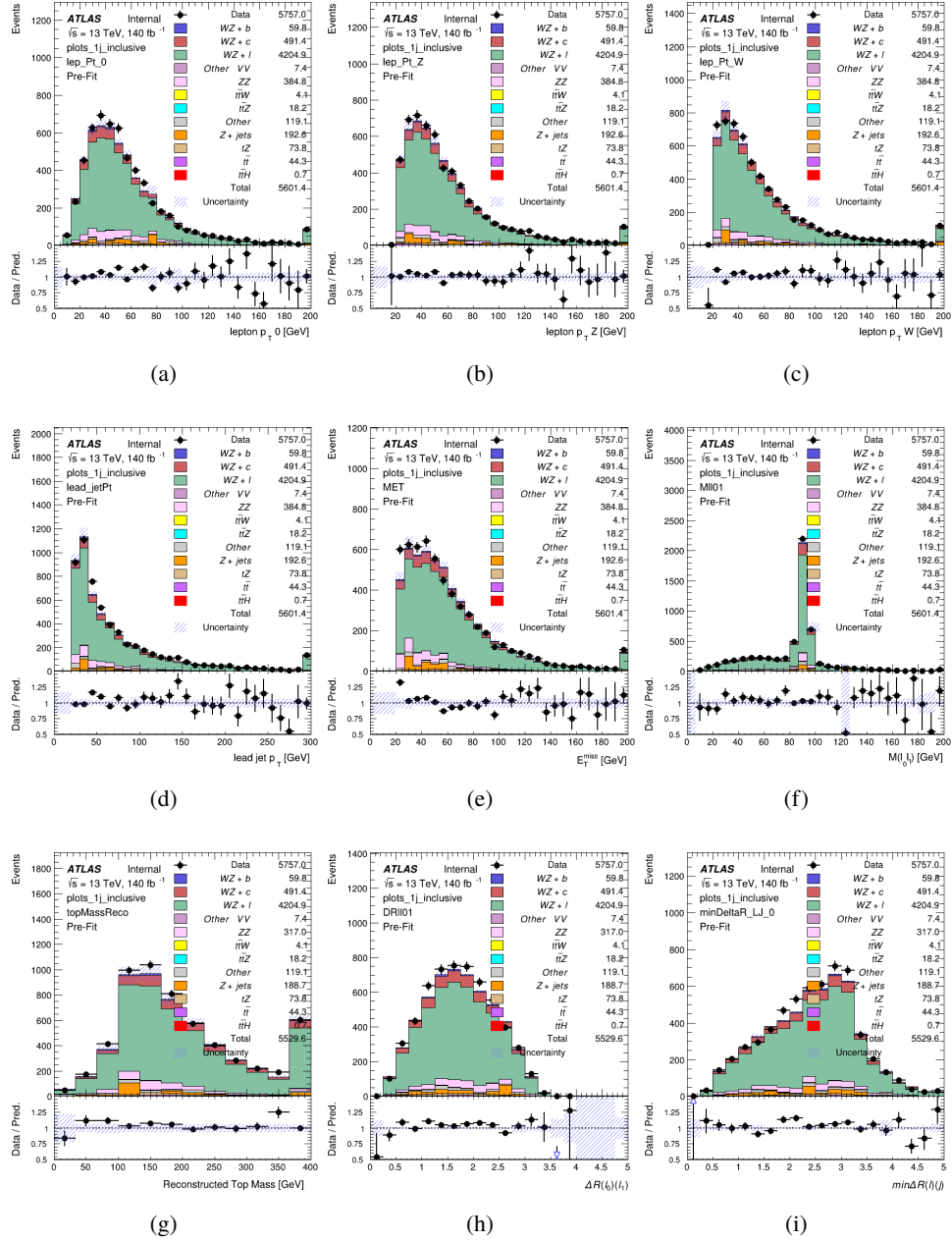


Figure 12.3: Comparisons between the data and MC distributions in the preselection region for (a) the p_T of the opposite sign lepton, (b) the p_T of the other lepton from the Z candidate, (c) the p_T of the lepton from the W candidate, (d) the leading jet p_T , (e) the E_T^{miss} , and (f) the invariant mass of leptons 0 and 1, (g) the reconstructed top mass, (h) $\Delta(R)$ between lepton 0 and 1, (i) the $\Delta(R)$ between the closest lepton and jet.

WZ Fit Region - 1j < 85% WP

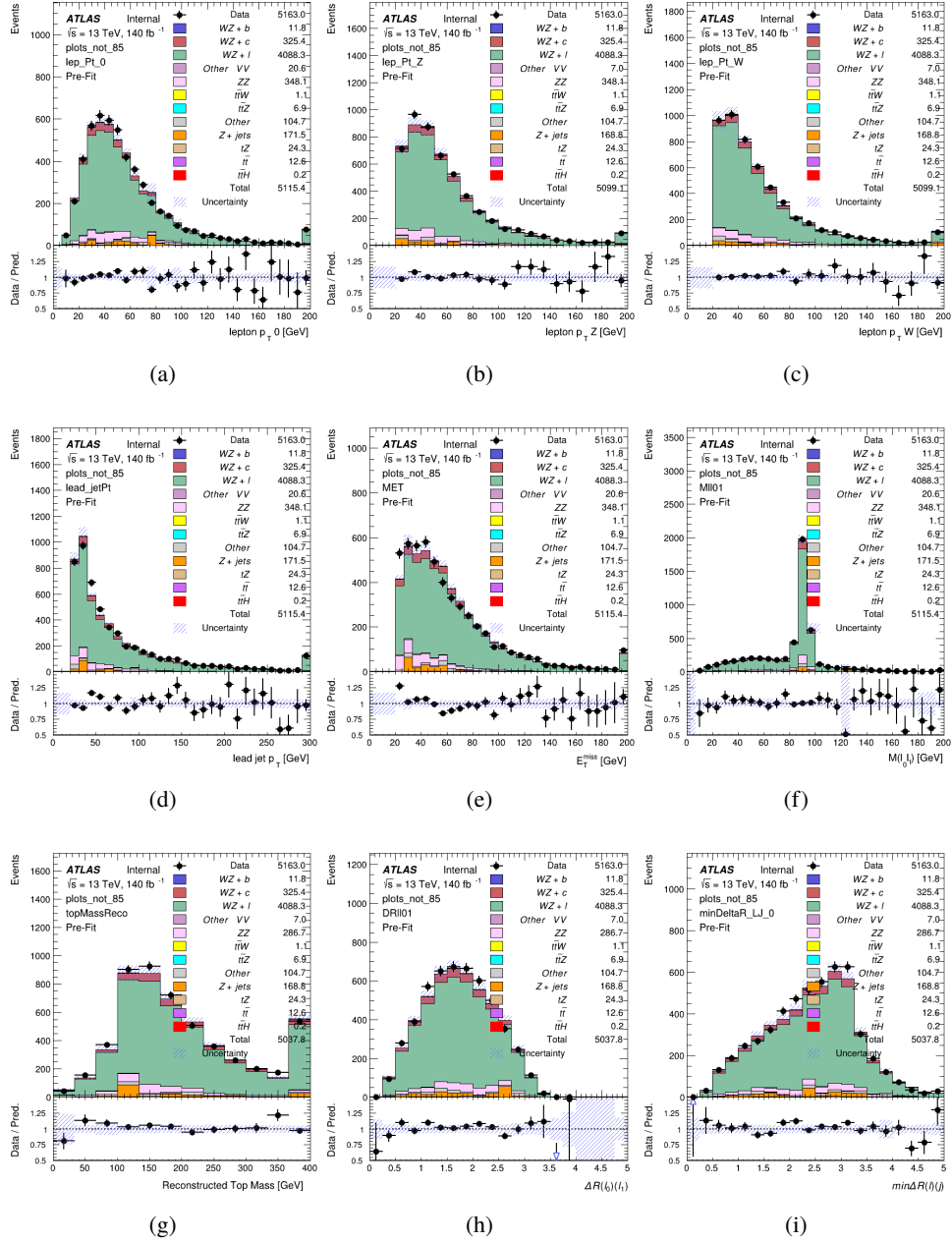


Figure 12.4: Comparisons between the data and MC distributions in the preselection region for (a) the p_T of the opposite sign lepton, (b) the p_T of the other lepton from the Z candidate, (c) the p_T of the lepton from the W candidate, (d) the leading jet p_T , (e) the E_T^{miss} , and (f) the invariant mass of leptons 0 and 1, (g) the reconstructed top mass, (h) $\Delta(R)$ between lepton 0 and 1, (i) the $\Delta(R)$ between the closest lepton and jet.

WZ Fit Region - 1j 77-85% WP

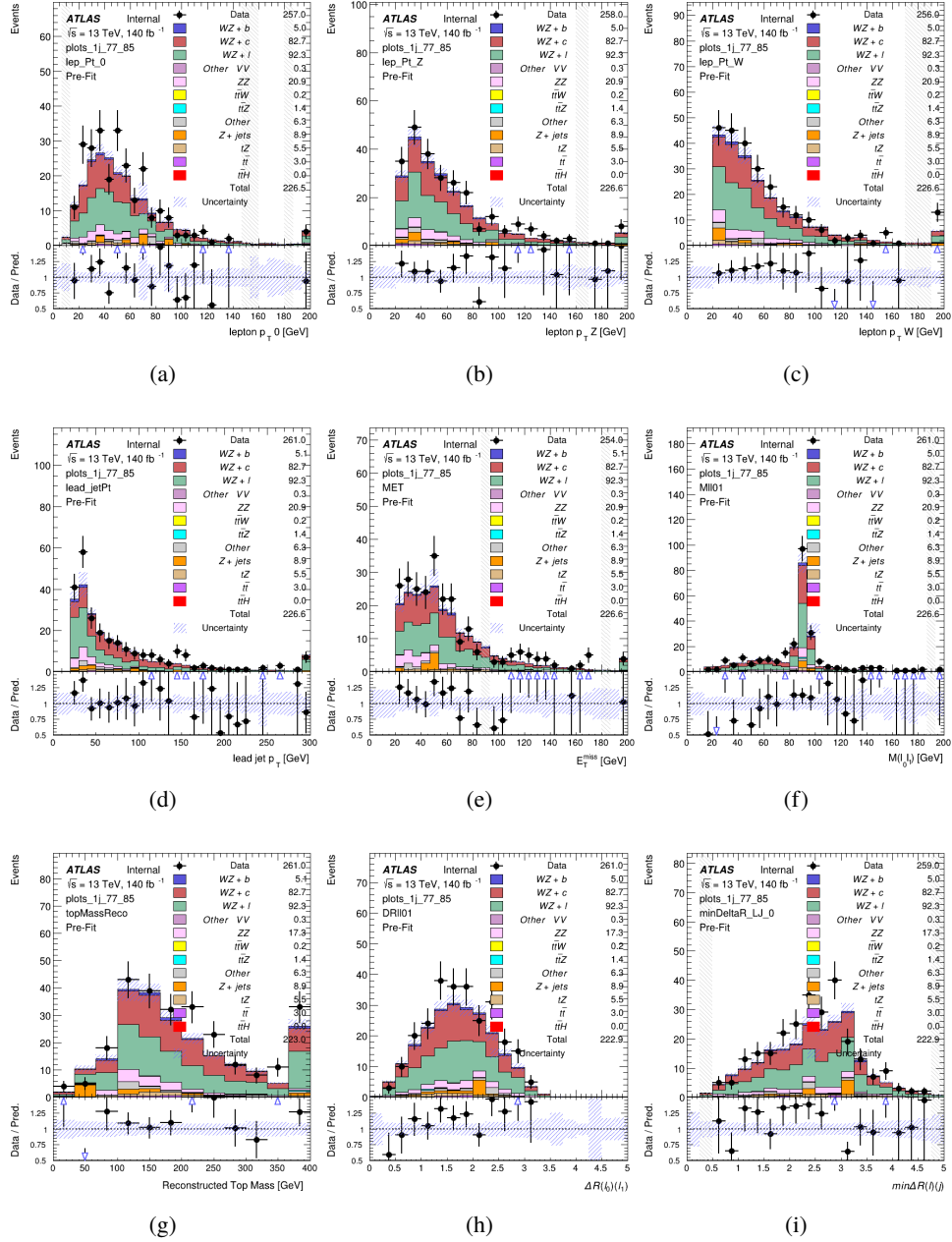


Figure 12.5: Comparisons between the data and MC distributions in the preselection region for (a) the p_T of the opposite sign lepton, (b) the p_T of the other lepton from the Z candidate, (c) the p_T of the lepton from the W candidate, (d) the leading jet p_T , (e) the E_T^{miss} , and (f) the invariant mass of leptons 0 and 1, (g) the reconstructed top mass, (h) $\Delta(R)$ between lepton 0 and 1, (i) the $\Delta(R)$ between the closest lepton and jet.

WZ Fit Region - 1j 70-77% WP

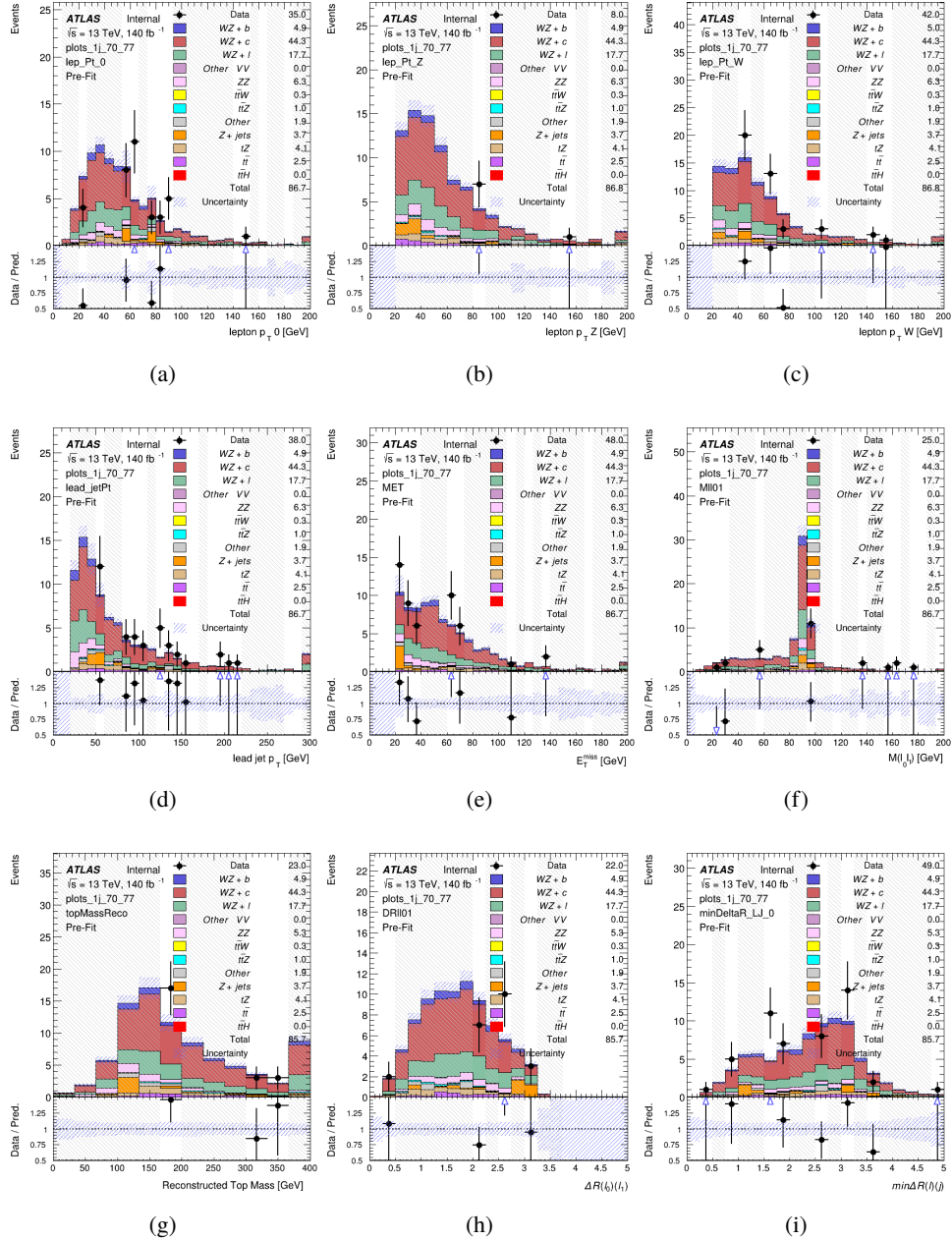


Figure 12.6: Comparisons between the data and MC distributions in the preselection region for (a) the p_T of the opposite sign lepton, (b) the p_T of the other lepton from the Z candidate, (c) the p_T of the lepton from the W candidate, (d) the leading jet p_T , (e) the E_T^{miss} , and (f) the invariant mass of leptons 0 and 1, (g) the reconstructed top mass, (h) $\Delta(R)$ between lepton 0 and 1, (i) the $\Delta(R)$ between the closest lepton and jet.

WZ Fit Region - 1j 60-70% WP

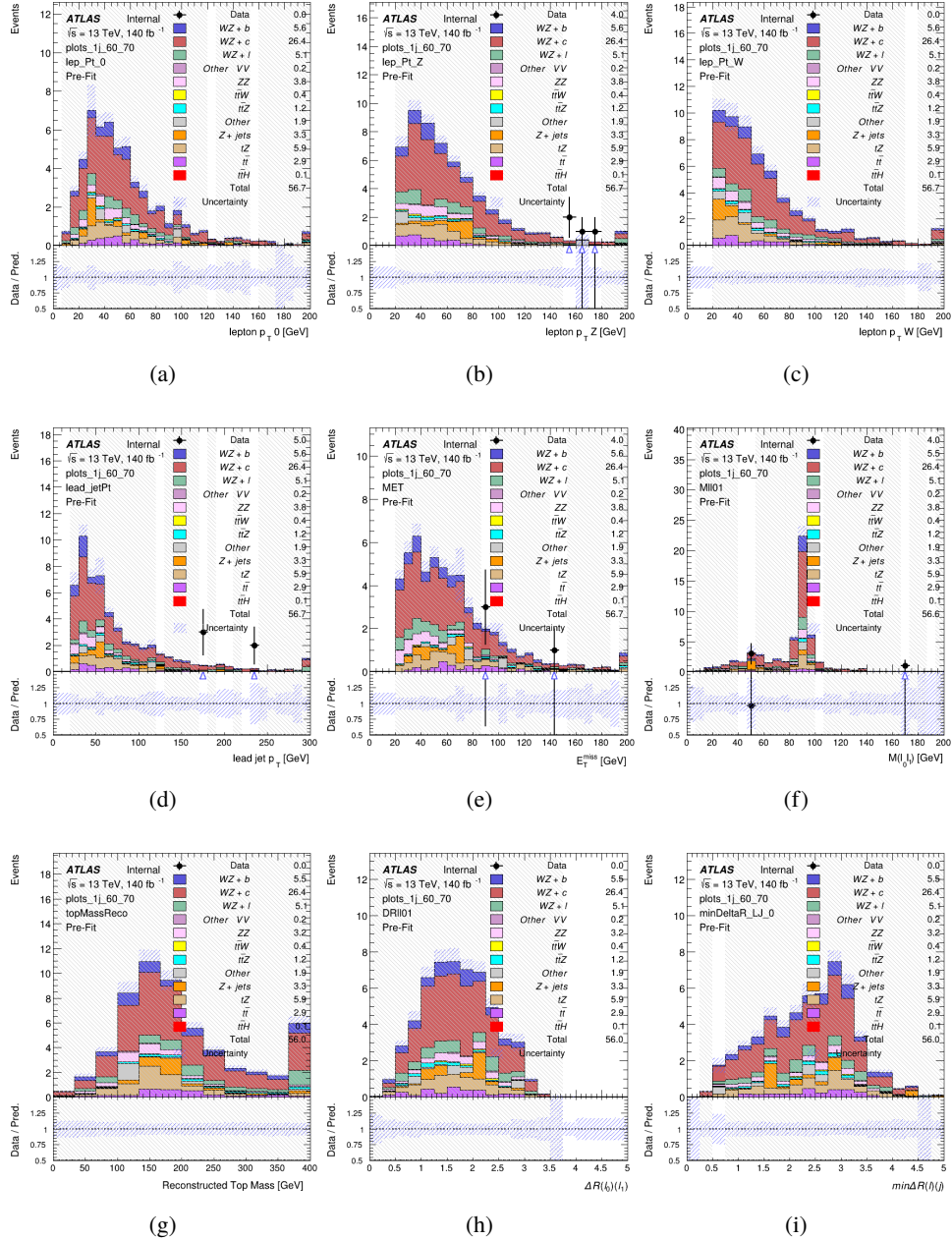


Figure 12.7: Comparisons between the data and MC distributions in the preselection region for (a) the p_T of the opposite sign lepton, (b) the p_T of the other lepton from the Z candidate, (c) the p_T of the lepton from the W candidate, (d) the leading jet p_T , (e) the E_T^{miss} , and (f) the invariant mass of leptons 0 and 1, (g) the reconstructed top mass, (h) $\Delta(R)$ between lepton 0 and 1, (i) the $\Delta(R)$ between the closest lepton and jet.

WZ Fit Region - 1j 60% WP

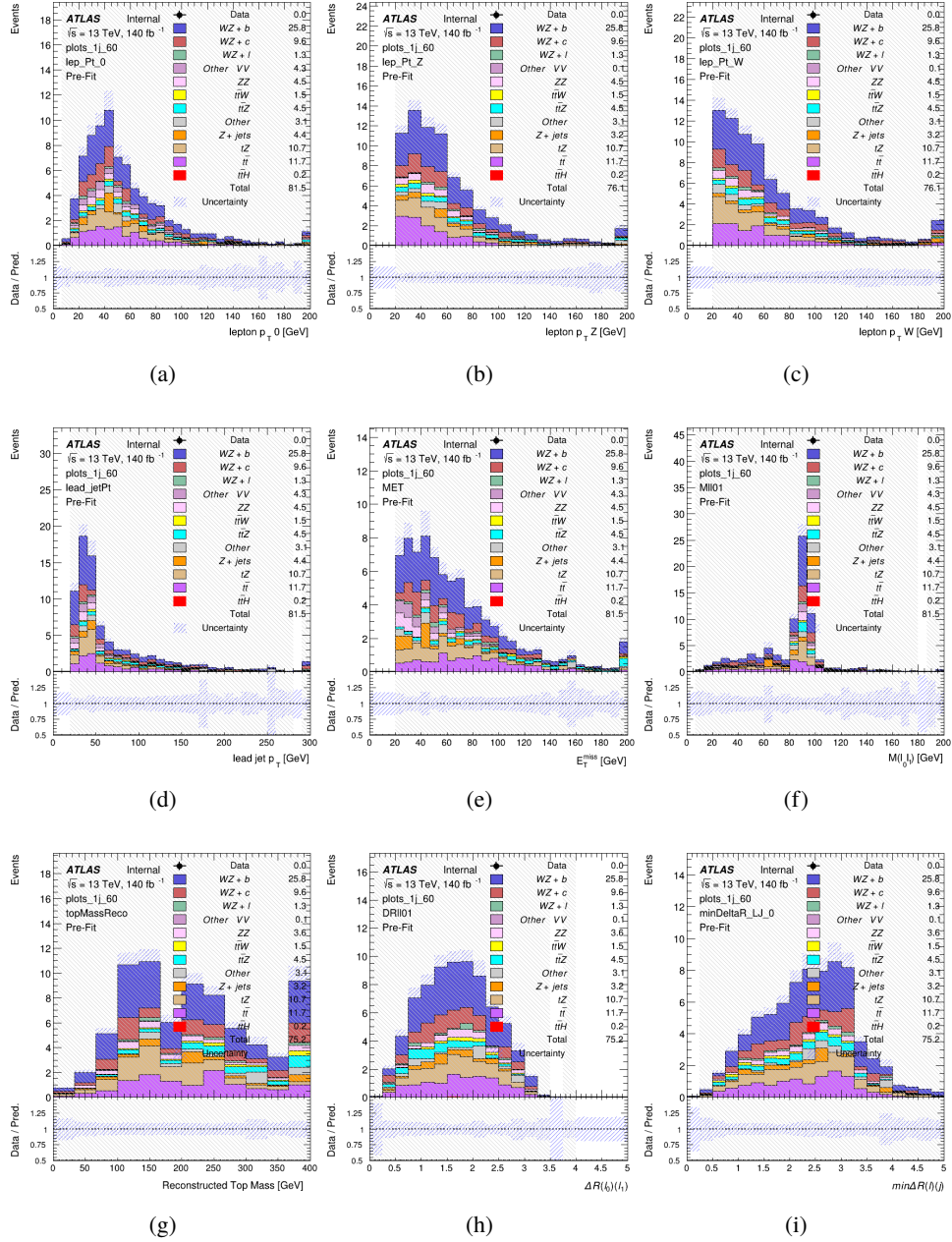


Figure 12.8: Comparisons between the data and MC distributions in the preselection region for (a) the p_T of the opposite sign lepton, (b) the p_T of the other lepton from the Z candidate, (c) the p_T of the lepton from the W candidate, (d) the leading jet p_T , (e) the E_T^{miss} , and (f) the invariant mass of leptons 0 and 1, (g) the reconstructed top mass, (h) $\Delta(R)$ between lepton 0 and 1, (i) the $\Delta(R)$ between the closest lepton and jet.

WZ Fit Region - tZ-CR

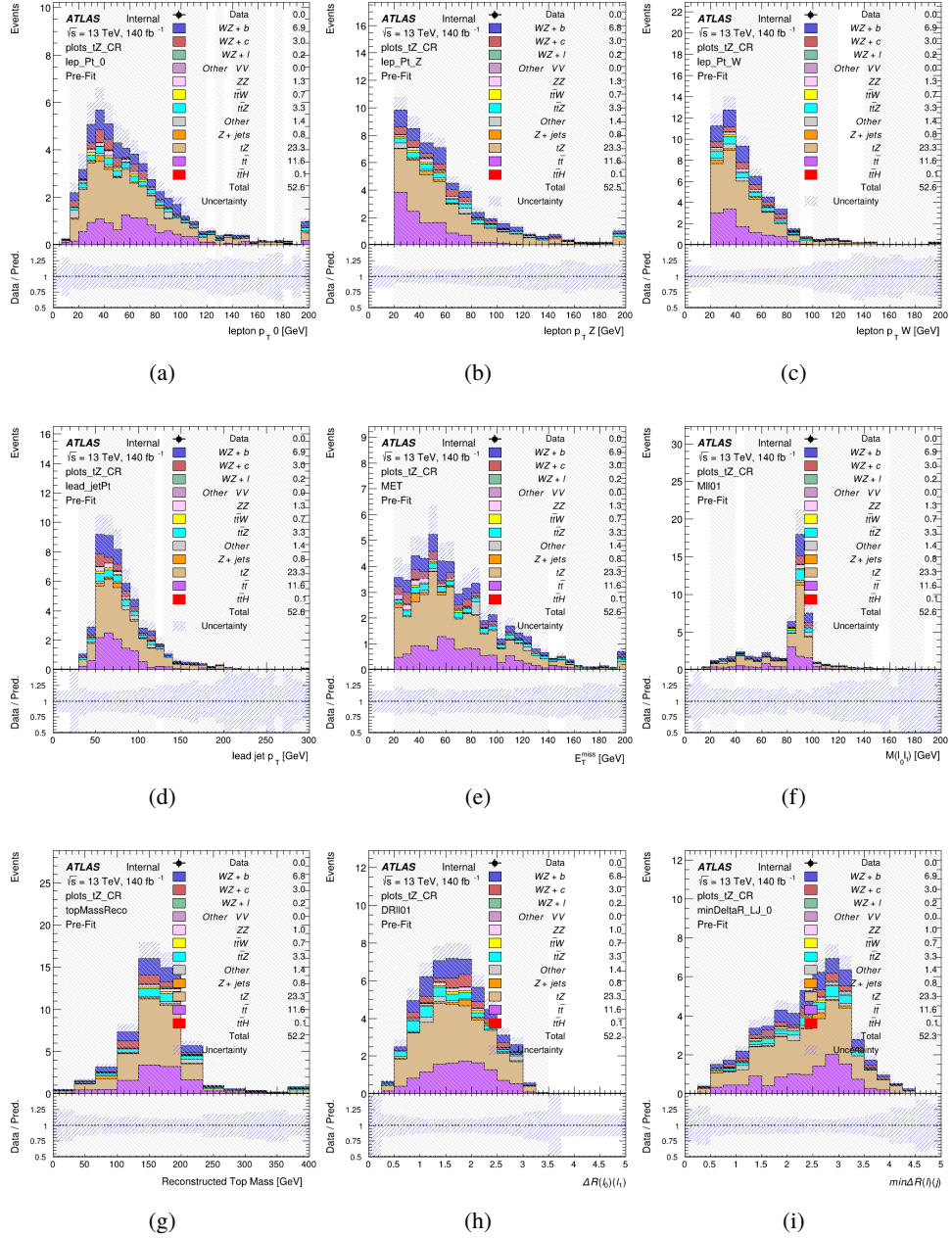


Figure 12.9: Comparisons between the data and MC distributions in the preselection region for (a) the p_T of the opposite sign lepton, (b) the p_T of the other lepton from the Z candidate, (c) the p_T of the lepton from the W candidate, (d) the leading jet p_T , (e) the E_T^{miss} , and (f) the invariant mass of leptons 0 and 1, (g) the reconstructed top mass, (h) $\Delta(R)$ between lepton 0 and 1, (i) the $\Delta(R)$ between the closest lepton and jet.

WZ Fit Region - 2j Inclusive

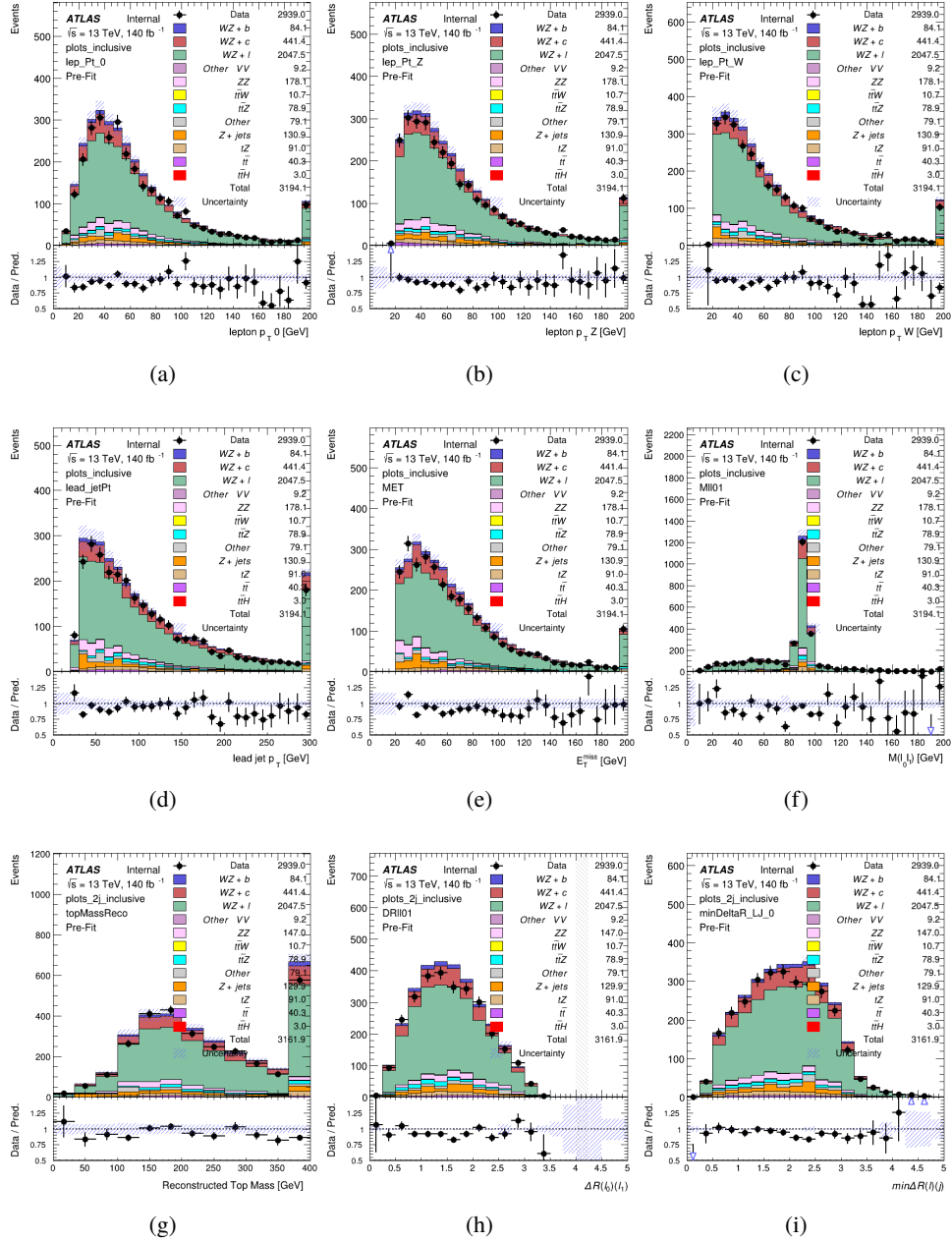


Figure 12.10: Comparisons between the data and MC distributions in the preselection region for (a) the p_T of the opposite sign lepton, (b) the p_T of the other lepton from the Z candidate, (c) the p_T of the lepton from the W candidate, (d) the leading jet p_T , (e) the E_T^{miss} , and (f) the invariant mass of leptons 0 and 1, (g) the reconstructed top mass, (h) $\Delta(R)$ between lepton 0 and 1, (i) the $\Delta(R)$ between the closest lepton and jet.

WZ Fit Region - 2j < 85% WP

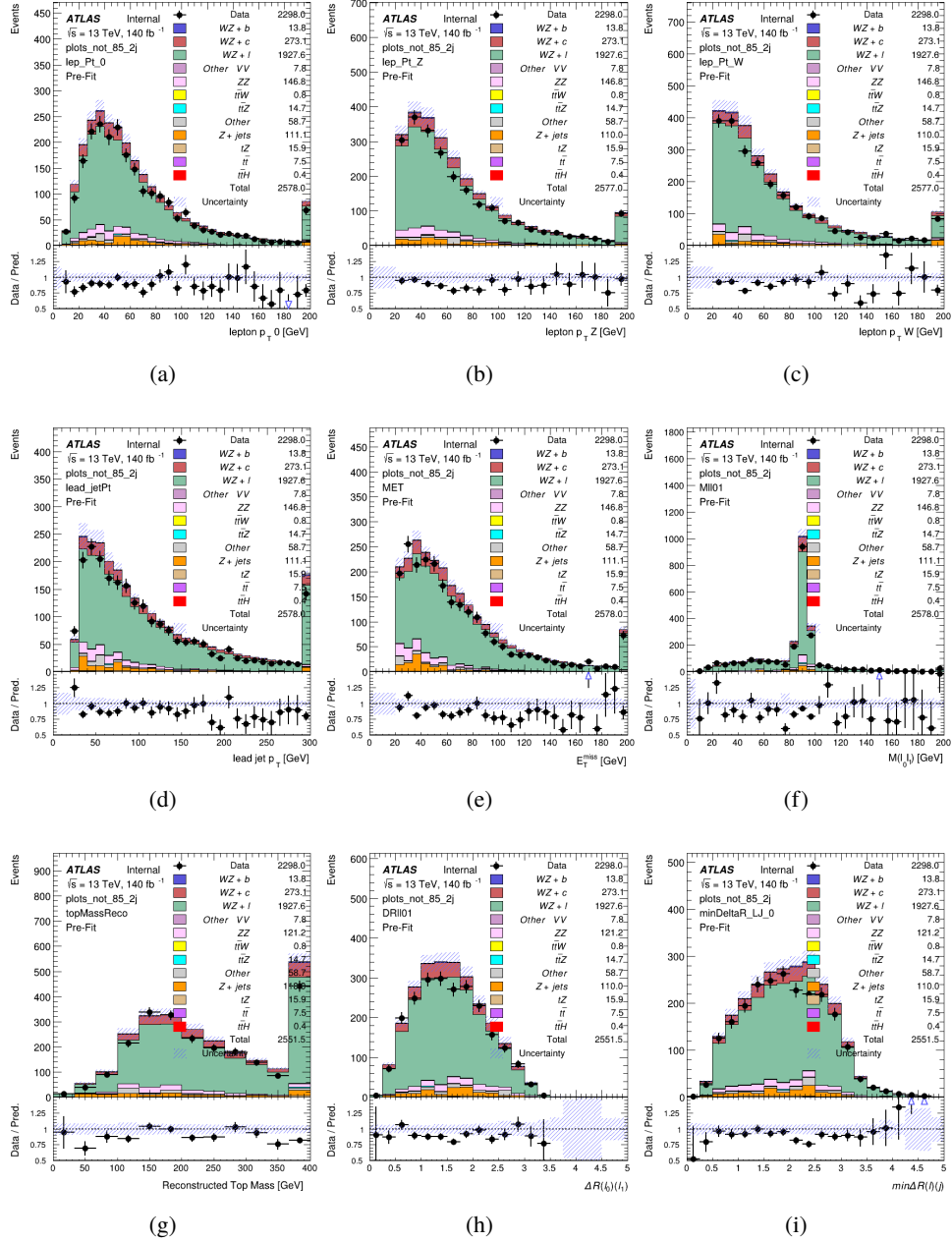


Figure 12.11: Comparisons between the data and MC distributions in the preselection region for (a) the p_T of the opposite sign lepton, (b) the p_T of the other lepton from the Z candidate, (c) the p_T of the lepton from the W candidate, (d) the leading jet p_T , (e) the E_T^{miss} , and (f) the invariant mass of leptons 0 and 1, (g) the reconstructed top mass, (h) $\Delta(R)$ between lepton 0 and 1, (i) the $\Delta(R)$ between the closest lepton and jet.

WZ Fit Region - 2j 77-85% WP

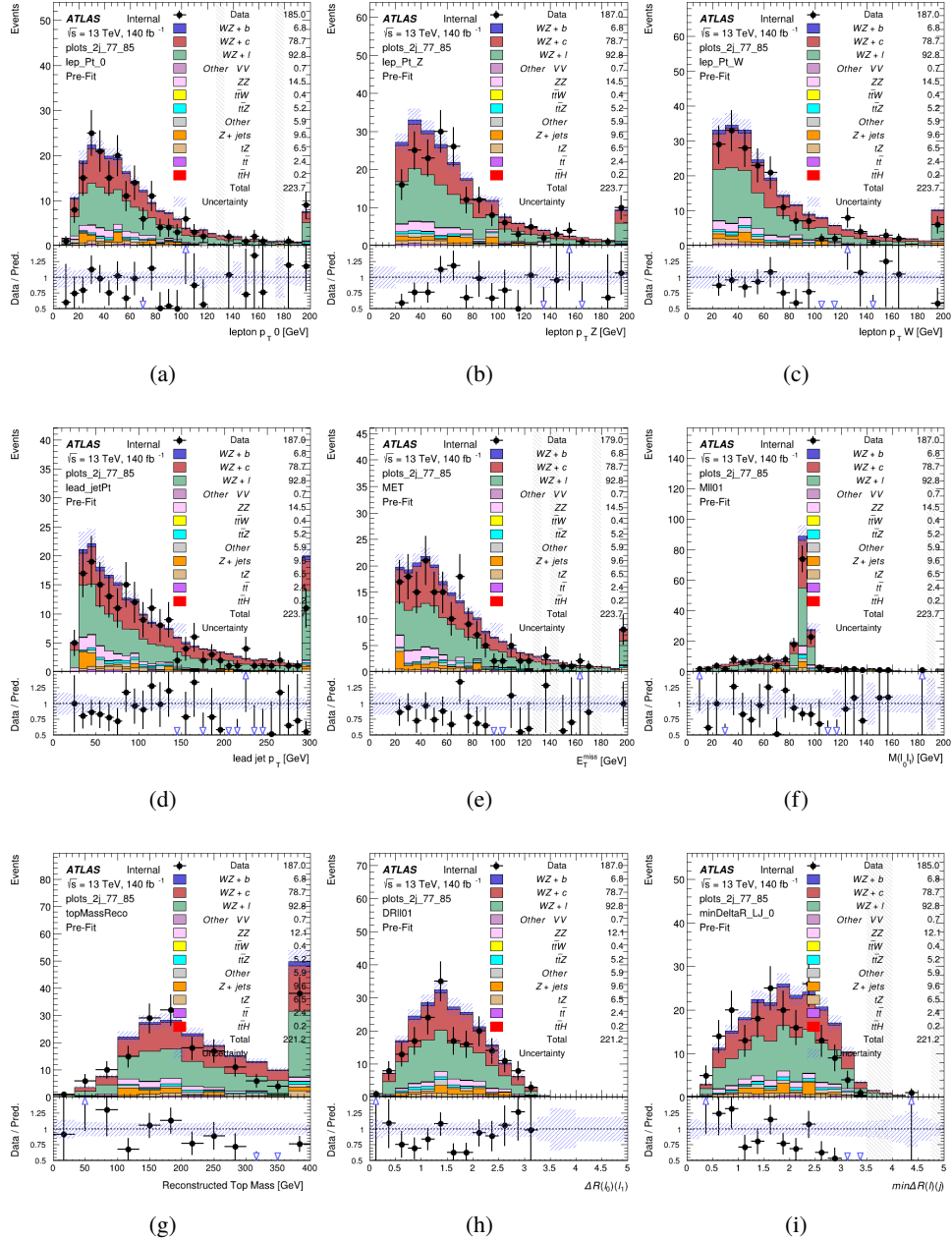


Figure 12.12: Comparisons between the data and MC distributions in the preselection region for (a) the p_T of the opposite sign lepton, (b) the p_T of the other lepton from the Z candidate, (c) the p_T of the lepton from the W candidate, (d) the leading jet p_T , (e) the E_T^{miss} , and (f) the invariant mass of leptons 0 and 1, (g) the reconstructed top mass, (h) $\Delta(R)$ between lepton 0 and 1, (i) the $\Delta(R)$ between the closest lepton and jet.

WZ Fit Region - 2j 70-77% WP

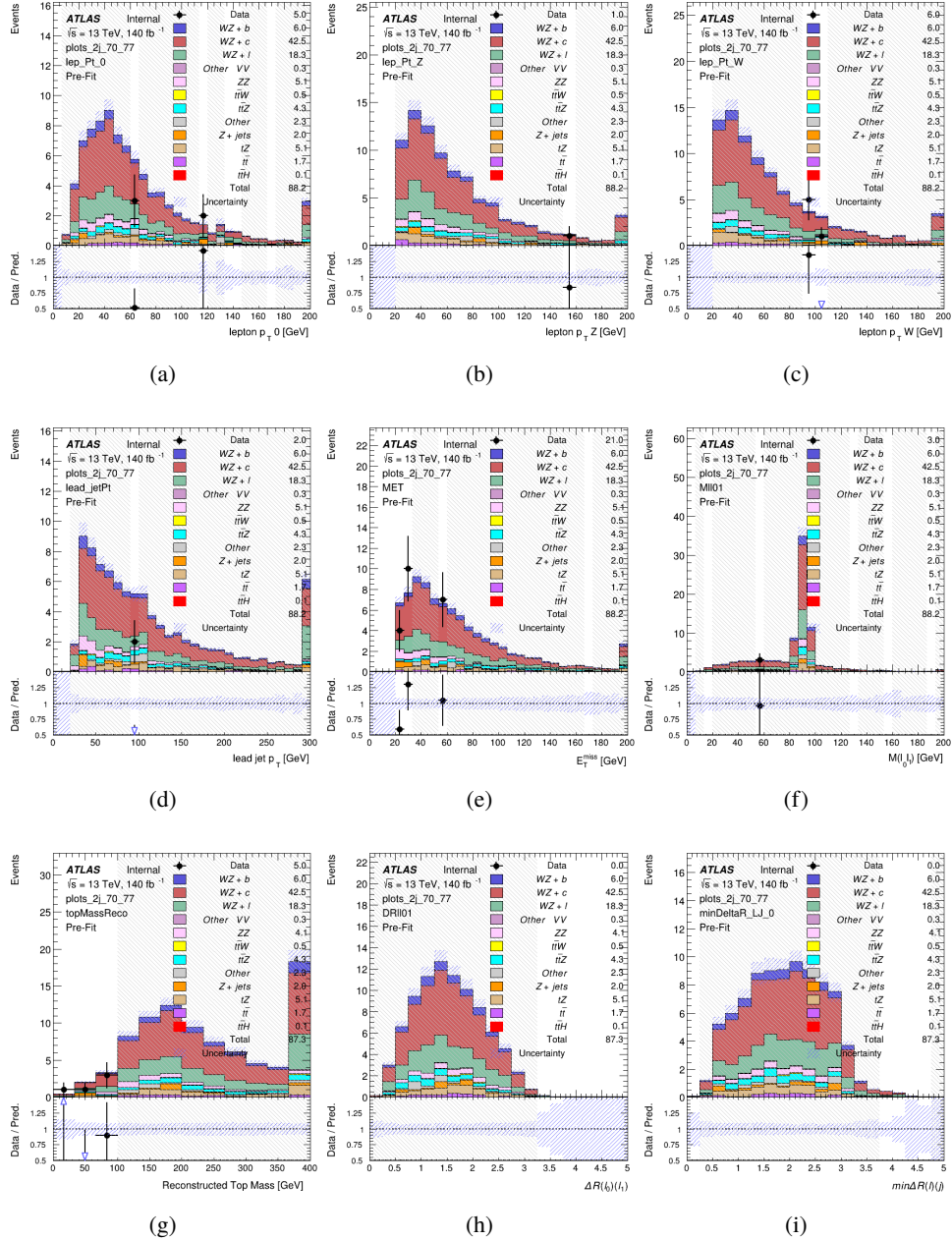


Figure 12.13: Comparisons between the data and MC distributions in the preselection region for (a) the p_T of the opposite sign lepton, (b) the p_T of the other lepton from the Z candidate, (c) the p_T of the lepton from the W candidate, (d) the leading jet p_T , (e) the E_T^{miss} , and (f) the invariant mass of leptons 0 and 1, (g) the reconstructed top mass, (h) $\Delta(R)$ between lepton 0 and 1, (i) the $\Delta(R)$ between the closest lepton and jet.

WZ Fit Region - 2j 60-70% WP

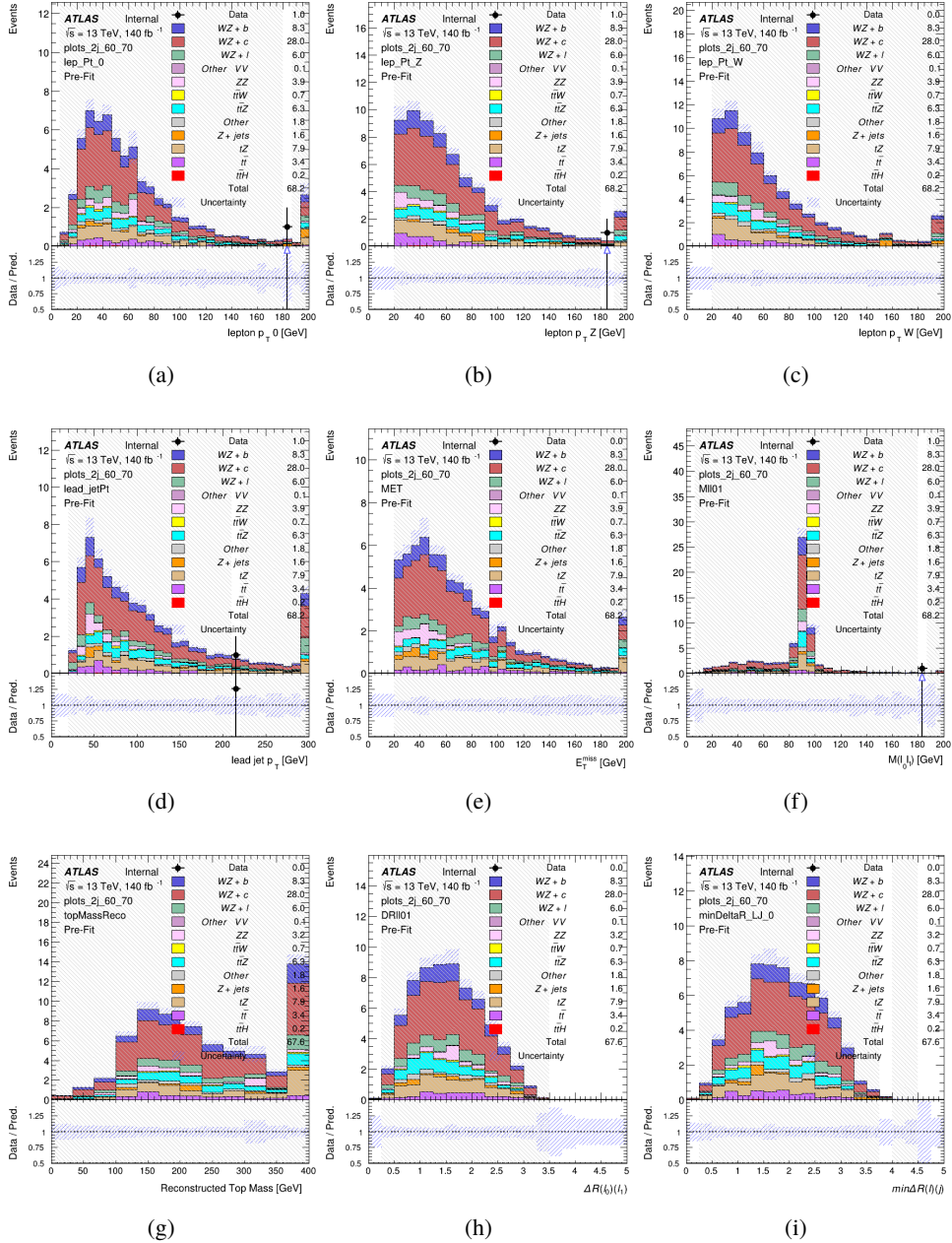


Figure 12.14: Comparisons between the data and MC distributions in the preselection region for (a) the p_T of the opposite sign lepton, (b) the p_T of the other lepton from the Z candidate, (c) the p_T of the lepton from the W candidate, (d) the leading jet p_T , (e) the E_T^{miss} , and (f) the invariant mass of leptons 0 and 1, (g) the reconstructed top mass, (h) $\Delta(R)$ between lepton 0 and 1, (i) the $\Delta(R)$ between the closest lepton and jet.

WZ Fit Region - 2j 60% WP

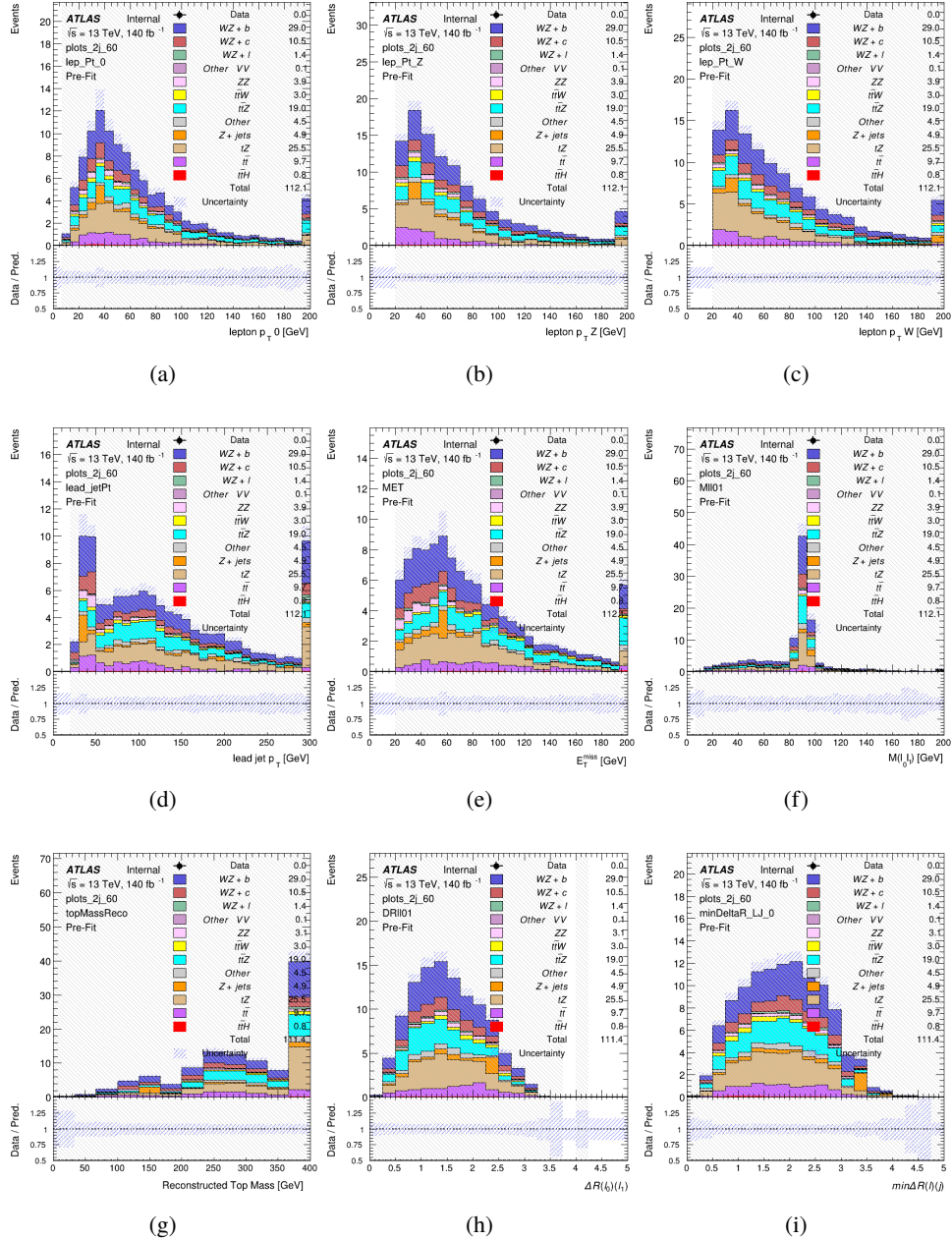


Figure 12.15: Comparisons between the data and MC distributions in the preselection region for (a) the p_T of the opposite sign lepton, (b) the p_T of the other lepton from the Z candidate, (c) the p_T of the lepton from the W candidate, (d) the leading jet p_T , (e) the E_T^{miss} , and (f) the invariant mass of leptons 0 and 1, (g) the reconstructed top mass, (h) $\Delta(R)$ between lepton 0 and 1, (i) the $\Delta(R)$ between the closest lepton and jet.

WZ Fit Region - tZ-CR-2j

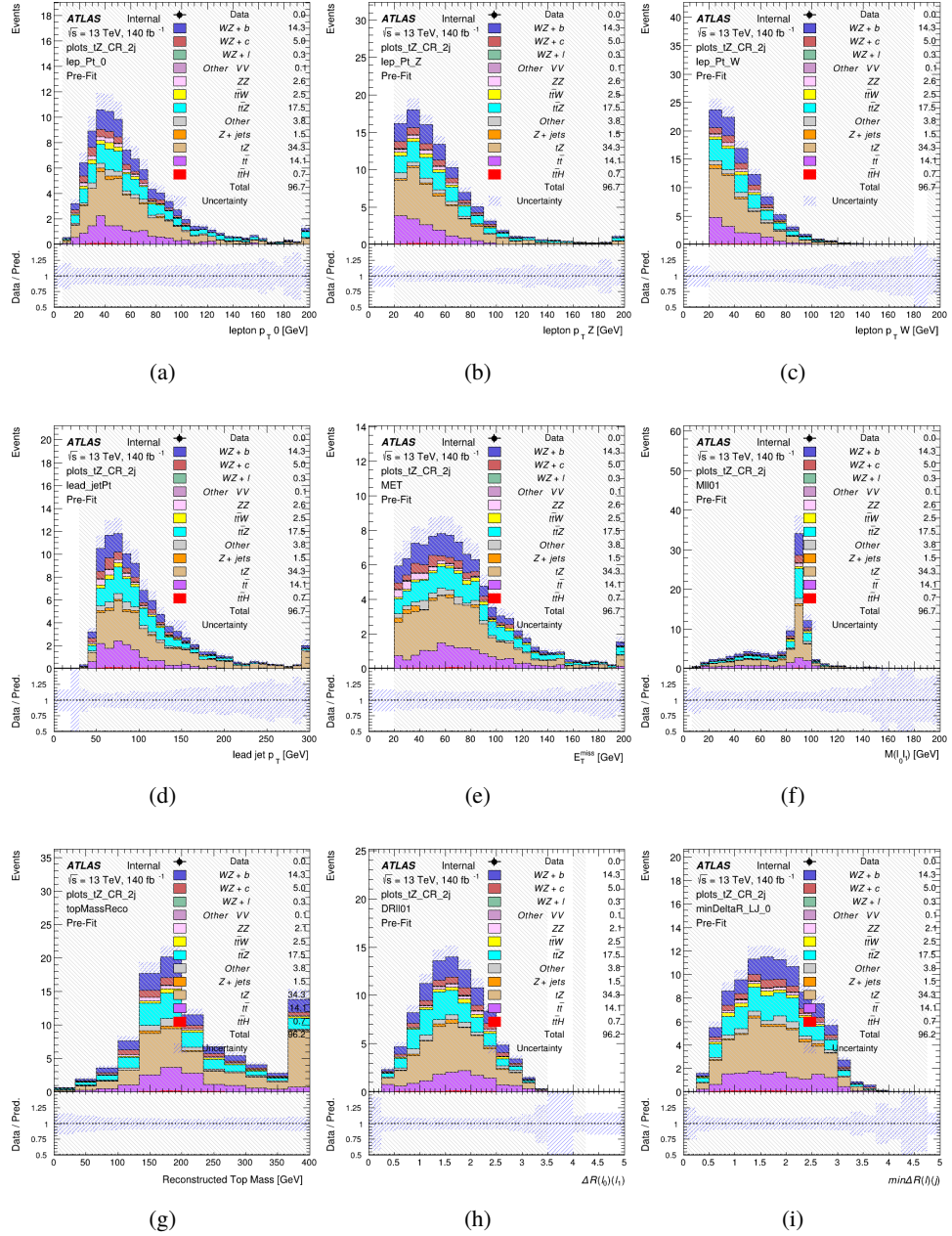


Figure 12.16: Comparisons between the data and MC distributions in the preselection region for (a) the p_T of the opposite sign lepton, (b) the p_T of the other lepton from the Z candidate, (c) the p_T of the lepton from the W candidate, (d) the leading jet p_T , (e) the E_T^{miss} , and (f) the invariant mass of leptons 0 and 1, (g) the reconstructed top mass, (h) $\Delta(R)$ between lepton 0 and 1, (i) the $\Delta(R)$ between the closest lepton and jet.

928 **12.3 Non-Prompt Lepton Estimation**

929 Two processes act as sources of non-prompt leptons appear in the analysis: $t\bar{t}$ and Z+jet
 930 production both produce two prompt leptons, and each contribute to the 31 region when an
 931 additional non-prompt lepton appears in the event. The contribution of these processes is
 932 estimated with Monte Carlo simulations, which are validated using enriched control regions.

933 **12.3.1 $t\bar{t}$ Validation**

934 $t\bar{t}$ events can produce two prompt leptons from the decay of each of the tops. These top decays
 935 produce two b-quarks, the decay of which can produce additional non-prompt leptons, which
 936 occasionally pass the event preselection. In order to validate that the Monte Carlo accurately
 937 simulates this process accurately, the MC prediction in a non-prompt $t\bar{t}$ enriched control region
 938 is compared to data.

939 The $t\bar{t}$ control region is similar to the preselection region - three leptons meeting the
 940 criteria described in Section 12 are required, and the requirements on E_T^{miss} remain the same.
 941 However, the selection requiring a lepton pair form a Z-candidate are reversed. Events where the
 942 invariant mass of any two opposite sign, same flavor leptons falls within 10 GeV of 91.2 GeV are
 943 rejected. This ensures the $t\bar{t}$ control region is orthogonal to the preselection region.

944 Further, because the jet multiplicity of $t\bar{t}$ events tends to be higher than WZ, the number
 945 of jets in each event is required to be greater than 1. As b-jets are almost invariably produced

⁹⁴⁶ from top decays, at least one b-tagged jet passing the 70% DL1r WP in each event is required.

⁹⁴⁷ Various kinematic plots of this region are shown in Figure 12.17.

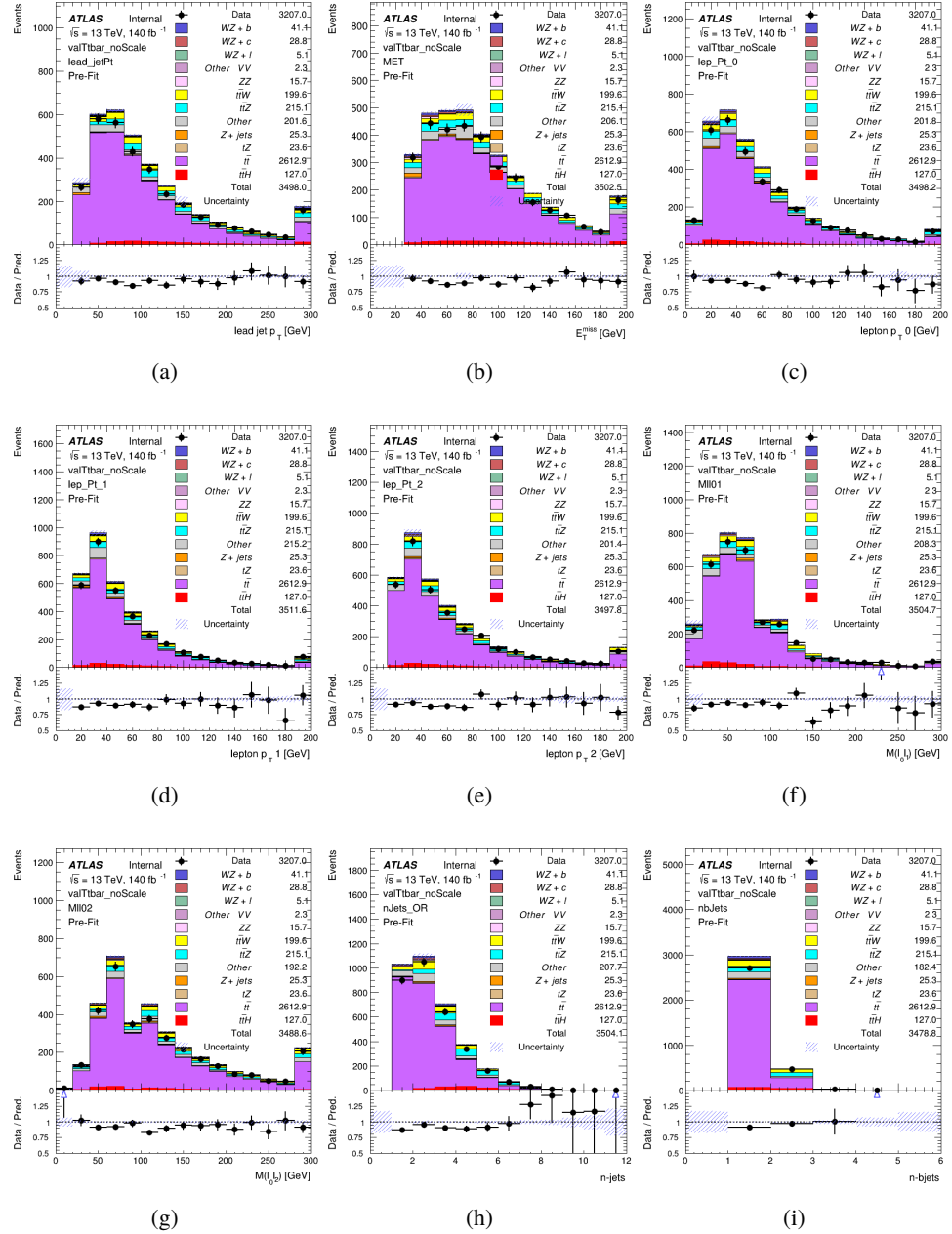


Figure 12.17: Comparisons between the data and MC distributions in the $t\bar{t}$ control region for (a) the p_T of the leading jet, (b) the missing transverse energy, (c) the p_T of lepton 0, (d) p_T of lepton 1, (e) p_T of lepton 2, (f) the invariant mass of leptons 0 and 1, (g) the invariant mass of leptons 0 and 2, (h) the number of jets, (i) the number of b-tagged jets.

948 The shape of each distribution agrees quite well between data and MC, with a constant
949 offset between the two. This is accounted for by applying a constant correction factor of 0.883
950 to the $t\bar{t}$ MC prediction. Plots showing the kinematics of the $t\bar{t}$ VR after this correction factor
951 has been applied are shown in Figure 12.18.

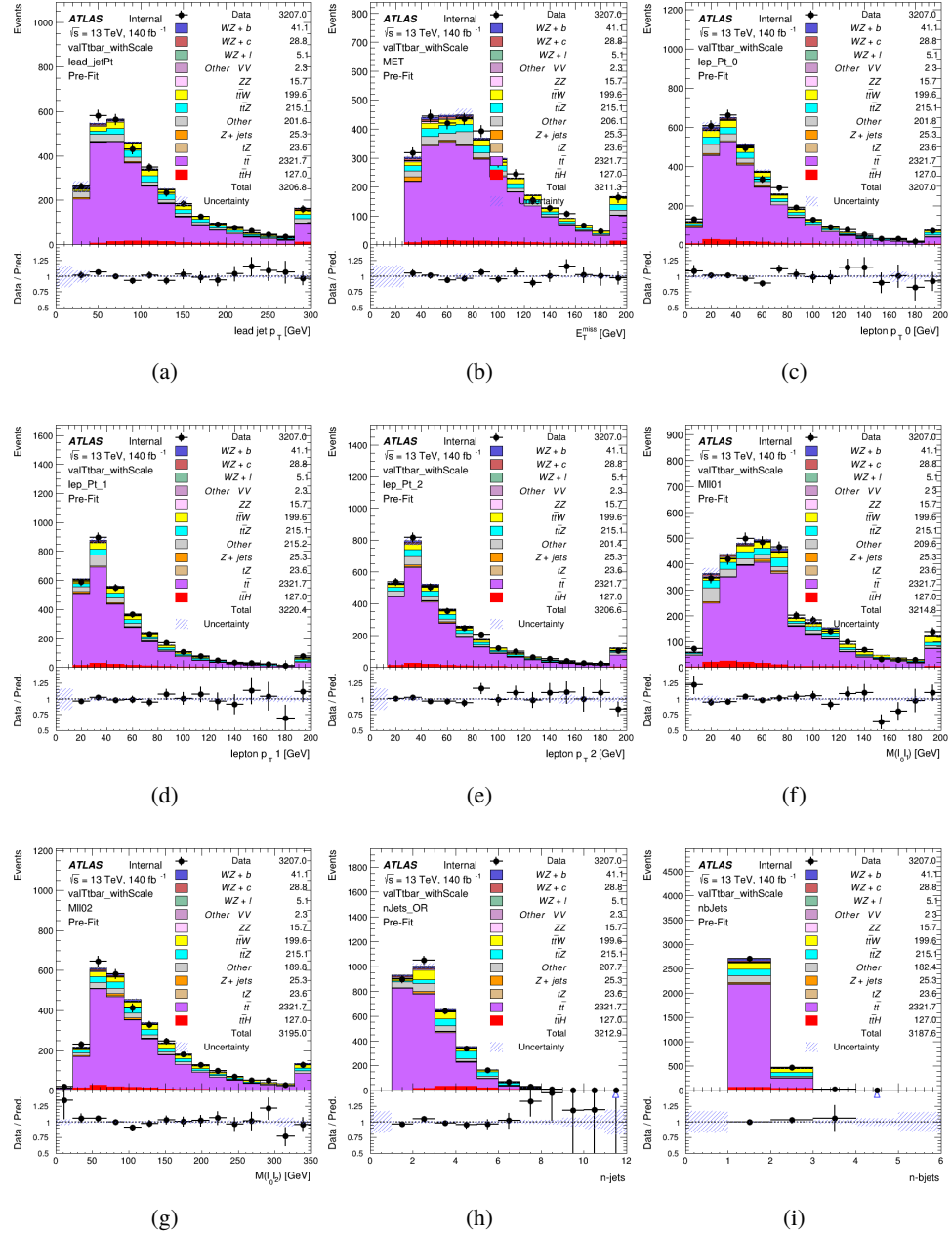


Figure 12.18: Comparisons between the data and MC distributions in the $t\bar{t}$ control region after the correction factor has been applied for (a) the p_T of the leading jet, (b) the missing transverse energy, (c) the p_T of lepton 0, (d) p_T of lepton 1, (e) p_T of lepton 2, (f) the invariant mass of leptons 0 and 1, (g) the invariant mass of leptons 0 and 2, (h) the number of jets, (i) the number of b-tagged jets.

952 The modeling is further validated by looking at the yield in the $t\bar{t}$ VR for each DL1r WP,
 953 giving a clearer correspondence to the signal regions used in the fit. Each region shown in Figure
 954 12.19 requires one or more jets pass the listed WP, with no jets passing the next highest WP.

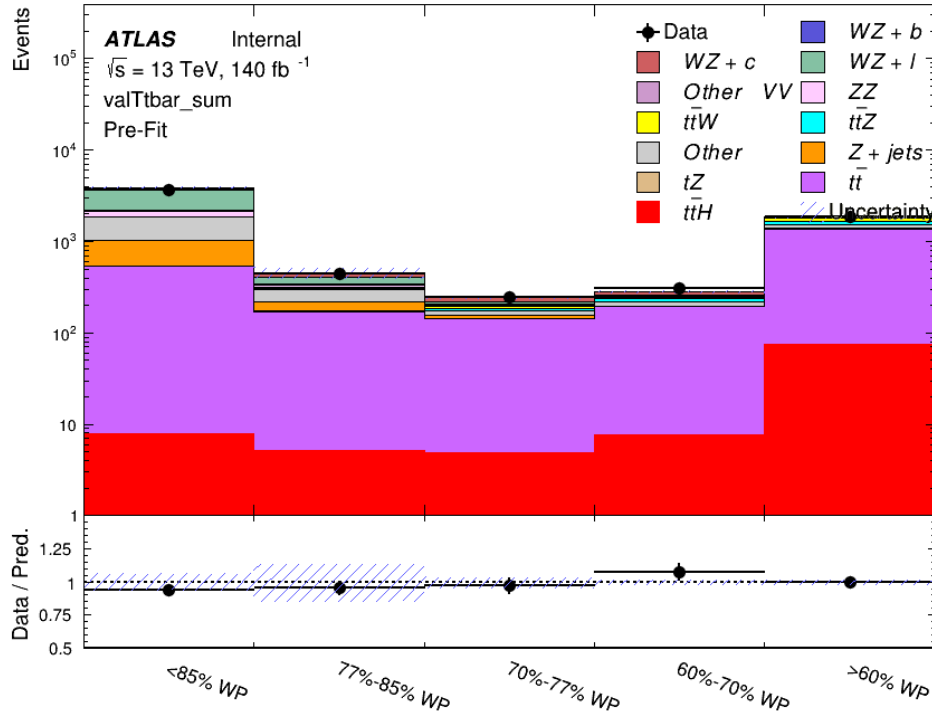


Figure 12.19: Data and MC comparisons for each DL1r WP for both 1-jet and 2-jet regions, after the $t\bar{t}$ VR selection and correction factor have been applied

955 As data and MC are found to agree within 20% for each of these working points, a 20%
 956 systematic uncertainty on the $t\bar{t}$ prediction is included for the analysis.

957 12.3.2 Z+jets Validation

958 Similar to $t\bar{t}$, a non-prompt Z +jets control region is produced in order to validate the MC
959 predictions. The lepton requirements remain the same as the preselection region. Because no
960 neutrinos are present for this process, the E_T^{miss} cut is reversed, requiring $E_T^{\text{miss}} < 30 \text{ GeV}$. This
961 also ensures this control region is orthogonal to the preselection region. Further, the number of
962 jets in each event is required to be greater than or equal to one. Various kinematic plots of this
963 region are shown below. The general agreement between data and MC in each of these suggests
964 that the non-prompt contribution of Z +jets is well modeled by Monte Carlo.

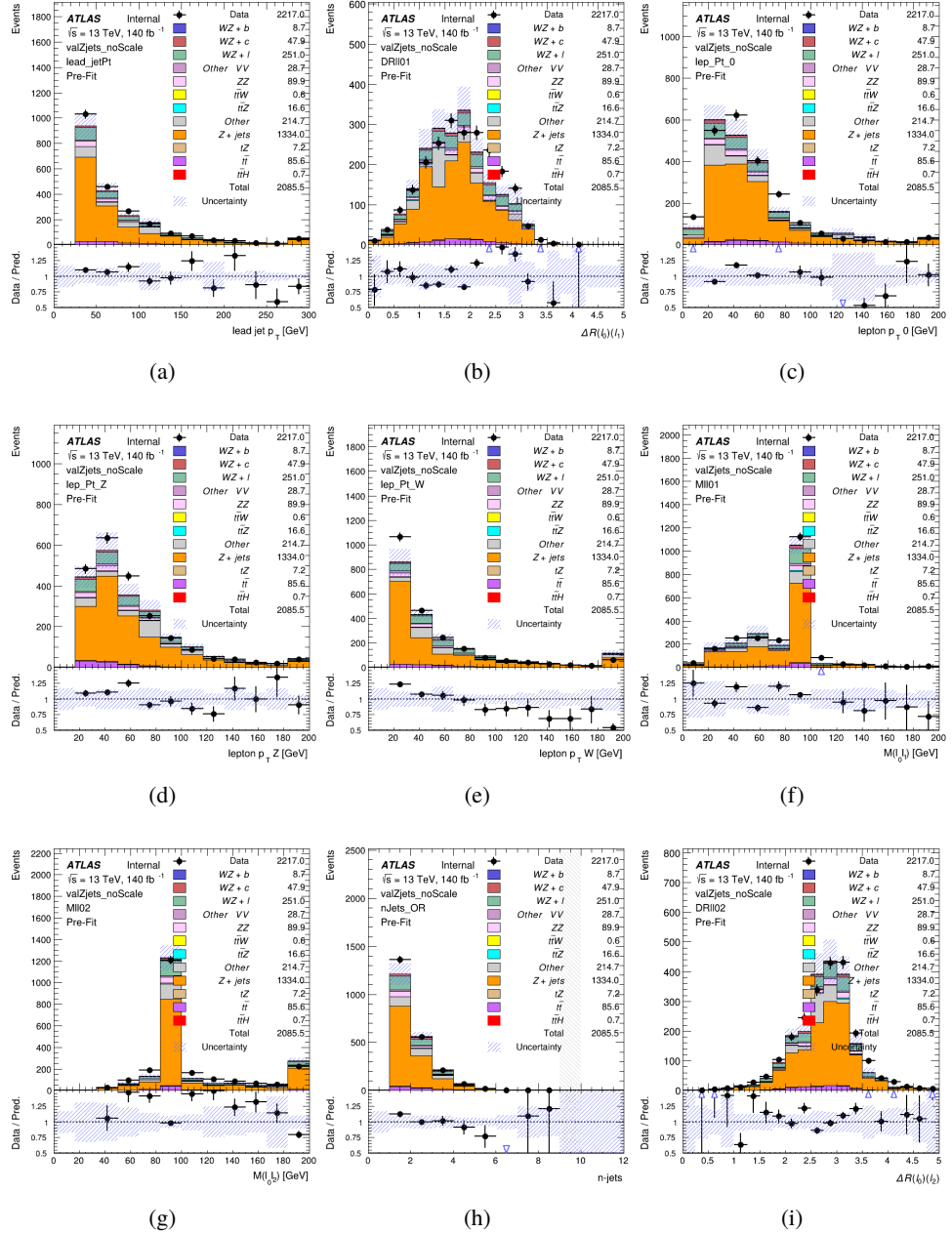


Figure 12.20: Comparisons between the data and MC distributions in the $Z+jets$ control region for (a) the p_T of the leading jet, (b) ΔR between leptons 0 and 1, (c) the p_T of lepton 0, (d) p_T of SS lepton from the Z candidate, (e) p_T of the SS lepton from the W candidate, (f) the invariant mass of leptons 0 and 1, (g) the invariant mass of leptons 0 and 2, (h) the number of jets, (i) ΔR between leptons 0 and 2. Includes only statistical uncertainties

965 While there is general agreement between data and MC within statistical uncertainty, the
966 shape of the p_T spectrum of the lepton from the W is found to differ. To account for this
967 discrepancy, a variable correction factor is applied to Z+jets. χ^2 minimization of the lepton 2 p_T
968 spectrum is performed to derive a correction factor of $1.53 - 6.6 * 10^{-6}(\text{lep}_\text{Pt}_W)$. Kinematic
969 plots of the Z + jets control region after this correction factor has been aplied are shown in Figure
970 [12.21](#).

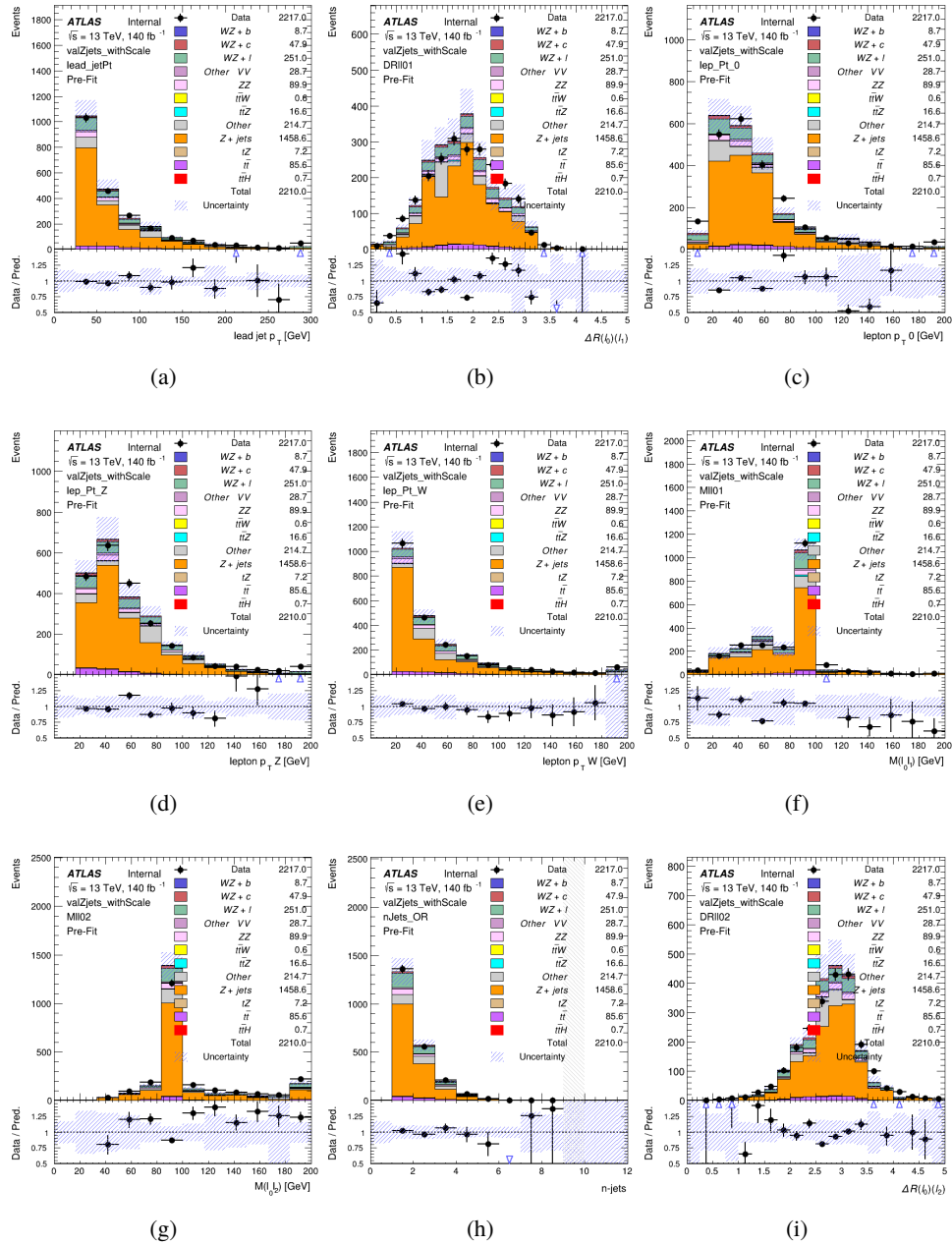


Figure 12.21: Comparisons between the data and MC distributions in the $Z + \text{jets}$ control region after the correction factor has been applied for (a) the p_T of the leading jet, (b) ΔR between leptons 0 and 1, (c) the p_T of lepton 0, (d) p_T of SS lepton from the Z candidate, (e) p_T of the SS lepton from the W candidate, (f) the invariant mass of leptons 0 and 1, (g) the invariant mass of leptons 0 and 2, (h) the number of jets, (i) ΔR between leptons 0 and 2

971 The modeling is further validated by looking at the yield in the Z+jets VR for each DL1r
 972 WP, giving a clearer correspondence to the signal regions used in the fit. Each region shown in
 973 Figure 12.22 requires one or more jets pass the listed WP, with no jets passing the next highest
 974 WP.

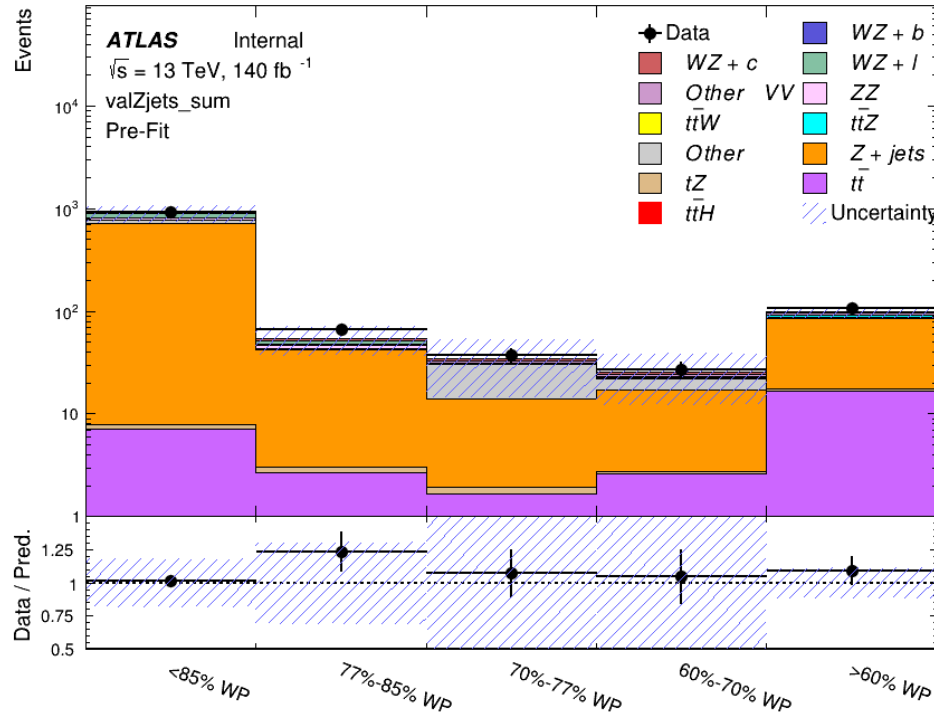


Figure 12.22: Data and MC comparisons for each DL1r WP for both 1-jet and 2-jet regions, after the Z+jets VR selection and correction factor have been applied

975 For each of the b-tagging working points considered, the data falls within 25% of the MC
 976 prediction once this correction factor has been applied. Therefore, a 25% systematic uncertainty
 977 is applied to Z + jets in the analysis.

978 13 tZ Interference Studies and Separation Multivariate Analysis

979 Because tZ produces a final state identical to signal, it represents a predominant background in
980 the most signal enriched regions. That is, the region with one jet passing the 60% DL1r WP.
981 Therefore, a boosted decision tree (BDT) algorithm is trained using TMVA [TMVA_guide] to
982 separate WZ + heavy flavor from tZ.

983 Separation between tZ and WZ + heavy flavor is achieved in part by reconstructing the
984 invariant mass of the top candidate, which clusters more closely to the top mass for tZ than WZ
985 + heavy flavor.

986 The result of this BDT is used to create a tZ enriched region in the fit, reducing its impact
987 on the measurement of WZ + heavy flavor.

988 13.1 Top Mass Reconstruction

989 The reconstruction of the top mass follows the procedure described in detail in section 6.1 of
990 [ttZ_paper]. The mass of the top quark candidate is reconstructed from the jet, the lepton not
991 included in the Z-candidate, and a reconstructed neutrino. In the case that there is one jet in the
992 event, there is only possible b-jet candidate. For events with two jets, the jet with the highest
993 DL1r score is used.

994 The neutrino from the W decay is expected to be the only source of E_T^{miss} . Therefore, the
 995 E_T and ϕ of the neutrino are taken from the E_T^{miss} measurement. This leaves the z-component
 996 of the neutrino momentum, $p_{\nu z}$ as the only unknown.

997 This unknown is solved for by taking the combined invariant mass of the lepton and
 998 neutrino to give the invariant mass of the W boson:

$$999 \quad (p_l + p_\nu)^2 = m_W^2$$

1000 Expanding this out into components, this equation gives:

$$1001 \quad \sqrt{p_{T\nu}^2 + p_{z\nu}^2} E_l = \frac{m_W^2 - m_l^2}{2} + p_{T\nu}(p_{lx}\cos\phi_\nu + p_{ly}\sin\phi_\nu) + p_{lz}p_{\nu z}$$

1002 This equation gives two solutions for $p_{\nu z}$. For cases where only one of these solutions is
 1003 real, that is taken as the value of $p_{\nu z}$. For instances with two real solutions, the one which is
 1004 shown to be correct in the largest fraction of simulations is taken. For cases when no real solution
 1005 is found, often because of detector effects, the value of E_T^{miss} is varied in decreasing increments
 1006 of 100 MeV until a real solution is found.

1007 The reconstructed top mass distribution for tZ and WZ + b can be seen in figure 13.1.

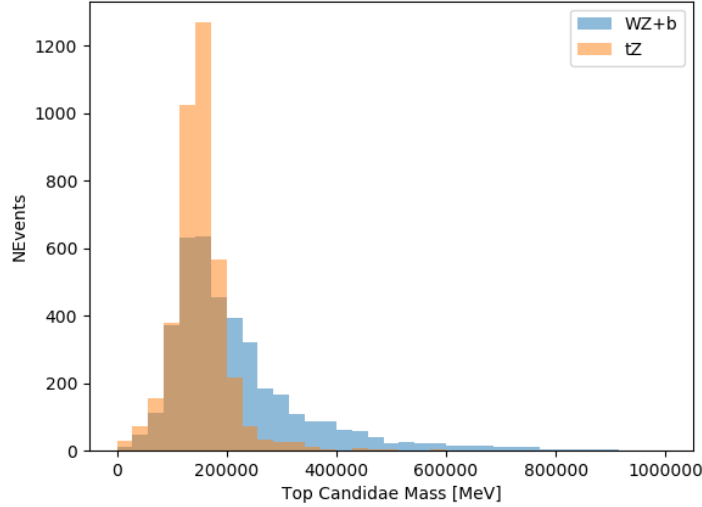


Figure 13.1: Reconstructed top mass distributions for tZ and WZ + b, measured in MeV.

13.2 tZ BDT

A Boosted Decision Tree (BDT), specifically XGBoost [xgboost_cite], is used to provide separation between tZ and WZ+b. The following kinematic variables are used as inputs:

- The invariant mass of the reconstructed top candidate
- p_T of each of the leptons, jet
- The invariant mass of each combination of lepton pairs, $M(l\bar{l})$
- E_T^{miss}
- Distance between each combination of leptons, $\Delta R(l\bar{l})$

- 1016 • Distance between each lepton and the jet, $\Delta R(lj)$

1017 The training samples included only events meeting the requirements of the 1-jet, $>60\%$
1018 region, i.e. passing all the selection described in section 12 and having exactly one jet which
1019 passes the tightest (60%) DL1r working point.

1020 The distributions of a few of these features for both signal and background is shown in
1021 figure 13.2.

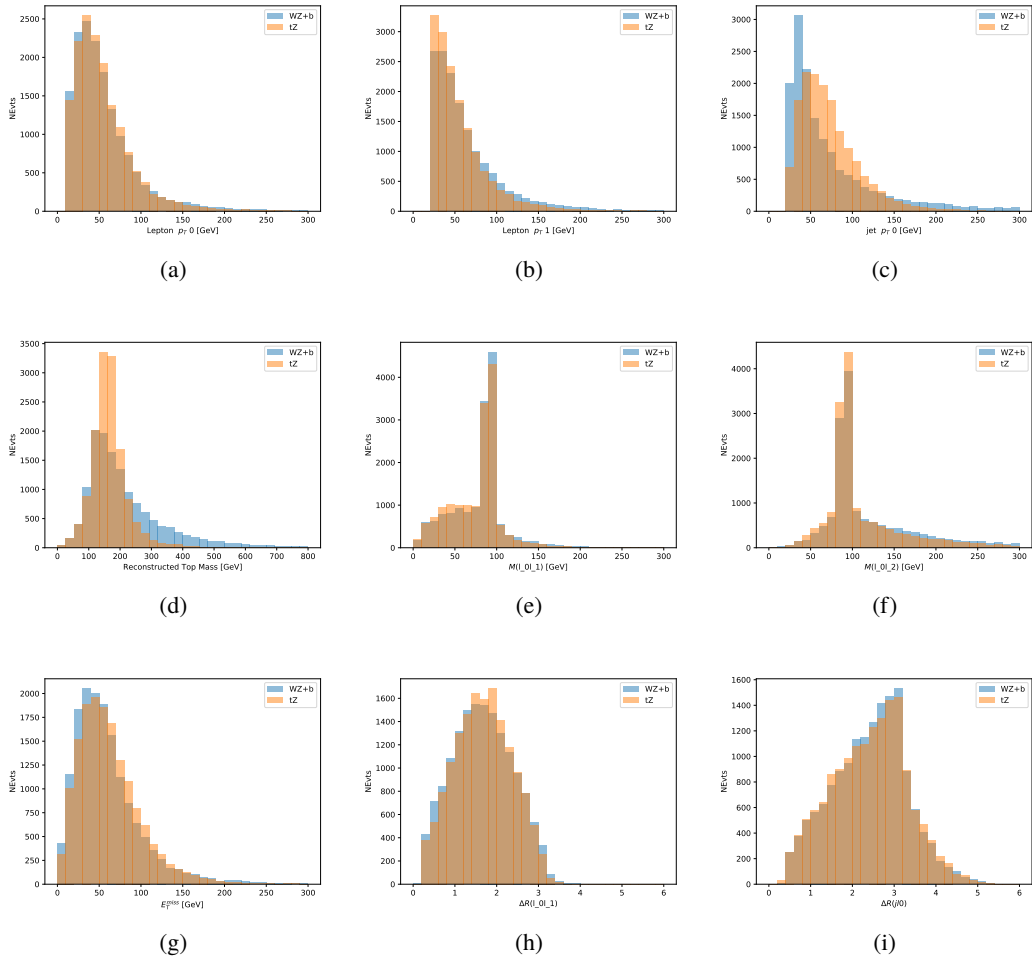


Figure 13.2: Distribution of input features of the BDT for signal (WZ) and background (tZ). Both are scaled to an equal number of events. (a), (b) and (c) show the p_T of lepton 0, lepton 1, and the jet, (d) show the reconstructed top mass, (e) and (f) show the invariant mass of leptons 0 and 1, leptons 0 and 2. (g) shows the E_T^{miss} of each event. (h) and (i) show the ΔR between lepton 0 and lepton 1, and the jet.

1022 A sample of 20,000 background (tZ) and signal (WZ+b) Monte Carlo events are used to
 1023 train the BDT. And additional 5,000 events are reserved for testing the model, in order to prevent
 1024 over-fitting. A total of 750 decision trees with a maximum depth of 6 branches are used to build
 1025 the model. These parameters are chosen empirically, by training several models with different

1026 parameters and selecting the one that gave the best separation for the test sample.

1027 The results of the BDT training are shown in figure 13.3. The output scores for both signal
 1028 and background events is shown on the left. The right shows the receiving operating characteristic
 1029 (ROC) curve that results from the MVA. The ROC curve represents the background rejection
 1030 as a function of signal efficiency, where each point on the curve represents a different response
 1031 score. The ROC curve of the BDT is compared to the performance of using an optimal set of flat
 1032 selections on the same set of input variables.

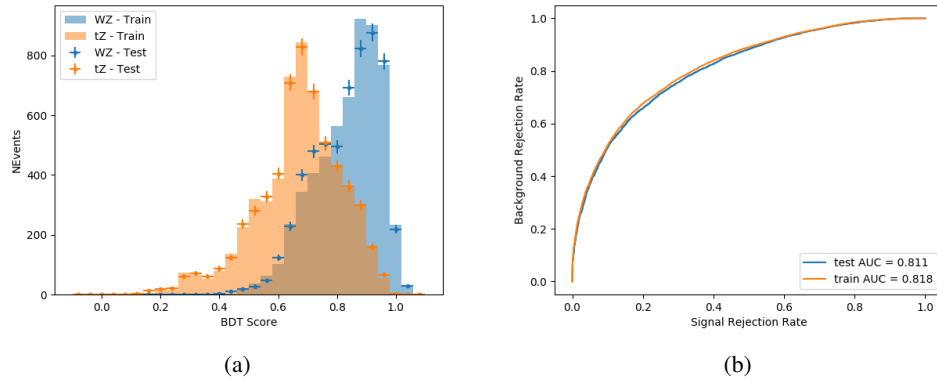


Figure 13.3: Distribution of the BDT response for signal and background events on the left, the ROC curve for the BDT on the right.

1033 The relative important of each input feature in the model, measured by how often they
 1034 appeared in the decision trees, is shown in figure 13.4.

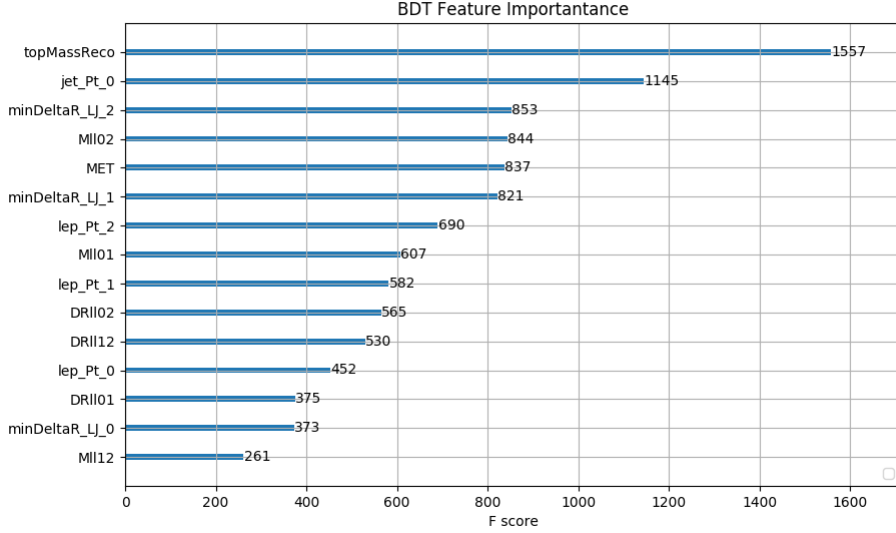


Figure 13.4: Relative importance of each input feature in the model.

1035 These results suggest that some amount of separation can be achieved between these two
 1036 processes, with a high BDT score selecting a set of events that is pure in $WZ + b$. A BDT score
 1037 of 0.725 is selected as a cutoff, where events with scores higher than this form a signal enriched
 1038 region, and events with scores lower than this form a tZ control region. This cutoff is selected by
 1039 varying the value of this cutoff in stat-only Asimov fits, and selecting the value that minimizes
 1040 the statistical uncertainty on $WZ + b$.

1041 14 Systematic Uncertainties

1042 The systematic uncertainties that are considered are summarized in Table 49. These are imple-
 1043 mented in the fit either as a normalization factors or as a shape variation or both in the signal

¹⁰⁴⁴ and background estimations. The numerical impact of each of these uncertainties is outlined in

¹⁰⁴⁵ Section 22.

Table 17: Sources of systematic uncertainty considered in the analysis.

Systematic uncertainty	Components
Luminosity	1
Pileup reweighting	1
Physics Objects	
Electron	6
Muon	15
Jet energy scale	28
Jet energy resolution	8
Jet vertex fraction	1
Jet flavor tagging	131
E_T^{miss}	3
Total (Experimental)	194
Signal Modeling	
Shape modelling	3
Renormalization and factorization scales	5
nJet Migration	4
Background Modeling	
Cross section	15
Renormalization and factorization scales	12
Total (Signal and background modeling)	35
Total (Overall)	229

¹⁰⁴⁶ The uncertainty in the combined integrated luminosity is derived from a calibration of the

¹⁰⁴⁷ luminosity scale performed for 13 TeV proton-proton collisions [**lumi**], [**LUCID2**].

¹⁰⁴⁸ The experimental uncertainties are related to the reconstruction and identification of light

¹⁰⁴⁹ leptons and b-tagging of jets, and to the reconstruction of E_T^{miss} . The TOTAL electron ID

¹⁰⁵⁰ correlation model is used, corresponding to 1 electron ID systematic. Electron ID is found to be

1051 a subleading systematic that is unconstrained by the fit, making it an appropriate choice for this
1052 analysis.

1053 The sources which contribute to the uncertainty in the jet energy scale (JES) [**jes**] are decom-
1054 posed into uncorrelated components and treated as independent sources in the analysis. The
1055 CategoryReduction model is used to account for JES uncertainties, which decomposes the uncer-
1056 tainties into 30 nuisance parameters included in the fit. The SimpleJER model is used to account
1057 for jet energy resolution (JER) uncertainties, and 8 JER uncertainty components included as
1058 NPs in the fit.

1059 The uncertainties in the b-tagging efficiencies measured in dedicated calibration analyses
1060 [**btag_cal**] are also decomposed into uncorrelated components. The large number of components
1061 for b-tagging is due to the calibration of the distribution of the MVA discriminant.

1062 The full list of systematic uncertainties considered in the analysis is summarized in Tables
1063 [18](#), [19](#) and [20](#).

1064

Experimental Systematics on Leptons and E_T^{miss}			
Type	Description	Systematics Name	Application
Trigger			
Scale Factors	Trigger Efficiency	lepSFTrigTight_MU(EL)_SF_Trigger_STAT(SYST)	Event Weight
Muons			
Efficiencies	Reconstruction and Identification	lepSFObjTight_MU_SF_ID_STAT(SYST)	Event Weight
	Isolation	lepSFObjTight_MU_SF_Isol_STAT(SYST)	Event Weight
	Track To Vertex Association	lepSFObjTight_MU_SF_TTVA_STAT(SYST)	Event Weight
p_T Scale	p_T Scale	MUONS_SCALE	p_T Correction
Resolution	Inner Detector Energy Resolution	MUONS_ID	p_T Correction
	Muon Spectrometer Energy Resolution	MUONS_MS	p_T Correction
Electrons			
Efficiencies	Reconstruction	lepSFObjTight_EL_SF_ID	Event Weight
	Identification	lepSFObjTight_EL_SF_Reco	Event Weight
	Isolation	lepSFObjTight_EL_SF_Isol	Event Weight
Scale Factor	Energy Scale	EG_SCALE_ALL	Energy Correction
Resolution	Energy Resolution	EG_RESOLUTION_ALL	Energy Correction
E_T^{miss}			
Soft Tracks Terms	Resolution	MET_SoftTrk_ResoPerp	p_T Correction
	Resolution	MET_SoftTrk_ResoPara	p_T Correction
	Scale	MET_SoftTrk_ScaleUp	p_T Correction
	Scale	MET_SoftTrk_ScaleDown	p_T Correction

Table 18: Summary of experimental systematics considered for leptons and E_T^{miss} . Includes type, description, name of systematic as used in the fit, and mode of application. The mode of application indicates the systematic evaluation, e.g. as an overall event re-weighting (Event Weight) or rescaling (p_T Correction).

Experimental Systematics on Jets			
Type	Origin	Systematics Name	Application
Jet Vertex Tagger		JVT	Event Weight
Energy Scale	Calibration Method	JET_21NP_ JET_EffectiveNP_1-19	p_T Correction p_T Correction
	η inter-calibration	JET_EtaIntercalibration_Modelling JET_EtaIntercalibration_NonClosure JET_EtaIntercalibration_TotalStat	p_T Correction p_T Correction p_T Correction
	High p_T jets	JET_SingleParticle_HighPt	p_T Correction
	Pile-Up	JET_Pileup_OffsetNPV JET_Pileup_OffsetMu JET_Pileup_PtTerm JET_Pileup_RhoTopology	p_T Correction p_T Correction p_T Correction p_T Correction
	Non Closure	JET_PunchThrough_MC15	p_T Correction
	Flavour	JET_Flavor_Response JET_BJES_Response JET_Flavor_Composition	p_T Correction p_T Correction p_T Correction
Resolution		JET_JER_SINGLE_NP	Event Weight

Table 19: Jet systematics take into account effects of jets calibration method, η inter-calibration, high p_T jets, pile-up, and flavor response. They are all diagonalised into effective parameters.

Experimental Systematics on b-tagging		
Type	Origin	Systematic Name
Scale Factors	DL1r b-tagger efficiency on b originated jets in bins of η	DL1r_Continuous_EventWeight_B0-29
	DL1r b-tagger efficiency on c originated jets in bins of η	DL1r_Continuous_EventWeight_C0-19
	DL1r b-tagger efficiency on light flavoured originated jets in bins of η and p_T	DL1r_Continuous_EventWeight_Light0-79
	DL1r b-tagger extrapolation efficiency	DL1r_Continuous_EventWeight_extrapolation DL1r_Continuous_EventWeight_extrapolation_from_charm

Table 20: Summary of experimental systematics to be included for b-tagging of jets in the analysis, using the continuous DL1r tagging algorithm. All of the b-tagging related systematics are applied as event weights. From left: type, description, and the name of systematic used in the fit.

1065 Theoretical uncertainties applied to MC predictions, including cross section, PDF, and scale
 1066 uncertainties are taken from theory calculations, with the exception of non-prompt and diboson
 1067 backgrounds. The cross-section uncertainty on tZ is taken from [tZ_paper]. Derivation of the
 1068 non-prompt background uncertainties, Z+jets and t \bar{t} , are explained in detail in Section 12.3.
 1069 These normalization uncertainties are chosen so as to account for the complete uncertainty in the
 1070 non-prompt contribution, and therefore no additional modelling uncertainties are considered for
 1071 Z+jets and t \bar{t} .

1072 The other VV + heavy flavor processes (namely VV+b and VV+charm, which primarily
 1073 consist of ZZ events) are also poorly understood, because these processes involve the same
 1074 physics as WZ + heavy flavor, and have also not been measured. Therefore, a conservative 50%

1075 uncertainty is applied to those samples. While this uncertainty is large, it is found to have little
 1076 impact on the significance of the final result.

1077 The theory uncertainties applied to the predominate background estimates are summarized
 1078 in Table 21.

Process	X-section [%]
tZ	X-sec: ± 15.2 QCD Scale: $^{+5.2}_{-1.3}$ PDF($+\alpha_S$): ± 1.2
t̄H (aMC@NLO+Pythia8)	QCD Scale: $^{+5.8}_{-9.2}$ PDF($+\alpha_S$): ± 3.6
t̄t Z (aMC@NLO+Pythia8)	QCD Scale: $^{+9.6}_{-11.3}$ PDF($+\alpha_S$): ± 4
t̄t W (aMC@NLO+Pythia8)	QCD Scale: $^{+12.9}_{-11.5}$ PDF($+\alpha_S$): ± 3.4
VV + b/charm (Sherpa 2.2.1)	± 50
VV + light (Sherpa 2.2.1)	± 6
t̄t	± 20
Z + jets	± 25
Others	± 50

Table 21: Summary of theoretical uncertainties for MC predictions in the analysis.

1079 Additional signal uncertainties are estimated by comparing estimates from the nominal Sherpa
 1080 WZ samples with alternate WZ samples generated with Powheg+PYTHIA8 (DSID 361601).
 1081 MC/MC scale factors are applied to make these comparisons. The shape of the templates used
 1082 in the fit are compared between these two samples for WZ + b, WZ + charm and WZ + light, as
 1083 shown in Figures 14.1 and 14.2. Each of these plots are normalized to unity in order to capture
 1084 differences in shape.

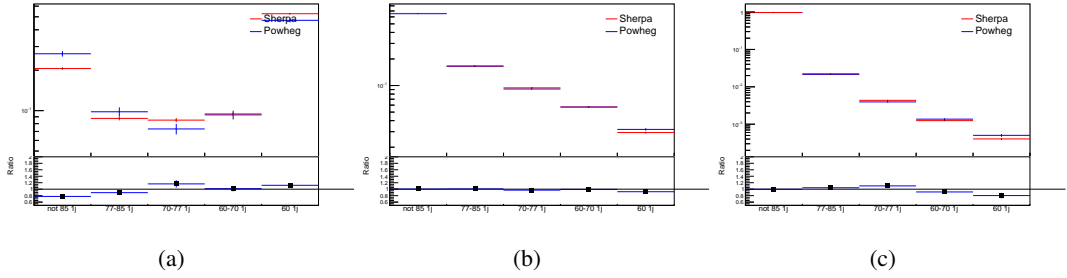


Figure 14.1: Comparison between Sherpa and Powheg predictions of the distribution of (a) WZ + b, (b) WZ + charm, and (c) WZ + light among the various b-tag WPs used in the 1-jet fit.

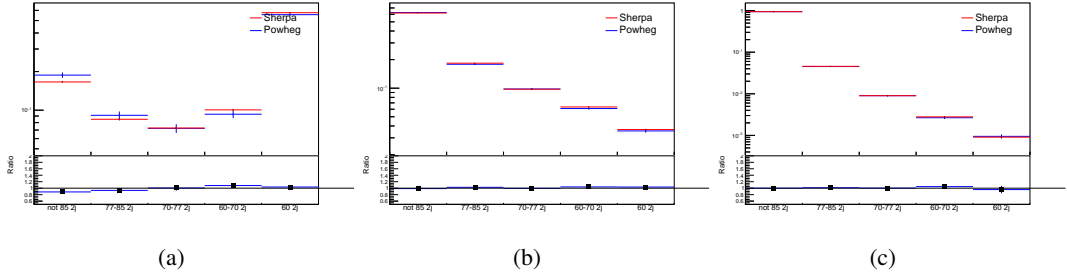


Figure 14.2: Comparison between Sherpa and Powheg predictions of the distribution of (a) WZ + b, (b) WZ + charm, and (c) WZ + light among the various b-tag WPs used in the 2-jet fit.

1085 Separate systematics are included in the fit for WZ + b, WZ + charm and WZ + light,
 1086 where the distribution among each of the fit regions is varied based on the prediction of the
 1087 Powheg sample.

1088 A similar approach is taken to account for uncertainties in migrations between the number of
 1089 reco and truth jets. The fraction of events with 1 truth jet which fall into the 1 jet bin versus the
 1090 2 jet bin at reco level is compared for Sherpa and Powheg. The same is done for events with 2
 1091 truth jets. This comparison is shown in figure 14.3.

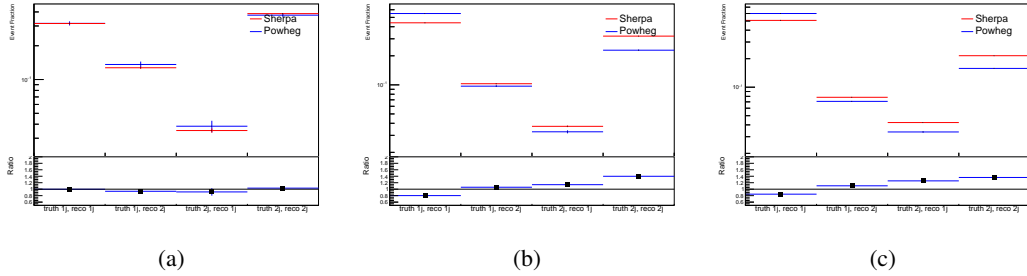


Figure 14.3: Comparison between Sherpa and Powheg predictions for truth jet migrations between the 1 and 2 jet reco bins for (a) WZ + b, (b) WZ + charm, and (c) WZ + light

1092 A systematic is included where events are shifted between the 1-jet and 2-jet regions based
 1093 on the differences between these two shapes. This is done independently for each of the WZ +
 1094 b, WZ + charm, and WZ + light templates.

1095 Additional systematics are included to account for the uncertainty in the contamination of
 1096 0 jet and 3 or more jet events (at truth level) in the 1 and 2 reco jet bins. Because these events
 1097 fall outside the scope of this measurement, these events are included as a background. As such,
 1098 a normalization, rather than a shape, uncertainty is applied for this background.

1099 The number of WZ events with 0-jets and ≥ 3 -jets in the reconstructed 1-jet and 2-jet
 1100 regions are compared for Sherpa and Powheg, as seen in figure 14.4. These differences are taken
 1101 as separate normalization systematics on the yield of WZ+0-jet and WZ+ ≥ 3 -jet events.

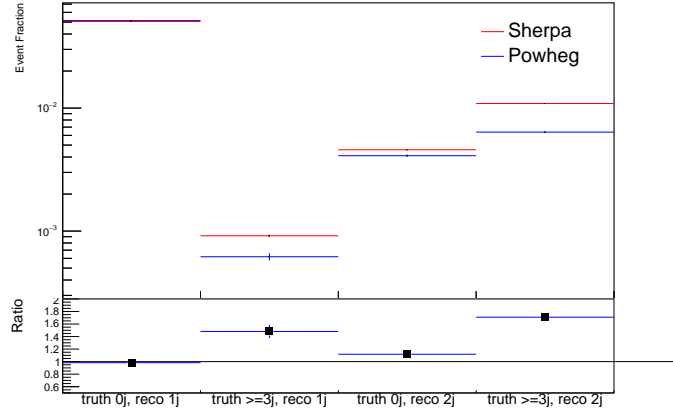


Figure 14.4: Comparison between Sherpa and Powheg predictions for 0 and ≥ 3 truth jet contributions in the 1 and 2 jet reco bins

15 Results

1102 A separate maximum-likelihood fit is performed over the 1-jet and 2-jet fit regions in order to
 1103 extract the best-fit value of the WZ + b-jet and WZ + charm jet contributions. The WZ + b,
 1104 WZ + charm and WZ + light contributions are allowed to float, with the remaining background
 1105 contributions are held fixed. **The current fit strategy treats the WZ + b-jet contribution as**
 1106 **the parameter of interest, with the normalization of the WZ + charm and the WZ + light**
 1107 **contributions taken as systematic uncertainties. This could however be adjusted, depending**
 1108 **on whether it is decided the goal of the analysis should be to measure WZ+b specifically or**
 1109 **WZ + heavy flavor overall.** The result of the fit is used to extract the cross-section of WZ +
 1110 heavy-flavor production.

1112 A maximum likelihood fit to data is performed simultaneously in the regions described

1113 in Section 12. The parameters μ_{WZ+b} , $\mu_{WZ+charm}$, $\mu_{WZ+light}$, where $\mu = \sigma_{\text{observed}}/\sigma_{\text{SM}}$, are
 1114 extracted from the fit.

1115 The Asimov fit for 1-jet events gives an expected μ value of $1.00^{+0.37}_{-0.35}(\text{stat})^{+0.24}_{-0.22}(\text{sys})$ for
 1116 $WZ + b$. The fitted cross-section modifiers for $WZ + \text{charm}$ and $WZ + \text{light}$ are $1.00 \pm 0.17 \pm 0.15$
 1117 and $1.00 \pm 0.04 \pm 0.07$, respectively.

1118 The expected cross-section of $WZ+b$ with 1 associated jet obtained from the fit is
 1119 $1.74^{+0.65}_{-0.61}(\text{stat})^{+0.42}_{-0.37}(\text{sys}) \text{ fb}$ with an expected significance of 2.2σ . The expected cross-section
 1120 of $WZ + \text{charm}$ is measured to be $14.6 \pm 2.5(\text{stat}) \pm 2.1(\text{sys}) \text{ fb}$, with a correlation of -0.23.

1121 For 2-jet events, the fit gives an expected μ value of $1.00^{+0.34}_{-0.33}(\text{stat})^{+0.29}_{-0.28}(\text{sys})$ for $WZ +$
 1122 b . The fitted cross-section modifiers for $WZ + \text{charm}$ and $WZ + \text{light}$ are $1.00 \pm 0.17 \pm 0.15$ and
 1123 $1.00 \pm 0.04 \pm 0.08$, respectively.

1124 The expected $WZ + b$ cross-section in the 2-jet region is $2.46^{+0.83}_{-0.81}(\text{stat})^{+0.073}_{-0.68}(\text{sys}) \text{ fb}$
 1125 with an expected significance of 2.6σ . The 2-jet expected cross-section of $WZ + \text{charm}$ is
 1126 $12.7 \pm 2.2(\text{stat}) \pm 2.0(\text{sys}) \text{ fb}$, and the correlation between $WZ + \text{charm}$ and $WZ + b$ is -0.26.

1127 15.1 1-jet Fit Results

1128 **The results of the fit are currently blinded.**

¹¹²⁹ The pre-fit yields in each of the regions used in the fit are shown in Table 15.1, and

¹¹³⁰ summarized in Figure 15.1.

¹¹³¹

Sample	1j, <85% WP	1j, 77%-85% WP	1j, 70%-77% WP	1j, 60%-70% WP	1j, >60% WP	tZ CR
WZ + b - 1j	8.1 ± 1.6	4.7 ± 0.5	4.6 ± 0.4	5.1 ± 0.4	18.2 ± 2.4	4.8 ± 0.6
WZ + c - 1j	260 ± 22	81 ± 6	43.1 ± 3.6	25.8 ± 2.6	9.4 ± 1.8	2.9 ± 0.6
WZ + l - 1j	3090 ± 250	91 ± 13	17 ± 3	4.9 ± 1.6	1.3 ± 0.4	0.2 ± 0.1
WZ + b - 2j	1.10 ± 0.37	0.44 ± 0.11	0.39 ± 0.06	0.62 ± 0.14	2.1 ± 0.5	0.59 ± 0.14
WZ + c - 2j	21 ± 5	5.6 ± 1.2	3.0 ± 0.7	2.0 ± 0.5	0.70 ± 0.20	0.30 ± 0.08
WZ + l - 2j	250 ± 60	5.7 ± 1.6	0.73 ± 0.53	0.31 ± 0.15	0.07 ± 0.06	0.01 ± 0.01
WZ - Other	13 ± 5	1.4 ± 0.4	0.42 ± 0.08	0.2 ± 0.01	0.30 ± 0.05	0.67 ± 0.15
Other VV	6.2 ± 0.6	0.2 ± 0.4	0.2 ± 0.04	0.07 ± 0.1	0.1 ± 0.1	0.1 ± 0.2
ZZ	336 ± 26	17.8 ± 2.1	4.3 ± 0.6	1.7 ± 0.5	0.36 ± 0.08	0.10 ± 0.03
t̄tW	1.1 ± 0.2	0.2 ± 0.1	0.3 ± 0.1	0.4 ± 0.1	1.5 ± 0.3	0.7 ± 0.2
t̄tZ	6.8 ± 1.2	1.4 ± 0.3	1.0 ± 0.2	1.2 ± 0.2	4.4 ± 0.8	3.2 ± 0.6
Z + jets	169 ± 38	8.9 ± 1.9	3.7 ± 0.8	3.3 ± 0.7	3.2 ± 0.7	0.8 ± 0.17
V + γ	45 ± 28	1.9 ± 2.4	0.1 ± 0.1	0.02 ± 0.01	1.0 ± 0.9	0.02 ± 0.03
tZ	24.3 ± 4.3	5.5 ± 1.1	4.1 ± 0.8	5.9 ± 1.1	10.7 ± 2.0	23 ± 4
tW	1.4 ± 0.8	0.2 ± 0.5	0.0 ± 0.2	0.7 ± 0.6	0.26 ± 0.42	0.39 ± 0.41
WtZ	2.3 ± 1.2	0.6 ± 0.3	0.3 ± 0.21	0.27 ± 0.2	1.1 ± 0.7	0.6 ± 0.5
VVV	12.4 ± 0.5	0.93 ± 0.06	0.35 ± 0.03	0.13 ± 0.02	0.14 ± 0.03	0.02 ± 0.01
VH	40 ± 6	2.6 ± 1.4	0.9 ± 0.8	0.7 ± 0.8	0.5 ± 0.6	0.0 ± 0.0
t̄t	12.1 ± 1.6	2.9 ± 0.6	2.5 ± 0.5	2.8 ± 0.5	11.2 ± 1.4	10.9 ± 1.5
t̄tH	0.24 ± 0.03	0.05 ± 0.01	0.04 ± 0.01	0.06 ± 0.01	0.20 ± 0.03	0.13 ± 0.02
Total	5010 ± 260	227 ± 24	88 ± 12	57 ± 8	76 ± 16	53 ± 8

Table 22: Pre-fit yields in each of the 1-jet fit regions.

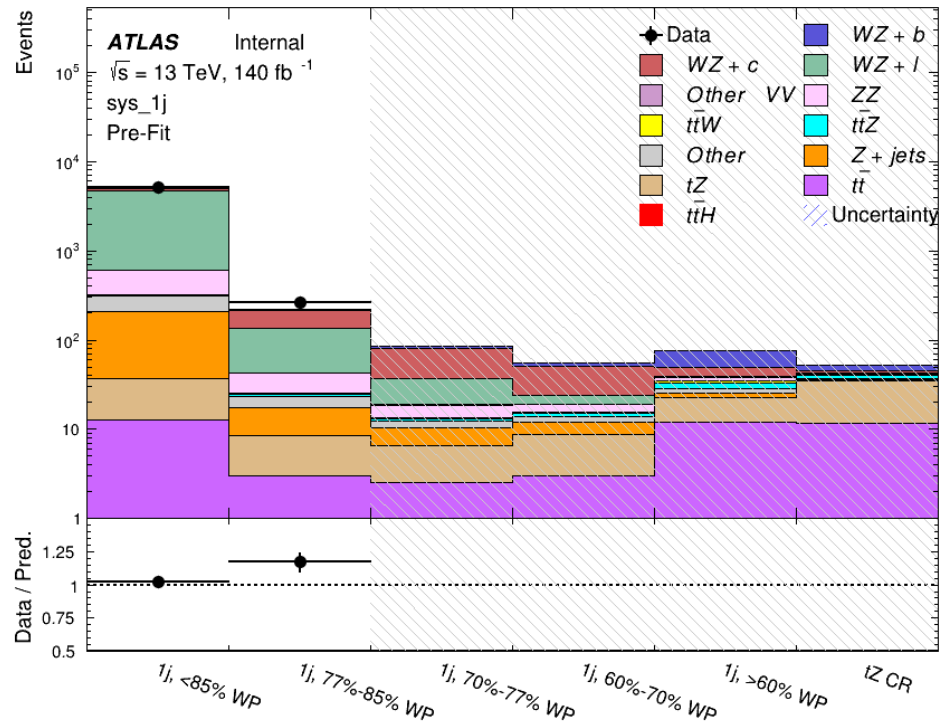


Figure 15.1: Pre-fit summary of the 1-jet fit regions.

1132

The post-fit yields in each region are summarized in Figure 15.1.

1133

	1j, <85% WP	1j, 77%-85% WP	1j, 70%-77% WP	1j, 60%-70% WP	1j, >60% WP	tZ CR
WZ + b	8.1 ± 4.9	4.7 ± 2.0	4.6 ± 2.0	5.1 ± 2.1	18 ± 10	5.0 ± 2.5
WZ + c	260 ± 60	80 ± 14	43 ± 7	26 ± 5	9.4 ± 2.3	2.9 ± 0.7
WZ + l	3090 ± 130	90 ± 11	17.3 ± 2.8	4.9 ± 1.6	1.3 ± 0.4	0.23 ± 0.1
WZ + b - 2j	1.10 ± 0.37	0.44 ± 0.11	0.39 ± 0.06	0.62 ± 0.14	2.1 ± 0.5	0.59 ± 0.1
WZ + c - 2j	21 ± 5	5.6 ± 1.2	3.0 ± 0.7	2.0 ± 0.5	0.70 ± 0.20	0.30 ± 0.0
WZ + l - 2j	250 ± 60	5.7 ± 1.6	0.73 ± 0.53	0.31 ± 0.15	0.07 ± 0.06	0.01 ± 0.0
WZ - Other	13 ± 5	1.4 ± 0.4	0.42 ± 0.08	0.2 ± 0.01	0.30 ± 0.05	0.67 ± 0.1
Other VV	6.2 ± 0.6	0.92 ± 0.07	0.02 ± 0.01	0.01 ± 0.01	0.01 ± 0.01	0.01 ± 0.0
ZZ	346 ± 57	19 ± 5	4.3 ± 0.8	2.7 ± 0.5	2.4 ± 0.1	2.1 ± 0.6
t̄tW	1.09 ± 0.21	0.2 ± 0.1	0.1 ± 0.1	0.4 ± 0.1	1.5 ± 0.3	0.1 ± 0.2
t̄tZ	6.8 ± 1.2	1.4 ± 0.3	1.0 ± 0.2	1.2 ± 0.2	4.4 ± 0.7	3.2 ± 0.5
rare Top	0.14 ± 0.04	0.04 ± 0.02	0.04 ± 0.0	0.1 ± 0.03	0.14 ± 0.04	0.15 ± 0.0
t̄tWW	0.04 ± 0.03	0.01 ± 0.02	0.01 ± 0.01	0.01 ± 0.01	0.01 ± 0.02	0.01 ± 0.0
Z + jets	169 ± 37	8.9 ± 1.9	3.7 ± 0.8	3.3 ± 0.7	3.2 ± 0.7	0.8 ± 0.2
W + jets	0.01 ± 0.01	0.01 ± 0.0				
V + γ	46 ± 28	1.9 ± 2.4	0.1 ± 0.1	0.0 ± 0.2	1.0 ± 0.9	0.0 ± 0.0
tZ	24 ± 4	5.5 ± 1.0	4.1 ± 0.8	5.9 ± 1.1	10.7 ± 1.8	23.3 ± 3.7
tW	1.37 ± 0.82	0.18 ± 0.26	0.01 ± 0.12	0.67 ± 0.64	0.26 ± 0.42	0.39 ± 0.4
WtZ	2.3 ± 1.2	0.6 ± 0.3	0.3 ± 0.2	0.3 ± 0.2	1.1 ± 0.6	0.6 ± 0.3
VVV	12.4 ± 0.4	0.9 ± 0.1	0.4 ± 0.1	0.13 ± 0.02	0.14 ± 0.03	0.02 ± 0.0
VH	40 ± 6	2.6 ± 1.4	0.9 ± 0.8	0.7 ± 0.8	0.4 ± 0.6	0.01 ± 0.0
t̄t	12.1 ± 1.6	2.9 ± 0.6	2.5 ± 0.5	2.8 ± 0.5	11.2 ± 1.5	10.9 ± 1.4
t̄tH	0.24 ± 0.03	0.05 ± 0.01	0.04 ± 0.01	0.06 ± 0.01	0.20 ± 0.03	0.13 ± 0.0
Total	5100 ± 110	227 ± 12	87 ± 6	56.7 ± 4.4	76 ± 9	52.5 ± 4.2

Table 23: Post-fit yields in each of the 1-jet fit regions.

1134

A post-fit summary plot of the 1-jet fitted regions is shown in Figure 15.2:

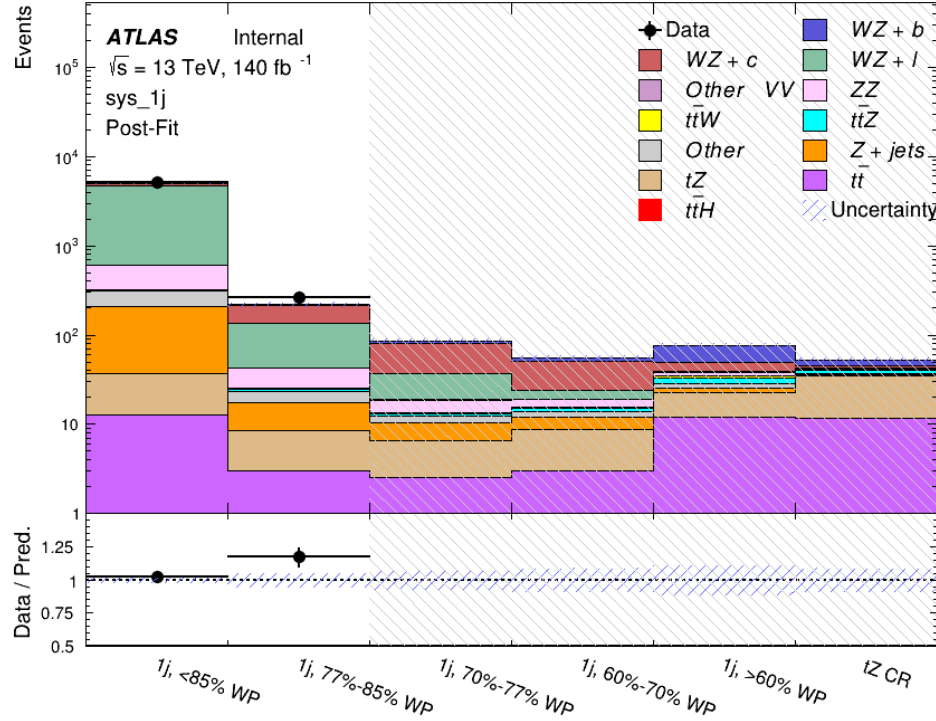


Figure 15.2: Post-fit summary of the 1-jet fit regions.

1135 As described in Section 21, there are 226 systematic uncertainties that are considered
 1136 as NPs in the fit. These NPs are constrained by Gaussian or log-normal probability density
 1137 functions. The latter are used for normalisation factors to ensure that they are always positive.
 1138 The expected number of signal and background events are functions of the likelihood. The prior
 1139 for each NP is added as a penalty term, decreasing the likelihood as it is shifted away from its
 1140 nominal value.

1141 The impact of each NP is calculated by performing the fit with the parameter of interest held
 1142 fixed, varied from its fitted value by its uncertainty, and calculating $\Delta\mu$ relative to the baseline

¹¹⁴³ fit. The impact of the most significant sources of systematic uncertainties is summarized in Table

¹¹⁴⁴ [24](#).

Uncertainty Source	$\Delta\mu$	
WZ + light cross-section	0.13	-0.12
WZ + charm cross-section	-0.10	0.12
Jet Energy Scale	0.08	0.13
tZ cross-section	-0.10	0.10
Jet Energy Resolution	-0.10	0.10
Luminosity	-0.08	0.09
Other Diboson + b cross-section	-0.07	0.07
Flavor tagging	0.05	0.05
t <bar>t</bar>	-0.05	0.05
WZ cross-section - QCD scale	-0.04	0.03
Total Systematic Uncertainty	0.28	0.32

Table 24: Summary of the most significant sources of systematic uncertainty on the measurement of WZ + b with exactly one associated jet.

¹¹⁴⁵ The ranking and impact of those nuisance parameters with the largest contribution to the

¹¹⁴⁶ overall uncertainty is shown in Figure [15.3](#).

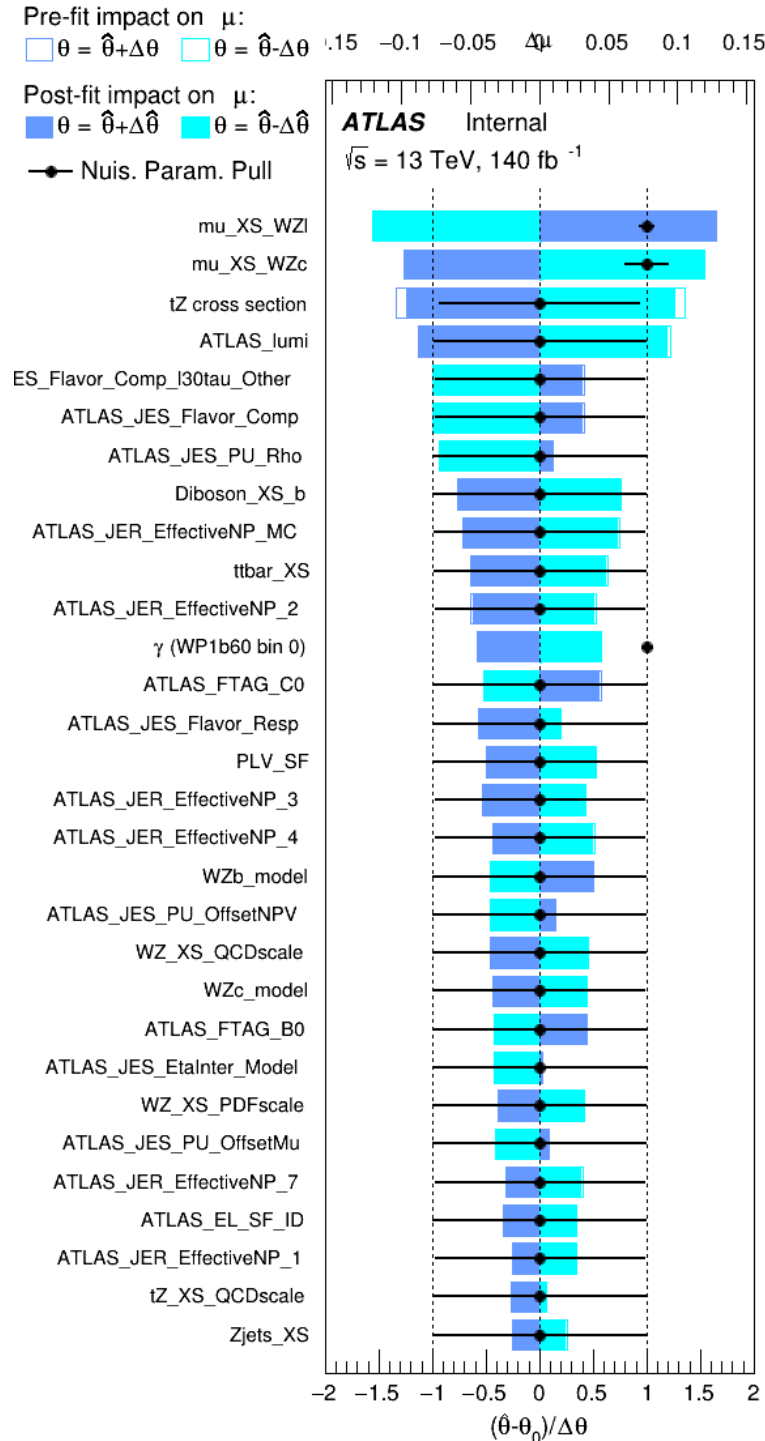


Figure 15.3: Impact of systematic uncertainties on the signal-strength of $WZ + b$ for events with exactly one jet

1147 The large impact of the Jet Energy Scale and Jet Flavor Tagging is unsurprising, as the
 1148 shape of the fit regions depends heavily on the modeling of the jets. The other major sources
 1149 of uncertainty come from background modelling and cross-section uncertainty. The pie charts
 1150 in Figure 15.4 show that for the modelling uncertainties that contribute most correspond to the
 1151 most significant backgrounds.

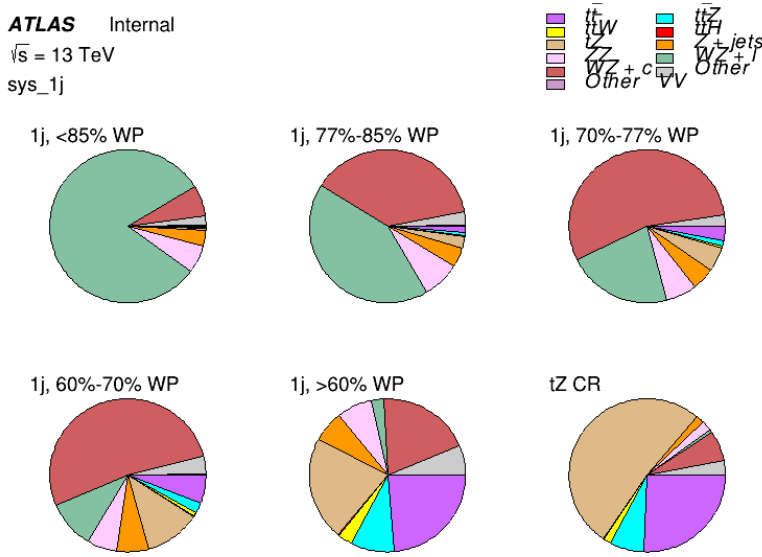


Figure 15.4: Post-fit background composition of the fit regions.

1152 The correlations between these nuisance parameters are summarized in Figure 15.5.

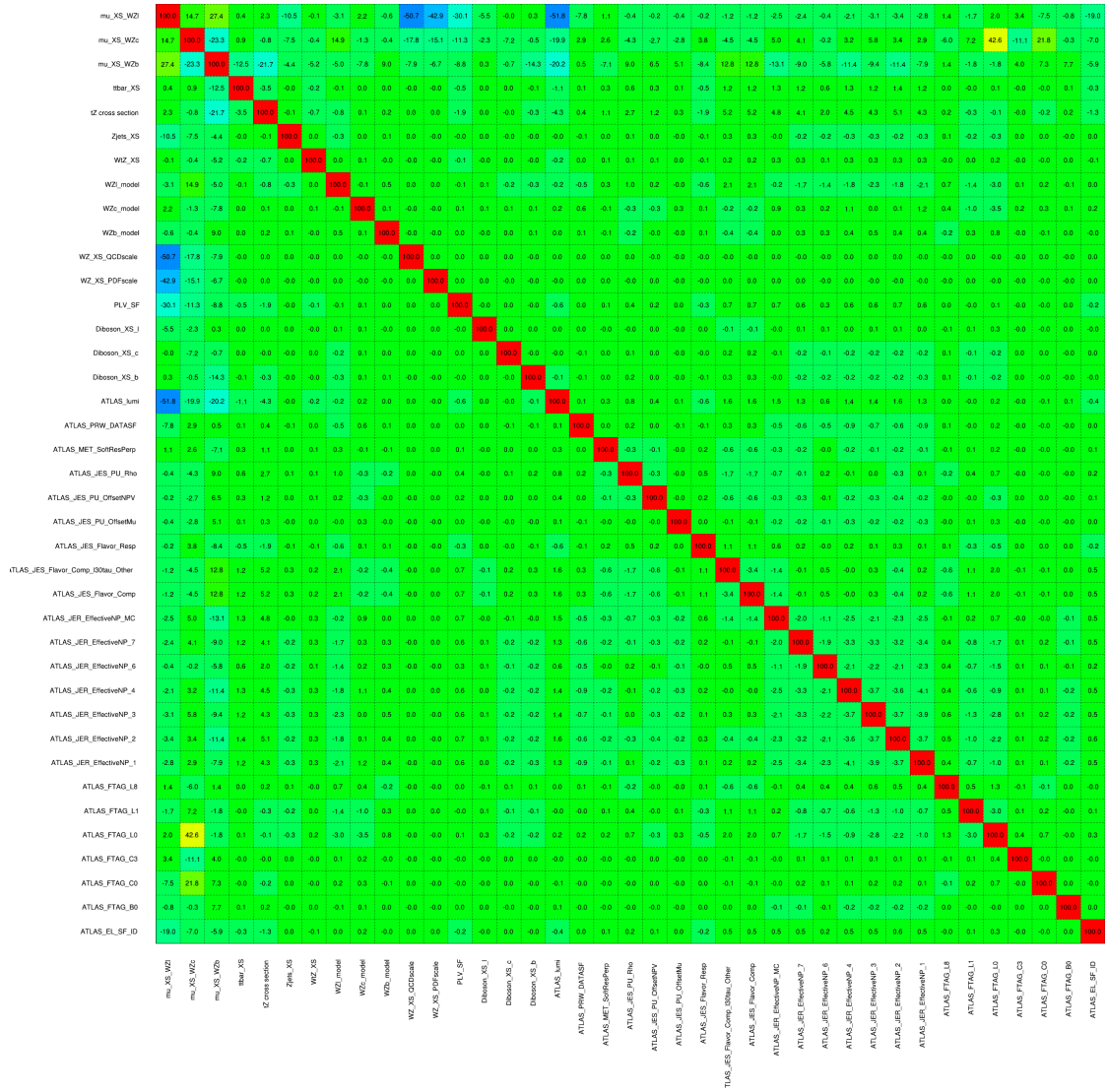


Figure 15.5: Correlations between nuisance parameters

1153 The negative correlations between $\mu_{WZ+charm}$ and μ_{WZ+b} and $\mu_{WZ+light}$ are expected:
1154 WZ + charm is present in both the WZ + b and WZ + light enriched regions, therefore increasing
1155 the fraction of charm requires increasing the fraction of WZ + b and WZ + light. This reasoning
1156 also explains the positive correlation between μ_{WZ+b} and $\mu_{WZ+light}$.

1157 Two of the major backgrounds in the region with the highest purity of $WZ + b$ are tZ and
1158 Other $VV + b$, explaining the negative correlations between μ_{WZ+b} and the tZ cross section, and
1159 the $VV + b$ cross section.

1160 The high correlation between the luminosity and $\mu_{WZ+light}$ arises from the fact that the
1161 uncertainty on $\mu_{WZ+light}$ is very low (around 4%). Small changes in luminosity cause a change
1162 in the yield of $WZ + light$ that is large compared to its uncertainty, producing a large correlation
1163 between these two parameters.

1164 **15.2 2-jet Fit Results**

1165 **The results of the fit are currently blinded.**

1166 Pre-fit yields in each of the 2-jet fit regions are shown in Figure 15.2.

	2j, <85% WP	2j, 77%-85% WP	2j, 70%-77% WP	2j, 60%-70% WP	2j, >60% WP	tZ CR 2j
WZ + b - 2j	3.1 ± 1.6	6.7 ± 0.5	5.6 ± 0.4	8.0 ± 0.6	31 ± 2	14 ± 1
WZ + c - 2j	180 ± 20	54 ± 6	41 ± 3	24 ± 3	11 ± 2	4.8 ± 0.6
WZ + l - 2j	1250 ± 150	90 ± 14	18 ± 3	5.8 ± 1.4	1.4 ± 0.4	0.25 ± 0.1
WZ + b - 1j	3.4 ± 0.6	1.52 ± 0.35	1.58 ± 0.23	1.95 ± 0.39	6.7 ± 1.1	1.9 ± 0.6
WZ + c - 1j	56 ± 14	17.6 ± 4.0	8.6 ± 2.2	6.3 ± 1.8	3.0 ± 0.9	0.7 ± 0.2
WZ + l - 1j	427 ± 120	24 ± 7	4.7 ± 2.3	1.6 ± 0.7	0.3 ± 0.2	0.01 ± 0.0
WZ - Other	129 ± 29	6.1 ± 4.6	1.2 ± 0.3	0.3 ± 0.2	2.9 ± 0.5	3.6 ± 0.6
Other VV	7.63 ± 0.63	0.6 ± 0.5	0.16 ± 0.03	0.01 ± 0.01	0.1 ± 0.1	0.1 ± 0.1
ZZ	135 ± 20	14.1 ± 3.2	4.7 ± 0.8	4.0 ± 0.6	4.1 ± 0.7	3.1 ± 0.5
t̄tW	0.8 ± 0.2	0.4 ± 0.1	0.5 ± 0.1	0.7 ± 0.2	4.3 ± 0.6	3.9 ± 0.6
t̄tZ	14.7 ± 2.2	5.6 ± 0.8	4.5 ± 0.7	6.5 ± 1.1	25.4 ± 4.0	21.9 ± 3.4
rare Top	0.14 ± 0.04	0.07 ± 0.03	0.03 ± 0.02	0.09 ± 0.03	0.37 ± 0.07	0.6 ± 0.1
t̄tWW	0.04 ± 0.03	0.02 ± 0.02	0.01 ± 0.01	0.01 ± 0.00	0.03 ± 0.03	0.01 ± 0.0
Z + jets	110.0 ± 22.9	9.6 ± 2.0	2.1 ± 0.50	1.6 ± 0.4	5.1 ± 1.1	1.5 ± 0.3
W + jets	0.0 ± 0.0	0.0 ± 0.0	0.0 ± 0.0	0.0 ± 0.0	0.0 ± 0.0	0.0 ± 0.0
V + γ	25 ± 18	0.5 ± 0.2	0.1 ± 0.1	0.1 ± 0.1	0.0 ± 0.02	0.05 ± 0.0
tZ	15.9 ± 2.9	6.9 ± 1.3	5.1 ± 1.0	8.0 ± 1.5	18.7 ± 3.2	36.4 ± 6.1
tW	0.9 ± 0.7	0.2 ± 0.3	0.0 ± 0.1	0.0 ± 0.0	0.8 ± 0.6	0.2 ± 0.2
WtZ	4.9 ± 2.5	1.5 ± 0.8	1.1 ± 0.6	1.3 ± 0.7	4.6 ± 2.4	3.3 ± 1.7
VVV	7.4 ± 0.3	1.0 ± 0.1	0.4 ± 0.1	0.2 ± 0.1	0.13 ± 0.03	0.04 ± 0.0
VH	19.5 ± 4.2	2.8 ± 1.6	0.7 ± 0.7	0.1 ± 0.2	0.0 ± 0.0	0.0 ± 0.0
t̄t	0.7 ± 0.4	0.1 ± 0.1	0.05 ± 0.06	0.15 ± 0.13	0.8 ± 0.5	2.3 ± 1.2
t̄t	6.8 ± 1.0	2.4 ± 0.5	1.8 ± 0.4	3.3 ± 0.6	8.4 ± 1.2	13.6 ± 1.1
t̄tH	0.4 ± 0.1	0.2 ± 0.1	0.16 ± 0.02	0.23 ± 0.03	0.94 ± 0.11	1.03 ± 0.1
Total	2580 ± 160	229 ± 24	89 ± 13	69 ± 11	120 ± 15	108 ± 11

Table 25: Pre-fit yields in each of the 2-jet fit regions.

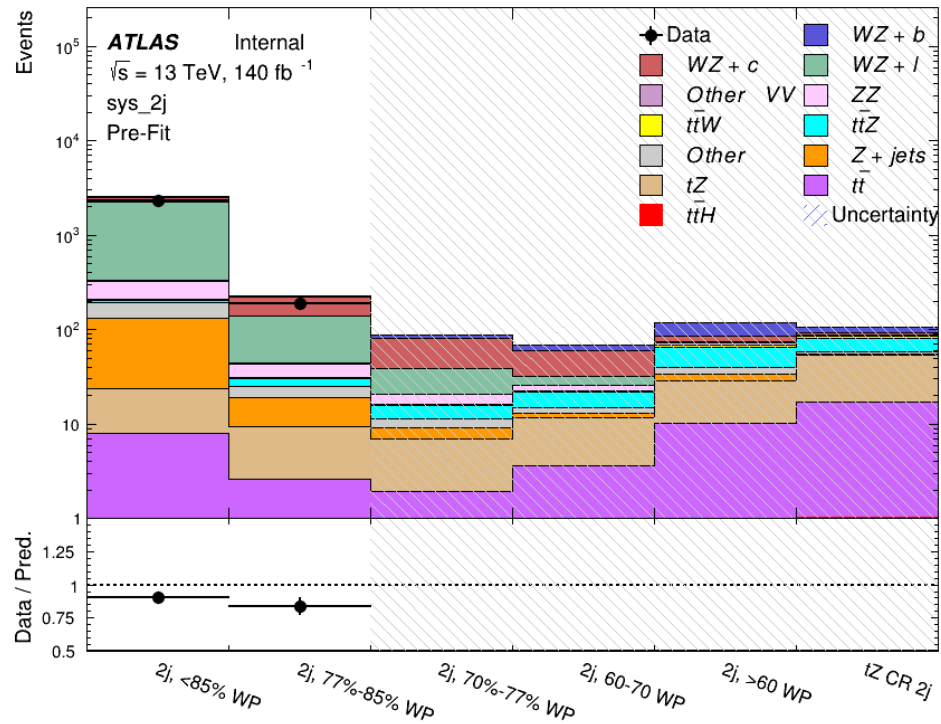


Figure 15.6: Pre-fit summary of the 2-jet fit regions.

1167

The post-fit yields in each region are summarized in Figure 15.2.

	2j, <85% WP	2j, 77%-85% WP	2j, 70%-77% WP	2j, 60%-70% WP	2j, >60% WP	tZ CR 2j
WZ + b	13 ± 6	6.7 ± 2.9	5.8 ± 2.5	8.0 ± 3.5	31 ± 13	14 ± 5
WZ + c	260 ± 60	77 ± 15	41 ± 8	26 ± 5	10.9 ± 2.4	4.8 ± 1.1
WZ + l	1860 ± 90	90 ± 12	17.6 ± 2.8	5.8 ± 1.3	1.4 ± 0.4	0.3 ± 0.2
WZ + b - 1j	3.4 ± 0.6	1.52 ± 0.35	1.58 ± 0.23	1.95 ± 0.39	6.7 ± 1.1	1.9 ± 0.6
WZ + c - 1j	56 ± 14	17.6 ± 4.0	8.6 ± 2.2	6.3 ± 1.8	3.0 ± 0.9	0.7 ± 0.2
WZ + l - 1j	427 ± 120	24 ± 7	4.7 ± 2.3	1.6 ± 0.7	0.3 ± 0.2	0.01 ± 0.0
WZ - Other	129 ± 29	6.1 ± 4.6	1.2 ± 0.3	0.3 ± 0.2	2.9 ± 0.5	3.6 ± 0.6
Other VV	7.6 ± 0.6	0.3 ± 0.3	0.3 ± 0.1	0.1 ± 0.06	0.03 ± 0.02	0.1 ± 0.1
ZZ	145 ± 30	11.3 ± 4.4	2.7 ± 1.6	1.0 ± 0.3	4.0 ± 0.1	2.4 ± 0.1
t̄tW	0.8 ± 0.2	0.4 ± 0.1	0.54 ± 0.12	0.74 ± 0.15	4.3 ± 0.6	3.9 ± 0.6
t̄tZ	14.7 ± 2.2	5.6 ± 0.8	4.5 ± 0.7	6.5 ± 1.0	25.4 ± 3.9	21.9 ± 3.0
rare Top	0.14 ± 0.04	0.07 ± 0.03	0.03 ± 0.02	0.09 ± 0.03	0.4 ± 0.1	0.6 ± 0.1
t̄tWW	0.04 ± 0.03	0.02 ± 0.02	0.01 ± 0.01	0.01 ± 0.01	0.03 ± 0.03	0.01 ± 0.0
Z + jets	110 ± 23	9.6 ± 2.0	2.1 ± 0.5	1.6 ± 0.4	5.1 ± 1.1	1.5 ± 0.3
W + jets	0.0 ± 0.0	0.0 ± 0.0				
V + γ	25 ± 19	0.5 ± 0.2	0.1 ± 0.1	0.13 ± 0.14	0.0 ± 0.02	0.05 ± 0.0
tZ	15.9 ± 2.7	6.9 ± 1.2	5.1 ± 0.9	8.0 ± 1.4	18.7 ± 3.0	36 ± 6
tW	0.1 ± 0.7	0.2 ± 0.3	0.0 ± 0.1	0.0 ± 0.0	0.8 ± 0.6	0.2 ± 0.2
WtZ	4.9 ± 2.5	1.5 ± 0.8	1.1 ± 0.6	1.3 ± 0.7	4.6 ± 2.3	3.3 ± 1.7
VVV	7.4 ± 0.3	1.0 ± 0.1	0.36 ± 0.03	0.19 ± 0.03	0.13 ± 0.03	0.04 ± 0.0
VH	19 ± 4	2.8 ± 1.6	0.7 ± 0.7	0.1 ± 0.2	0.0 ± 0.0	0.0 ± 0.0
t̄t	6.8 ± 1.0	2.4 ± 0.5	1.8 ± 0.4	3.3 ± 0.6	8.4 ± 1.2	13.6 ± 1.7
t̄tH	0.40 ± 0.05	0.19 ± 0.03	0.16 ± 0.02	0.23 ± 0.03	0.94 ± 0.11	1.03 ± 0.1
Total	2580 ± 60	229 ± 11	89 ± 6	69.1 ± 4.1	120 ± 10	108 ± 6

Table 26: Post-fit yields in each of the 2-jet fit regions.

¹¹⁶⁸

A post-fit summary of the fitted regions is shown in Figure 15.7:

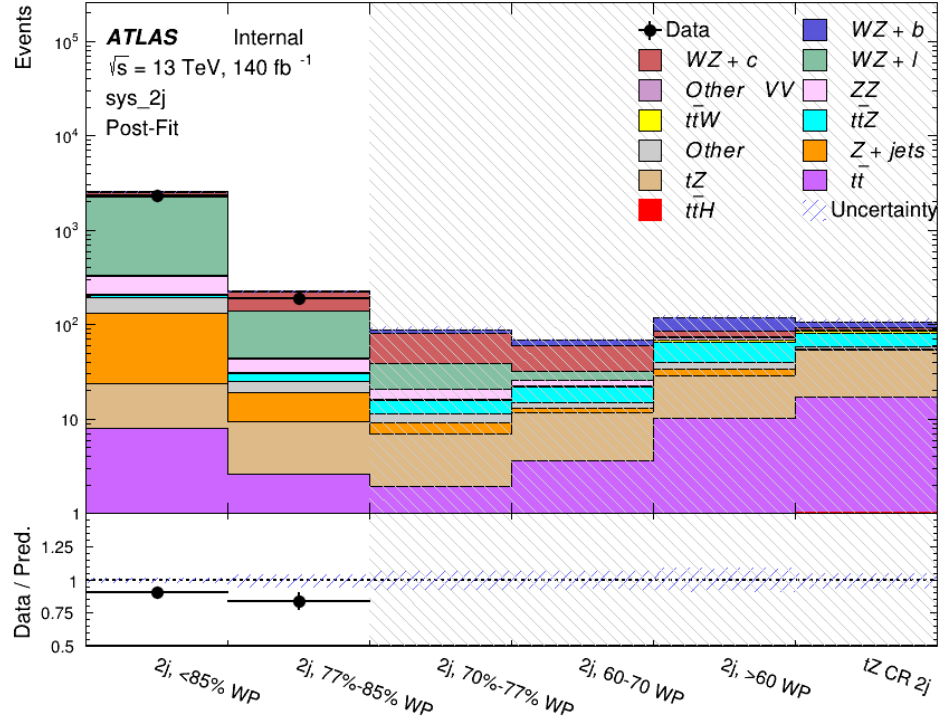


Figure 15.7: Post-fit summary of the fit over 2-jet regions.

1169 The same set of systematic uncertainties consider for the 1-jet fit are included in the 2-jet
 1170 fit as well. The impact of the most significant systematic uncertainties is summarized in Table
 1171 [27](#).

Uncertainty Source	$\Delta\mu$	
WZ + c cross-section	-0.1	0.14
Luminosity	-0.11	0.12
tZ cross-section	-0.11	0.11
Jet Energy Scale	-0.11	0.11
ttZ cross-section - QCD scale	-0.08	0.09
WZ + l cross-section	0.08	-0.07
WtZ cross-section	-0.07	0.07
Flavor tagging	0.05	0.05
Other VV + b cross-section	-0.05	0.05
Jet Energy Resolution	-0.04	0.04
Total	0.29	0.31

Table 27: Summary of the most significant sources of systematic uncertainty on the measurement of WZ + b 2-jet events.

¹¹⁷² The ranking and impact of those nuisance parameters with the largest contribution to the
¹¹⁷³ overall uncertainty is shown in Figure 15.8.

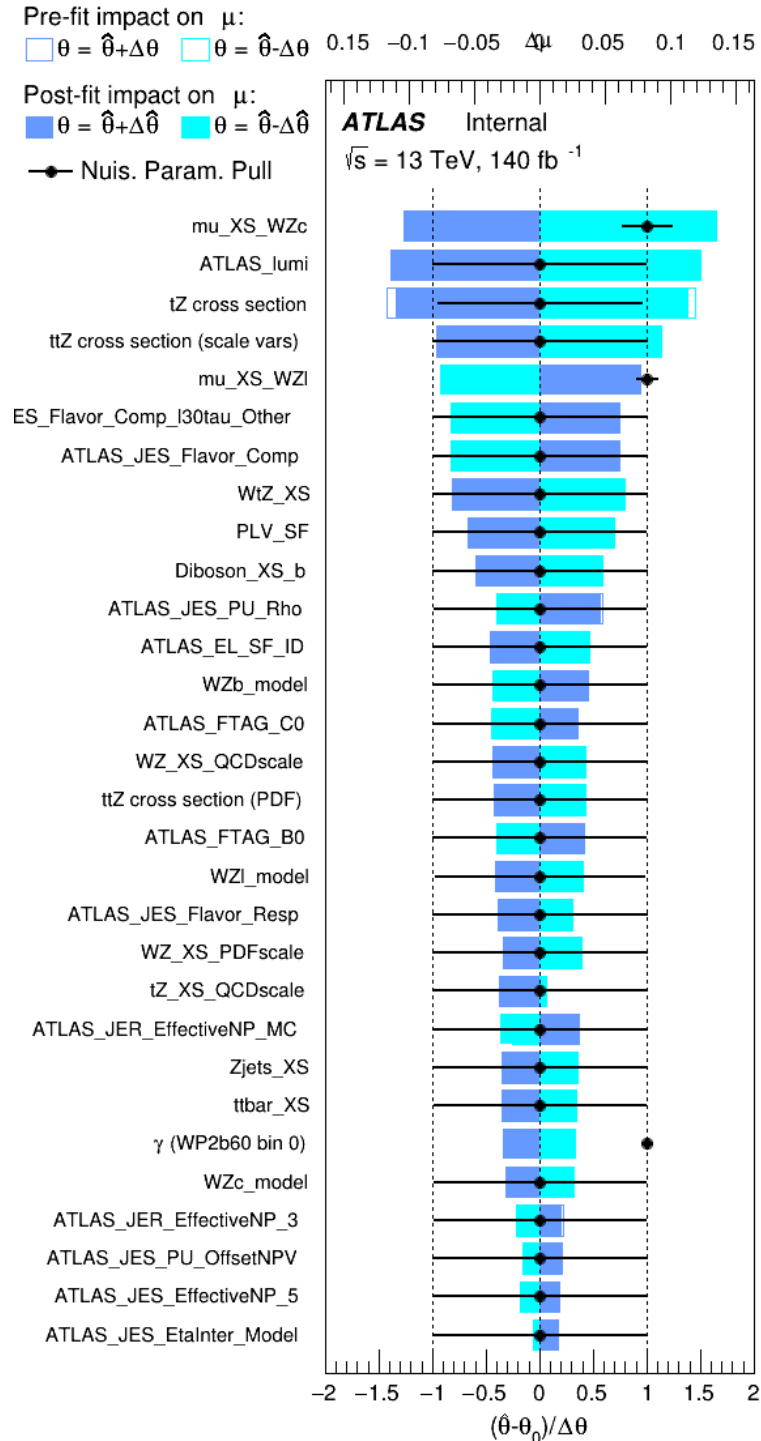


Figure 15.8: Impact of systematic uncertainties on the signal-strength of $WZ + b$ in 2-jet events.

1174 The large impact of the Jet Energy Scale and Jet Flavor Tagging is unsurprising, as the
 1175 shape of the fit regions depends heavily on the modeling of the jets. The other major sources
 1176 of uncertainty come from background modelling and cross-section uncertainty. The pie charts
 1177 in Figure 15.9 show that for the modelling uncertainties that contribute most correspond to the
 1178 most significant backgrounds.

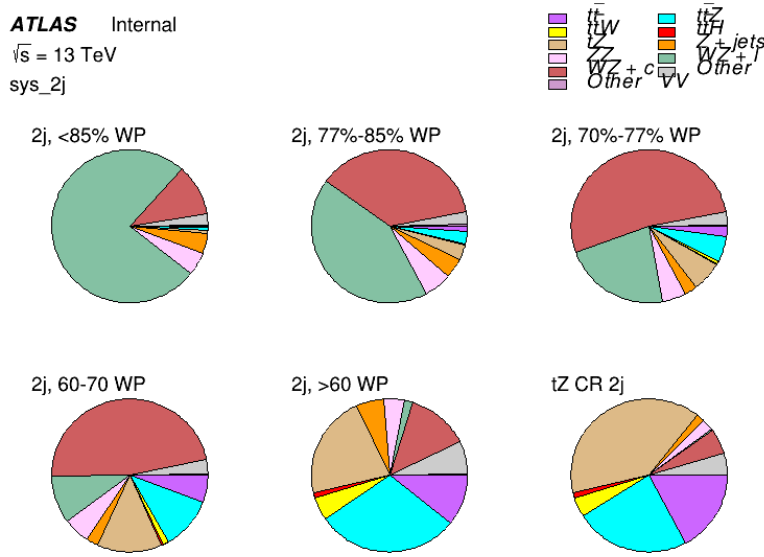


Figure 15.9: Post-fit background composition of the 2-jet fit regions.

1179 The correlations between these nuisance parameters are summarized in Figure 15.10.



Figure 15.10: Correlations between nuisance parameters in the 2-jet fit

As in the 1-jet case, no significant, unexpected correlations are found between nuisance parameters.

Part V**Differential Studies of $t\bar{t}H$ Multilepton****16 Data and Monte Carlo Samples**

1185 For both data and Monte Carlo (MC) simulations, samples were prepared in the xAOD format,
1186 which was used to produced a xAOD based on the HIGG8D1 derivation framework. This framework
1187 was designed for the main $t\bar{t}H$ multi-lepton analysis. Because this analysis targets events with
1188 multiple light leptons, as well as tau hadrons, this framework skims the dataset of any events that
1189 do not meet at least one of the following requirements:

- 1190 • at least two light leptons within a range $|\eta| < 2.6$, with leading lepton $p_T > 15$ GeV and
1191 subleading lepton $p_T > 5$ GeV
- 1192 • at least one light lepton with $p_T > 15$ GeV within a range $|\eta| < 2.6$, and at least two hadronic
1193 taus with $p_T > 15$ GeV.

1194 Samples were then generated from these HIGG8D1 derivations using a modified version of
1195 AnalysisBase version 21.2.127.

1196 16.1 Data Samples

1197 The study uses proton-proton collision data collected by the ATLAS detector from 2015 through
 1198 2018, which represents an integrated luminosity of 139 fb^{-1} and an energy of $\sqrt{s} = 13 \text{ TeV}$. All
 1199 data used in this analysis was included in one the following Good Run Lists:

- 1200 • data15_13TeV.periodAllYear_DetStatus-v79-repro20-02_DQDefects-00-02-02
 _PHYS_StandardGRL_All_Good_25ns.xml
- 1202 • data16_13TeV.periodAllYear_DetStatus-v88-pro20-21_DQDefects-00-02-04
 _PHYS_StandardGRL_All_Good_25ns.xml
- 1204 • data17_13TeV.periodAllYear_DetStatus-v97-pro21-13_Unknown_PHYS_StandardGRL
 _All_Good_25ns_Triggerno17e33prim.xml
- 1206 • data18_13TeV.periodAllYear_DetStatus-v102-pro22-04_Unknown_PHYS_StandardGRL
 _All_Good_25ns_Triggerno17e33prim.xml

1208 16.2 Monte Carlo Samples

1209 Several Monte Carlo (MC) generators were used to simulate both signal and background pro-
 1210 cesses. For all of these, the effects of the ATLAS detector are simulated in Geant4. The specific
 1211 event generator used for each of these MC samples is listed in table 28.

Table 28: The configurations used for event generation of signal and background processes, including the event generator, matrix element (ME) order, parton shower algorithm, and parton distribution function (PDF).

Process	Event generator	ME order	Parton Shower	PDF
t̄H	MG5_AMC (MG5_AMC)	NLO (NLO)	PYTHIA 8 (HERWIG++)	NNPDF 3.0 NLO [Ball:2014uwa] (CT10 [ct10])
t̄W	MG5_AMC (SHERPA 2.1.1)	NLO (LO multileg)	PYTHIA 8 (SHERPA)	NNPDF 3.0 NLO (NNPDF 3.0 NLO)
t̄(Z/γ* → ll)	MG5_AMC	NLO	PYTHIA 8	NNPDF 3.0 NLO
VV	SHERPA 2.2.2	MEPS NLO	SHERPA	CT10
t̄t	POWHEG-BOX v2 [powheggtt]	NLO	PYTHIA 8	NNPDF 3.0 NLO
t̄γ	MG5_AMC	LO	PYTHIA 8	NNPDF 2.3 LO
tZ	MG5_AMC	LO	PYTHIA 6	CTEQ6L1
tHqb	MG5_AMC	LO	PYTHIA 8	CT10
tHW	MG5_AMC (SHERPA 2.1.1)	NLO (LO multileg)	HERWIG++ (SHERPA)	CT10 (NNPDF 3.0 NLO)
tWZ	MG5_AMC	NLO	PYTHIA 8	NNPDF 2.3 LO
t̄t, t̄t̄t̄	MG5_AMC	LO	PYTHIA 8	NNPDF 2.3 LO
t̄tW+W-	MG5_AMC	LO	PYTHIA 8	NNPDF 2.3 LO
s-, t-channel, Wt single top	Powheg-Box v1 [powhegstp]	NLO	PYTHIA 6	CT10
qqVV, VVV Z → l+l-	SHERPA 2.2.1	MEPS NLO	SHERPA	NNPDF 3.0 NLO

17 Object Reconstruction

¹²¹² All analysis channels considered in this note share a common object selection for leptons and jets, as well as a shared trigger selection.

17.1 Trigger Requirements

¹²¹⁶ Events are required to be selected by dilepton triggers, as summarized in table 29.

Dilepton triggers (2015)	
$\mu\mu$ (asymm.)	HLT_mu18_mu8noL1
ee (symm.)	HLT_2e12_lhloose_L12EM10VH
$e\mu, \mu e$ (\sim symm.)	HLT_e17_lhloose_mu14
Dilepton triggers (2016)	
$\mu\mu$ (asymm.)	HLT_mu22_mu8noL1
ee (symm.)	HLT_2e17_lhvloose_nod0
$e\mu, \mu e$ (\sim symm.)	HLT_e17_lhloose_nod0_mu14
Dilepton triggers (2017)	
$\mu\mu$ (asymm.)	HLT_mu22_mu8noL1
ee (symm.)	HLT_2e24_lhvloose_nod0
$e\mu, \mu e$ (\sim symm.)	HLT_e17_lhloose_nod0_mu14
Dilepton triggers (2018)	
$\mu\mu$ (asymm.)	HLT_mu22_mu8noL1
ee (symm.)	HLT_2e24_lhvloose_nod0
$e\mu, \mu e$ (\sim symm.)	HLT_e17_lhloose_nod0_mu14

Table 29: List of lowest p_T -threshold, un-prescaled dilepton triggers used for 2015-2018 data taking.

17.2 Light Leptons

1217 Electron candidates are reconstructed from energy clusters in the electromagnetic calorimeter that
 1218 are associated with charged particle tracks reconstructed in the inner detector [**ATLAS-CONF-2016-024**].
 1219
 1220 Electron candidates are required to have $p_T > 10$ GeV and $|\eta_{\text{cluster}}| < 2.47$. Candidates in the
 1221 transition region between different electromagnetic calorimeter components, $1.37 < |\eta_{\text{cluster}}| <$
 1222 1.52, are rejected. A multivariate likelihood discriminant combining shower shape and track
 1223 information is used to distinguish prompt electrons from nonprompt leptons, such as those
 1224 originating from hadronic showers.

1225 To further reduce the non-prompt contribution, the track of each electron is required to

1226 originate from the primary vertex; requirements are imposed on the transverse impact parameter
1227 significance ($|d_0|/\sigma_{d_0}$) and the longitudinal impact parameter ($|\Delta z_0 \sin \theta_\ell|$).

1228 Muon candidates are reconstructed by combining inner detector tracks with track segments
1229 or full tracks in the muon spectrometer [**PERF-2014-05**]. Muon candidates are required to have
1230 $p_T > 10$ GeV and $|\eta| < 2.5$. All leptons are required to be isolated, and pass a non-prompt BDT
1231 selection described in detail in [**ttH_paper**].

1232 **17.3 Jets**

1233 Jets are reconstructed from calibrated topological clusters built from energy deposits in the
1234 calorimeters [**ATL-PHYS-PUB-2015-015**], using the anti- k_t algorithm with a radius parameter
1235 $R = 0.4$. Jets with energy contributions likely arising from noise or detector effects are removed
1236 from consideration [**ATLAS-CONF-2015-029**], and only jets satisfying $p_T > 25$ GeV and
1237 $|\eta| < 2.5$ are used in this analysis. For jets with $p_T < 60$ GeV and $|\eta| < 2.4$, a jet-track
1238 association algorithm is used to confirm that the jet originates from the selected primary vertex,
1239 in order to reject jets arising from pileup collisions [**PERF-2014-03**].

1240 **17.4 Missing Transverse Energy**

1241 Because all $t\bar{t}H - ML$ channels considered include multiple neutrinos, missing transverse
1242 energy (E_T^{miss}) is present in each event. The missing transverse momentum vector is defined as
1243 the inverse of the sum of the transverse momenta of all reconstructed physics objects as well

1244 as remaining unclustered energy, the latter of which is estimated from low- p_T tracks associated
1245 with the primary vertex but not assigned to a hard object [**ATL-PHYS-PUB-2015-027**].

1246 **18 Higgs Momentum Reconstruction**

1247 Reconstructing the momentum of the Higgs boson is a particular challenge for channels with
1248 leptons in the final state: Because all channels include at least two neutrinos in the final state, the
1249 Higgs can never be fully reconstructed. However, the momentum spectrum can be well predicted
1250 by a neural network when provided with the four-vectors of the Higgs Boson decay products, as
1251 shown in section 18.1. With this in mind, several layers of MVAs are used to reconstruction the
1252 Higgs momentum.

1253 The first layer is a model designed to select which jets are most likely to be the b-jets that
1254 came from the top decay, detailed in section 18.2. As described in section 18.3, the kinematics
1255 of these jets are fed into the second layer, which is designed to identify the decay products of
1256 the Higgs Boson itself. The kinematics of these particles are then fed into yet another neural-
1257 network, which predicts the momentum of the Higgs (18.4). MVAs are also used in the analysis
1258 to determine the decay of the Higgs boson in the 3l channel (18.5).

1259 Models are trained on Monte Carlo simulations of $t\bar{t}H$ events generated using MG5_AMC.
1260 Specifically, events DSIDs 346343-5, 345873-5, and 345672-4 are used for training.

1261 For all of these models, the Keras neural network framework, with Tensorflow as the
1262 backend, is used, and the number of hidden layers and nodes are determined using grid search
1263 optimization. Each neural network uses the LeakyReLU activation function, a learning rate
1264 of 0.01, and the Adam optimization algorithm, as alternatives are found to either decrease or
1265 have no impact on performance. Batch normalization is applied after each layer. For the
1266 classification algorithms (b-jet matching, Higgs reconstruction, and 3l decay identification)
1267 binary-cross entropy is used as the loss function, while the p_T reconstruction algorithm uses
1268 MSE.

1269 The specific inputs features used for each model are arrived at through a process of trial
1270 and error - features considered potentially useful are tried, and those that are found to increase
1271 performance are included. While each model includes a relatively large number of features,
1272 some using upwards of 30, this inclusive approach is found to maximize the performance of each
1273 model while decreasing the variance compared to a reduced number of inputs. Each input feature
1274 is validated by comparing MC simulations to 80 fb^{-1} of data, as shown in the sections below.

1275 **18.1 Decay Candidate Reconstruction**

1276 Machine Learning algorithms are trained to identify the decay products of the Higgs Boson
1277 using MC simulations of $t\bar{t}H$ events. These include light leptons and jets. Reconstructed
1278 physics objects are matched to truth level particles, in order to identify the parents of these

1279 reconstructed objects. The kinematics of the decay product candidates as well as event level
1280 variables are used as inputs.

1281 Leptons considered as possible Higgs and top decay candidates are required to pass the
1282 selection described in section 17.2. For jets, however, it is found that a large fraction that originate
1283 from either the top decay or the Higgs decay fall outside the selection described in section 17.3.
1284 Specifically, jets from the Higgs decay tend to be soft, with 32% having $p_T < 25$ GeV. Therefore
1285 jets with $p_T < 15$ GeV are considered as possible candidates in the models described below. By
1286 contrast, less than 5% of the jets originating from the Higgs fall below this p_T . The jets are found
1287 to be well modeled even down to this low p_T threshold, as shown in section 20.1. The impact of
1288 using different p_T selection for the jet candidates is considered in detail in section A.5. As they
1289 are expected to originate from the primary vertex, jets are also required to pass a JVT cut.

1290 18.2 b-jet Identification

1291 Including the kinematics of the b-jets that originate from the top decay is found to improve the
1292 identification of the Higgs decay products, and improve the accuracy with which the Higgs
1293 momentum can be reconstructed. Because these b-jets are reconstructed by the detector with
1294 high efficiency (just over 90% of the time), and can be identified relatively consistently, the first
1295 step in reconstructing the Higgs is selecting the b-jets from the top decay.

1296 Exactly two b-jets are expected in the final state of $t\bar{t}H - \text{ML}$ events. However, in both
1297 the 3l and 2lSS channels, only one or more b-tagged jets are required (where the 70% DL1r b-tag

1298 working point is used). Therefore, for events which have exactly one, or more than two, b-tagged
 1299 jets, deciding which combination of jets correspond to the top decay is non-trivial. Further,
 1300 events with 1 b-tagged jet represent just over half of all $t\bar{t}H - ML$ events. Of those, both b-jets
 1301 are reconstructed by the detector 75% of the time. Therefore, rather than adjusting the selection
 1302 to require exactly 2 b-tagged jets, and losing more than half of the signal events, a neural network
 1303 is used to predict which pair of jets is most likely to correspond to truth b-jets.

1304 Once the network is trained, all possible pairings of jets are fed into the model, and the pair
 1305 of jets with the highest output score are taken to be b-jets in successive steps of the analysis.

1306 **18.2.1 2lSS Channel**

1307 For the 2lSS channel, the input features shown in table 30 are used for training. Here j_0 and j_1
 1308 are the two jet candidates, while l_0 and l_1 are the two leptons in the event, both ordered by p_T . jet
 1309 DL1r is an integer corresponding to the calibrated b-tagging working points reached by each jet,
 1310 where 5 represents the tightest working point and 1 represents the loosest. The variables nJets
 1311 DL1r 60% and nJets DL1r 85% represent the number of jets in the event passing the 60% and
 1312 85% b-tag working points, respectively.

1313 As there are far more incorrect combinations than correct ones, by a factor of more than
 1314 20:1, the training set is resampled to reduce the fraction of incorrect combinations. A random
 1315 sample of 5 million incorrect entries are used for training, along with close 1 million correct

jet p_T 0	jet p_T 1	Lepton p_T 0
Lepton p_T 1	jet η 0	jet η 1
$\Delta R(j_0)(j_1)$	$M(j_0 j_1)$	$\Delta R(l_0)(j_0)$
$\Delta R(l_0)(j_1)$	$\Delta R(l_1)(j_0)$	$\Delta R(l_1)(j_1)$
$M(l_0 j_0)$	$M(l_0 j_1)$	$M(l_1 j_0)$
$M(l_1 j_1)$	jet DL1r 0	jet DL1r 1
nJets OR DL1r 85	nJets OR DL1r 60	$\Delta R(j_0 l_0)(j_1 l_1)$
$\Delta R(j_0 l_1)(j_1 l_0)$	$p_T(j_0 j_1 l_0 l_1 E_T^{\text{miss}})$	$M(j_0 j_1 l_0 l_1 E_T^{\text{miss}})$
$\Delta\phi(j_0)(E_T^{\text{miss}})$	$\Delta\phi(j_1)(E_T^{\text{miss}})$	HT jets
nJets	E_T^{miss}	

Table 30: Input features used in the b-jet identification algorithm for the 2lSS channel

1316 entries. 10% of the dataset is set aside for testing, leaving around 5 million datapoints for
 1317 training.

1318 The difference between the distributions for a few of these features for the correct(i.e.
 1319 both jets are truth b-jets), and incorrectcombinations are shown in figure 18.1. The correct and
 1320 incorrect contributions are scaled to the same integral, so as to better demonstrate the differences
 1321 in the distributions.

1322 The modeling of these inputs is validated against data, with figure 18.2 showing good
 1323 general agreement between data and MC. Plots for the complete list of features can found in
 1324 section A.

1325 Based on the results of grid search evaluation, the optimal architecture is found to include
 1326 5 hidden layers with 40 nodes each. No regularizer or dropout is added to the network, as
 1327 overfitting is found to not be an issue. The output score distribution as well as the ROC curve for

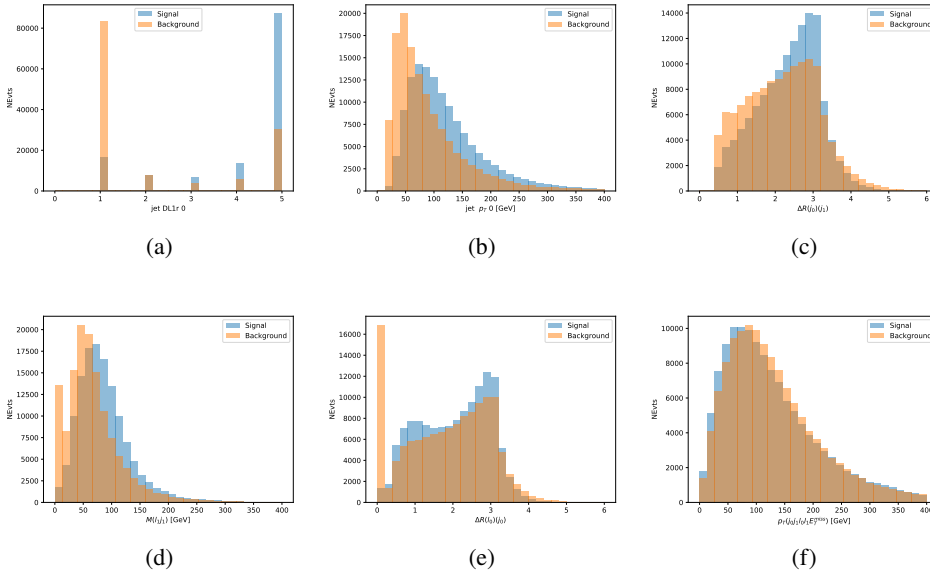


Figure 18.1: Input features for top2lSS training. The signal in blue represents events where both jet candidates are truth b-jets from top decays, and the orange is all other combinations. Each are scaled to the same number of events. (a) shows the DL1r working point of leading jet, (b) shows the p_T of the leading jet, (c) shows the ΔR of the two jets, (d) the invariant mass of lepton 1 and jet 1, (e) the ΔR of lepton 0 and jet 0, and (f) the p_T of both jets, both leptons, and the E_T^{miss} .

1328 the trained model are shown in figure 18.2.1. The model is found to identify the correct pairing
 1329 of jets for 73% of 2lSS signal events on test data.

1330 For point of comparison, a naïve approach to identify b-jets is used as well: The two jets
 1331 which pass the highest DL1r b-tag working point are assumed to be the b-jets from the top decay.
 1332 In the case that multiple jets meet the same b-tag working point, the jet with higher p_T is used.
 1333 This method identifies the correct jet pair 65% of the time.

1334 The accuracy of the model for different values of n-bjets, compared to this naive approach,
 1335 is shown in table 31.

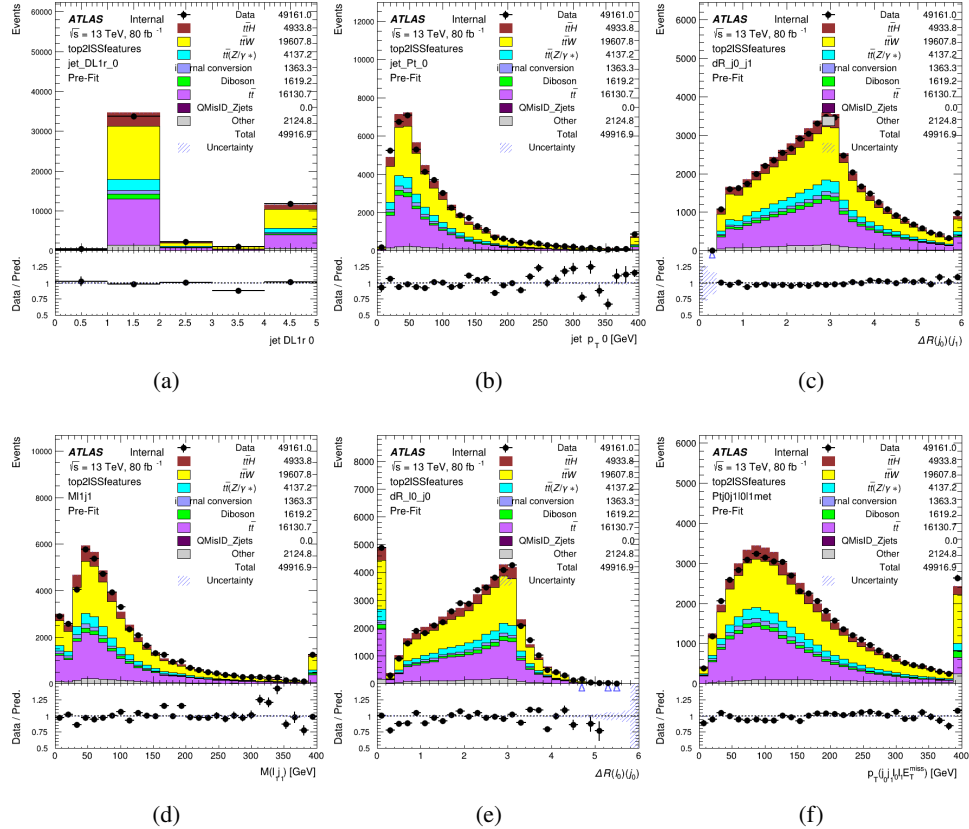


Figure 18.2: Data/MC comparisons of input features for top2ISS training for 80 fb^{-1} of data. (a) shows the DL1r working point of leading jet, (b) shows the p_T of the leading jet, (c) shows the ΔR of the two jets, (d) the invariant mass of lepton 1 and jet 1, (e) the ΔR of lepton 0 and jet 0, and (f) the p_T of both jets, both leptons, and the E_T^{miss} .

b-jet Selection	Neural Network	Naive
1 b-jet	58.6%	42.1%
2 b-jets	88.4%	87.1%
≥ 3 b-jets	61.7%	53.3%
Overall	73.9%	67.2%

Table 31: Accuracy of the NN in identifying b-jets from tops in 2ISS events for, compared to the accuracy of taking the two highest b-tagged jets.

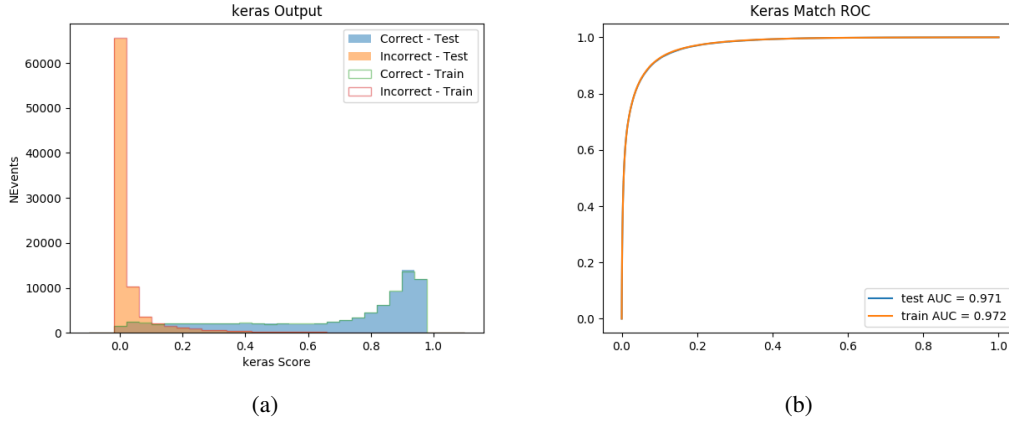


Figure 18.3: Results of the b-jet identification algorithm for the 2lSS channel, showing (a) the output score of the NN for correct and incorrect combinations of jets. (b) the ROC curve of the output, showing background rejection as a function of signal efficiency

1336 18.2.2 3l Channel

1337 The input features used in the 3l channel are listed in table 32, with the same naming convention
1338 as the 2lSS channel.

jet p_T 0	jet p_T 1	jet η 0
jet η 1	Lepton p_T 0	Lepton p_T 1
Lepton p_T 2	$\Delta R(j_0)(j_1)$	$M(j_0 j_1)$
$\Delta R(l_0)(j_0)$	$\Delta R(l_1)(j_0)$	$\Delta R(l_2)(j_0)$
$\Delta R(l_0)(j_1)$	$\Delta R(l_1)(j_1)$	$\Delta R(l_2)(j_1)$
$M(l_0 j_0)$	$M(l_1 j_0)$	$M(l_2 j_0)$
$M(l_0 j_1)$	$M(l_1 j_1)$	$M(l_2 j_1)$
$\Delta R(j_0 l_0)(j_1 l_1)$	$\Delta R(j_0 l_0)(j_1 l_2)$	$\Delta R(j_0 l_1)(j_1 l_0)$
$\Delta R(j_0 l_2)(j_1 l_0)$	jet DL1r 0	jet DL1r 1
$p_T(j_0 j_1 l_0 l_1 l_2 E_T^{\text{miss}})$	$M(t j_0 j_1 l_0 l_1 l_2 E_T^{\text{miss}})$	$\Delta\phi(j_0)(E_T^{\text{miss}})$
$\Delta\phi(j_1)(E_T^{\text{miss}})$	HT Lepton	HT jets
nJets	E_T^{miss}	nJets OR DL1r 85
nJets OR DL1r 60		

Table 32: Input features for the b-jet identification algorithm in the 3l channel.

1339 A few of these features are shown in figure 18.4, comparing the distributions for correct

1340 and incorrect combinations of jets.

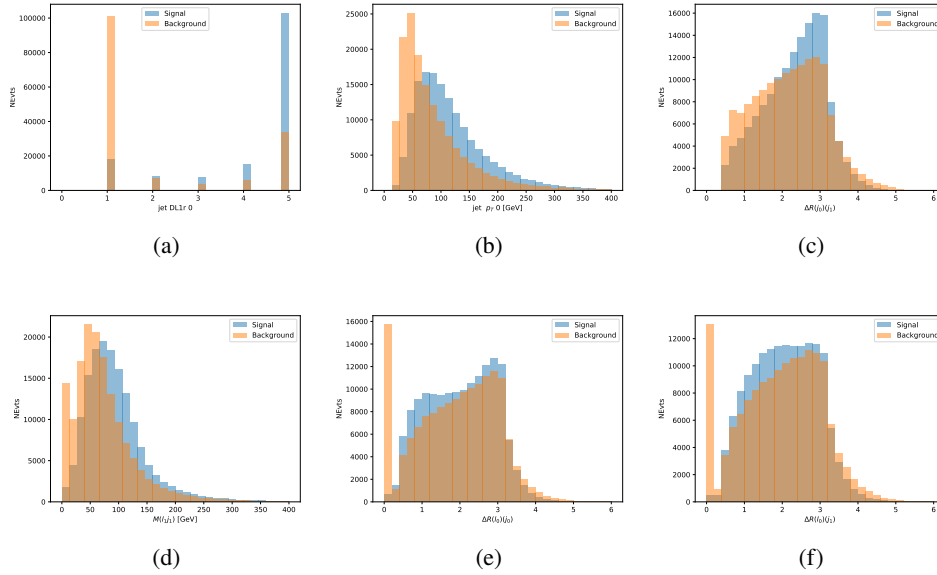


Figure 18.4: Input features for top3l training. The signal in blue represents events where both jet candidates are truth b-jets from top decays, and the orange is all other combinations. Scaled to the same number of events. (a) show the DL1r WP of jet 0, (b) the p_T of jet 0, (c) ΔR between jet 0 and jet 1, (d) the invariant mass of lepton 1 and jet 1, (e) ΔR between lepton 0 and jet 0, and (f) ΔR between lepton 0 and jet 1

1341 The modeling of these inputs is validated against data, with figure 18.5 showing good
1342 general agreement between data and MC. Plots for the complete list of features can found in
1343 section A.

1344 Again, the dataset is downsized to reduce the ratio of correct and incorrect combination
1345 from 20:1, to 5:1. Around 7 million events are used for training, with 10% set aside for testing.
1346 Based on the results of grid search evaluation, the optimal architecture is found to include 5
1347 hidden layers with 60 nodes each. The output score distribution as well as the ROC curve for the
1348 trained model are shown in figure 18.2.2.

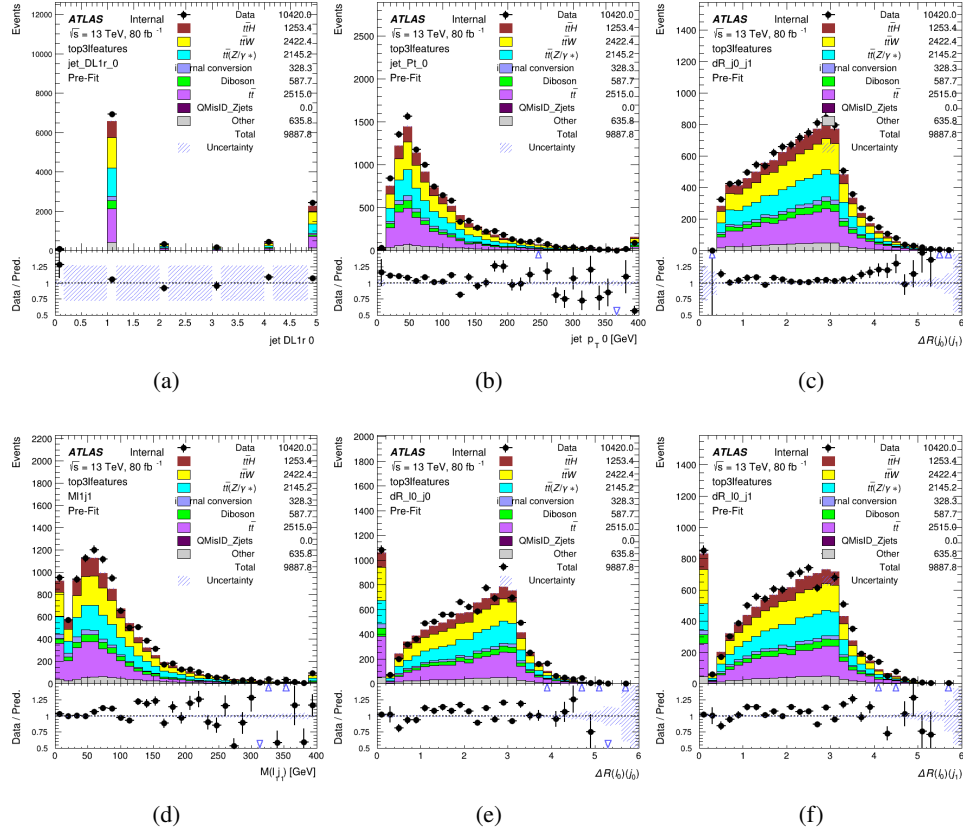


Figure 18.5: Data/MC comparisons of input features for top3l training for 80 fb^{-1} of data. (a) show the DL1r WP of jet 0, (b) the p_T of jet 0, (c) ΔR between jet 0 and jet 1, (d) the invariant mass of lepton 1 and jet 1, (e) ΔR between lepton 0 and jet 0, and (f) ΔR between lepton 0 and jet 1

1349 This procedure is found to identify the correct pairing of jets for nearly 80% of 3l signal
 1350 events. The accuracy of the model is summarized in table 33.

Table 33: Accuracy of the NN in identifying b-jets from tops, compared to the naive method of taking the highest b-tagged jets.

	NN	Naive
1 b-jet	69.0%	48.9%
2 b-jets	89.6%	88.3%
≥ 3 b-jets	55.7%	52.3%
Overall	79.8%	70.2%

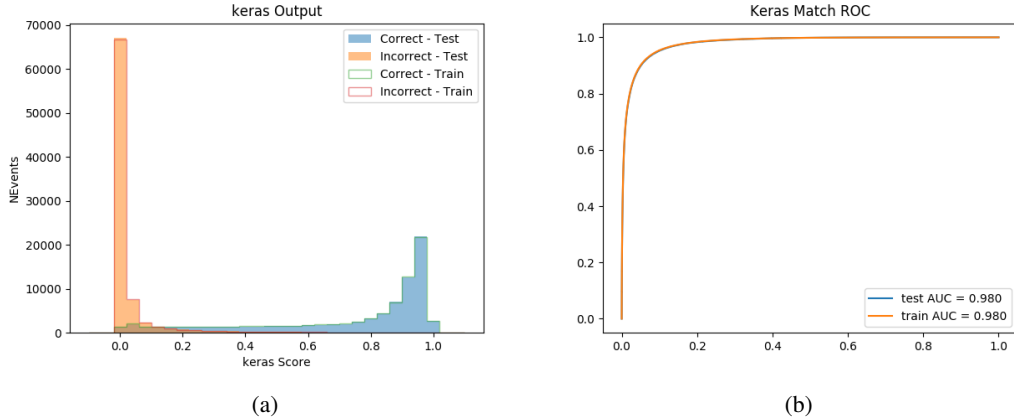


Figure 18.6: Results of the b-jet identification algorithm for the 3l channel, showing (a) the output score of the NN for correct and incorrect combinations of jets. (b) the ROC curve of the output, showing background rejection as a function of signal efficiency

18.3 Higgs Reconstruction

1351 Techniques similar to the b-jet identification algorithms are employed to select the decay products
 1352 of the Higgs: kinematics of all possible combinations of reconstructed objects are fed into a neural
 1353 network to determine which of those is most mostly to be the decay products of the Higgs.

1355 Again separate models are used for the 2lSS and 3l channels, while the 3l channel has now
 1356 been split into two: $t\bar{t}H$ events with three leptons in the final state include both instances where
 1357 the Higgs decays into a lepton (and a neutrino) and a pair of jets, and instances where the Higgs
 1358 decays to two leptons.

1359 3l events are therefore categorized as either semi-leptonic (3lS) or fully-leptonic (3lF). In
 1360 the semi-leptonic case the reconstructed decay products consist of two jets and a single leptons.
 1361 For the fully-leptonic case, the decay products include 2 of the three leptons associated with the

1362 event. For training the models, events are separated into these two categories using truth level
1363 information. A separate MVA, described in section 18.5, is used to make this distinction at reco
1364 level and determine which model to use.

1365 For all channels, the models described in section 18.2 are used to identify b-jet candidates,
1366 whose kinematics are used to identify the Higgs decay products. These jets are not considered
1367 as possible candidates for the Higgs decay, justified by the fact that these models are found to
1368 misidentify jets from the Higgs decay as jets from the top decay less than 1% of the time.

1369 **18.3.1 2lSS Channel**

1370 For the 2lSS channel, the Higgs decay products include one light lepton and two jets. The neural
1371 network is trained on the kinematics of different combinations of leptons and jets, as well as the
1372 b-jets identified in section 18.2, with the specific input features listed in table 34.

Lepton p_T H	Lepton p_T T	jet p_T 0
jet p_T 1	top p_T 0	top p_T 1
top η 0	top η 1	jet η 0
jet η 1	jet Phi 0	jet Phi 1
Lepton η H	Lepton η T	$\Delta R(j_0)(j_1)$
$\Delta R(l_H)(j_0)$	$\Delta R(l_H)(j_1)$	$M(j_0 j_1)$
$M(l_H j_0)$	$M(l_H j_1)$	$\Delta R(l_H)(b_0)$
$\Delta R(l_H)(b_1)$	$\Delta R(l_T)(b_0)$	$\Delta R(l_T)(b_1)$
$\Delta R(j_0 j_1)(l_H)$	$\Delta R(j_0 j_1)(l_T)$	$\Delta R(j_0 j_1)(b_0)$
$\Delta R(j_0 j_1)(b_1)$	$\Delta R(j_0)(b_0)$	$\Delta R(j_0)(b_1)$
$\Delta R(j_1)(b_0)$	$\Delta R(j_1)(b_1)$	$M(j_0 j_1 l_H)$
$p_T(j_0 j_1 l_H l_T b_0 b_1 E_T^{\text{miss}})$	topScore	E_T^{miss}
nJets	HT jets	

Table 34: Input features used to identify the Higgs decay products in 2ISS events

1373 Here j_0 and j_1 , and l_H are the jet and lepton decay candidates, respectively. The other
 1374 lepton in the event is labeled l_T , as it is assumed to have come from the decay of one of the top
 1375 quarks. b_0 and b_1 are the two b-jets identified by the b-jet identification algorithm. The b-jet
 1376 Reco Score is the output of the b-jet reconstruction algorithm.

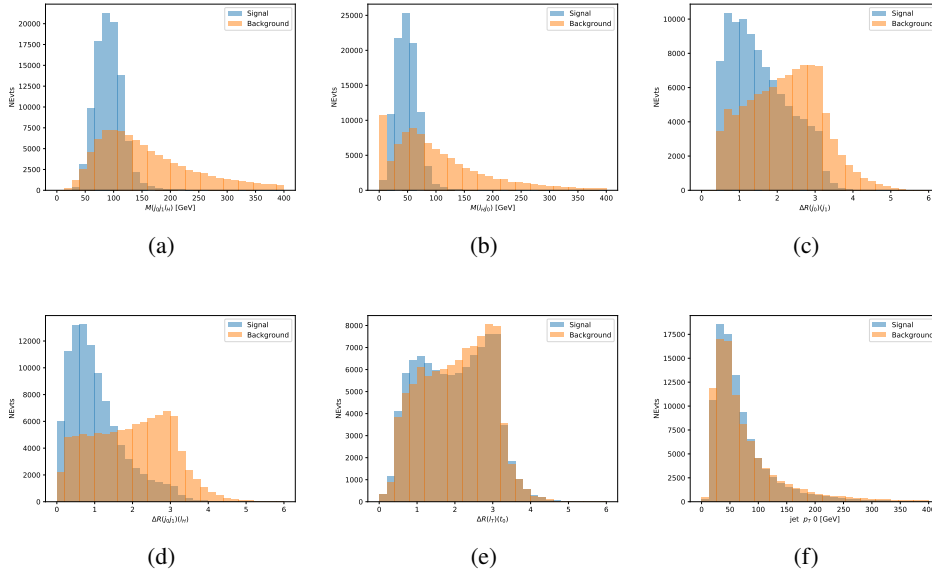


Figure 18.7: Input features for higgs2lSS training. The signal in blue represents events where both jet candidates are truth b-jets from top decays, and the orange is all other combinations. Scaled to the same number of events. (a) shows the invariant mass of the two jet candidates and the lepton candidate, (b) the invariant mass of jet 0 and the lepton candidate, (c) ΔR between the jet candidates, (d) ΔR between jet 0 + jet 1 and the lepton candidate, (e) ΔR between the lepton from the top and the leading b-jet, (f) the p_T of jet 0.

1377 The modeling of these inputs is validated against data, with figure 18.2 showing good
 1378 general agreement between data and MC. Plots for the complete list of features can found in
 1379 section A.

1380 A neural network consisting of 7 hidden layers with 60 nodes each is trained on around 2
 1381 million events, with an additional 200,000 reserved for testing the model. In order to compensate

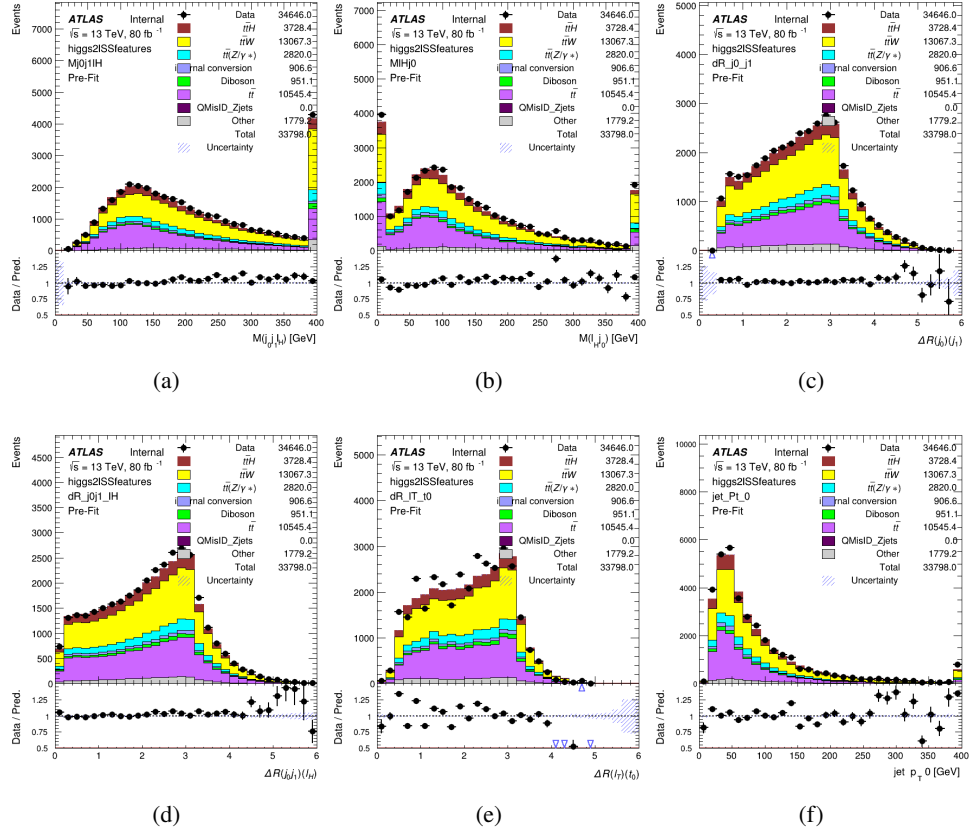


Figure 18.8: Data/MC comparisons of input features for higgs2lSS training for 80 fb^{-1} of data. (a) shows the invariant mass of the two jet candidates and the lepton candidate, (b) the invariant mass of jet 0 and the lepton candidate, (c) ΔR between the jet candidates, (d) ΔR between jet 0 + jet 1 and the lepton candidate, (e) ΔR between the lepton from the top and the leading b-jet, (f) the p_T of jet 0.

for large number of incorrect combinations, these have been downsampled such that the correct combinations represent over 10% of the training set. The output of the NN is summarized in figure 18.3.1.

The neural network identifies the correct combination 55% of the time. It identifies the correct lepton 85% of the time, and selects the correct lepton and at least one of the correct jets 81% of the time.

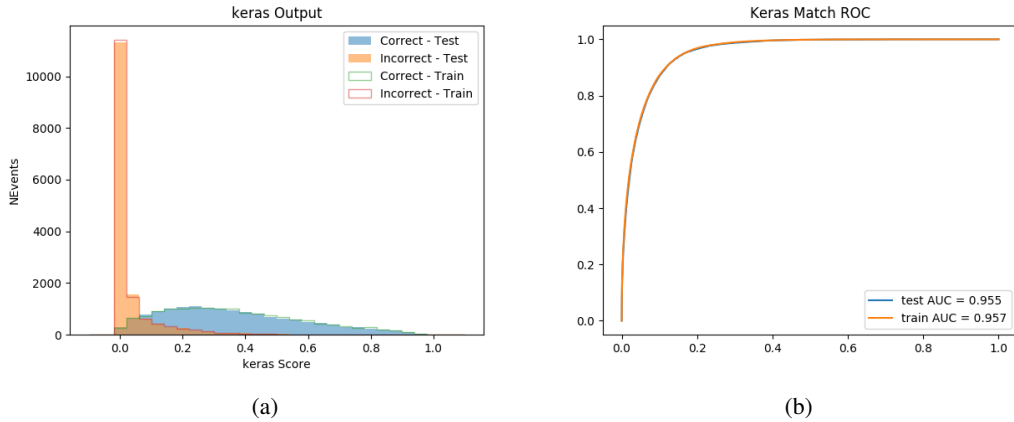


Figure 18.9: Result of the Higgs reconstruction algorithm in the 2lSS channel, showing (a) the output score of the NN for correct and incorrect combinations of jets scaled to an equal number of events, and (b) the ROC curve of the output, showing background rejection as a function of signal efficiency

18.3.2 3l Semi-leptonic Channel

For 3l $t\bar{t}H$ where the Higgs decay semi-leptonically, the decay products include one of the three leptons and two jets. In this case, the other two leptons originated from the decay of the tops, meaning the opposite-sign (OS) lepton cannot have come from the Higgs. This leaves only the two same-sign (SS) leptons as possible Higgs decay products.

Lepton $p_T H$	Lepton $p_T T_0$	Lepton $p_T T_1$
jet $p_T 0$	jet $p_T 1$	top $p_T 0$
top $p_T 1$	jet $\eta 0$	jet $\eta 1$
jet $\phi 0$	jet $\phi 1$	$\Delta R(j_0)(j_1)$
$M(j_0 j_1)$	$\Delta R(l_H)(j_0)$	$\Delta R(l_H)(j_1)$
$\Delta R(j_0 j_1)(l_H)$	$\Delta R(j_0 j_1)(l_{T_1})$	$\Delta R(l_{T_0})(l_{T_1})$
$\Delta R(l_H)(l_{T_1})$	$M(j_0 j_1 l_{T_0})$	$M(j_0 j_1 l_{T_1})$
$M(j_0 j_1 l_H)$	$\Delta R(j_0 j_1 l_H)(l_{T_0})$	$\Delta R(j_0 j_1 l_H)(l_{T_1})$
$\Delta\phi(j_0 j_1 l_H)(E_T^{\text{miss}})$	$p_T(j_0 j_1 l_H l_{T_0} l_{T_1} b_0 b_1 E_T^{\text{miss}})$	$M(j_0 j_1 b_0)$
$M(j_0 j_1 b_1)$	$\Delta R(l_{T_0})(b_0)$	$\Delta R(l_{T_0})(b_1)$
$\Delta R(l_{T_1})(b_0)$	$\Delta R(l_{T_1})(b_1)$	$\Delta R(j_0)(b_0)$
$\Delta R(j_0)(b_1)$	$\Delta R(j_1)(b_0)$	$\Delta R(j_1)(b_1)$
topScore	MET	HT jets
nJets		

Table 35: Input features used to identify the Higgs decay products in 3lS events

1393 Here j_0 and j_1 , and l_H are the jet and lepton decay candidates, respectively. The other
 1394 two leptons in the event are labeled as l_{T0} and l_{T1} . b_0 and b_1 are the two b-jets identified by
 1395 the b-jet identification algorithm. The b-jet Reco Score is the output of the Higgs reconstruction
 1396 algorithm.

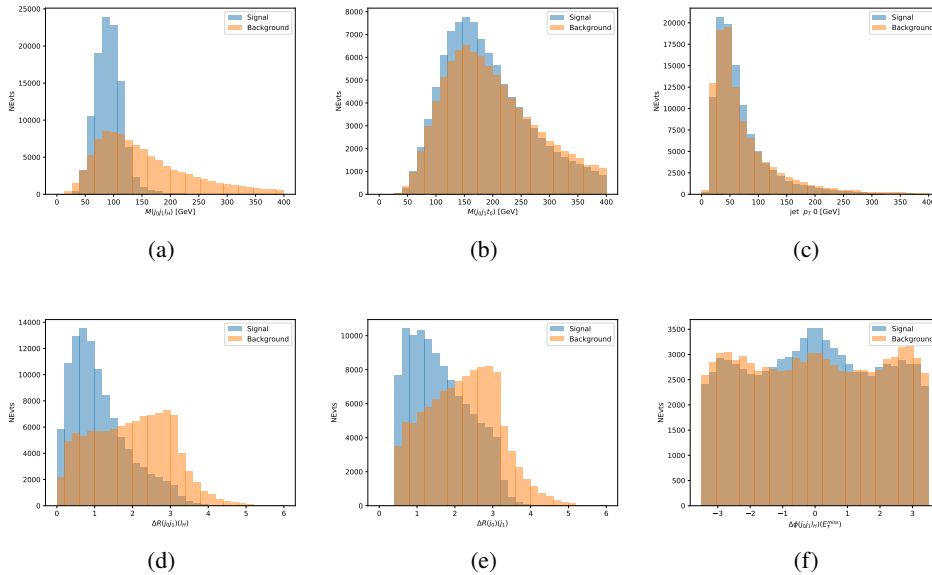


Figure 18.10: Input features for higgs3lS training. The signal in blue represents events where both jet candidates are truth b-jets from top decays, and the orange is all other combinations. Scaled to the same number of events.

1397 The modeling of these inputs is validated against data, with figure 18.11 showing good
 1398 general agreement between data and MC. Plots for the complete list of features can found in
 1399 appendix A.1.

1400 A neural network of 7 hidden layers with 70 nodes each is trained on 1.8 million events.
 1401 Once again, incorrect combinations are downsampled, such that the correct combinations are
 1402 around 10% of the training set. 10% of the dataset is reserved for testing. The output of the NN

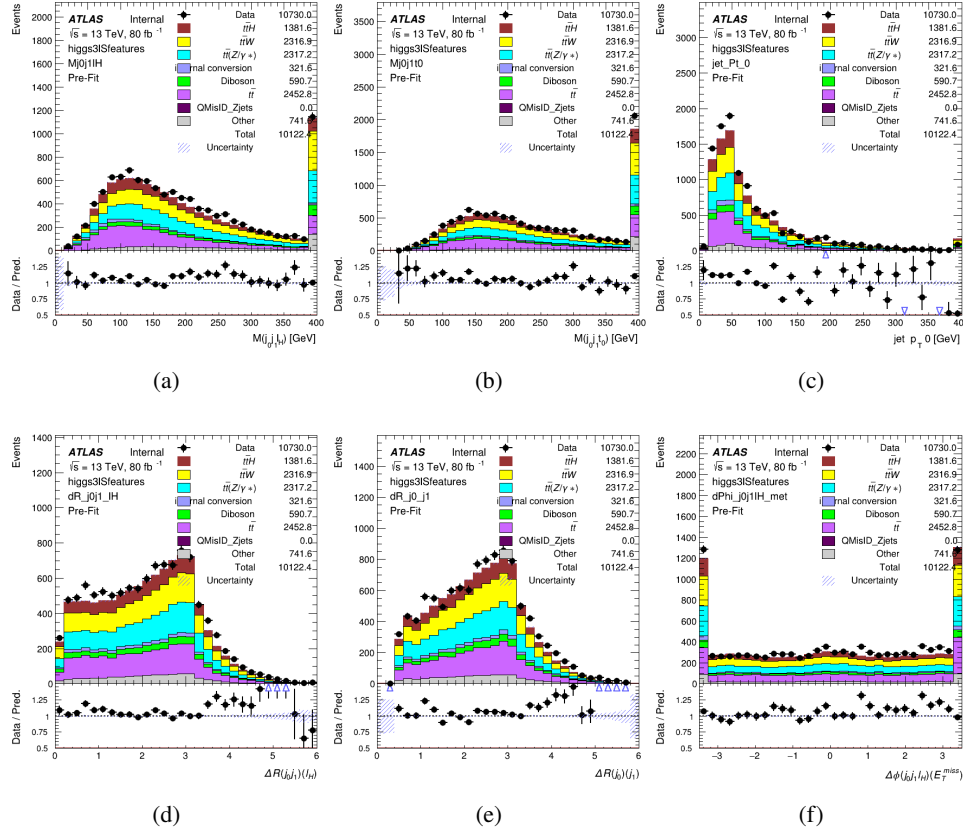


Figure 18.11: Data/MC comparisons of input features for higgs3IS training for 80 fb^{-1} of data.

is summarized in figure 18.3.2.

The neural network identifies the correct combination 64% of the time. It identifies the correct lepton 85% of the time, and selects the correct lepton and at least one of the correct jets 83% of the time.

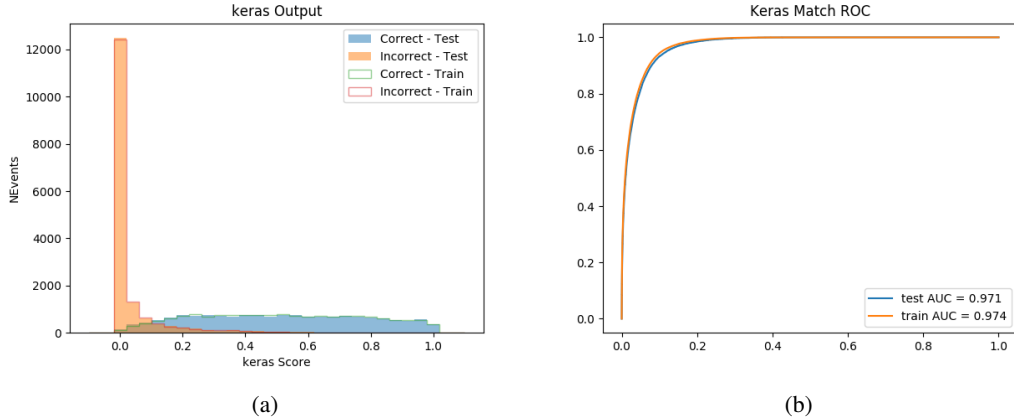


Figure 18.12: Results of the Higgs reconstruction algorithm in the 3lS channel, showing (a) the output score of the NN for correct and incorrect combinations of jets, scaled to an equal number of entries.,. (b) the ROC curve of the output, showing background rejection as a function of signal efficiency

1407 18.3.3 3l Fully-leptonic Channel

1408 In the fully-leptonic 3l case, the goal is identify which two of the three leptons originated from
 1409 the Higgs decay. Since one of these two must be the OS lepton, this problem is reduced to
 1410 determining which of the two SS leptons originated from the Higgs. The kinematics of both
 1411 possibilities are used for training, one where the SS lepton from the Higgs is correctly labeled,
 1412 and one where it is not.

Lepton $p_T H_1$	Lepton $p_T H_0$	Lepton $p_T T$
top $p_T 0$	top $p_T 1$	$\Delta\phi(l_{H_1})(E_T^{\text{miss}})$
$\Delta\phi(l_T)(E_T^{\text{miss}})$	$M(l_{H_0}l_{H_1})$	$M(l_{H_1}l_T)$
$M(l_{H_0}l_T)$	$\Delta R(l_{H_0})(l_{H_1})$	$\Delta R(l_{H_1})(l_T)$
$\Delta R(l_{H_0})(l_T)$	$\Delta R(l_{H_0}l_{H_1})(l_T)$	$\Delta R(l_{H_0}l_T)(l_{H_1})$
$\Delta R(l_{H_0}l_{H_1})(b_0)$	$\Delta R(l_{H_0}l_{H_1})(b_1)$	$\Delta R(l_{H_0}b_0)$
$M(l_{H_0}b_0)$	$\Delta R(l_{H_0}b_1)$	$M(l_{H_0}b_1)$
$\Delta R(l_{H_1}b_0)$	$M(l_{H_1}b_0)$	$\Delta R(l_{H_1}b_1)$
$M(l_{H_1}b_1)$	E_T^{miss}	topScore

Table 36: Input features used to identify the Higgs decay products in 3lF events

1413 Here l_{H0} and l_{H1} are the Higgs decay candidates. The other lepton in the event is labeled
 1414 l_T . b_0 and b_1 are the two b-jets identified by the b-jet identification algorithm. The b-jet Reco
 1415 Score is the output of the Higgs reconstruction algorithm.

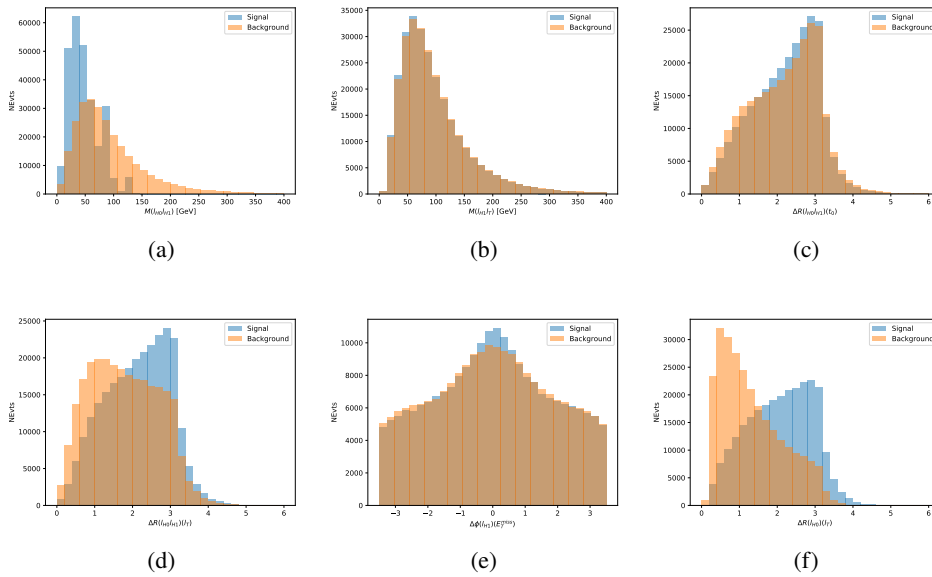


Figure 18.13: Input features for higgs3lF training. The signal in blue represents events where both jet candidates are truth b-jets from top decays, and the orange is all other combinations. Scaled to the same number of events.

1416 The modeling of these inputs is validated against data, with figure 18.14 showing good
 1417 general agreement between data and MC. Plots for the complete list of features can found in
 1418 section A.

1419 A neural network consisting of 5 nodes and 60 hidden units is trained on 800,000 events,
 1420 with 10% of the dataset reserved for testing. The output of the model is summarized in figure
 1421 18.3.3.

1422 The correct lepton is identified by the model for 80% of events in the testing data set.

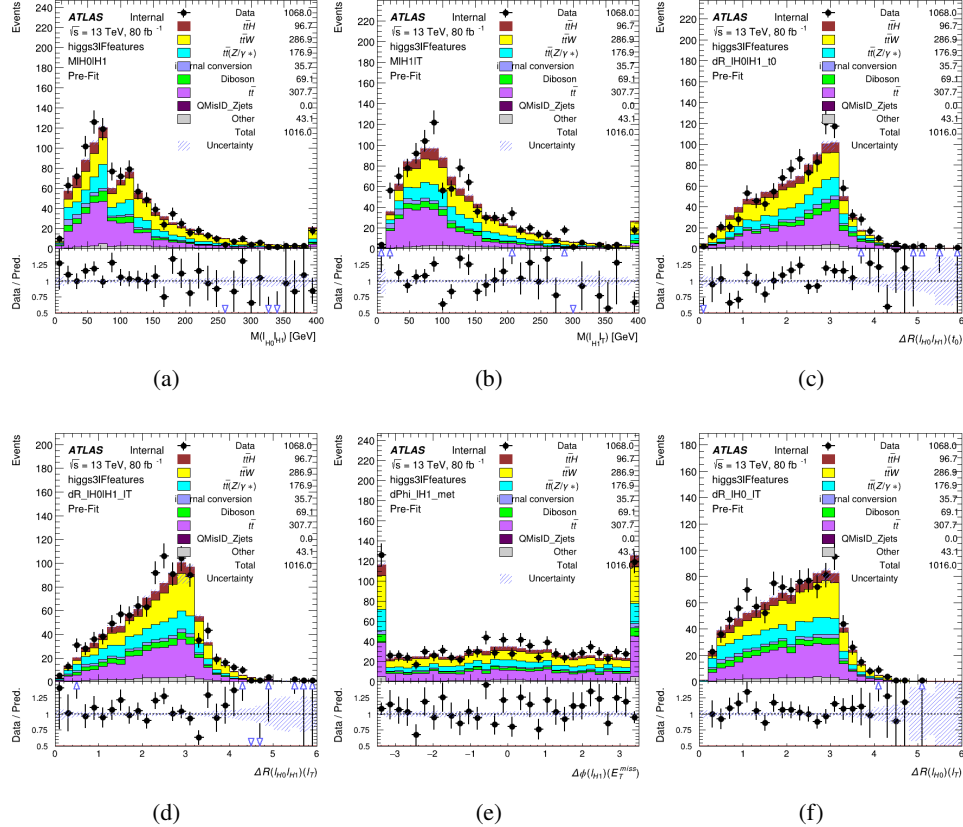


Figure 18.14: Data/MC comparisons of input features for higgs3IF training for 80 fb^{-1} of data.

18.4 p_T Prediction

Once the most probable decay products have been identified, their kinematics are used as inputs to a regression model which attempts to predict the momentum of the Higgs Boson. Once again, a DNN is used. Input variables representing the b-jets and leptons not from the Higgs decay are included as well, as these are found to improve performance. The truth p_T of the Higgs, as predicted by MC, are used as labels. Separate models are built for each channel - 2lSS, 3l Semi-leptonic and 3l Fully-leptonic.

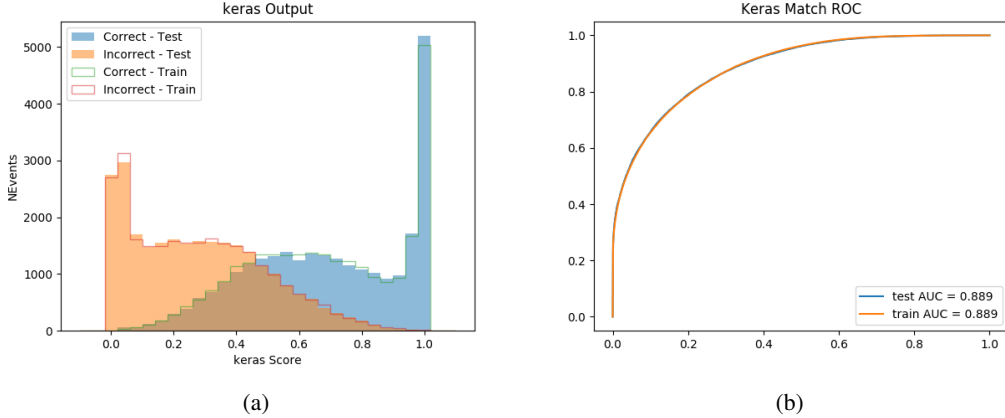


Figure 18.15: (a) the output score of the NN for correct and incorrect combinations of jets. (a) the ROC curve of the output, showing background rejection as a function of signal efficiency

1430 As a two-bin fit is targeted for the final result, some metrics evaluating the performance
 1431 of the models aim to show how well it distinguished between "high p_T " and "low p_T " events. A
 1432 cutoff point of 150 GeV is used to define these two categories.

1433 Because the analysis uses a two bin fit of the Higgs p_T , the momentum reconstruction
 1434 could be treated as a binary classification problem, rather than a regression problem. This
 1435 approach is explored in detail in section A.4, and is found not to provide any significant increase
 1436 in sensitivity. The regression approach is used because it provides more flexibility for future
 1437 analyses, as it is independent of the cutoff between high and low p_T , as well as the number of
 1438 bins. Further, a regression allows the output of the neural network to be more clearly understood,
 1439 as it can be directly compared to a physics observable.

1440 18.4.1 2lSS Channel

1441 The input variables listed in table 37 are used to predict the Higgs p_T in the 2lSS channel. Here
1442 j_0 and j_1 are the two jets identified as Higgs decay products. The lepton identified as originating
1443 from the Higgs is labeled l_H , while the other lepton is labeled l_T , as it is assumed to have come
1444 from the decay of one of the top quarks. b_0 and b_1 are the two b-jets identified by the b-jet
1445 identification algorithm. The Higgs Reco Score and b-jet Reco Score are the outputs of the Higgs
1446 reconstruction algorithm, and the b-jet identification algorithm, respectively.

HT	$M(j_0 j_1)$	$M(j_0 j_1 l_H)$
$M(l_H j_0)$	$M(l_H j_1)$	$p_T(b_0 b_1)$
$p_T(j_0 j_1 l_H)$	$\Delta\phi(j_0 j_1 l_H)(E_T^{\text{miss}})$	$\Delta R(j_0)(j_1)$
$\Delta R(j_0 j_1)(l_H)$	$\Delta R(j_0 j_1 l_H)(l_T)$	$\Delta R(j_0 j_1 l_H)(b_0)$
$\Delta R(j_0 j_1 l_H)(b_1)$	$\Delta R(l_H)(j_0)$	$\Delta R(l_H)(b_0)$
$\Delta R(l_H)(b_1)$	$\Delta R(l_T)(b_0)$	$\Delta R(l_T)(b_1)$
$\Delta R(b_0)(b_1)$	Higgs Reco Score	jet η 0
jet η 1	jet Phi 0	jet Phi 1
jet p_T 0	jet p_T 1	Lepton η H
Lepton ϕ H	Lepton p_T H	Lepton p_T T
E_T^{miss}	nJets	b-jet Reco Score
b-jet p_T 0	b-jet p_T 1	

Table 37: Input features for reconstructing the Higgs p_T spectrum for 2lSS events

1447 The optimal neural network architecture for this channel is found to consist of 7 hidden
 1448 layers with 60 nodes each. The input data set includes 1.2 million events, 10% of which is used
 1449 for testing, the other 90% for training. Training is found to converge after around 150 epochs.

1450 To evaluate the performance of the model, the predicted p_T spectrum is compared to the
 1451 truth Higgs p_T in figure 18.16. In order to visualize the model performance more clearly, in (a)
 1452 of that figure, the color of each point is determined by Kernel Density Estimation (KDE). The
 1453 color shown represents the logarithm of the output from KDE, to counteract the large number of
 1454 low p_T events. For that same reason, each column of the histogram shown in (b) of figure 18.16
 1455 is normalized to unity. This plot therefore demonstrates what the model predicts for each slice
 1456 of truth p_T .

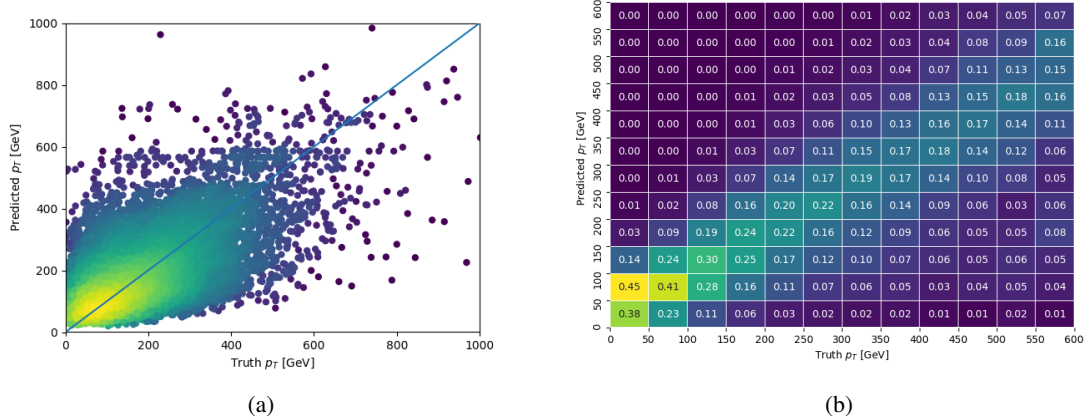


Figure 18.16: The regressed Higgs momentum spectrum as a function of the truth p_T for 2lSS $t\bar{t}H$ events in (a) a scatterplot, where the color of each point represents the log of the point density, based on Gaussian Kernel Density Estimation, and (b) a histogram where each column has been normalized to one.

1457 We are also interested in how well the model distinguishes between events with $p_T < 150$
 1458 GeV and > 150 GeV. Figure 18.17 demonstrates the NN output for high and low p_T events based

1459 on this cutoff.

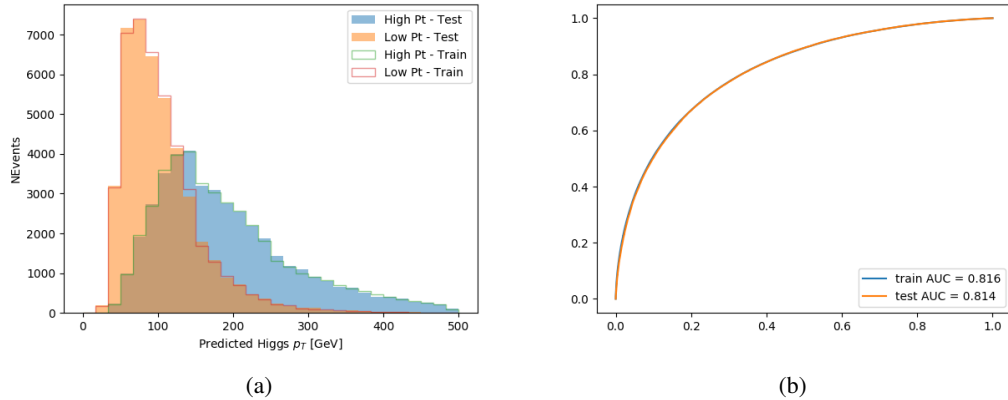


Figure 18.17: (a) shows the reconstructed Higgs p_T for 2lSS events with truth $p_T > 150$ GeV and < 150 GeV, while (b) shows the ROC curve for those two sets of events.

1460 **18.4.2 3l Semi-leptonic Channel**

1461 The following input features are used to predict the Higgs p_T for events in the 3lS channel:

HT jets	MET	$M(j_0 j_1)$
$M(j_0 j_1 l_H)$	$M(j_0 j_1 l_{T0})$	$M(j_0 j_1 l_{T1})$
$M(j_0 j_1 b_0)$	$M(j_0 j_1 b_1)$	$M(b_0 l_{T0})$
$M(b_0 l_{T1})$	$M(b_1 l_{T0})$	$M(b_1 l_{T1})$
$\Delta\phi(j_0 j_1 l_H)(E_T^{\text{miss}})$	$\Delta R(j_0)(j_1)$	$\Delta R(j_0 j_1)(l_H)$
$\Delta R(j_0 j_1)(l_{T1})$	$\Delta R(j_0 j_1)(b_0)$	$\Delta R(j_0 j_1)(b_1)$
$\Delta R(j_0 j_1 l_H)(l_{T0})$	$\Delta R(j_0 j_1 l_H)(l_{T1})$	$\Delta R(j_0 j_1 l_H)(b_0)$
$\Delta R(j_0 j_1 l_H)(b_1)$	$\Delta R(l_H)(j_0)$	$\Delta R(l_H)(j_1)$
$\Delta R(l_H)(l_{T1})$	$\Delta R(l_{T0})(l_{T1})$	$\Delta R(l_{T0})(b_0)$
$\Delta R(l_{T0})(b_1)$	$\Delta R(l_{T1})(b_0)$	$\Delta R(l_{T1})(b_1)$
higgsScore	jet η 0	jet η 1
jet ϕ 0	jet ϕ 1	jet p_T 0
jet p_T 1	Lepton η H	Lepton ϕ H
Lepton p_T H	Lepton p_T T0	Lepton p_T T1
nJets	topScore	b-jet p_T 0
b-jet p_T 1		

Table 38: Input features for reconstructing the Higgs p_T spectrum for 3lS events

Again, j_0 and j_1 are the two jets identified as Higgs decay products, ordered by p_T . The lepton identified as originating from the Higgs is labeled l_H , while the other two leptons are labeled l_{T0} and l_{T1} . b_0 and b_1 are the two b-jets identified by the b-jet identification algorithm. The Higgs Reco Score and b-jet Reco Score are the outputs of the Higgs reconstruction algorithm, and the b-jet identification algorithm, respectively.

The optimal neural network architecture for this channel is found to consist of 7 hidden layers with 80 nodes each. The inputdata set includes one million events, 10% of which is used for testing, the other 90% for training. Training is found to converge after around 150 epochs.

To evaluate the performance of the model, the predicted p_T spectrum is compared to the truth Higgs p_T in figure 18.18. Once again, (a) of 18.18 shows a scatterplots of predicted vs truth p_T , where the color of each point corresponds to the log of the relative KDE at that point. Each column of the the histogram in (b) is normalized to unity, to better demonstrate the output of the NN for each slice of truth p_T .

Figure 18.19 shows (a) the output of the NN for events with truth p_T less than and greater than 150 GeV and (b) the ROC curve demonstrating how well the NN distinguishes high and low p_T events.

18.4.3 3l Fully-leptonic Channel

The features listed in 39 are used to construct a model for predictin the Higgs p_T for 3lF events.

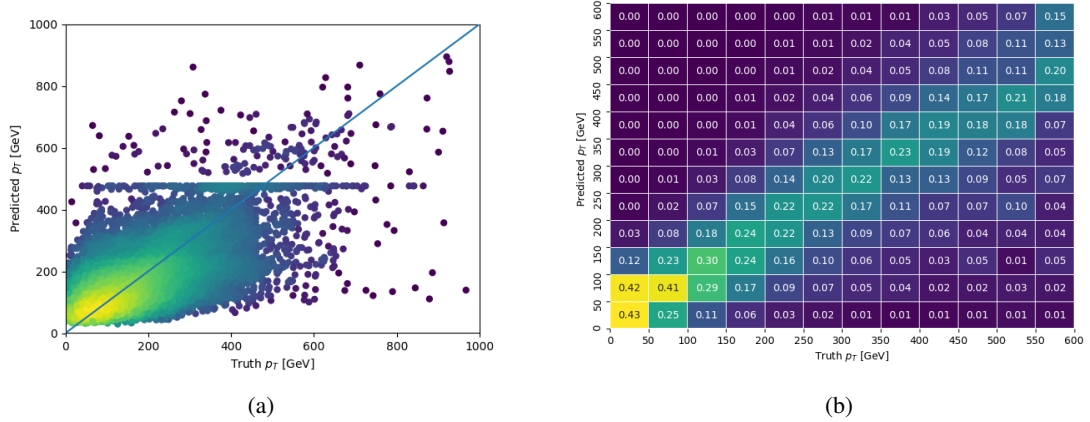


Figure 18.18: The regressed Higgs momentum spectrum as a function of the truth p_T for 3lS $t\bar{t}H$ events in (a) a scatterplot, where the color of each point represents the log of the point density, based on Gaussian Kernel Density Estimation, and (b) a histogram where each column has been normalized to one.

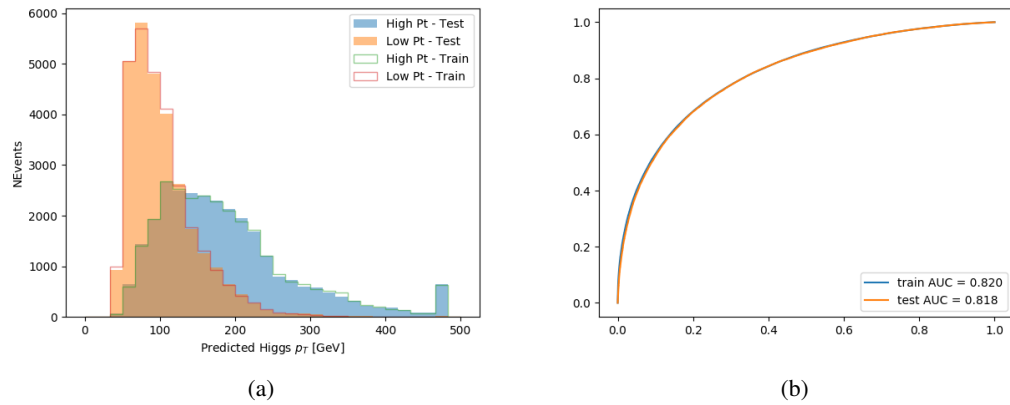


Figure 18.19: (a) shows the reconstructed Higgs p_T for 3lS events with truth $p_T > 150$ GeV and < 150 GeV, while (b) shows the ROC curve for those two sets of events.

HT	$M(l_{H0}l_{H1})$	$M(l_{H0}l_T)$
$M(l_{H0}b_0)$	$M(l_{H0}b_1)$	$M(l_{H1}l_T)$
$M(l_{H1}b_0)$	$M(l_{H1}b_1)$	$\Delta R(l_{H0})(l_{H1})$
$\Delta R(l_{H0})(l_T)$	$\Delta R(l_{H0}l_{H1})(l_T)$	$\Delta R(l_{H0}l_T)(l_{H1})$
$\Delta R(l_{H1})(l_T)$	$\Delta R(l_{H0}b_0)$	$\Delta R(l_{H0}b_1)$
$\Delta R(l_{H1}b_1)$	$\Delta R(l_{H1}b_0)$	higgsScore
Lepton η H_0	Lepton η H_1	Lepton η T
Lepton p_T H_0	Lepton p_T H_1	Lepton p_T T
E_T^{miss}	topScore	b-jet p_T 0
b-jet p_T 1		

Table 39: Input features for reconstructing the Higgs p_T spectrum for 3lF events

1480 l_{H0} and l_{H1} represent the two leptons identified by the Higgs reconstruction model as
 1481 originating from the Higgs, while l_T is the other lepton in the event. The Higgs Reco Score and
 1482 b-jet Reco Score are the outputs of the Higgs reconstruction algorithm, and b-jet identification
 1483 algorithm, respectively.

1484 The optimal neural network architecture for this channel is found to consist of 5 hidden
 1485 layers with 40 nodes each. The input data set includes 400,000 events, 10% of which is used for
 1486 testing, the other 90% for training. Training is found to converge after around 150 epochs.

1487 The predicted transverse momentum, as a function of the truth p_T , is shown in figure
 1488 [18.20](#).

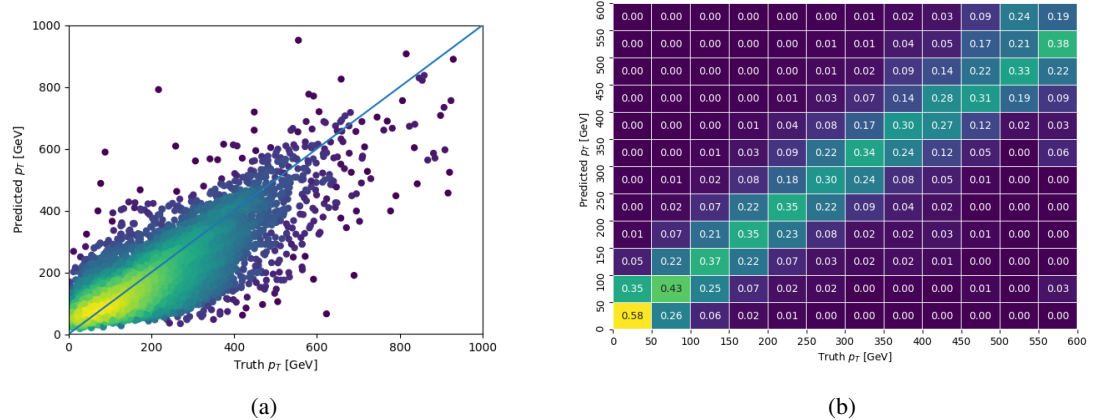


Figure 18.20: The regressed Higgs momentum spectrum as a function of the truth p_T for 3lF $t\bar{t}H$ events in (a) a scatterplot, where the color of each point represents the log of the point density, based on Gaussian Kernel Density Estimation, and (b) a histogram where each column has been normalized to one.

1489 When split into high and low p_T , based on a cutoff of 150 GeV, the

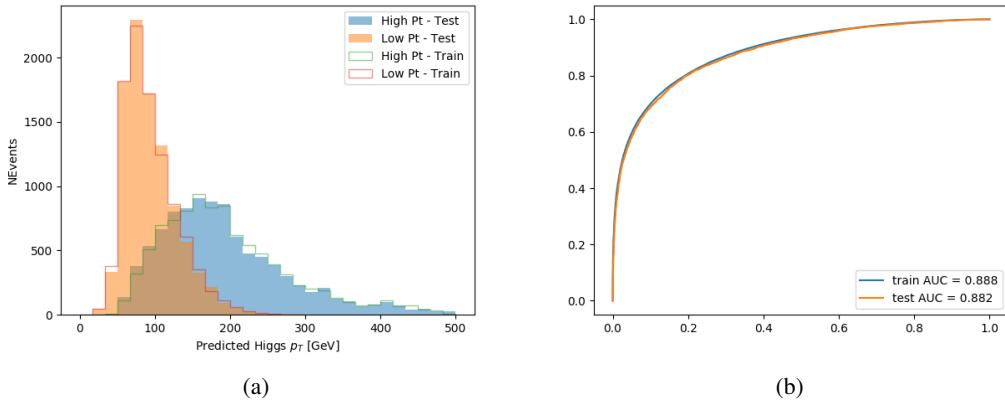


Figure 18.21: (a) shows the reconstructed Higgs p_T for 3lF events with truth $p_T > 150$ GeV and < 150 GeV, while (b) shows the ROC curve for those two sets of events.

1490 18.5 3l Decay Mode

1491 In the 3l channel, there are two possible ways for the Higgs to decay, both involving intermediate
 1492 W boson pairs: Either both W bosons decay leptonically, in which case the reconstructed decay
 1493 consists of two leptons (referred as the fully-leptonic 3l channel), or one W decays leptonically
 1494 and the other hadronically, giving two jets and one lepton in the final state (referred to as the
 1495 semi-leptonic 3l channel). In order to accurately reconstruct the Higgs, it is necessary to identify
 1496 which of these decays took place for each 3l event.

1497 The kinematics of each event, along with the output scores of the Higgs and top recon-
 1498 struction algorithms, are used to distinguish these two possible decay modes. The particular
 1499 inputs used are listed in table 40.

HT jets	$M(l_0 t_0)$	$M(l_0 t_1)$
$M(l_1 t_0)$	$M(l_1 t_1)$	$M(l_0 l_1)$
$M(l_0 l_2)$	$M(l_1 l_2)$	$\Delta R(l_0 t_0)$
$\Delta R(l_0 t_1)$	$\Delta R(l_1 t_0)$	$\Delta R(l_1 t_1)$
$\Delta R(l l_0 1)$	$\Delta R(l l_0 2)$	$\Delta R(l l_1 2)$
Lepton η 0	Lepton η 1	Lepton η 2
Lepton ϕ 0	Lepton ϕ 1	Lepton ϕ 2
Lepton p_T 0	Lepton p_T 1	Lepton p_T 2
E_T^{miss}	nJets	nJets OR DL1r 60
nJets OR DL1r 85	score3lF	score3lS
topScore	total charge	

Table 40: Input features used to distinguish semi-leptonic and fully-leptonic Higgs decays in the 3l channel.

1500 Here l_0 is the opposite charge lepton, l_1 and l_2 are the two SS leptons order by ΔR
 1501 from lepton 0. score3lF and score3lS are the outputs of the 3lS and 3lF Higgs reconstruction
 1502 algorithms, while topScore is the output of the b-jet identification algorithm.

1503 A neural network with 5 hidden layers, each with 50 nodes, is trained to distinguish these
 1504 two decay modes. The output of the model is summarized in figure 18.22.

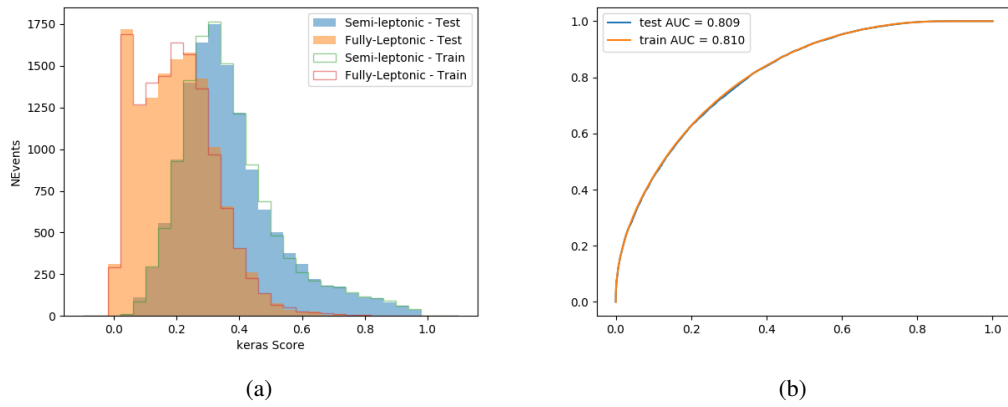


Figure 18.22: (a) shows the output of the decay separation NN for Semi-leptonic (blue) and Fully-leptonic (orange) 3l events, scaled to equal area. (b) shows the ROC curve for those two sets of events.

1505 A cutoff of 0.23 is determined to be optimal for separating 3lS and 3lF in the fit.

1506 19 Signal Region Definitions

1507 Events are divided into two channels based on the number of leptons in the final state: one with
 1508 two same-sign leptons, the other with three leptons. The 3l channel includes events where both
 1509 leptons originated from the Higgs boson as well as events where only one of the leptons

1510 19.1 Pre-MVA Event Selection

1511 A preselection is applied to define orthogonal analysis channels based on the number of leptons
1512 in each event. For the 2lSS channel, the following preselection is used:

- 1513 • Two very tight, same-charge, light leptons with $p_T > 20 \text{ GeV}$

- 1514 • ≥ 4 reconstructed jets, ≥ 1 b-tagged jets

- 1515 • No reconstructed tau candidates

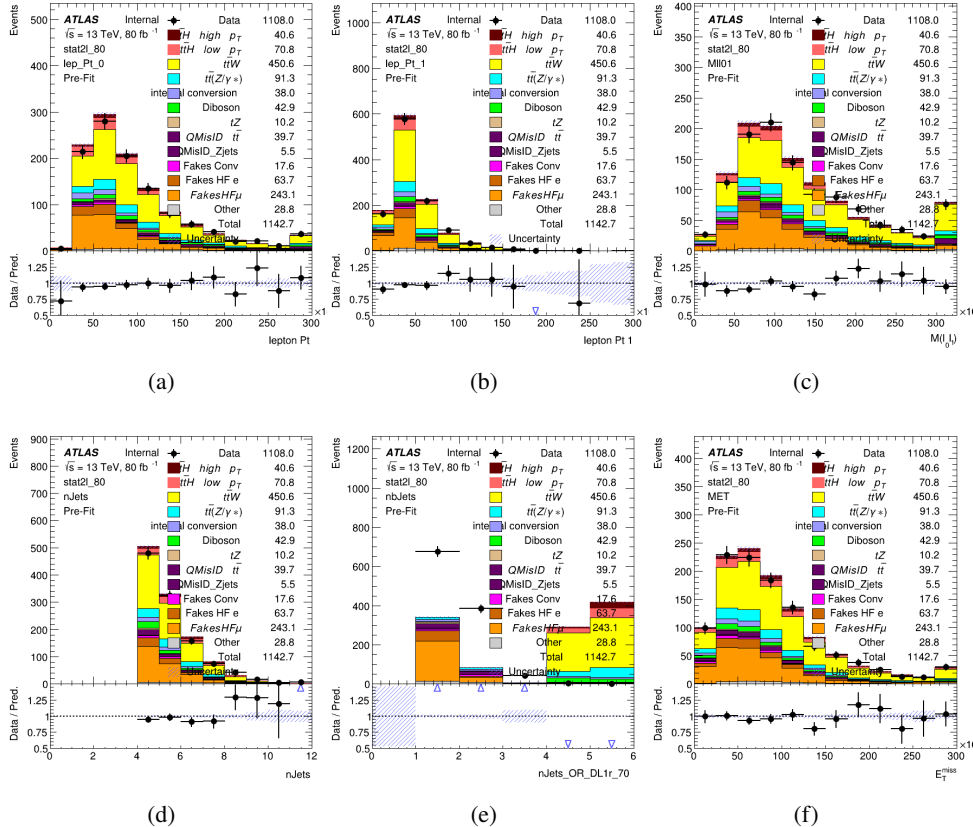
1516 The event yield after the 2lSS preselection has been applied, for MC and data at 80 fb^{-1} ,
1517 is shown in table 41.

	Yields
t̄H high p _T	36.19 ± 0.23
t̄H low p _T	63.58 ± 0.31
t̄W	440.64 ± 2.32
t̄Z/γ	91.84 ± 0.79
t̄lllowmass	8.47 ± 0.28
rareTop	24.2099 ± 0.40
VV	38.7927 ± 0.55
tZ	3e-05 ± 5.47-06
QMISID t̄	39.90 ± 2.36
QMISID Zjets	5.49 ± 0.67
t̄ int. conv.	12.74 ± 1.40
t̄ + γ int. conv.	12.09 ± 0.58
t̄ Conv.	13.55 ± 1.43
t̄ + γ Conv.	5.35 ± 0.38
t̄ HF e	59.92 ± 2.89
t̄ + γ HF e	0.51 ± 0.15
t̄ HF μ	224.57 ± 5.62
t̄ + γ HF μ	1.60 ± 0.23
Z + jets internal conv	3e-05 ± 5.47e-06
Z + jets conv	0.62 ± 0.21
Z + jets HF e	0.14 ± 0.13
Z + jets HF μ	0.82 ± 0.26
Single top Conv	2.27 ± 0.53
Single top HF e	2.33 ± 0.50
Single top HF μ	11.12 ± 1.07
Three top	2.22 ± 0.02
Four top	13.09 ± 0.16
t̄WW	10.985 ± 0.30
tW	3e-05 ± 5.47-06
WtZ	9.07 ± 0.44
VVV	0.30 ± 0.04
VH	0.59 ± 1.55
Total	1133.11 ± 7.69
Data	1108

Table 41: Event yield in the 2ISS preselection region.

1518

figure 20.1. Good general agreement is found.

Figure 19.1: Data/MC comparisons of the 2lSS pre-selection region. (a) and (b) show the p_T of leptons 0 and 1, (c) shows the invariant mass of lepton 0 and 1, (d) shows the jet multiplicity, (e) the b-tagged jet multiplicity, and (f) the missing transverse energy.

1519

For the 3l channel, the following selection is applied:

1520

- Three light leptons with total charge ± 1
- Same charge leptons are required to be very tight, with $p_T > 20$ GeV
- Opposite charge lepton must be loose, with $p_T > 10$ GeV

1522

- 1523 • ≥ 2 reconstructed jets, ≥ 1 b-tagged jets
- 1524 • No reconstructed tau candidates
- 1525 • $|M(l^+l^-) - 91.2 \text{ GeV}| > 10 \text{ GeV}$ for all opposite-charge, same-flavor lepton pairs
- 1526 The event yield after the 3l preselection has been applied, for MC and data at 80 fb^{-1} , is
- 1527 shown in table 19.1.

	Yields
t̄H high p _T	18.40 ± 0.13
t̄H low p _T	29.91 ± 0.16
t̄W	134.22 ± 1.25
t̄Z/γ	88.47 ± 0.73
t̄lllowmass	2.77 ± 0.16
rareTop	15.05 ± 0.32
VV	34.54 ± 0.54
tZ	2e-05 ± 4.47-06
QMisID t̄t	1.80 ± 0.59
QMisID Zjets	0.02 ± 0.02
t̄t internal conversion	4.34 ± 0.43
t̄t + γ internal conversion	5.83 ± 0.42
t̄t Conv.	4.71 ± 0.45
t̄t + γ Conv.	2.64 ± 0.27
t̄t HF e	27.44 ± 1.05
t̄t + γ HF e	0.27 ± 0.11
t̄t HF μ	89.21 ± 1.92
t̄t + γ HF μ	0.94 ± 0.16
Z + jets conv	0.09 ± 0.19
Z + jets HF e	0.25 ± 0.15
Z + jets HF μ	2.41 ± 0.95
Single top Conv	0.58 ± 0.61
Single top HF e	1.50 ± 0.43
Single top HF μ	4.62 ± 0.85
Three top	0.96 ± 0.02
Four top	5.58 ± 0.10
t̄WW	5.45 ± 0.21
WtZ	8.71 ± 0.42
VVV	0.81 ± 0.02
Total	492.14 ± 3.22
Data	535

Table 42: Yields of the analysis

1528

Comparisons of kinematic distributions for data and MC in this region are shown in figure

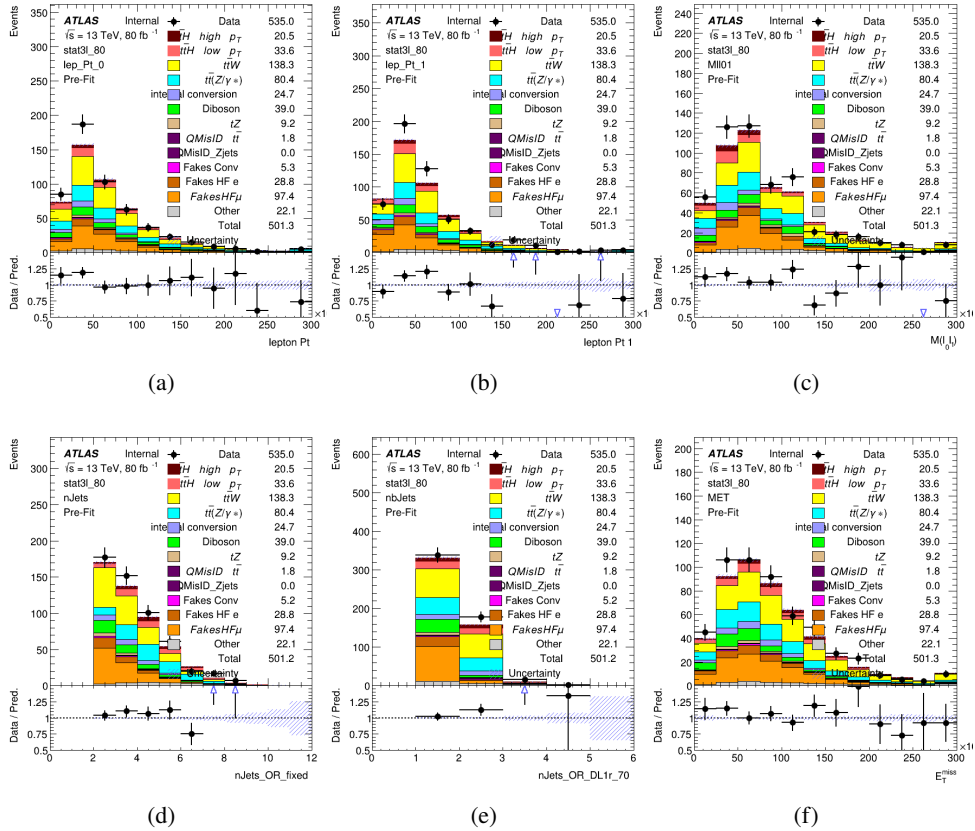
1529 **20.2.**

Figure 19.2: Data/MC comparisons of the 3l pre-selection region. (a) and (b) show the p_T of leptons 0 and 1, (c) shows the invariant mass of lepton 0 and 1, (d) shows the jet multiplicity, (e) the b-tagged jet multiplicity, and (f) the missing transverse energy.

1530

19.2 Event MVA

1531

Separate multi-variate analysis techniques (MVAs) are used in order to distinguish signal events from background for each analysis channel - 2lSS, 3l semi-leptonic (3lS), and 3l fully leptonic (3lF). In particular, Boosted Decision Tree (BDT) algorithms are produced with XGBoost

1534 [xgboost] are trained using the kinematics of signal and background events derived from Monte
1535 Carlo simulations. Events are weighted in the BDT training by the weight of each Monte Carlo
1536 event.

1537 Because the background composition differs for events with a high reconstructed Higgs p_T
1538 compared to events with low reconstructed Higgs p_T , separate MVAs are produced for high and
1539 low p_T regions. This is found to provide better significance than attempting to build an inclusive
1540 model, as demonstrated in appendix A.2. A cutoff of 150 GeV is used. This gives a total of 6
1541 background rejection MVAs - explicitly, 2lSS high p_T , 2lSS low p_T , 3lS high p_T , 3lS low p_T ,
1542 3lF high p_T , and 3lF low p_T .

1543 The following features are used in both the high and low p_T 2lSS BDTs:

HT	$M(\text{lep}, E_T^{\text{miss}})$	$M(l_0 l_1)$
binHiggs p_T 2ISS	$\Delta R(l_0)(l_1)$	diLepton type
higgsRecoScore	jet η 0	jet η 1
jet ϕ 0	jet ϕ 1	jet p_T 0
jet p_T 1	Lepton η 0	Lepton η 1
Lepton ϕ 0	Lepton ϕ 1	Lepton p_T 0
Lepton p_T 1	E_T^{miss}	$\min \Delta R(l_0)(\text{jet})$
$\min \Delta R(l_1)(\text{jet})$	$\min \Delta R(\text{Lepton})(\text{bjet})$	mjjMax frwdJet
nJets	nJets OR DL1r 60	nJets OR DL1r 70
nJets OR DL1r 85	topRecoScore	

Table 43: Input features used to distinguish signal and background events in the 2ISS channel.

1544

While for each of the 31 BDTs, the features listed below are used for training:

$M(\text{lep}, E_T^{\text{miss}})$	$M(l_0 l_1)$	$M(l_0 l_1 l_2)$
$M(l_0 l_2)$	$M(l_1 l_2)$	$\text{binHiggs } p_T \text{ 3lF}$
$\text{binHiggs } p_T \text{ 3lS}$	$\Delta R(l_0)(l_1)$	$\Delta R(l_0)(l_2)$
$\Delta R(l_1)(l_2)$	decayScore	higgsRecoScore3lF
higgsRecoScore3lS	$\text{jet } \eta \text{ 0}$	$\text{jet } \eta \text{ 1}$
$\text{jet } \phi \text{ 0}$	$\text{jet } \phi \text{ 1}$	$\text{jet } p_T \text{ 0}$
$\text{jet } p_T \text{ 1}$	$\text{Lepton } \eta \text{ 0}$	$\text{Lepton } \eta \text{ 1}$
$\text{Lepton } \eta \text{ 2}$	$\text{Lepton } \phi \text{ 0}$	$\text{Lepton } \phi \text{ 1}$
$\text{Lepton } \phi \text{ 2}$	$\text{Lepton } p_T \text{ 0}$	$\text{Lepton } p_T \text{ 1}$
$\text{Lepton } p_T \text{ 2}$	E_T^{miss}	$\min \Delta R(l_0)(\text{jet})$
$\min \Delta R(l_1)(\text{jet})$	$\min \Delta R(l_2)(\text{jet})$	$\min \Delta R(\text{Lepton})(\text{bjet})$
$mjj\text{Max frwdJet}$	$n\text{Jets}$	$n\text{Jets OR DL1r 60}$
$n\text{Jets OR DL1r 70}$	$n\text{Jets OR DL1r 85}$	topScore

Table 44: Input features used to distinguish signal and background events in the 3l channel.

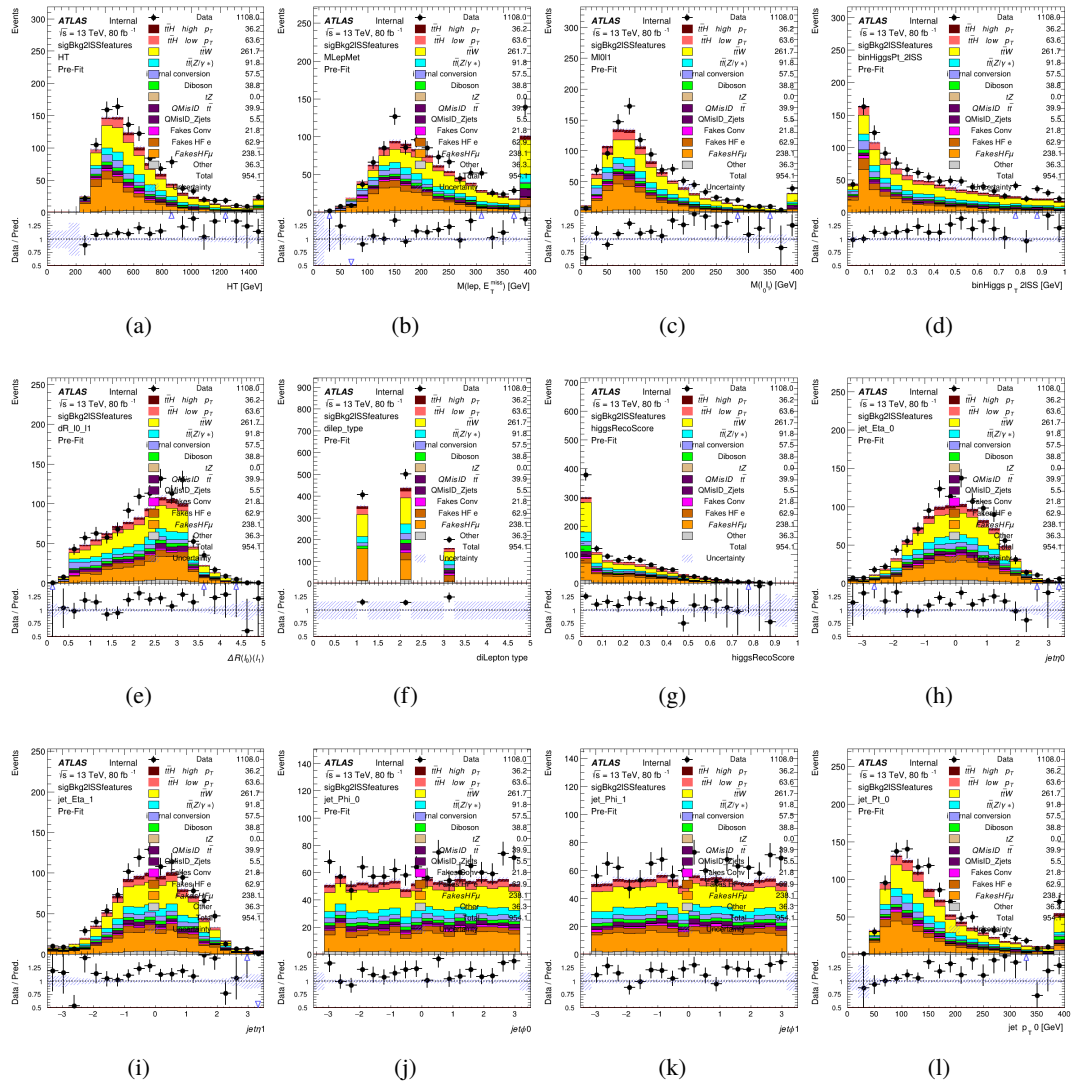


Figure 19.3:

1545 The BDTs are produced with a maximum tree depth of 6, using AUC as the target loss
 1546 function.

1547 Output distributions of each MVA comparing MC prediction to data at 80 fb^{-1} are shown
 1548 in figures 19.7-19.2.

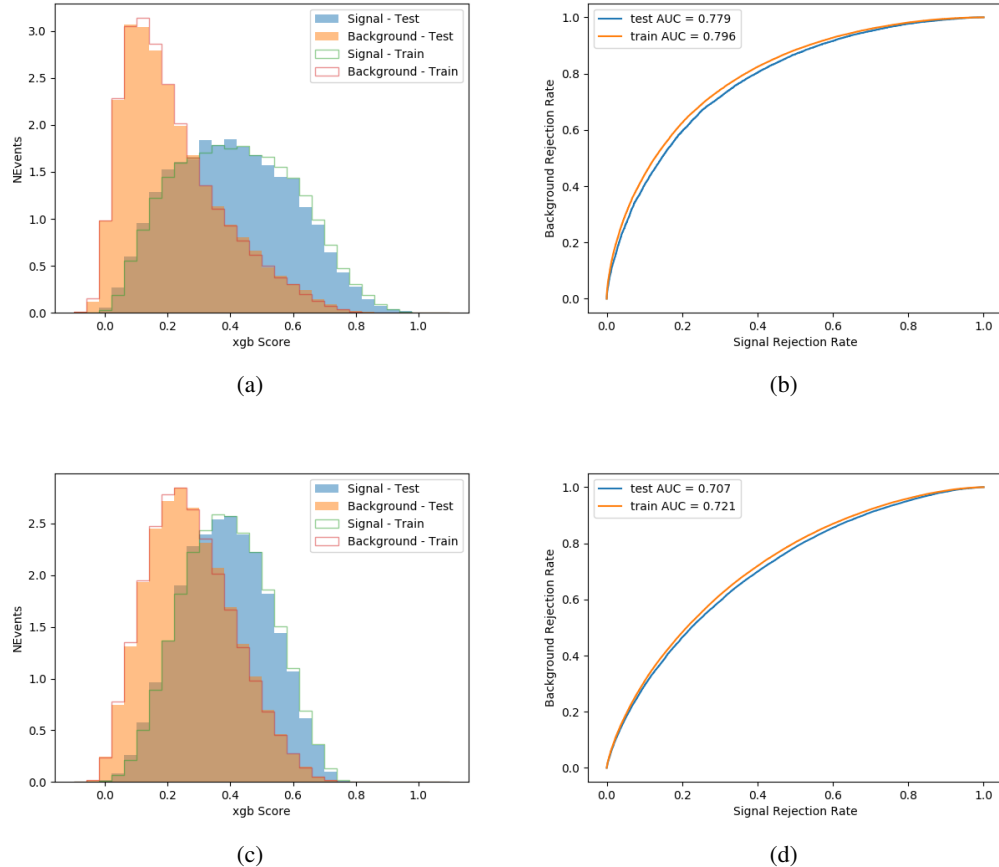


Figure 19.4:

1549 **19.3 Signal Region Definitions**

1550 Once pre-selection has been applied, channels are further refined based on the MVAs described
1551 above. The output of the model described in section 18.5 is used to separate the three channel
1552 into two - Semi-leptonic and Fully-leptonic - based on the predicted decay mode of the Higgs
1553 boson. This leaves three orthogonal signal regions - 2lSS, 3lS, and 3lF.

1554 For each event, depending on the number of leptons as well as whether the p_T of the Higgs

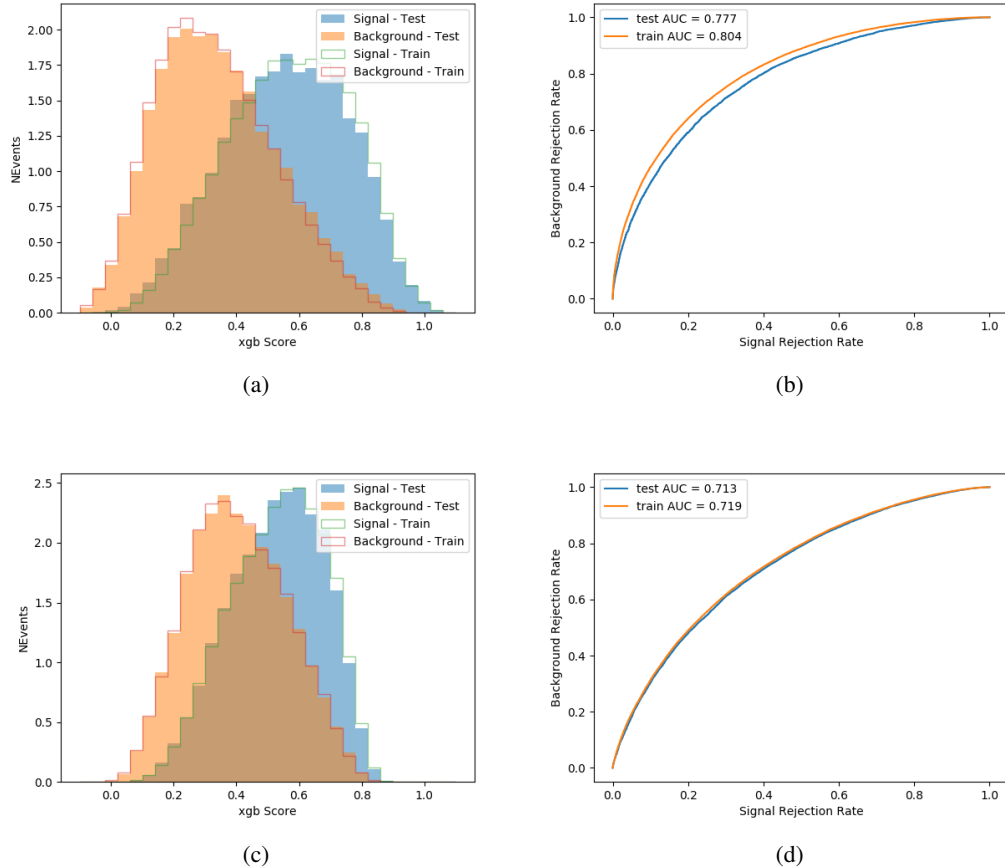


Figure 19.5:

1555 is predicted to be high (> 150 GeV) or low (< 150 GeV), a cut on the appropriate background
 1556 rejection MVA is applied. The particular cut values, listed in table 45, are determined by
 1557 maximizing S/\sqrt{B} in each region.

1558 The event preselection and MVA selection define the three signal regions. These signal
 1559 region definitions are summarized in table 46.

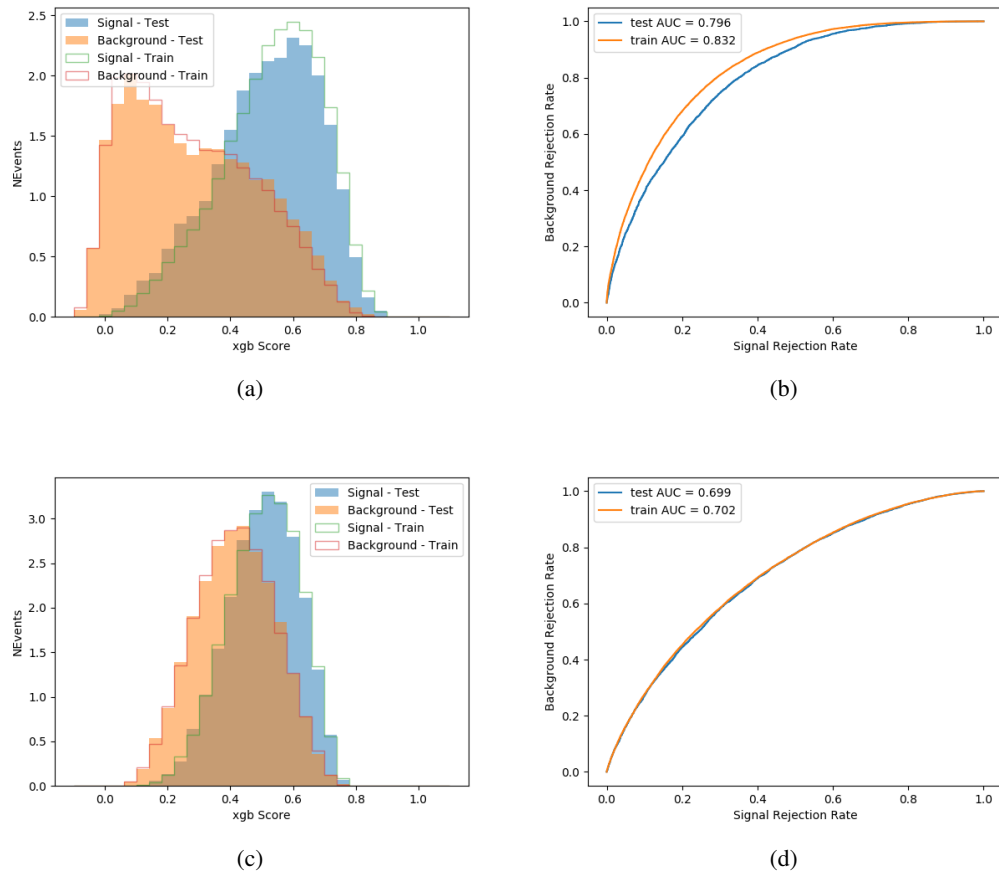
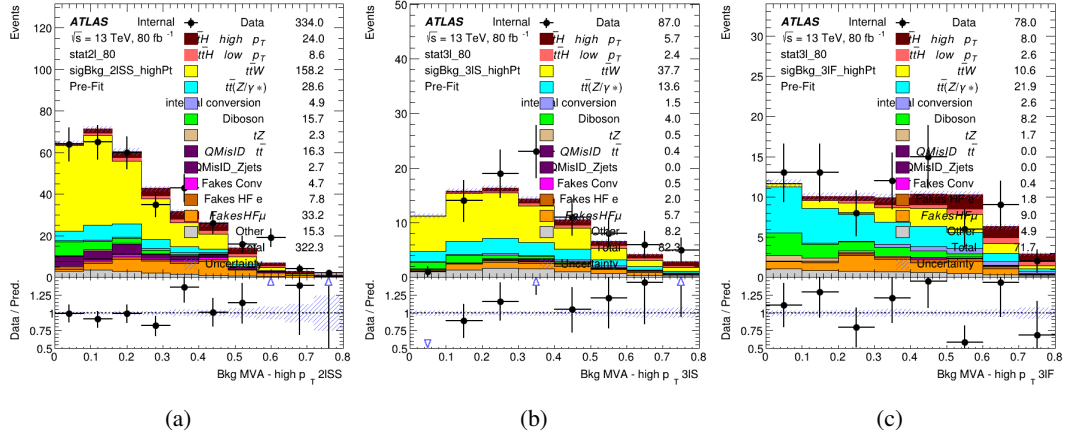
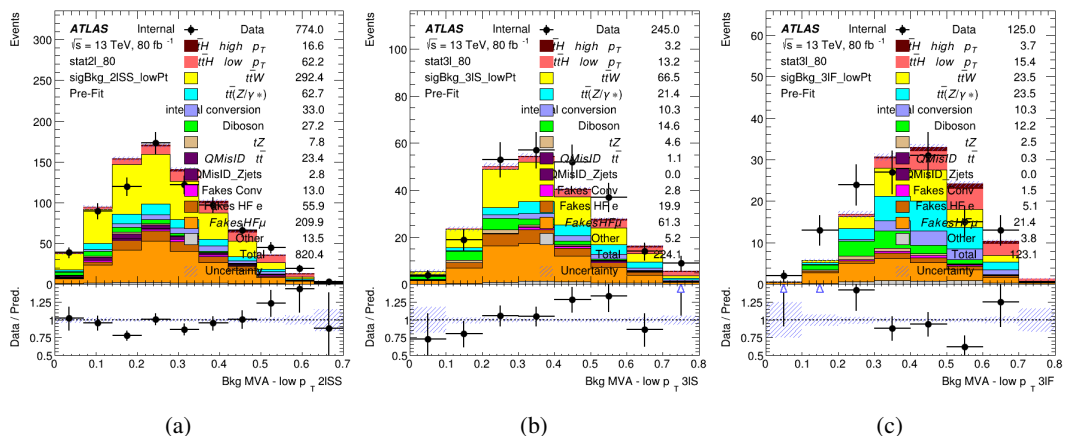


Figure 19.6:

Channel	BDT Score
2lSS high p_T	0.36
2lSS low p_T	0.34
3lS high p_T	0.51
3lS low p_T	0.43
3lF high p_T	0.33
3lF low p_T	0.41

Table 45: Cutoff values on background rejection MVA score applied to signal regions.

Figure 19.7: Output score of the high p_T BDTs in the (a) 2ISS, (b) 3IS, and (c) 3IF channelsFigure 19.8: Output score of the low p_T BDTs in the (a) 2ISS, (b) 3IS, and (c) 3IF channels

Region	Selection
2ISS	Two same charge tight leptons with $p_T > 20 \text{ GeV}$ $N_{\text{jets}} \geq 4, N_{\text{b-jets}} \geq 1$ b-tagged jets Zero τ_{had} $H_{p_T}^{\text{pred}} > 150 \text{ GeV}$ and BDT score > 0.36 or $H_{p_T}^{\text{pred}} < 150 \text{ GeV}$ and BDT score > 0.34
3IS	Three light leptons with total charge ± 1 Two tight SS leptons, $p_T > 20 \text{ GeV}$ One loose OS lepton, $p_T > 10 \text{ GeV}$ $N_{\text{jets}} \geq 2, N_{\text{b-jets}} \geq 1$ b-tagged jets Zero τ_{had} $ M(l^+l^-) - 91.2 \text{ GeV} > 10 \text{ GeV}$ for all OSSF lepton pairs Decay NN Score < 0.23 $H_{p_T}^{\text{pred}} > 150 \text{ GeV}$ and BDT score > 0.51 or $H_{p_T}^{\text{pred}} > 150 \text{ GeV}$ and BDT score > 0.43
3IF	Three light leptons with total charge ± 1 Two tight SS leptons, $p_T > 20 \text{ GeV}$ One loose OS lepton, $p_T > 10 \text{ GeV}$ $N_{\text{jets}} \geq 2, N_{\text{b-jets}} \geq 1$ b-tagged jets Zero τ_{had} $ M(l^+l^-) - 91.2 \text{ GeV} > 10 \text{ GeV}$ for all OSSF lepton pairs Decay NN Score > 0.23 $H_{p_T}^{\text{pred}} > 150 \text{ GeV}$ and BDT score > 0.33 or $H_{p_T}^{\text{pred}} > 150 \text{ GeV}$ and BDT score > 0.41

Table 46: Selection applied to define the three signal regions used in the fit.

20 Background Rejection MVA

- ¹⁵⁶⁰ Events are divided into two channels based on the number of leptons in the final state: one with
- ¹⁵⁶² two same-sign leptons, the other with three leptons. The 3l channel includes events where both
- ¹⁵⁶³ leptons originated from the Higgs boson as well as events where only one of the leptons

1564 20.1 Pre-MVA Event Selection

1565 A preselection is applied to define orthogonal analysis channels based on the number of leptons
 1566 in each event. For the 2lSS channel, the following preselection is used:

- 1567 • Two very tight, same-charge, light leptons with $p_T > 20$ GeV

- 1568 • ≥ 4 reconstructed jets, ≥ 1 b-tagged jets

- 1569 • No reconstructed tau candidates

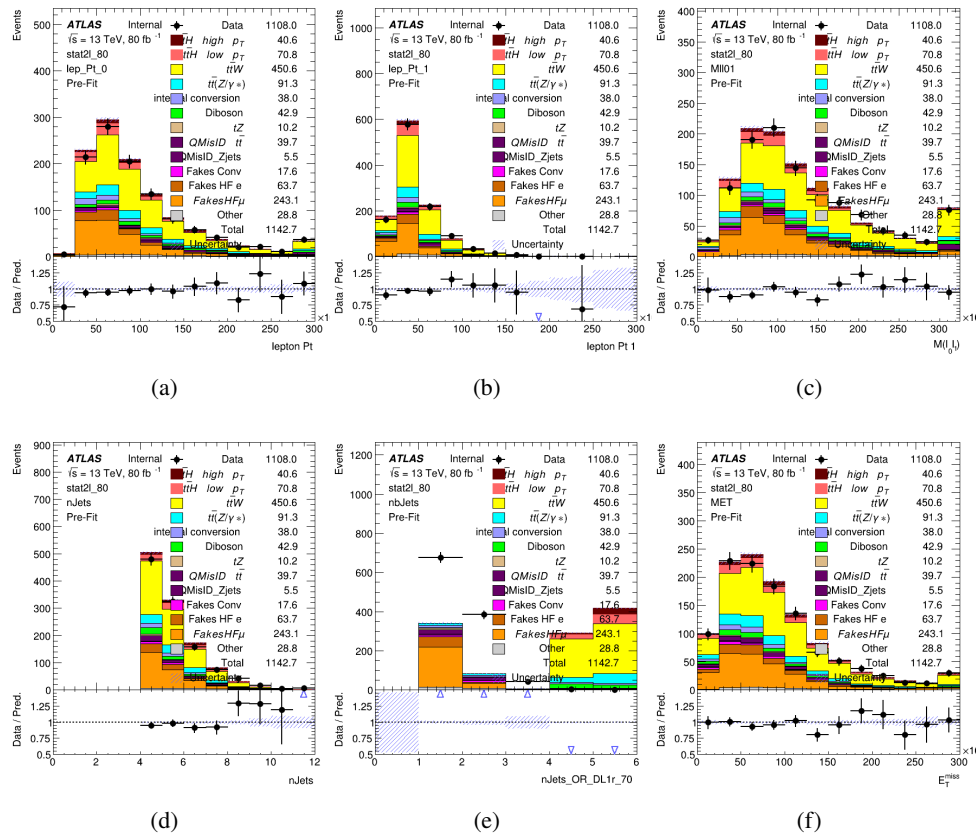


Figure 20.1:

1570 For the 3l channel, the following selection is applied:

- 1571 • Three light leptons with total charge ± 1
- 1572 • Same charge leptons are required to be very tight, with $p_T > 20 \text{ GeV}$
- 1573 • Opposite charge lepton must be loose, with $p_T > 10 \text{ GeV}$
- 1574 • $>= 2$ reconstructed jets, $>= 1$ b-tagged jets
- 1575 • No reconstructed tau candidates
- 1576 • $|M(l^+l^-) - 91.2 \text{ GeV}| > 10 \text{ GeV}$ for all opposite-charge, same-flavor lepton pairs

1577 **20.2 Event MVA**

1578 Separate multi-variate analysis techniques (MVAs) are used in order to distinguish signal events
1579 from background for each analysis channel - 2lSS, 3l semi-leptonic (3lS), and 3l fully leptonic
1580 (3lF). In particular, Boosted Decision Tree (BDT) algorithms are produced with XGBoost
1581 [**xgboost**] are trained using the kinematics of signal and background events derived from Monte
1582 Carlo simulations. Events are weighted in the BDT training by the weight of each Monte Carlo
1583 event.

1584 Because the background composition differs for events with a high reconstructed Higgs p_T
1585 compared to events with low reconstructed Higgs p_T , separate MVAs are produced for high and

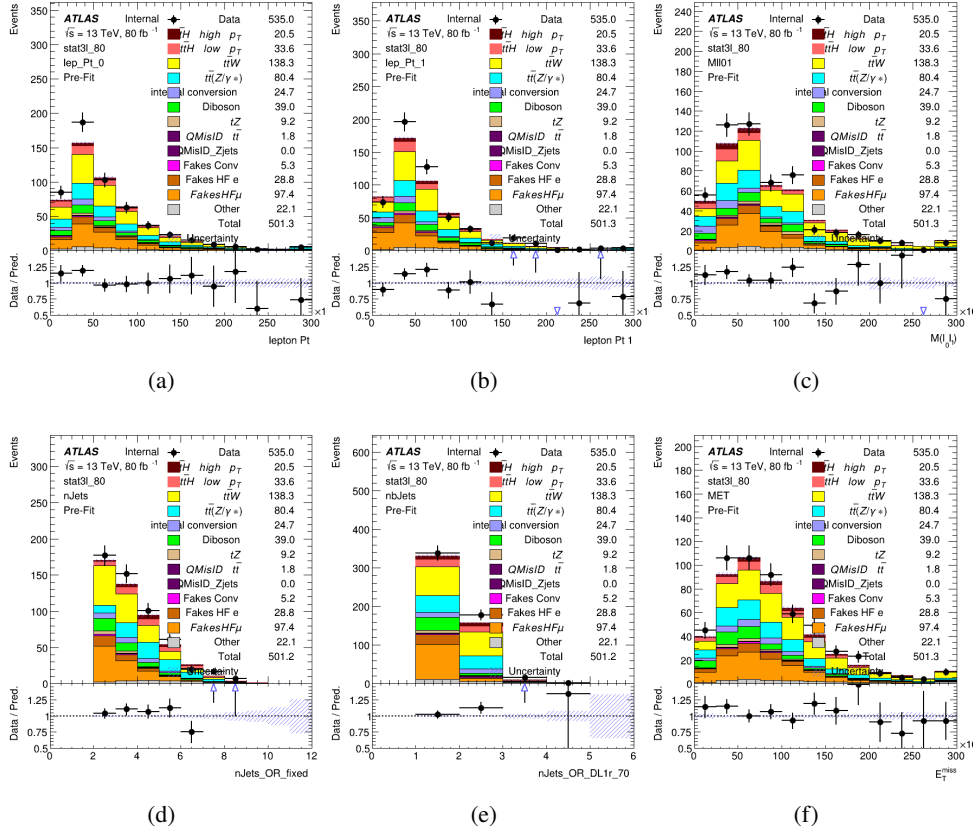


Figure 20.2:

1586 low p_T regions. This is found to provide better significance than attempting to build an inclusive
 1587 model, as demonstrated in appendix A.2. A cutoff of 150 GeV is used. This gives a total of 6
 1588 background rejection MVAs - explicitly, 2lSS high p_T , 2lSS low p_T , 3lS high p_T , 3lS low p_T ,
 1589 3lF high p_T , and 3lF low p_T .

1590 The following features are used in both the high and low p_T 2lSS BDTs:

HT	$M(\text{lep}, E_T^{\text{miss}})$	$M(l_0 l_1)$
binHiggs p_T 2ISS	$\Delta R(l_0)(l_1)$	diLepton type
higgsRecoScore	jet η 0	jet η 1
jet ϕ 0	jet ϕ 1	jet p_T 0
jet p_T 1	Lepton η 0	Lepton η 1
Lepton ϕ 0	Lepton ϕ 1	Lepton p_T 0
Lepton p_T 1	E_T^{miss}	$\min \Delta R(l_0)(\text{jet})$
$\min \Delta R(l_1)(\text{jet})$	$\min \Delta R(\text{Lepton})(\text{bjet})$	mjjMax frwdJet
nJets	nJets OR DL1r 60	nJets OR DL1r 70
nJets OR DL1r 85	topRecoScore	

Table 47: Input features used to distinguish signal and background events in the 2ISS channel.

1591

While for each of the 31 BDTs, the features listed below are used for training:

$M(\text{lep}, E_T^{\text{miss}})$	$M(l_0 l_1)$	$M(l_0 l_1 l_2)$
$M(l_0 l_2)$	$M(l_1 l_2)$	$\text{binHiggs } p_T \text{ 3lF}$
$\text{binHiggs } p_T \text{ 3lS}$	$\Delta R(l_0)(l_1)$	$\Delta R(l_0)(l_2)$
$\Delta R(l_1)(l_2)$	decayScore	higgsRecoScore3lF
higgsRecoScore3lS	$\text{jet } \eta \text{ 0}$	$\text{jet } \eta \text{ 1}$
$\text{jet } \phi \text{ 0}$	$\text{jet } \phi \text{ 1}$	$\text{jet } p_T \text{ 0}$
$\text{jet } p_T \text{ 1}$	$\text{Lepton } \eta \text{ 0}$	$\text{Lepton } \eta \text{ 1}$
$\text{Lepton } \eta \text{ 2}$	$\text{Lepton } \phi \text{ 0}$	$\text{Lepton } \phi \text{ 1}$
$\text{Lepton } \phi \text{ 2}$	$\text{Lepton } p_T \text{ 0}$	$\text{Lepton } p_T \text{ 1}$
$\text{Lepton } p_T \text{ 2}$	E_T^{miss}	$\min \Delta R(l_0)(\text{jet})$
$\min \Delta R(l_1)(\text{jet})$	$\min \Delta R(l_2)(\text{jet})$	$\min \Delta R(\text{Lepton})(\text{bjet})$
$mjj\text{Max frwdJet}$	$n\text{Jets}$	$n\text{Jets OR DL1r 60}$
$n\text{Jets OR DL1r 70}$	$n\text{Jets OR DL1r 85}$	topScore

Table 48: Input features used to distinguish signal and background events in the 3l channel.

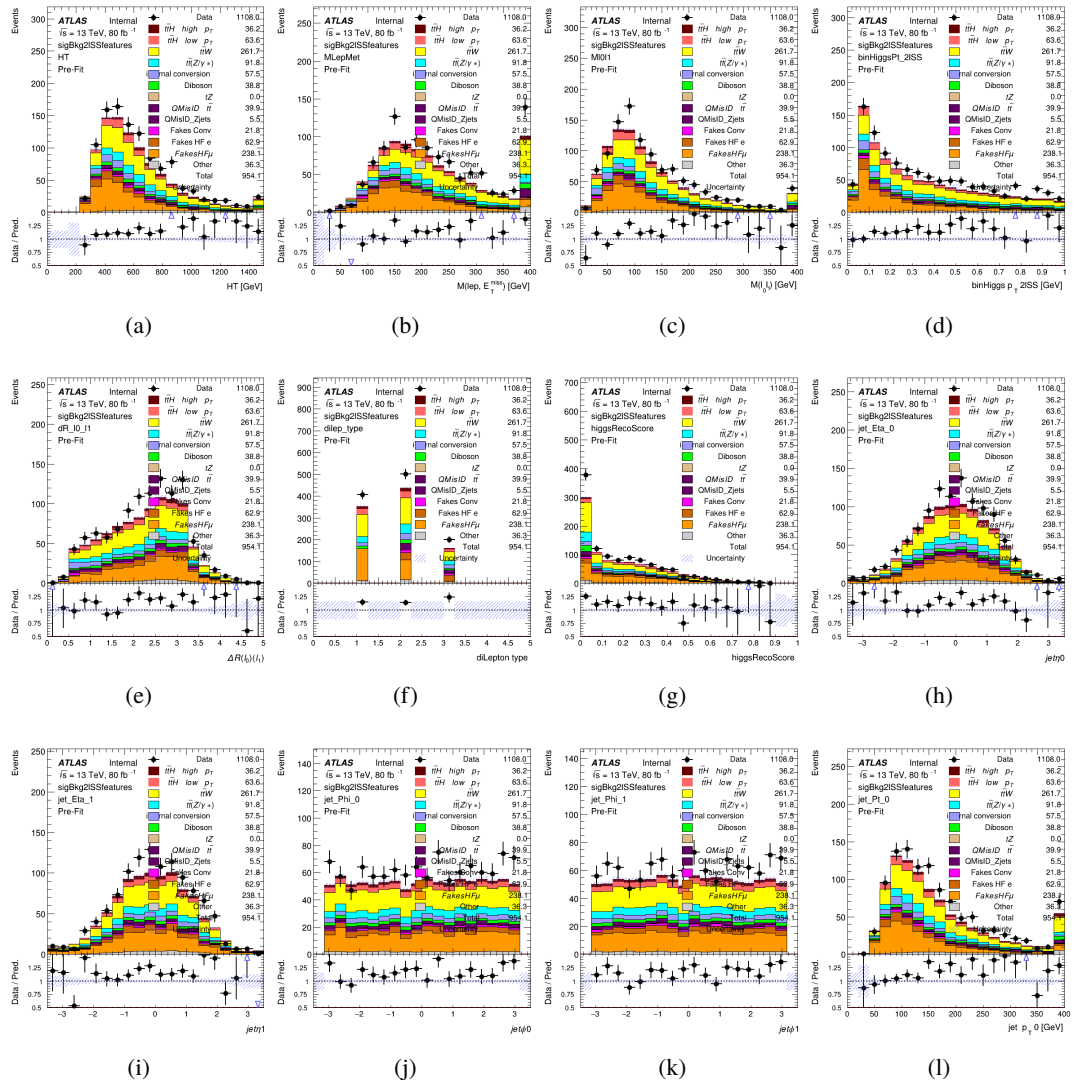


Figure 20.3:

1592 The BDTs are produced with a maximum tree depth of 6, using AUC as the target loss
1593 function.

1594 Output distributions of each MVA comparing MC prediction to data at 80 fb^{-1} are shown
1595 in figure 20.2.

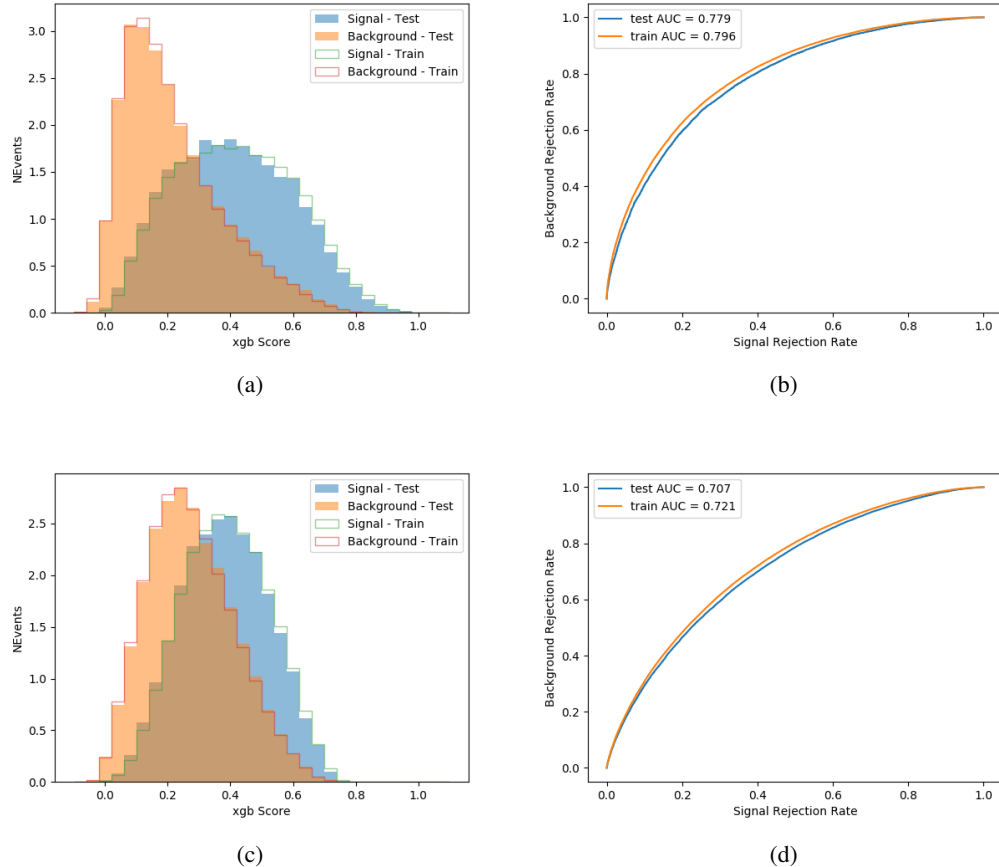


Figure 20.4:

1596 **20.3 Signal Region Definitions**

1597 Once pre-selection has been applied, channels are further refined based on the MVAs described
 1598 above. The output of the model described in section 18.5 is used to separate the three channel
 1599 into two - Semi-leptonic and Fully-leptonic - based on the predicted decay mode of the Higgs
 1600 boson.

1601 For each event, depending on the channel as well as the predicted p_T of the Higgs derived

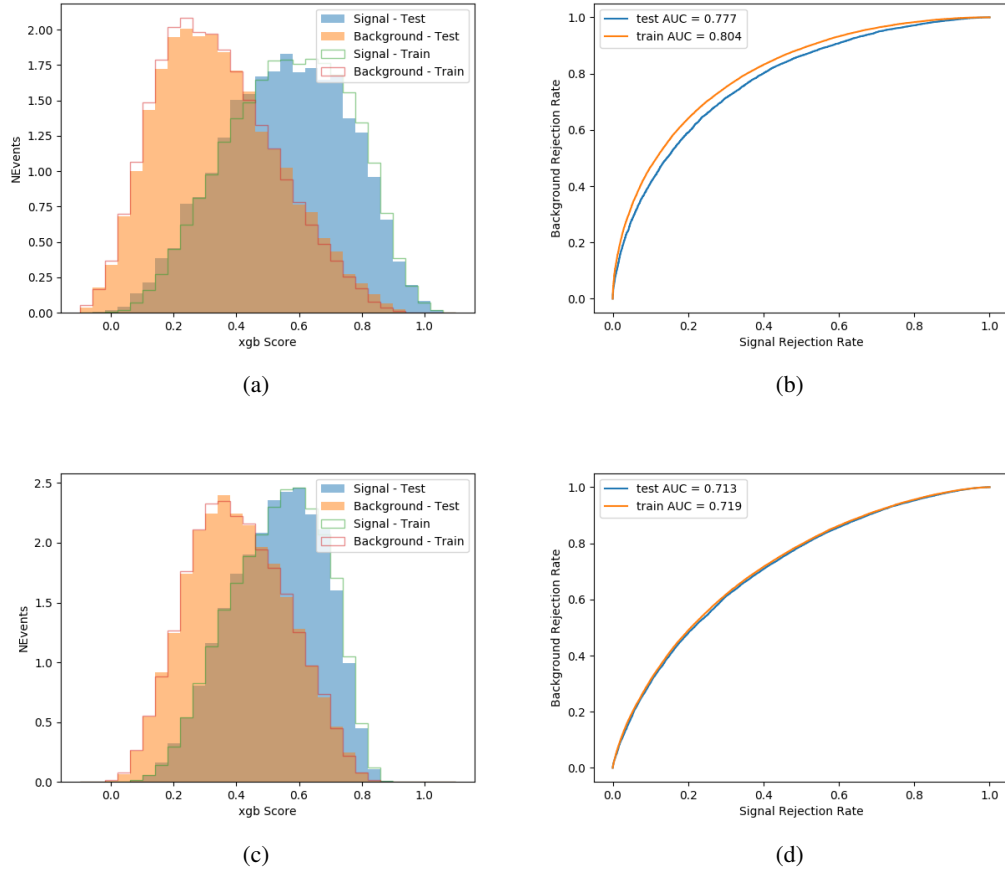


Figure 20.5:

from the algorithm described in section 18.4, a cut on the appropriate background rejection
 1602 algorithm is applied. The specific selection used, and the event yield in each channel after this
 1603 selection has been applied, is summarized below.
 1604

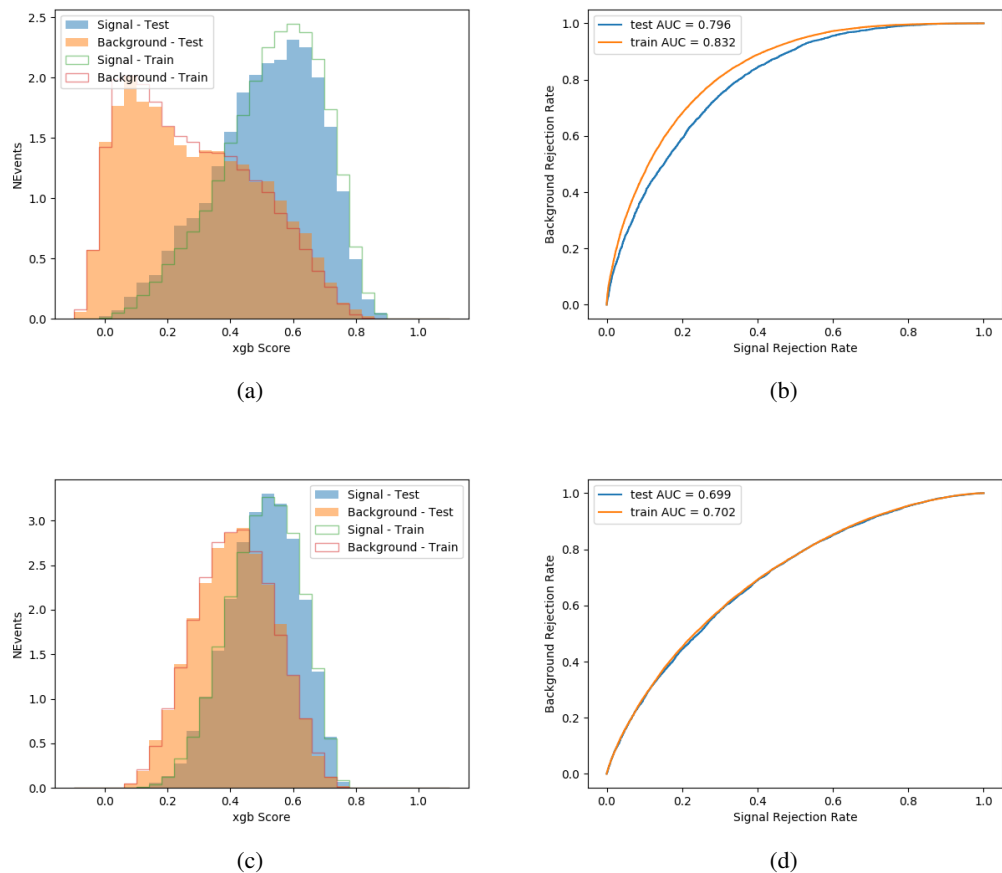


Figure 20.6:

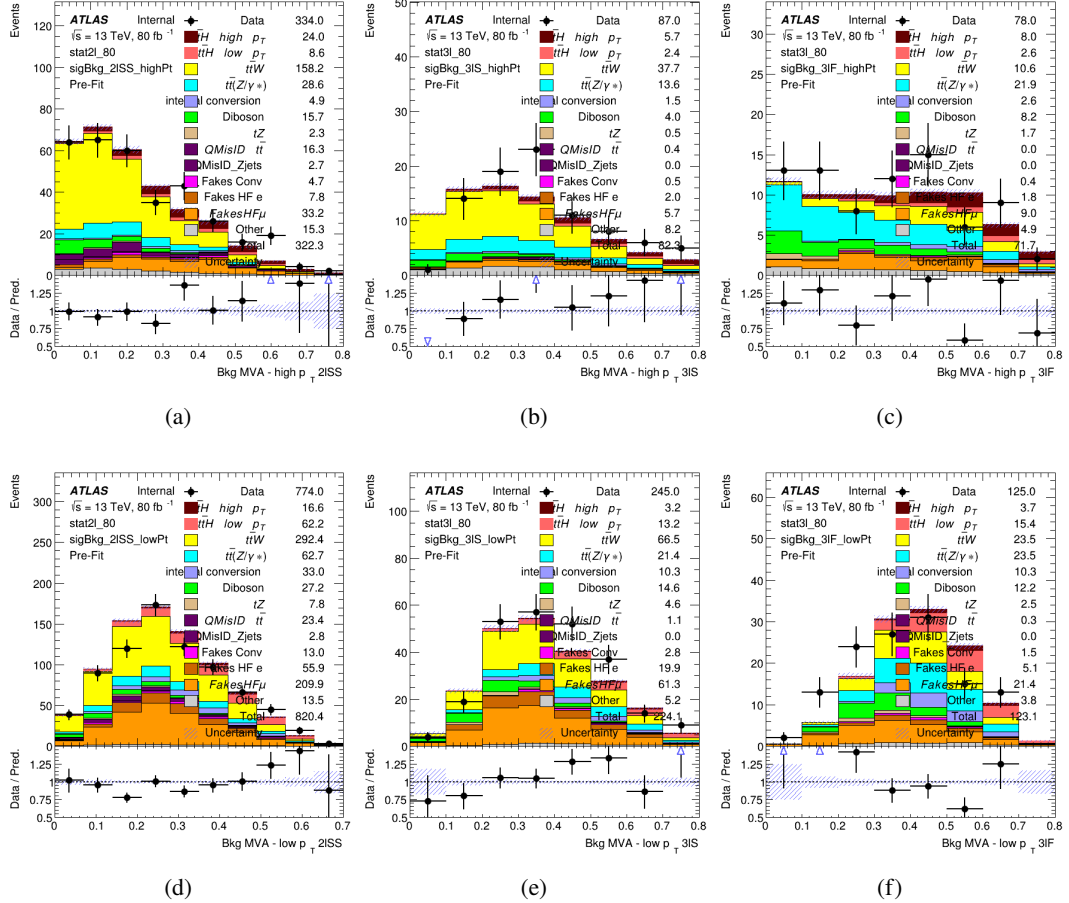


Figure 20.7: scores

1605 **20.3.1 2ISS**1606 **20.3.2 3l – Semi – leptonic**1607 **20.3.3 3l – Fully – leptonic**1608 **21 Systematic Uncertainties**

1609 The systematic uncertainties that are considered are summarized in table 49. These are implemented in the fit either as a normalization factors or as a shape variation or both in the signal
 1610 25th March 2021 – 22:11

¹⁶¹¹ and background estimations. The numerical impact of each of these uncertainties is outlined in
¹⁶¹² section 22.

Table 49: Sources of systematic uncertainty considered in the analysis. Some of the systematic uncertainties are split into several components, as indicated by the number in the rightmost column.

Systematic uncertainty	Components
Luminosity	1
Pileup reweighting	1
Physics Objects	
Electron	6
Muon	15
Jet energy scale and resolution	28
Jet vertex fraction	1
Jet flavor tagging	131
E_T^{miss}	3
Total (Experimental)	186
Background Modeling	
Cross section	24
Renormalization and factorization scales	10
Parton shower and hadronization model	2
Shower tune	4
Total (Signal and background modeling)	40
Background Modeling	
Cross section	24
Renormalization and factorization scales	10
Parton shower and hadronization model	2
Shower tune	4
Total (Signal and background modeling)	40
Total (Overall)	226

¹⁶¹³ The uncertainty in the combined 2015+2016 integrated luminosity is derived from a
¹⁶¹⁴ calibration of the luminosity scale using x-y beam-separation scans performed in August 2015
¹⁶¹⁵ and May 2016 [**lumi**].

¹⁶¹⁶ The experimental uncertainties are related to the reconstruction and identification of light
¹⁶¹⁷ leptons and b-tagging of jets, and to the reconstruction of E_T^{miss} . The sources which contribute

1618 to the uncertainty in the jet energy scale [**jes**] are decomposed into uncorrelated components and
1619 treated as independent sources in the analysis.

1620 The uncertainties in the b-tagging efficiencies measured in dedicated calibration analyses
1621 [**btag_cal**] are also decomposed into uncorrelated components. The large number of components
1622 for b-tagging is due to the calibration of the distribution of the BDT discriminant.

1623 The systematic uncertainties associated with the signal and background processes are
1624 accounted for by varying the cross-section of each process within its uncertainty.

1625 22 Results

1626 Unblinded results are shown for the 80 fb^{-1} data set, as well as MC only projections of results
1627 using the full Run-2, 140 fb^{-1} dataset.

1628 22.1 Results - 80 fb^{-1}

1629 A maximum likelihood fit is performed simultaneously over the reconstructed Higgs p_T spectrum
1630 in the three signal regions, 2lSS, 3lS, and 3lF, shown in figure 22.1. The $t\bar{t}H$ MC is split into
1631 high and low p_T , based on whether the truth p_T of the Higgs is above or below 150 GeV. The
1632 parameters $\mu_{t\bar{t}H\text{high}p_T}$ and $\mu_{t\bar{t}H\text{low}p_T}$, where $\mu = \sigma_{\text{observed}}/\sigma_{\text{SM}}$, are extracted from the fit.

1633 As the data collected from 2015-2017 has been unblinded for $t\bar{t}H$ – ML channels, rep-
 1634 resenting 80 fb^{-1} , those events are unblinded.

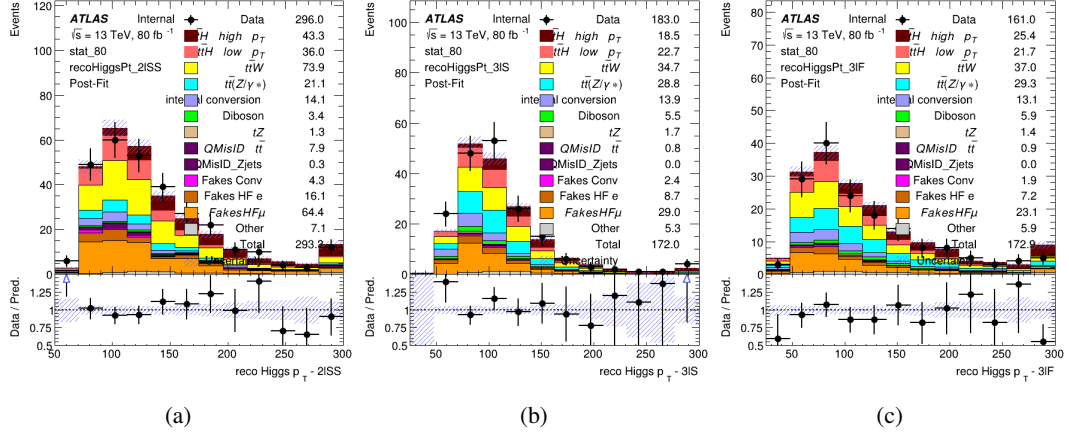


Figure 22.1: Post-fit distributions of the reconstructed Higgs p_T in the three signal regions, (a) 2lSS, (b) 3lS, and (c) 3lF, for 80 fb^{-1} of MC

1635 A post-fit summary of the fitted regions is shown in figure 22.2.

1636 The μ values for high and low p_T Higgs are shown in 50.

$$\begin{aligned}\mu_{t\bar{t}H \text{ high } p_T} &= 1.0^{+0.0}_{-0.0} (\text{stat})^{+0.0}_{-0.0} (\text{sys}) \\ \mu_{t\bar{t}H \text{ low } p_T} &= 1.0^{+0.0}_{-0.0} (\text{stat})^{+0.0}_{-0.0} (\text{sys})\end{aligned}$$

Table 50: Best fit μ values for $t\bar{t}H$ high p_T and $t\bar{t}H$ low p_T , where $\mu = \sigma_{\text{obs}}/\sigma_{\text{pred}}$

1637 **Need to add something about systematics here**

1638 The background composition of each of the fit regions is shown in figure 22.3.

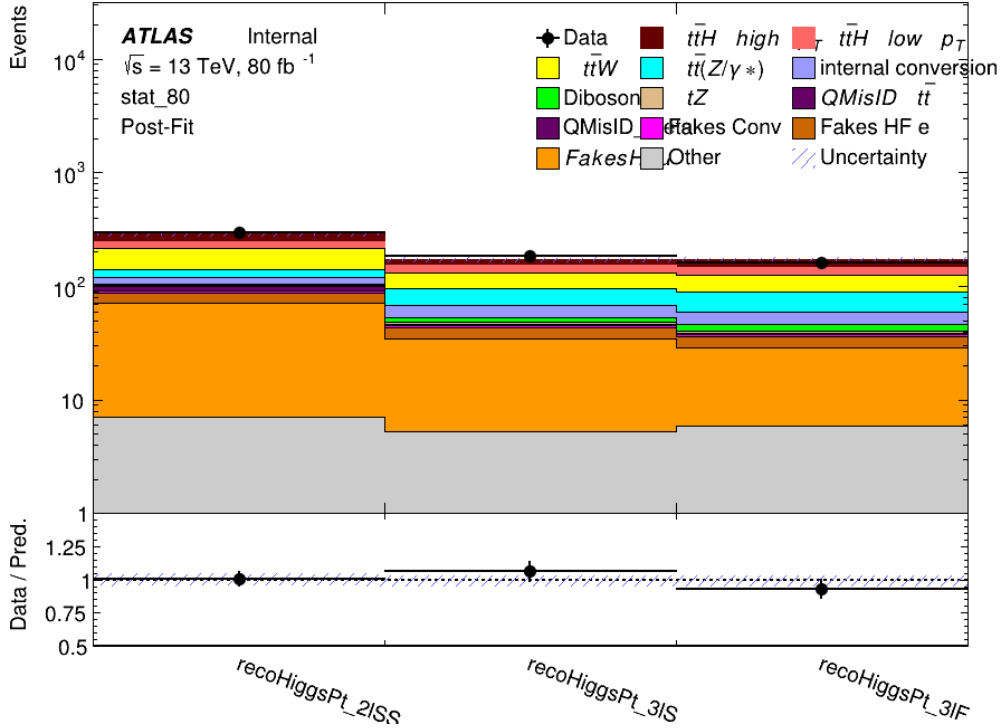


Figure 22.2: Post-fit summary of the yields in each signal region.

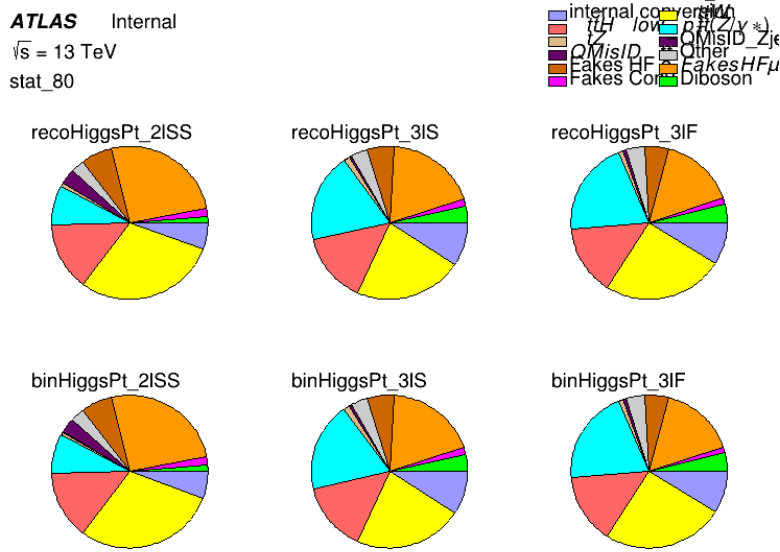


Figure 22.3: Background composition of the fit regions.

1639 22.2 Projected Results - 140 fb^{-1}

1640 As data collected in 2018 has not yet been unblinded for $t\bar{t}H - \text{ML}$ at the time of this note, data
 1641 from that year remains blinded. Instead, an Asimov fit is performed - with the MC prediction
 1642 being used both as the SM prediction as well as the data in the fit - in order to give expected
 1643 results.

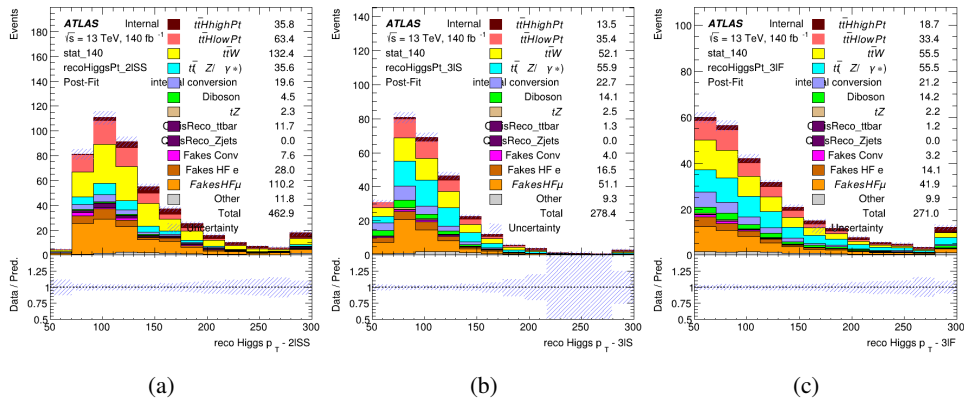


Figure 22.4: Blinded post-fit distributions of the reconstructed Higgs p_T in the three signal regions, (a) 2lSS, (b) 3lS, and (c) 3lF, for 140 fb^{-1} of data

1644 The μ values for high and low p_T Higgs are shown in 51.

$$\begin{aligned}\mu_{t\bar{t}H_{highp_T}} &= 1.0^{+0.0} (\text{stat})^{+0.0} (\text{sys}) \\ \mu_{t\bar{t}H_{lowp_T}} &= 1.0^{+0.0} (\text{stat})^{+0.0} (\text{sys})\end{aligned}$$

Table 51: Best fit μ values for $t\bar{t}H$ high p_T and $t\bar{t}H$ low p_T , where $\mu = \sigma_{\text{obs}} / \sigma_{\text{pred}}$

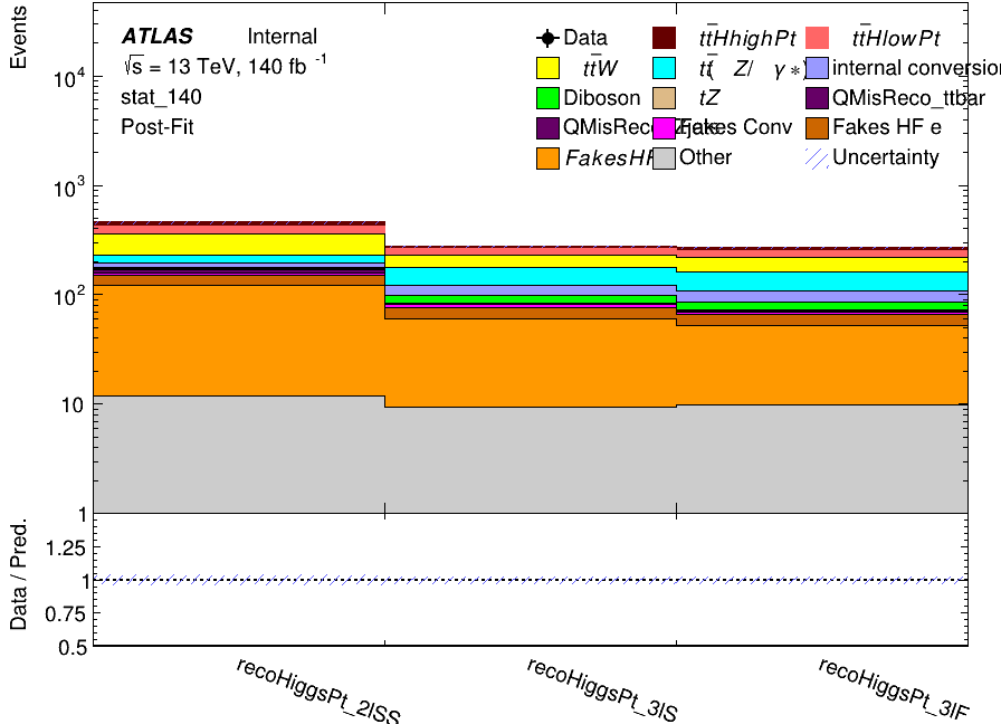


Figure 22.5: Post-fit summary of fit.

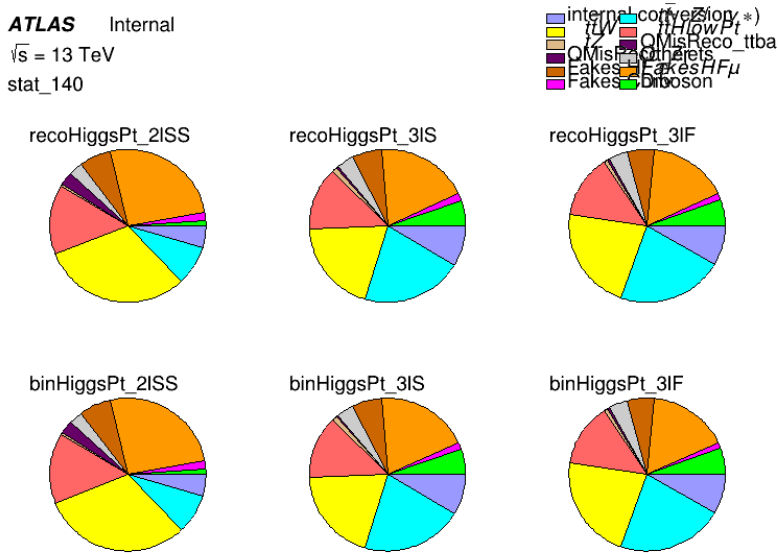


Figure 22.6: Background composition of the fit regions.

1645 Part VI**1646 Conclusion**

1647 As search for the effects of dimension-six operators on $t\bar{t}H$ production is performed. An effective
1648 field theory approached is used to parameterize the effects of high energy physics on the Higgs
1649 momentum spectrum. The momentum spectrum is reconstructed using various MVA techniques,
1650 and the limits on dimension-six operators are limited to X.

¹⁶⁵¹ **List of contributions**

¹⁶⁵²

1653 **Appendices**

1654 **.1 Non-prompt lepton MVA**

1655 A lepton MVA has been developed to better reject non-prompt leptons than stand-
1656 ard cut based selections based upon impact parameter, isolation and PID. The name of this
1657 MVA is `PromptLeptonIso`. The full set of studies and detailed explanation can be found in
1658 [`ttW_fullR2`].

1659 The decays of W and Z bosons are commonly selected by the identification of one or two
1660 electrons or muons. The negligible lifetimes of these bosons mean that the leptons produced in the
1661 decay originate from the interaction vertex and are thus labelled “prompt”. Analyses using these
1662 light leptons impose strict reconstruction quality, isolation and impact parameter requirements
1663 to remove “fake” leptons. A significant source of the fake light leptons are non-prompt leptons
1664 produced in decays of hadrons that contain bottom (b) or charm (c) quarks. Such hadrons
1665 typically have microscopically significant lifetimes that can be detected experimentally.

1666 These non-prompt leptons can also pass the tight selection criteria. In analyses that
1667 involve top (t) quarks, which decay almost exclusively into a W boson and a b quark, non-
1668 prompt leptons from the semileptonic decay of bottom and charm hadrons can be a significant
1669 source of background events. This is particularly the case in the selection of same-sign dilepton
1670 and multilepton final states.

1671 The main idea is to identify non-prompt light leptons using lifetime information associated
1672 with a track jet that matches the selected light lepton. This lifetime information is computed
1673 using tracks contained within the jet. Typically, lepton lifetime is determined using the impact
1674 parameter of the track reconstructed by the inner tracking detector which is matched to the recon-

1675 structured lepton. Using additional reconstructed charged particle tracks increases the precision of
 1676 identifying the displaced decay vertex of bottom or charm hadrons that produced a non-prompt
 1677 light lepton. The MVA also includes information related to the isolation of the lepton to reject
 1678 non-prompt leptons. `PromptLeptonIso` is a gradient boosted BDT. The training of the BDT
 1679 is performed on leptons selected from the PowHEG+PYTHIA6 non-allhad $t\bar{t}$ MC sample. Eight
 1680 variables are used to train the BDT in order to discriminate between prompt and non-prompt
 1681 leptons. The track jets that are matched to the non-prompt leptons correspond to jets initiated by
 1682 b or c quarks, and may contain a displaced vertex. Consequently, three of the selected variables
 1683 are used to identify b-tag jets by standard ATLAS flavour tagging algorithms. Two variables use
 1684 the relationship between the track jet and lepton: the ratio of the lepton p_T with respect to the
 1685 track jet p_T and ΔR between the lepton and the track jet axis. Finally three additional variables
 1686 test whether the reconstructed lepton is isolated: the number of tracks collected by the track jet
 1687 and the lepton track and calorimeter isolation variables. Table 52 describes the variables used
 1688 to train the BDT algorithm. The choice of input variables has been extensively discussed with
 1689 Egamma, Muon, Tracking, and Flavour Tagging CP groups.

Variable	Description
N_{track} in track jet	Number of tracks collected by the track jet
$\text{IP2 log}(P_b/P_{\text{light}})$	Log-likelihood ratio between the b and light jet hypotheses with the IP2D algorithm
$\text{IP3 log}(P_b/P_{\text{light}})$	Log-likelihood ratio between the b and light jet hypotheses with the IP3D algorithm
$N_{\text{TrkAtVtx}} \text{ SV} + \text{JF}$	Number of tracks used in the secondary vertex found by the SV1 algorithm in addition to the number of tracks from secondary vertices found by the JetFitter algorithm with at least two tracks
$p_T^{\text{lepton}}/p_T^{\text{track jet}}$	The ratio of the lepton p_T and the track jet p_T
$\Delta R(\text{lepton}, \text{track jet})$	ΔR between the lepton and the track jet axis
$p_T^{\text{VarCone30}}/p_T$	Lepton track isolation, with track collecting radius of $\Delta R < 0.3$
$E_T^{\text{TopoCone30}}/p_T$	Lepton calorimeter isolation, with topological cluster collecting radius of $\Delta R < 0.3$

Table 52: A table of the variables used in the training of `PromptLeptonIso`.

1690 The efficiency of the tight `PromptLeptonIso` working point is measured using the tag
1691 and probe method with $Z \rightarrow \ell^+ \ell^-$ events. Such calibration are performed by analysers from
1692 this analysis in communication with the Egamma and Muon combined performance groups. The
1693 scale factor are approximately 0.92 for $10 < p_T < 15$ GeV, and averaging at 0.98 to 0.99 for
1694 higher p_T leptons. An extra systematic is applied to muons within $\Delta R < 0.6$ of a calorimeter
1695 jet, since there is a strong dependence on the scale factor due to the presence of these jets. For
1696 electrons, the dominant systematics is coming from pile-up dependence. Overall the systematics
1697 are a maximum of 3% at low p_T and decreasing at a function of p_T .

1698 **.2 Non-prompt CR Modelling**

1699 In order to further validate the modeling in each of the non-prompt CRs, additional
 1700 kinematic plots are made in the Z+jets CR and $t\bar{t}$ CR in each of the continuous b-tag regions.

1701 In the case of the Z+jets CR, the p_T spectrum of the lepton originating from the W
 1702 candidate is shown, as this is the distribution used to extract the scale factor applied to Z+jets.
 1703 These plots are shown in Figures .7 and .8.

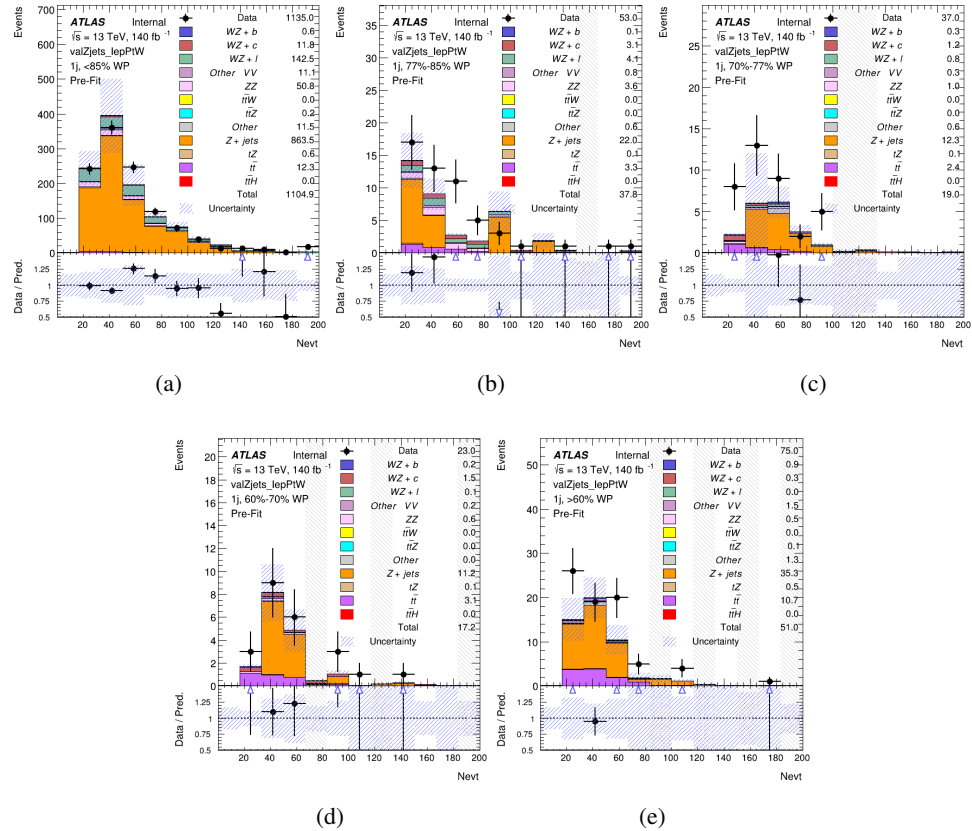


Figure .7: Comparisons between the data and MC distributions in the Z+jets CR for each of the 1-jet b-tag working point regions

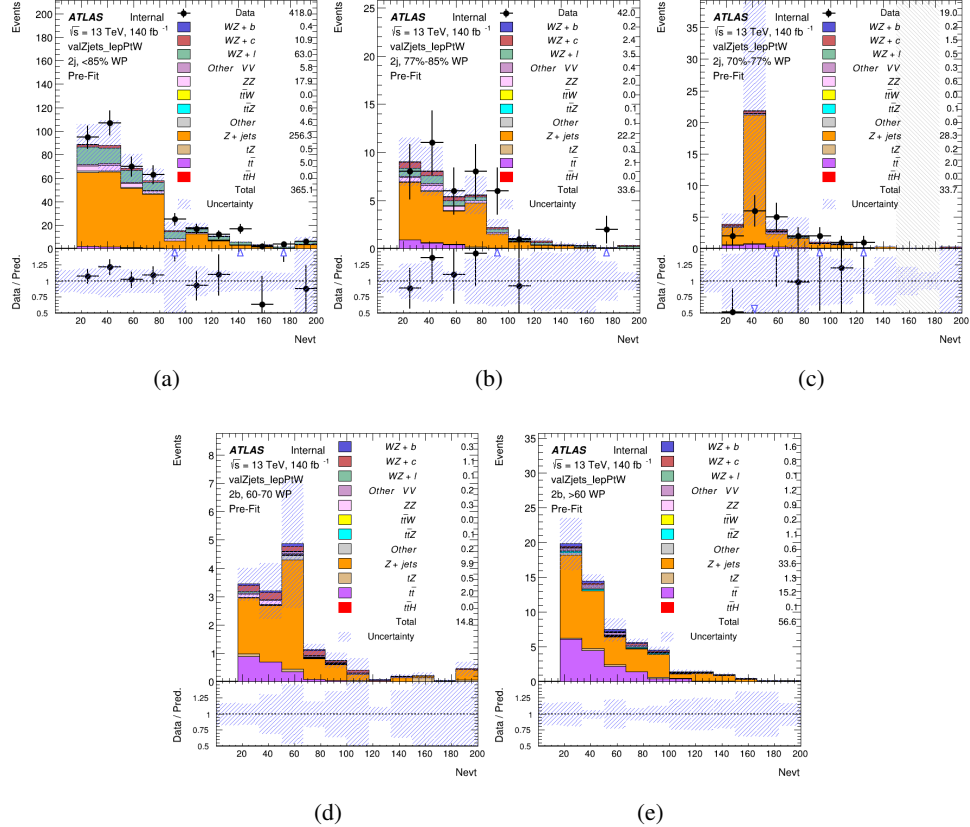


Figure .8: Comparisons between the data and MC distributions in the $Z+jets$ CR for each of the 2-jet b-tag working point regions

1704 The same is shown for the $t\bar{t}$ CR, but the p_T of the OS lepton is used instead as a
 1705 representation of the modeling, as the lepton from the W is not well defined for $t\bar{t}$ events. These
 1706 plots are shown in Figures .9 and .10.

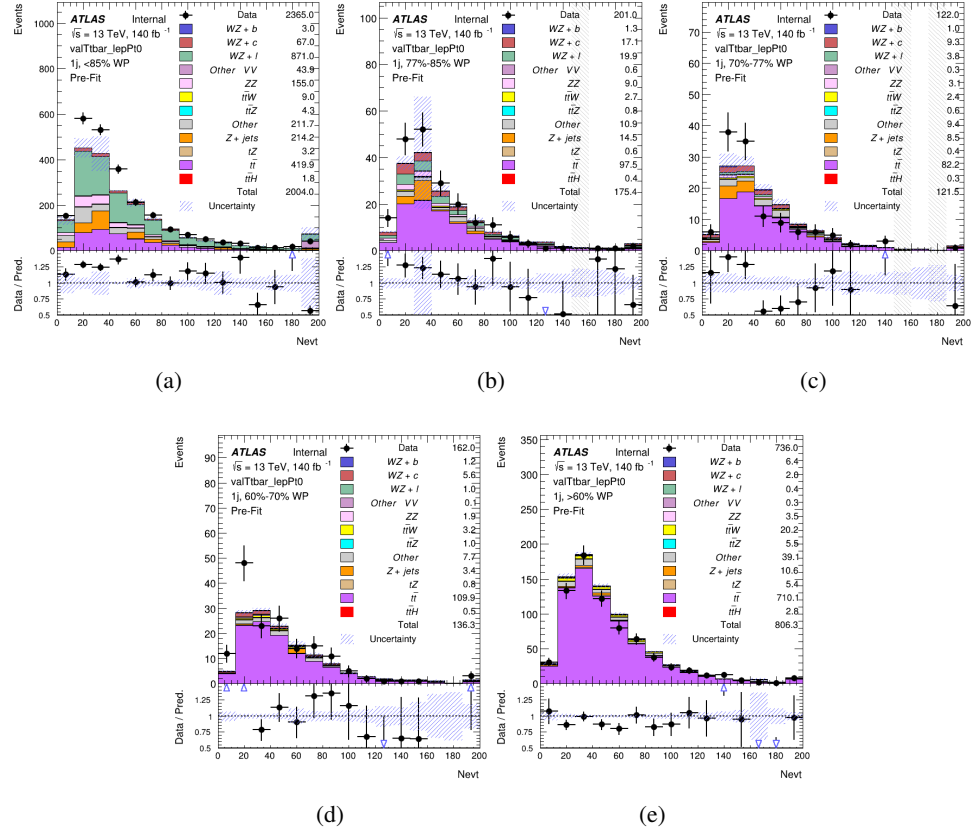


Figure .9: Comparisons between the data and MC distributions in the $t\bar{t}$ CR for each of the 1-jet b-tag working point regions

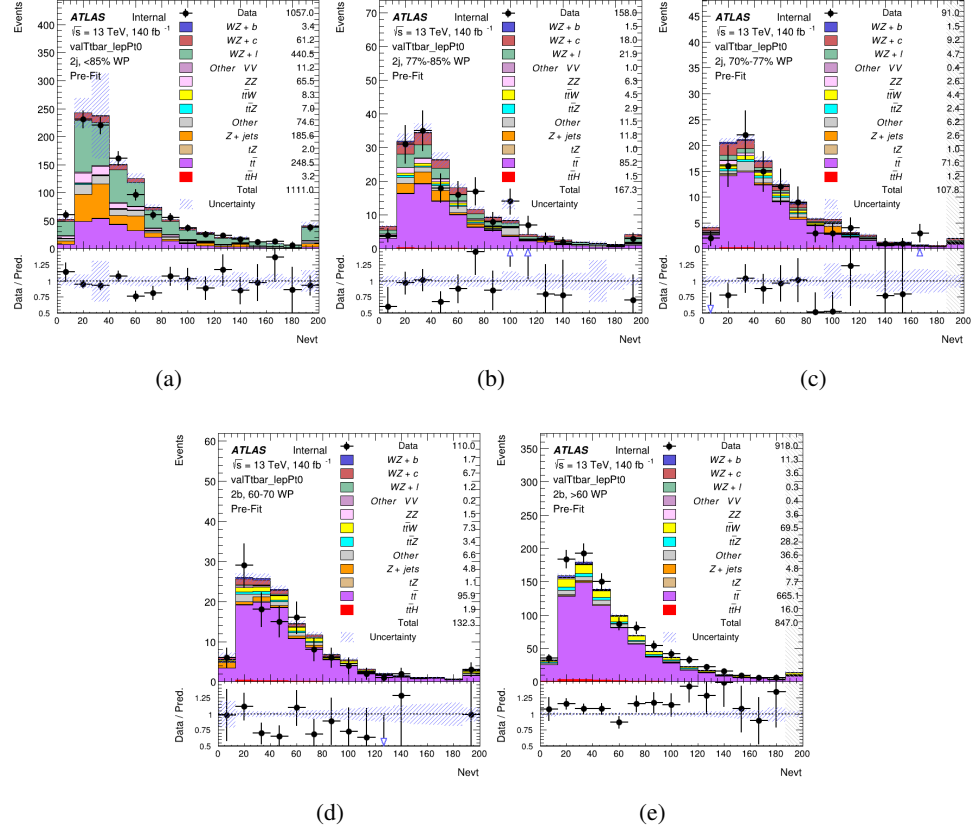


Figure 10: Comparisons between the data and MC distributions in the $t\bar{t}$ CR for each of the 2-jet b-tag working point regions

1707 **.3 tZ Interference Studies**

1708 Because it includes an on-shell Z boson as well as a b-jet and W from the top decay, tZ
1709 production represents an identical final state to WZ + b-jet. This implies the possibility of matrix
1710 level interference between these two processes not accounted for in the Monte Carlo simulations,
1711 which consider the two processes independently. Truth level studies are performed in order to
1712 estimate the impact of these interference effects.

1713 In order to estimate the matrix level interference effects between tZ and WZ + b-jet, two
1714 different sets of simulations are produced using MadGraph 5 [**Madgraph**] - one which simulates
1715 these two processes independently, and another where they are produced simultaneously, such
1716 that interference effects are present. These two sets of samples are then compared, and the
1717 difference between them can be taken to represent any interference effects.

1718 MadGraph simulations of 10,000 tZ and 10,000 WZ + b-jet events are produced, along
1719 with 20,000 events where both are present, in the fiducial region where three leptons and at least
1720 one jet are produced.

1721 A selection mimicking the preselection used in the main analysis is applied to the samples:
1722 The SS leptons are required to have $p_T > 20$ GeV, and > 10 GeV is required for the OS lepton.
1723 The associated b-jet is required to have $p_T > 25$ GeV, and all physics objects are required to fall
1724 in a range of $|\eta| < 2.5$.

1725 The kinematics of these samples after the selection has been applied are shown below:

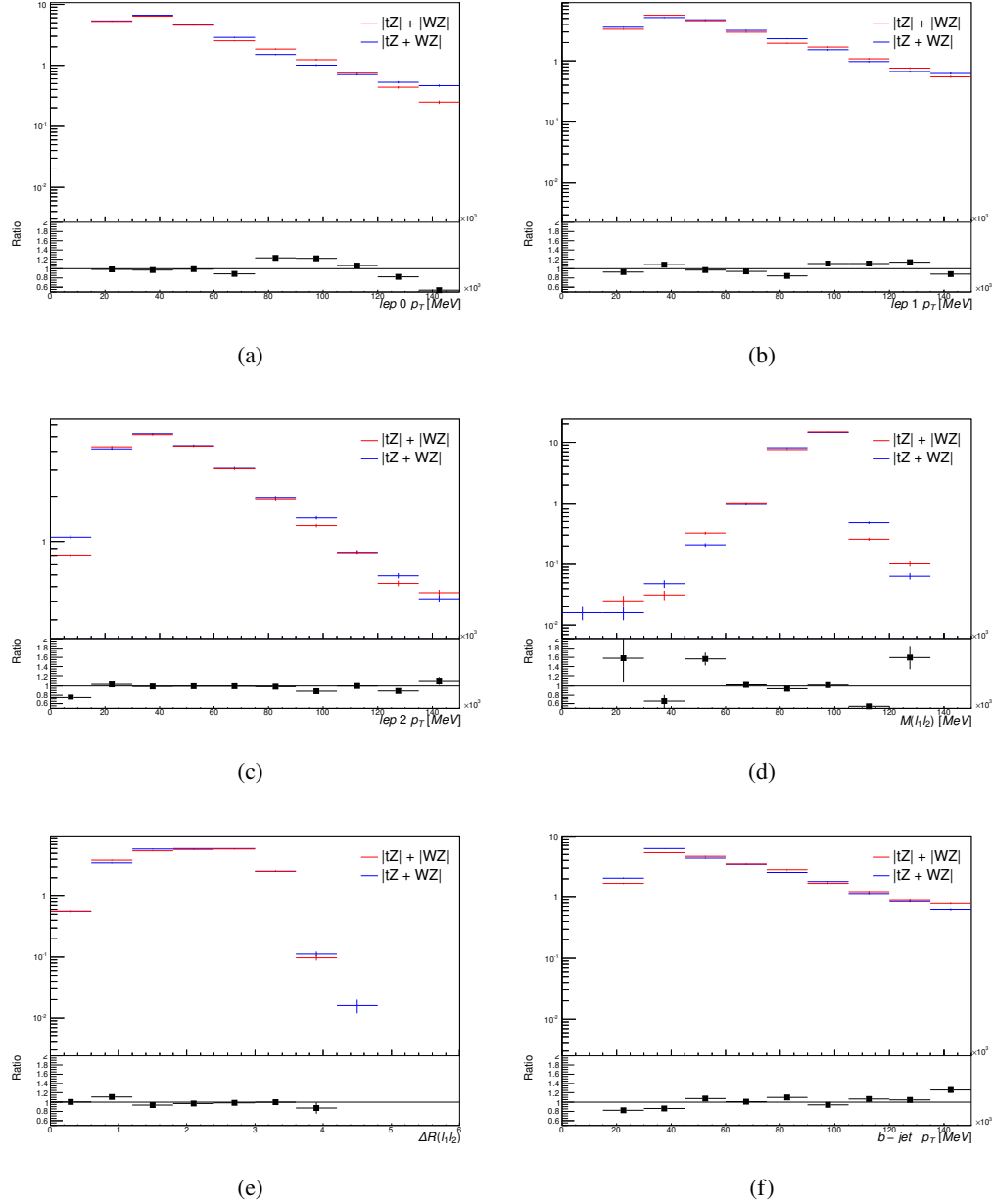


Figure .11: Comparisons between (a) the p_T of the lepton from the W, (b) and (c) show the p_T of the lepton from the Z, (d) the invariant mass of the Z-candidate, (e) ΔR of the leptons from the Z, and (f) the p_T of the b-jet, for WZ and tZ events generated with interference effects (blue) and without interference effects (red).

1726 The overall cross-section of the two methods agree within error, and no significant differ-
1727 ences in the kinematic distributions are seen. It is therefore concluded that interference effects
1728 do not significantly impact the results.

¹⁷²⁹ **.4 Alternate tZ Inclusive Fit**

1730 While tZ is often considered as a distinct process from WZ + b, this could also be
 1731 considered part of the signal. Alternate studies are performed where, using the same framework
 1732 as the nominal analysis, a measurement of WZ + b is performed that includes tZ as part of
 1733 WZ+b.

1734 Because of this change, the tZ CR is no longer necessary, and only the five pseudo-
 1735 continuous b-tag regions are used in the fit. Further, systematics related to the tZ cross-section
 1736 are removed from the fit, as they are now encompassed by the normalization measurement of
 1737 WZ + b. All other systematic uncertainties are carried over from the nominal analysis.

1738 A post-fit summary of the 1-jet regions used in the fit are shown in Figure .12.

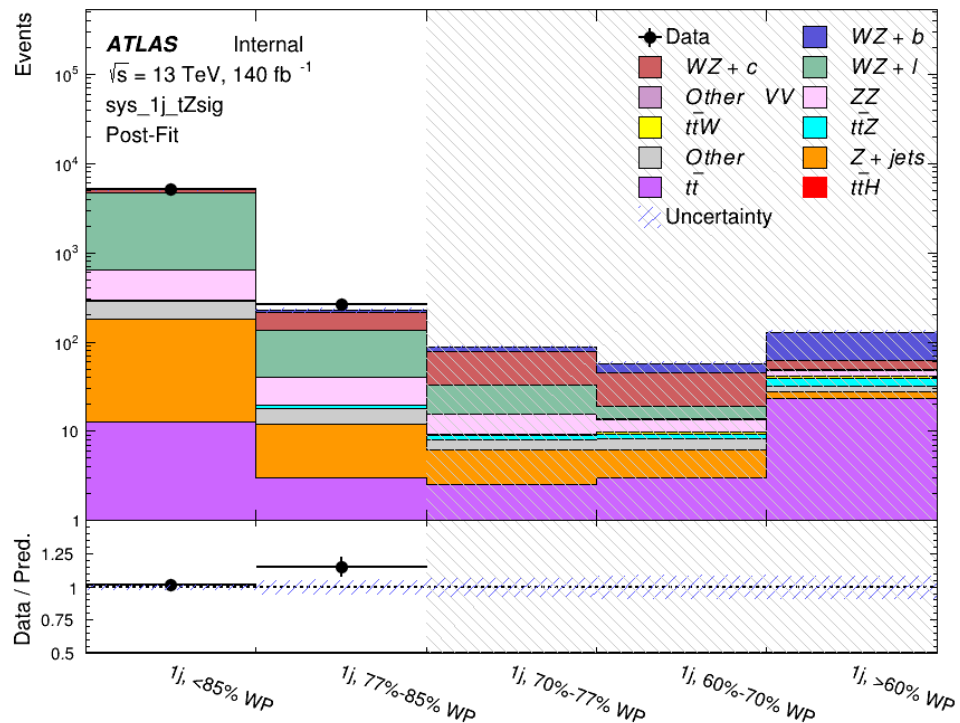


Figure .12: Post-fit summary of the 1-jet fit regions.

₁₇₃₉ An expected WZ + b cross-section of $4.1^{+0.78}_{-0.74}(\text{stat})^{+0.53}_{-0.52}(\text{sys}) \text{ fb}$ is extracted from the fit,

₁₇₄₀ with an expected significance of 4.0σ .

₁₇₄₁ The impact of the predominate systematics are summarized in Table 53.

Uncertainty Source	$\Delta\mu$	
WZ + light cross-section	0.08	-0.08
Jet Energy Scale	-0.06	0.08
Luminosity	-0.05	0.06
WZ + charm cross-section	-0.04	0.05
Other Diboson + b cross-section	-0.04	0.04
WZ cross-section - QCD scale	-0.04	0.03
$t\bar{t}$ cross-section	-0.03	0.03
Jet Energy Resolution	-0.03	0.03
Flavor tagging	-0.03	0.03
Z+jets cross section	-0.02	0.02
Total Systematic Uncertainty	-0.15	0.16

Table 53: Summary of the most significant sources of systematic uncertainty on the measurement of WZ + b with exactly one associated jet.

₁₇₄₂ A post-fit summary of the 2-jet regions used in the fit are shown in Figure .13.

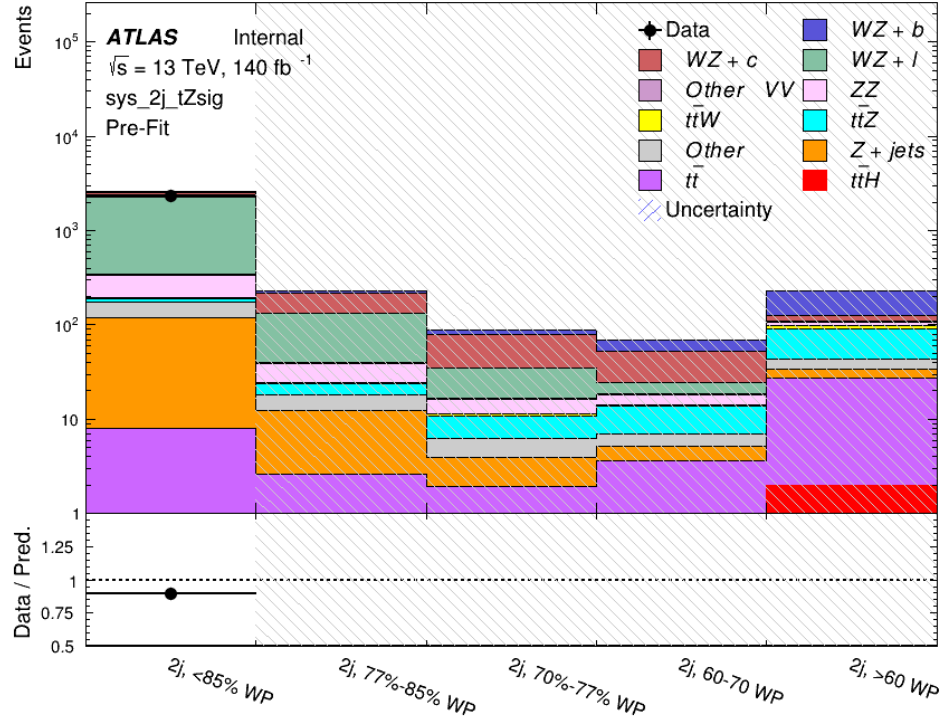


Figure .13: Post-fit summary of the 2-jet fit regions.

1743 An expected $WZ + b$ cross-section of $5.9^{+0.9}_{-0.9}(\text{stat})^{+0.9}_{-0.8}(\text{sys}) \text{ fb}$ is extracted from the fit,
 1744 with an expected significance of 5.3σ .

The impact of the predominate systematics are summarized in Table 54.

Uncertainty Source	$\Delta\mu$	
Luminosity	-0.07	0.07
Jet Energy Scale	0.06	0.05
ttZ cross-section - QCD scale	-0.05	0.05
WZ+l cross-section	0.05	-0.05
WZ+c cross-section	-0.03	0.05
WtZ cross-section	-0.03	0.03
WZ cross-section QCDscale	-0.03	0.03
Diboson cross-section b	-0.03	0.03
WZ cross-section - PDF	-0.03	0.03
Flavor Tagging	0.03	0.02
Total Systematic Uncertainty	-0.14	0.16

Table 54: Summary of the most significant sources of systematic uncertainty on the measurement of WZ + b with exactly one associated jet.

1746 .5 DSID list

Data:

```
data15_13TeV.AllYear.physics_Main.PhysCont.DAOD_HIGG8D1.grp15_v01_p4134
data16_13TeV.AllYear.physics_Main.PhysCont.DAOD_HIGG8D1.grp16_v01_p4134
data17_13TeV.AllYear.physics_Main.PhysCont.DAOD_HIGG8D1.grp17_v01_p4134
data18_13TeV.AllYear.physics_Main.PhysCont.DAOD_HIGG8D1.grp18_v01_p4134
```

mc16a:

```
mc16_13TeV.361603.PowhegPy8EG_CT10nloME_AZNLOCTEQ6L1_ZZllll_mll4.deriv.DAOD_HIGG8D1.e4475_s3126_r9364_r9315_p4133
mc16_13TeV.361602.PowhegPy8EG_CT10nloME_AZNLOCTEQ6L1_WZlvvv_mll4.deriv.DAOD_HIGG8D1.e4054_s3126_r9364_r9315_p4133
mc16_13TeV.361604.PowhegPy8EG_CT10nloME_AZNLOCTEQ6L1_ZZvvll_mll4.deriv.DAOD_HIGG8D1.e4475_s3126_r9364_r9315_p4133
mc16_13TeV.361600.PowhegPy8EG_CT10nloME_AZNLOCTEQ6L1_WWlvvv.deriv.DAOD_HIGG8D1.e4616_s3126_r9364_r9315_p4133
mc16_13TeV.361605.PowhegPy8EG_CT10nloME_AZNLOCTEQ6L1_ZZvvvv_mll4.deriv.DAOD_HIGG8D1.e4054_s3126_s3136_r9364_r9315_p4133
mc16_13TeV.361601.PowhegPy8EG_CT10nloME_AZNLOCTEQ6L1_WZlVll_mll4.deriv.DAOD_HIGG8D1.e4475_s3126_r9364_r9315_p4133
mc16_13TeV.364286.Sherpa_222_NNPDF30NNLO_llvjj_ss_EW4.deriv.DAOD_HIGG8D1.e6055_e5984_s3126_r9364_r9315_p3983 mc16_13TeV.364285.Sherpa_222_NNPDF30NNLO_llvjj_EW6_OFPlus.deriv.DAOD_HIGG8D1.e7421_e5984_s3126_r9364_r9315_p4133
mc16_13TeV.364740.MGPy8EG_NNPDF30NLO_A14NNPDF23LO_lvlljj_EW6_SFPlus.deriv.DAOD_HIGG8D1.e7421_e5984_s3126_r9364_r9315_p4133
mc16_13TeV.364742.MGPy8EG_NNPDF30NLO_A14NNPDF23LO_lvlljj_EW6_SFPlus.deriv.DAOD_HIGG8D1.e7421_e5984_s3126_r9364_r9315_p4133
mc16_13TeV.364253.Sherpa_222_NNPDF30NNLO_llv.deriv.DAOD_HIGG8D1.e5916_s3126_r9364_r9315_p4133
mc16_13TeV.364250.Sherpa_222_NNPDF30NNLO_lll.deriv.DAOD_HIGG8D1.e5894_s3126_r9364_r9315_p4133
mc16_13TeV.364254.Sherpa_222_NNPDF30NNLO_llv.deriv.DAOD_HIGG8D1.e5916_s3126_r9364_r9315_p4133
mc16_13TeV.364255.Sherpa_222_NNPDF30NNLO_lvvv.deriv.DAOD_HIGG8D1.e5916_s3126_r9364_r9315_p4133
mc16_13TeV.410155.aMcAtNloPythia8EvtGen_MEN30NLO_A14N23LO_ttW.deriv.DAOD_HIGG8D1.e5070_s3126_r9364_r9315_p4133
mc16_13TeV.410156.aMcAtNloPythia8EvtGen_MEN30NLO_A14N23LO_ttZnunu.deriv.DAOD_HIGG8D1.e5070_s3126_r9364_r9315_p4133
mc16_13TeV.410157.aMcAtNloPythia8EvtGen_MEN30NLO_A14N23LO_ttZqq.deriv.DAOD_HIGG8D1.e5070_s3126_r9364_r9315_p4133
mc16_13TeV.410218.aMcAtNloPythia8EvtGen_MEN30NLO_A14N23LO_ttee.deriv.DAOD_HIGG8D1.e5070_s3126_r9364_r9315_p4133
mc16_13TeV.410219.aMcAtNloPythia8EvtGen_MEN30NLO_A14N23LO_ttmumu.deriv.DAOD_HIGG8D1.e5070_s3126_r9364_r9315_p4133
mc16_13TeV.410220.aMcAtNloPythia8EvtGen_MEN30NLO_A14N23LO_ttautau.deriv.DAOD_HIGG8D1.e5070_s3126_r9364_r9315_p4133
mc16_13TeV.410276.aMcAtNloPythia8EvtGen_MEN30NLO_A14N23LO_ttee_mll_1_5.deriv.DAOD_HIGG8D1.e6087_e5984_s3126_r9364_r9315_p4133
mc16_13TeV.410277.aMcAtNloPythia8EvtGen_MEN30NLO_A14N23LO_ttmumu_mll_1_5.deriv.DAOD_HIGG8D1.e6087_e5984_s3126_r9364_r9315_p4133
mc16_13TeV.410278.aMcAtNloPythia8EvtGen_MEN30NLO_A14N23LO_ttautau_mll_1_5.deriv.DAOD_HIGG8D1.e6087_e5984_s3126_r9364_r9315_p4133
mc16_13TeV.410397.MadGraphPythia8EvtGen_ttbar_wbee_MEN30LO_A14N23LO.deriv.DAOD_HIGG8D1.e6086_e5984_s3126_r9364_r9315_p4133
mc16_13TeV.410398.MadGraphPythia8EvtGen_ttbar_wbmumu_MEN30LO_A14N23LO.deriv.DAOD_HIGG8D1.e6086_e5984_s3126_r9364_r9315_p4133
```

mc16_13TeV.410399.MadGraphPythia8EvtGen_ttbar_wbtautau_MEN30LO_A14N23LO.deriv.DAOD_HIGG8D1.e6086_e5984_s3126_r9364_r9315_p4133
 mc16_13TeV.410658.PhPy8EG_A14_tchan_BW50_lept_top.deriv.DAOD_HIGG8D1.e6671_e5984_s3126_r9364_r9315_p4133
 mc16_13TeV.410659.PhPy8EG_A14_tchan_BW50_lept_antitop.deriv.DAOD_HIGG8D1.e6671_e5984_s3126_r9364_r9315_p4133
 mc16_13TeV.410644.PowhegPythia8EvtGen_A14_singletop_schan_lept_top.deriv.DAOD_HIGG8D1.e6527_e5984_s3126_r9364_r9315_p4133
 mc16_13TeV.410645.PowhegPythia8EvtGen_A14_singletop_schan_lept_antitop.deriv.DAOD_HIGG8D1.e6527_e5984_s3126_r9364_r9315_p4133
 mc16_13TeV.304014.MadGraphPythia8EvtGen_A14NNPDF23_3top_SM.deriv.DAOD_HIGG8D1.e4324_s3126_r9364_r9315_p4133
 mc16_13TeV.410080.MadGraphPythia8EvtGen_A14NNPDF23_4topSM.deriv.DAOD_HIGG8D1.e4111_s3126_r9364_r9315_p4133
 mc16_13TeV.410081.MadGraphPythia8EvtGen_A14NNPDF23_ttbarWW.deriv.DAOD_HIGG8D1.e4111_s3126_r9364_r9315_p4133
 mc16_13TeV.364100.Sherpa_221_NNPDF30NNLO_Zmumu_MAXHTPTV0_70_CVetoBVeto.deriv.DAOD_HIGG8D1.e5271_s3126_r9364_r9315_p4133
 mc16_13TeV.364101.Sherpa_221_NNPDF30NNLO_Zmumu_MAXHTPTV0_70_CFilterBVeto.deriv.DAOD_HIGG8D1.e5271_s3126_r9364_r9315_p4133
 mc16_13TeV.364102.Sherpa_221_NNPDF30NNLO_Zmumu_MAXHTPTV0_70_BFilter.deriv.DAOD_HIGG8D1.e5271_s3126_r9364_r9315_p4133
 mc16_13TeV.364103.Sherpa_221_NNPDF30NNLO_Zmumu_MAXHTPTV70_140_CVetoBVeto.deriv.DAOD_HIGG8D1.e5271_s3126_r9364_r9315_p4133
 mc16_13TeV.364104.Sherpa_221_NNPDF30NNLO_Zmumu_MAXHTPTV70_140_CFilterBVeto.deriv.DAOD_HIGG8D1.e5271_s3126_r9364_r9315_p4133
 mc16_13TeV.364106.Sherpa_221_NNPDF30NNLO_Zmumu_MAXHTPTV140_280_CVetoBVeto.deriv.DAOD_HIGG8D1.e5271_s3126_r9364_r9315_p4133
 mc16_13TeV.364107.Sherpa_221_NNPDF30NNLO_Zmumu_MAXHTPTV140_280_CFilterBVeto.deriv.DAOD_HIGG8D1.e5271_s3126_r9364_r9315_p4133
 mc16_13TeV.364108.Sherpa_221_NNPDF30NNLO_Zmumu_MAXHTPTV140_280_BFilter.deriv.DAOD_HIGG8D1.e5271_s3126_r9364_r9315_p4133
 mc16_13TeV.364109.Sherpa_221_NNPDF30NNLO_Zmumu_MAXHTPTV280_500_CVetoBVeto.deriv.DAOD_HIGG8D1.e5271_s3126_r9364_r9315_p4133
 mc16_13TeV.364110.Sherpa_221_NNPDF30NNLO_Zmumu_MAXHTPTV280_500_CFilterBVeto.deriv.DAOD_HIGG8D1.e5271_s3126_r9364_r9315_p4133
 mc16_13TeV.364111.Sherpa_221_NNPDF30NNLO_Zmumu_MAXHTPTV280_500_BFilter.deriv.DAOD_HIGG8D1.e5271_e5984_s3126_r9364_r9315_p4133
 mc16_13TeV.364112.Sherpa_221_NNPDF30NNLO_Zmumu_MAXHTPTV500_1000.deriv.DAOD_HIGG8D1.e5271_s3126_r9364_r9315_p4133
 mc16_13TeV.364113.Sherpa_221_NNPDF30NNLO_Zmumu_MAXHTPTV1000_E_CMS.deriv.DAOD_HIGG8D1.e5271_s3126_r9364_r9315_p4133
 mc16_13TeV.364114.Sherpa_221_NNPDF30NNLO_Zee_MAXHTPTV0_70_CVetoBVeto.deriv.DAOD_HIGG8D1.e5299_s3126_r9364_r9315_p4133
 mc16_13TeV.364115.Sherpa_221_NNPDF30NNLO_Zee_MAXHTPTV0_70_CFilterBVeto.deriv.DAOD_HIGG8D1.e5299_s3126_r9364_r9315_p4133
 mc16_13TeV.364116.Sherpa_221_NNPDF30NNLO_Zee_MAXHTPTV0_70_BFilter.deriv.DAOD_HIGG8D1.e5299_s3126_r9364_r9315_p4133
 mc16_13TeV.364117.Sherpa_221_NNPDF30NNLO_Zee_MAXHTPTV70_140_CVetoBVeto.deriv.DAOD_HIGG8D1.e5299_s3126_r9364_r9315_p4133
 mc16_13TeV.364118.Sherpa_221_NNPDF30NNLO_Zee_MAXHTPTV70_140_CFilterBVeto.deriv.DAOD_HIGG8D1.e5299_s3126_r9364_r9315_p4133
 mc16_13TeV.364119.Sherpa_221_NNPDF30NNLO_Zee_MAXHTPTV70_140_BFilter.deriv.DAOD_HIGG8D1.e5299_s3126_r9364_r9315_p4133
 mc16_13TeV.364120.Sherpa_221_NNPDF30NNLO_Zee_MAXHTPTV140_280_CVetoBVeto.deriv.DAOD_HIGG8D1.e5299_s3126_r9364_r9315_p4133
 mc16_13TeV.364121.Sherpa_221_NNPDF30NNLO_Zee_MAXHTPTV140_280_CFilterBVeto.deriv.DAOD_HIGG8D1.e5299_s3126_r9364_r9315_p4133
 mc16_13TeV.364122.Sherpa_221_NNPDF30NNLO_Zee_MAXHTPTV140_280_BFilter.deriv.DAOD_HIGG8D1.e5299_s3126_r9364_r9315_p4133

mc16_13TeV.364123.Sherpa_221_NNPDF30NNLO_Zee_MAXHTPTV280_500_CVetoBVeto.deriv.DAOD_HIGG8D1.e5299_s3126_r9364_r9315_p4133
 mc16_13TeV.364124.Sherpa_221_NNPDF30NNLO_Zee_MAXHTPTV280_500_CFilterBVeto.deriv.DAOD_HIGG8D1.e5299_s3126_r9364_r9315_p4133
 mc16_13TeV.364125.Sherpa_221_NNPDF30NNLO_Zee_MAXHTPTV280_500_BFilter.deriv.DAOD_HIGG8D1.e5299_s3126_r9364_r9315_p4133
 mc16_13TeV.364125.Sherpa_221_NNPDF30NNLO_Zee_MAXHTPTV280_500_BFilter.deriv.DAOD_HIGG8D1.e5299_e5984_s3126_r9364_r9315_p4133
 mc16_13TeV.364126.Sherpa_221_NNPDF30NNLO_Zee_MAXHTPTV500_1000.deriv.DAOD_HIGG8D1.e5299_s3126_r9364_r9315_p4133
 mc16_13TeV.364127.Sherpa_221_NNPDF30NNLO_Zee_MAXHTPTV1000_E_CMS.deriv.DAOD_HIGG8D1.e5299_s3126_r9364_r9315_p4133
 mc16_13TeV.364128.Sherpa_221_NNPDF30NNLO_Ztautau_MAXHTPTV0_70_CVetoBVeto.deriv.DAOD_HIGG8D1.e5307_s3126_r9364_r9315_p4133
 mc16_13TeV.364129.Sherpa_221_NNPDF30NNLO_Ztautau_MAXHTPTV0_70_CFilterBVeto.deriv.DAOD_HIGG8D1.e5307_s3126_r9364_r9315_p4133
 mc16_13TeV.364130.Sherpa_221_NNPDF30NNLO_Ztautau_MAXHTPTV0_70_BFilter.deriv.DAOD_HIGG8D1.e5307_s3126_r9364_r9315_p4133
 mc16_13TeV.364131.Sherpa_221_NNPDF30NNLO_Ztautau_MAXHTPTV70_140_CVetoBVeto.deriv.DAOD_HIGG8D1.e5307_s3126_r9364_r9315_p4133
 mc16_13TeV.364132.Sherpa_221_NNPDF30NNLO_Ztautau_MAXHTPTV70_140_CFilterBVeto.deriv.DAOD_HIGG8D1.e5307_s3126_r9364_r9315_p4133
 mc16_13TeV.364133.Sherpa_221_NNPDF30NNLO_Ztautau_MAXHTPTV70_140_BFilter.deriv.DAOD_HIGG8D1.e5307_s3126_r9364_r9315_p4133
 mc16_13TeV.364134.Sherpa_221_NNPDF30NNLO_Ztautau_MAXHTPTV140_280_CVetoBVeto.deriv.DAOD_HIGG8D1.e5307_s3126_r9364_r9315_p4133
 mc16_13TeV.364135.Sherpa_221_NNPDF30NNLO_Ztautau_MAXHTPTV140_280_CFilterBVeto.deriv.DAOD_HIGG8D1.e5307_s3126_r9364_r9315_p4133
 mc16_13TeV.364136.Sherpa_221_NNPDF30NNLO_Ztautau_MAXHTPTV140_280_BFilter.deriv.DAOD_HIGG8D1.e5307_s3126_r9364_r9315_p4133
 mc16_13TeV.364137.Sherpa_221_NNPDF30NNLO_Ztautau_MAXHTPTV280_500_CVetoBVeto.deriv.DAOD_HIGG8D1.e5307_e5984_s3126_r9364_r9315_p4133
 mc16_13TeV.364137.Sherpa_221_NNPDF30NNLO_Ztautau_MAXHTPTV280_500_CFilterBVeto.deriv.DAOD_HIGG8D1.e5307_s3126_r9364_r9315_p4133
 mc16_13TeV.364138.Sherpa_221_NNPDF30NNLO_Ztautau_MAXHTPTV280_500_BFilter.deriv.DAOD_HIGG8D1.e5313_s3126_r9364_r9315_p4133
 mc16_13TeV.364139.Sherpa_221_NNPDF30NNLO_Ztautau_MAXHTPTV280_500_BFilter.deriv.DAOD_HIGG8D1.e5313_s3126_r9364_r9315_p4133
 mc16_13TeV.364140.Sherpa_221_NNPDF30NNLO_Ztautau_MAXHTPTV500_1000.deriv.DAOD_HIGG8D1.e5307_s3126_r9364_r9315_p4133
 mc16_13TeV.364141.Sherpa_221_NNPDF30NNLO_Ztautau_MAXHTPTV1000_E_CMS.deriv.DAOD_HIGG8D1.e5307_s3126_r9364_r9315_p4133
 mc16_13TeV.364198.Sherpa_221_NN30NNLO_Zmm_Mll10_40_MAXHTPTV0_70_BVeto.deriv.DAOD_HIGG8D1.e5421_s3126_r9364_r9315_p4133
 mc16_13TeV.364199.Sherpa_221_NN30NNLO_Zmm_Mll10_40_MAXHTPTV0_70_BFilter.deriv.DAOD_HIGG8D1.e5421_s3126_r9364_r9315_p4133
 mc16_13TeV.364200.Sherpa_221_NN30NNLO_Zmm_Mll10_40_MAXHTPTV70_280_BVeto.deriv.DAOD_HIGG8D1.e5421_s3126_r9364_r9315_p4133
 mc16_13TeV.364201.Sherpa_221_NN30NNLO_Zmm_Mll10_40_MAXHTPTV70_280_BFilter.deriv.DAOD_HIGG8D1.e5421_s3126_r9364_r9315_p4133
 mc16_13TeV.364202.Sherpa_221_NN30NNLO_Zmm_Mll10_40_MAXHTPTV280_E_CMS_BVeto.deriv.DAOD_HIGG8D1.e5421_s3126_r9364_r9315_p4133
 mc16_13TeV.364203.Sherpa_221_NN30NNLO_Zmm_Mll10_40_MAXHTPTV280_E_CMS_BFilter.deriv.DAOD_HIGG8D1.e5421_s3126_r9364_r9315_p4133
 mc16_13TeV.364204.Sherpa_221_NN30NNLO_Zee_Mll10_40_MAXHTPTV0_70_BVeto.deriv.DAOD_HIGG8D1.e5421_s3126_r9364_r9315_p4133
 mc16_13TeV.364205.Sherpa_221_NN30NNLO_Zee_Mll10_40_MAXHTPTV0_70_BFilter.deriv.DAOD_HIGG8D1.e5421_s3126_r9364_r9315_p4133
 mc16_13TeV.364206.Sherpa_221_NN30NNLO_Zee_Mll10_40_MAXHTPTV70_280_BVeto.deriv.DAOD_HIGG8D1.e5421_s3126_r9364_r9315_p4133
 mc16_13TeV.364207.Sherpa_221_NN30NNLO_Zee_Mll10_40_MAXHTPTV70_280_BFilter.deriv.DAOD_HIGG8D1.e5421_s3126_r9364_r9315_p4133

mc16_13TeV.364208.Sherpa_221_NN30NNLO_Zee_Mll10_40_MAXHTPTV280_E_CMS_BVeto.deriv.DAOD_HIGG8D1.e5421_s3126_r9364_r9315_p4133
 mc16_13TeV.364209.Sherpa_221_NN30NNLO_Zee_Mll10_40_MAXHTPTV280_E_CMS_BFilter.deriv.DAOD_HIGG8D1.e5421_s3126_r9364_r9315_p4133
 mc16_13TeV.364210.Sherpa_221_NN30NNLO_Ztt_Mll10_40_MAXHTPTV0_70_BVeto.deriv.DAOD_HIGG8D1.e5421_s3126_r9364_r9315_p4133
 mc16_13TeV.364211.Sherpa_221_NN30NNLO_Ztt_Mll10_40_MAXHTPTV0_70_BFilter.deriv.DAOD_HIGG8D1.e5421_s3126_r9364_r9315_p4133
 mc16_13TeV.364212.Sherpa_221_NN30NNLO_Ztt_Mll10_40_MAXHTPTV70_280_BVeto.deriv.DAOD_HIGG8D1.e5421_s3126_r9364_r9315_p4133
 mc16_13TeV.364213.Sherpa_221_NN30NNLO_Ztt_Mll10_40_MAXHTPTV70_280_BFilter.deriv.DAOD_HIGG8D1.e5421_s3126_r9364_r9315_p4133
 mc16_13TeV.364214.Sherpa_221_NN30NNLO_Ztt_Mll10_40_MAXHTPTV280_E_CMS_BVeto.deriv.DAOD_HIGG8D1.e5421_s3126_r9364_r9315_p4133
 mc16_13TeV.364215.Sherpa_221_NN30NNLO_Ztt_Mll10_40_MAXHTPTV280_E_CMS_BFilter.deriv.DAOD_HIGG8D1.e5421_s3126_r9364_r9315_p4133
 mc16_13TeV.364156.Sherpa_221_NNPDF30NNLO_Wmunu_MAXHTPTV0_70_CVetoBVeto.deriv.DAOD_HIGG8D1.e5340_s3126_r9364_r9315_p4133
 mc16_13TeV.364157.Sherpa_221_NNPDF30NNLO_Wmunu_MAXHTPTV0_70_CFilterBVeto.deriv.DAOD_HIGG8D1.e5340_s3126_r9364_r9315_p4133
 mc16_13TeV.364157.Sherpa_221_NNPDF30NNLO_Wmunu_MAXHTPTV0_70_CFilterBVeto.deriv.DAOD_HIGG8D1.e5340_e5984_s3126_r9364_r9315_p4133
 mc16_13TeV.364158.Sherpa_221_NNPDF30NNLO_Wmunu_MAXHTPTV0_70_BFilter.deriv.DAOD_HIGG8D1.e5340_s3126_r9364_r9315_p4133
 mc16_13TeV.364159.Sherpa_221_NNPDF30NNLO_Wmunu_MAXHTPTV70_140_CVetoBVeto.deriv.DAOD_HIGG8D1.e5340_s3126_r9364_r9315_p4133
 mc16_13TeV.364160.Sherpa_221_NNPDF30NNLO_Wmunu_MAXHTPTV70_140_CFilterBVeto.deriv.DAOD_HIGG8D1.e5340_s3126_r9364_r9315_p4133
 mc16_13TeV.364161.Sherpa_221_NNPDF30NNLO_Wmunu_MAXHTPTV70_140_BFilter.deriv.DAOD_HIGG8D1.e5340_s3126_r9364_r9315_p4133
 mc16_13TeV.364162.Sherpa_221_NNPDF30NNLO_Wmunu_MAXHTPTV140_280_CVetoBVeto.deriv.DAOD_HIGG8D1.e5340_s3126_r9364_r9315_p4133
 mc16_13TeV.364163.Sherpa_221_NNPDF30NNLO_Wmunu_MAXHTPTV140_280_CFilterBVeto.deriv.DAOD_HIGG8D1.e5340_s3126_r9364_r9315_p4133
 mc16_13TeV.364163.Sherpa_221_NNPDF30NNLO_Wmunu_MAXHTPTV140_280_CFilterBVeto.deriv.DAOD_HIGG8D1.e5340_e5984_s3126_s3136_r9364_r9315_p4133
 mc16_13TeV.364164.Sherpa_221_NNPDF30NNLO_Wmunu_MAXHTPTV140_280_BFilter.deriv.DAOD_HIGG8D1.e5340_s3126_r9364_r9315_p4133
 mc16_13TeV.364165.Sherpa_221_NNPDF30NNLO_Wmunu_MAXHTPTV280_500_CVetoBVeto.deriv.DAOD_HIGG8D1.e5340_s3126_r9364_r9315_p4133
 mc16_13TeV.364166.Sherpa_221_NNPDF30NNLO_Wmunu_MAXHTPTV280_500_CFilterBVeto.deriv.DAOD_HIGG8D1.e5340_s3126_r9364_r9315_p4133
 mc16_13TeV.364167.Sherpa_221_NNPDF30NNLO_Wmunu_MAXHTPTV280_500_BFilter.deriv.DAOD_HIGG8D1.e5340_e5984_s3126_r9364_r9315_p4133
 mc16_13TeV.364167.Sherpa_221_NNPDF30NNLO_Wmunu_MAXHTPTV280_500_BFilter.deriv.DAOD_HIGG8D1.e5340_s3126_r9364_r9315_p4133
 mc16_13TeV.364168.Sherpa_221_NNPDF30NNLO_Wmunu_MAXHTPTV500_1000.deriv.DAOD_HIGG8D1.e5340_s3126_r9364_r9315_p4133
 mc16_13TeV.364169.Sherpa_221_NNPDF30NNLO_Wmunu_MAXHTPTV1000_E_CMS.deriv.DAOD_HIGG8D1.e5340_s3126_r9364_r9315_p4133
 mc16_13TeV.364170.Sherpa_221_NNPDF30NNLO_Wenu_MAXHTPTV0_70_CVetoBVeto.deriv.DAOD_HIGG8D1.e5340_s3126_r9364_r9315_p4133
 mc16_13TeV.364171.Sherpa_221_NNPDF30NNLO_Wenu_MAXHTPTV0_70_CFilterBVeto.deriv.DAOD_HIGG8D1.e5340_e5984_s3126_r9364_r9315_p4133
 mc16_13TeV.364171.Sherpa_221_NNPDF30NNLO_Wenu_MAXHTPTV0_70_CFilterBVeto.deriv.DAOD_HIGG8D1.e5340_s3126_r9364_r9315_p4133
 mc16_13TeV.364172.Sherpa_221_NNPDF30NNLO_Wenu_MAXHTPTV0_70_BFilter.deriv.DAOD_HIGG8D1.e5340_s3126_r9364_r9315_p4133
 mc16_13TeV.364173.Sherpa_221_NNPDF30NNLO_Wenu_MAXHTPTV70_140_CVetoBVeto.deriv.DAOD_HIGG8D1.e5340_s3126_r9364_r9315_p4133
 mc16_13TeV.364174.Sherpa_221_NNPDF30NNLO_Wenu_MAXHTPTV70_140_CFilterBVeto.deriv.DAOD_HIGG8D1.e5340_s3126_r9364_r9315_p4133

mc16_13TeV.364175.Sherpa_221_NNPDF30NNLO_Wenu_MAXHTPTV70_140_BFilter.deriv.DAOD_HIGG8D1.e5340_e5984_s3126_s3136_r9364_r9315_p4133
 mc16_13TeV.364175.Sherpa_221_NNPDF30NNLO_Wenu_MAXHTPTV70_140_BFilter.deriv.DAOD_HIGG8D1.e5340_s3126_r9364_r9315_p4133
 mc16_13TeV.364176.Sherpa_221_NNPDF30NNLO_Wenu_MAXHTPTV140_280_CVetoBVeto.deriv.DAOD_HIGG8D1.e5340_s3126_r9364_r9315_p4133
 mc16_13TeV.364177.Sherpa_221_NNPDF30NNLO_Wenu_MAXHTPTV140_280_CFilterBVeto.deriv.DAOD_HIGG8D1.e5340_s3126_r9364_r9315_p4133
 mc16_13TeV.364177.Sherpa_221_NNPDF30NNLO_Wenu_MAXHTPTV140_280_CFilterBVeto.deriv.DAOD_HIGG8D1.e5340_e5984_s3126_s3136_r9364_r9315_p4133
 mc16_13TeV.364178.Sherpa_221_NNPDF30NNLO_Wenu_MAXHTPTV140_280_BFilter.deriv.DAOD_HIGG8D1.e5340_s3126_r9364_r9315_p4133
 mc16_13TeV.364179.Sherpa_221_NNPDF30NNLO_Wenu_MAXHTPTV280_500_CVetoBVeto.deriv.DAOD_HIGG8D1.e5340_s3126_r9364_r9315_p4133
 mc16_13TeV.364180.Sherpa_221_NNPDF30NNLO_Wenu_MAXHTPTV280_500_CFilterBVeto.deriv.DAOD_HIGG8D1.e5340_s3126_r9364_r9315_p4133
 mc16_13TeV.364181.Sherpa_221_NNPDF30NNLO_Wenu_MAXHTPTV280_500_BFilter.deriv.DAOD_HIGG8D1.e5340_e5984_s3126_r9364_r9315_p4133
 mc16_13TeV.364181.Sherpa_221_NNPDF30NNLO_Wenu_MAXHTPTV280_500_BFilter.deriv.DAOD_HIGG8D1.e5340_s3126_r9364_r9315_p4133
 mc16_13TeV.364182.Sherpa_221_NNPDF30NNLO_Wenu_MAXHTPTV500_1000.deriv.DAOD_HIGG8D1.e5340_s3126_r9364_r9315_p4133
 mc16_13TeV.364183.Sherpa_221_NNPDF30NNLO_Wenu_MAXHTPTV1000_E_CMS.deriv.DAOD_HIGG8D1.e5340_s3126_r9364_r9315_p4133
 mc16_13TeV.364184.Sherpa_221_NNPDF30NNLO_Wtaunu_MAXHTPTV0_70_CVetoBVeto.deriv.DAOD_HIGG8D1.e5340_s3126_r9364_r9315_p4133
 mc16_13TeV.364185.Sherpa_221_NNPDF30NNLO_Wtaunu_MAXHTPTV0_70_CFilterBVeto.deriv.DAOD_HIGG8D1.e5340_e5984_s3126_r9364_r9315_p4133
 mc16_13TeV.364185.Sherpa_221_NNPDF30NNLO_Wtaunu_MAXHTPTV0_70_CFilterBVeto.deriv.DAOD_HIGG8D1.e5340_s3126_r9364_r9315_p4133
 mc16_13TeV.364186.Sherpa_221_NNPDF30NNLO_Wtaunu_MAXHTPTV0_70_BFilter.deriv.DAOD_HIGG8D1.e5340_s3126_r9364_r9315_p4133
 mc16_13TeV.364187.Sherpa_221_NNPDF30NNLO_Wtaunu_MAXHTPTV70_140_CVetoBVeto.deriv.DAOD_HIGG8D1.e5340_s3126_r9364_r9315_p4133
 mc16_13TeV.364188.Sherpa_221_NNPDF30NNLO_Wtaunu_MAXHTPTV70_140_CFilterBVeto.deriv.DAOD_HIGG8D1.e5340_s3126_r9364_r9315_p4133
 mc16_13TeV.364189.Sherpa_221_NNPDF30NNLO_Wtaunu_MAXHTPTV70_140_BFilter.deriv.DAOD_HIGG8D1.e5340_s3126_r9364_r9315_p4133
 mc16_13TeV.364190.Sherpa_221_NNPDF30NNLO_Wtaunu_MAXHTPTV140_280_CVetoBVeto.deriv.DAOD_HIGG8D1.e5340_e5984_s3126_r9364_r9315_p4133
 mc16_13TeV.364190.Sherpa_221_NNPDF30NNLO_Wtaunu_MAXHTPTV140_280_CVetoBVeto.deriv.DAOD_HIGG8D1.e5340_s3126_r9364_r9315_p4133
 mc16_13TeV.364191.Sherpa_221_NNPDF30NNLO_Wtaunu_MAXHTPTV140_280_CFilterBVeto.deriv.DAOD_HIGG8D1.e5340_s3126_r9364_r9315_p4133
 mc16_13TeV.364191.Sherpa_221_NNPDF30NNLO_Wtaunu_MAXHTPTV140_280_CFilterBVeto.deriv.DAOD_HIGG8D1.e5340_e5984_s3126_s3136_r9364_r9315_p4133
 mc16_13TeV.364192.Sherpa_221_NNPDF30NNLO_Wtaunu_MAXHTPTV140_280_BFilter.deriv.DAOD_HIGG8D1.e5340_s3126_r9364_r9315_p4133
 mc16_13TeV.364193.Sherpa_221_NNPDF30NNLO_Wtaunu_MAXHTPTV280_500_CVetoBVeto.deriv.DAOD_HIGG8D1.e5340_s3126_r9364_r9315_p4133
 mc16_13TeV.364193.Sherpa_221_NNPDF30NNLO_Wtaunu_MAXHTPTV280_500_CVetoBVeto.deriv.DAOD_HIGG8D1.e5340_e5984_s3126_s3136_r9364_r9315_p4133
 mc16_13TeV.364194.Sherpa_221_NNPDF30NNLO_Wtaunu_MAXHTPTV280_500_CFilterBVeto.deriv.DAOD_HIGG8D1.e5340_s3126_r9364_r9315_p4133
 mc16_13TeV.364194.Sherpa_221_NNPDF30NNLO_Wtaunu_MAXHTPTV280_500_CFilterBVeto.deriv.DAOD_HIGG8D1.e5340_e5984_s3126_s3136_r9364_r9315_p4133
 mc16_13TeV.364195.Sherpa_221_NNPDF30NNLO_Wtaunu_MAXHTPTV280_500_BFilter.deriv.DAOD_HIGG8D1.e5340_s3126_r9364_r9315_p4133
 mc16_13TeV.364196.Sherpa_221_NNPDF30NNLO_Wtaunu_MAXHTPTV500_1000.deriv.DAOD_HIGG8D1.e5340_s3126_r9364_r9315_p4133
 mc16_13TeV.364197.Sherpa_221_NNPDF30NNLO_Wtaunu_MAXHTPTV1000_E_CMS.deriv.DAOD_HIGG8D1.e5340_s3126_r9364_r9315_p4133

mc16_13TeV.364500.Sherpa_222_NNPDF30NNLO_eegamma_pty_7_15.deriv.DAOD_HIGG8D1.e5928_e5984_s3126_r9364_r9315_p4133
mc16_13TeV.364501.Sherpa_222_NNPDF30NNLO_eegamma_pty_15_35.deriv.DAOD_HIGG8D1.e5928_e5984_s3126_r9364_r9315_p4133
mc16_13TeV.364502.Sherpa_222_NNPDF30NNLO_eegamma_pty_35_70.deriv.DAOD_HIGG8D1.e5928_e5984_s3126_r9364_r9315_p4133
mc16_13TeV.364503.Sherpa_222_NNPDF30NNLO_eegamma_pty_70_140.deriv.DAOD_HIGG8D1.e5928_e5984_s3126_r9364_r9315_p4133
mc16_13TeV.364504.Sherpa_222_NNPDF30NNLO_eegamma_pty_140_E_CMS.deriv.DAOD_HIGG8D1.e5928_e5984_s3126_r9364_r9315_p4133
mc16_13TeV.364505.Sherpa_222_NNPDF30NNLO_mumugamma_pty_7_15.deriv.DAOD_HIGG8D1.e5928_e5984_s3126_r9364_r9315_p4133
mc16_13TeV.364506.Sherpa_222_NNPDF30NNLO_mumugamma_pty_15_35.deriv.DAOD_HIGG8D1.e5988_e5984_s3126_r9364_r9315_p4133
mc16_13TeV.364507.Sherpa_222_NNPDF30NNLO_mumugamma_pty_35_70.deriv.DAOD_HIGG8D1.e5928_e5984_s3126_r9364_r9315_p4133
mc16_13TeV.364508.Sherpa_222_NNPDF30NNLO_mumugamma_pty_70_140.deriv.DAOD_HIGG8D1.e5928_e5984_s3126_r9364_r9315_p4133
mc16_13TeV.364509.Sherpa_222_NNPDF30NNLO_mumugamma_pty_140_E_CMS.deriv.DAOD_HIGG8D1.e5928_e5984_s3126_r9364_r9315_p4133
mc16_13TeV.364510.Sherpa_222_NNPDF30NNLO_tautaugamma_pty_7_15.deriv.DAOD_HIGG8D1.e5928_s3126_r9364_r9315_p4133
mc16_13TeV.364511.Sherpa_222_NNPDF30NNLO_tautaugamma_pty_15_35.deriv.DAOD_HIGG8D1.e5928_s3126_r9364_r9315_p4133
mc16_13TeV.364512.Sherpa_222_NNPDF30NNLO_tautaugamma_pty_35_70.deriv.DAOD_HIGG8D1.e5928_s3126_r9364_r9315_p4133
mc16_13TeV.364513.Sherpa_222_NNPDF30NNLO_tautaugamma_pty_70_140.deriv.DAOD_HIGG8D1.e5982_s3126_r9364_r9315_p4133
mc16_13TeV.364514.Sherpa_222_NNPDF30NNLO_tautaugamma_pty_140_E_CMS.deriv.DAOD_HIGG8D1.e5928_s3126_r9364_r9315_p4133
mc16_13TeV.364521.Sherpa_222_NNPDF30NNLO_enugamma_pty_7_15.deriv.DAOD_HIGG8D1.e5928_s3126_r9364_r9315_p4133
mc16_13TeV.364522.Sherpa_222_NNPDF30NNLO_enugamma_pty_15_35.deriv.DAOD_HIGG8D1.e5928_s3126_r9364_r9315_p4133
mc16_13TeV.364523.Sherpa_222_NNPDF30NNLO_enugamma_pty_35_70.deriv.DAOD_HIGG8D1.e5928_s3126_r9364_r9315_p4133
mc16_13TeV.364524.Sherpa_222_NNPDF30NNLO_enugamma_pty_70_140.deriv.DAOD_HIGG8D1.e5928_s3126_r9364_r9315_p4133
mc16_13TeV.364525.Sherpa_222_NNPDF30NNLO_enugamma_pty_140_E_CMS.deriv.DAOD_HIGG8D1.e5928_s3126_r9364_r9315_p4133
mc16_13TeV.364525.Sherpa_222_NNPDF30NNLO_enugamma_pty_140_E_CMS.deriv.DAOD_HIGG8D1.e5928_e5984_s3126_r9364_r9315_p4133
mc16_13TeV.364526.Sherpa_222_NNPDF30NNLO_munugamma_pty_7_15.deriv.DAOD_HIGG8D1.e5928_s3126_r9364_r9315_p4133
mc16_13TeV.364527.Sherpa_222_NNPDF30NNLO_munugamma_pty_15_35.deriv.DAOD_HIGG8D1.e5928_s3126_r9364_r9315_p4133
mc16_13TeV.364528.Sherpa_222_NNPDF30NNLO_munugamma_pty_35_70.deriv.DAOD_HIGG8D1.e5928_s3126_r9364_r9315_p4133
mc16_13TeV.364529.Sherpa_222_NNPDF30NNLO_munugamma_pty_70_140.deriv.DAOD_HIGG8D1.e5928_s3126_r9364_r9315_p4133
mc16_13TeV.364530.Sherpa_222_NNPDF30NNLO_munugamma_pty_140_E_CMS.deriv.DAOD_HIGG8D1.e5928_s3126_r9364_r9315_p4133
mc16_13TeV.364530.Sherpa_222_NNPDF30NNLO_munugamma_pty_140_E_CMS.deriv.DAOD_HIGG8D1.e5928_e5984_s3126_r9364_r9315_p4133
mc16_13TeV.364531.Sherpa_222_NNPDF30NNLO_taunugamma_pty_7_15.deriv.DAOD_HIGG8D1.e5928_s3126_r9364_r9315_p4133
mc16_13TeV.364532.Sherpa_222_NNPDF30NNLO_taunugamma_pty_15_35.deriv.DAOD_HIGG8D1.e5928_s3126_r9364_r9315_p4133
mc16_13TeV.364533.Sherpa_222_NNPDF30NNLO_taunugamma_pty_35_70.deriv.DAOD_HIGG8D1.e5928_s3126_r9364_r9315_p4133
mc16_13TeV.364534.Sherpa_222_NNPDF30NNLO_taunugamma_pty_70_140.deriv.DAOD_HIGG8D1.e5928_s3126_r9364_r9315_p4133

mc16_13TeV.364535.Sherpa_222_NNPDF30NNLO_taunugamma_pty_140_E_CMS.deriv.DAOD_HIGG8D1.e5928_s3126_r9364_r9315_p4133
 mc16_13TeV.364535.Sherpa_222_NNPDF30NNLO_taunugamma_pty_140_E_CMS.deriv.DAOD_HIGG8D1.e5928_e5984_s3126_r9364_r9315_p4133
 mc16_13TeV.410560.MadGraphPythia8EvtGen_A14_tZ_4fl_tchan_noAllHad.deriv.DAOD_HIGG8D1.e5803_s3126_r9364_r9315_p4133
 mc16_13TeV.410013.PowhegPythiaEvtGen_P2012_Wt_inclusive_top.deriv.DAOD_HIGG8D1.e3753_s3126_r9364_r9315_p4133
 mc16_13TeV.410014.PowhegPythiaEvtGen_P2012_Wt_inclusive_antitop.deriv.DAOD_HIGG8D1.e3753_s3126_r9364_r9315_p4133
 mc16_13TeV.410408.aMcAtNloPythia8EvtGen_tWZ_Ztoll_minDR1.deriv.DAOD_HIGG8D1.e6423_e5984_s3126_r9364_r9315_p4133
 mc16_13TeV.364242.Sherpa_222_NNPDF30NNLO_WWW_3l3v_EW6.deriv.DAOD_HIGG8D1.e5887_s3126_r9364_r9315_p4133
 mc16_13TeV.364243.Sherpa_222_NNPDF30NNLO_WWZ_4l2v_EW6.deriv.DAOD_HIGG8D1.e5887_s3126_r9364_r9315_p4133
 mc16_13TeV.364244.Sherpa_222_NNPDF30NNLO_WWZ_2l4v_EW6.deriv.DAOD_HIGG8D1.e5887_s3126_r9364_r9315_p4133
 mc16_13TeV.364245.Sherpa_222_NNPDF30NNLO_WZZ_5l1v_EW6.deriv.DAOD_HIGG8D1.e5887_s3126_r9364_r9315_p4133
 mc16_13TeV.364246.Sherpa_222_NNPDF30NNLO_WZZ_3l3v_EW6.deriv.DAOD_HIGG8D1.e5887_s3126_r9364_r9315_p4133
 mc16_13TeV.364247.Sherpa_222_NNPDF30NNLO_ZZZ_6l0v_EW6.deriv.DAOD_HIGG8D1.e5887_s3126_r9364_r9315_p4133
 mc16_13TeV.364248.Sherpa_222_NNPDF30NNLO_ZZZ_4l2v_EW6.deriv.DAOD_HIGG8D1.e5887_s3126_r9364_r9315_p4133
 mc16_13TeV.364249.Sherpa_222_NNPDF30NNLO_ZZZ_2l4v_EW6.deriv.DAOD_HIGG8D1.e5887_s3126_r9364_r9315_p4133
 mc16_13TeV.342284.Pythia8EvtGen_A14NNPDF23LO_WH125_inc.deriv.DAOD_HIGG8D1.e4246_s3126_r9364_r9315_p4133
 mc16_13TeV.342285.Pythia8EvtGen_A14NNPDF23LO_ZH125_inc.deriv.DAOD_HIGG8D1.e4246_s3126_r9364_r9315_p4133
 mc16_13TeV.341998.aMcAtNloHppEG_UEEE5_CTEQ6L1_CT10ME_tWH125_gamgam_yt_plus1.deriv.DAOD_HIGG8D1.e4394_e5984_s3126_r9364_r9315_p4133
 mc16_13TeV.410389.MadGraphPythia8EvtGen_A14NNPDF23_ttgamma_nonallhadronic.deriv.DAOD_HIGG8D1.e6155_e5984_s3126_r9364_r9315_p4133
 mc16_13TeV.410470.PhPy8EG_A14_ttbar_hdamp258p75_nonallhad.deriv.DAOD_HIGG8D1.e6337_e5984_s3126_r9364_r9315_p4133
 mc16_13TeV.410472.PhPy8EG_A14_ttbar_hdamp258p75_dil.deriv.DAOD_HIGG8D1.e6348_e5984_s3126_r9364_r9315_p4133
 mc16_13TeV.346343.PhPy8EG_A14NNPDF23_NNPDF30ME_ttH125_allhad.deriv.DAOD_HIGG8D1.e7148_e5984_s3126_r9364_r9315_p4133
 mc16_13TeV.346344.PhPy8EG_A14NNPDF23_NNPDF30ME_ttH125_semilep.deriv.DAOD_HIGG8D1.e7148_e5984_s3126_r9364_r9315_p4133
 mc16_13TeV.346345.PhPy8EG_A14NNPDF23_NNPDF30ME_ttH125_dilep.deriv.DAOD_HIGG8D1.e7148_e5984_s3126_r9364_r9315_p4133

mc16d:

mc16_13TeV.364253.Sherpa_222_NNPDF30NNLO_lllv.deriv.DAOD_HIGG8D1.e5916_e5984_s3126_r10201_r10210_p4133
 mc16_13TeV.364250.Sherpa_222_NNPDF30NNLO_llll.deriv.DAOD_HIGG8D1.e5894_e5984_s3126_r10201_r10210_p4133
 mc16_13TeV.364254.Sherpa_222_NNPDF30NNLO_llvv.deriv.DAOD_HIGG8D1.e5916_e5984_s3126_r10201_r10210_p4133
 mc16_13TeV.364255.Sherpa_222_NNPDF30NNLO_lvvv.deriv.DAOD_HIGG8D1.e5916_e5984_s3126_r10201_r10210_p4133
 mc16_13TeV.410155.aMcAtNloPythia8EvtGen_MEN30NLO_A14N23LO_ttW.deriv.DAOD_HIGG8D1.e5070_e5984_s3126_r10201_r10210_p4133
 mc16_13TeV.410156.aMcAtNloPythia8EvtGen_MEN30NLO_A14N23LO_ttZnunu.deriv.DAOD_HIGG8D1.e5070_e5984_s3126_r10201_r10210_p4133

mc16_13TeV.410157.aMcAtNloPythia8EvtGen_MEN30NLO_A14N23LO_ttZqq.deriv.DAOD_HIGG8D1.e5070_e5984_s3126_r10201_r10210_p4133
 mc16_13TeV.410218.aMcAtNloPythia8EvtGen_MEN30NLO_A14N23LO_ttee.deriv.DAOD_HIGG8D1.e5070_e5984_s3126_r10201_r10210_p4133
 mc16_13TeV.410219.aMcAtNloPythia8EvtGen_MEN30NLO_A14N23LO_ttmumu.deriv.DAOD_HIGG8D1.e5070_e5984_s3126_r10201_r10210_p4133
 mc16_13TeV.410220.aMcAtNloPythia8EvtGen_MEN30NLO_A14N23LO_ttautau.deriv.DAOD_HIGG8D1.e5070_e5984_s3126_r10201_r10210_p4133
 mc16_13TeV.410276.aMcAtNloPythia8EvtGen_MEN30NLO_A14N23LO_ttee_mll_1_5.deriv.DAOD_HIGG8D1.e6087_e5984_s3126_r10201_r10210_p4133
 mc16_13TeV.410277.aMcAtNloPythia8EvtGen_MEN30NLO_A14N23LO_ttmumu_mll_1_5.deriv.DAOD_HIGG8D1.e6087_e5984_s3126_r10201_r10210_p4133
 mc16_13TeV.410278.aMcAtNloPythia8EvtGen_MEN30NLO_A14N23LO_ttautau_mll_1_5.deriv.DAOD_HIGG8D1.e6087_e5984_s3126_r10201_r10210_p4133
 mc16_13TeV.410397.MadGraphPythia8EvtGen_ttbar_wbee_MEN30LO_A14N23LO.deriv.DAOD_HIGG8D1.e6086_e5984_s3126_r10201_r10210_p4133
 mc16_13TeV.410398.MadGraphPythia8EvtGen_ttbar_wbmumu_MEN30LO_A14N23LO.deriv.DAOD_HIGG8D1.e6086_e5984_s3126_r10201_r10210_p4133
 mc16_13TeV.410399.MadGraphPythia8EvtGen_ttbar_wbtautau_MEN30LO_A14N23LO.deriv.DAOD_HIGG8D1.e6086_e5984_s3126_r10201_r10210_p4133
 mc16_13TeV.410658.PhPy8EG_A14_tchan_BW50_lept_top.deriv.DAOD_HIGG8D1.e6671_e5984_s3126_r10201_r10210_p4133
 mc16_13TeV.410659.PhPy8EG_A14_tchan_BW50_lept_antitop.deriv.DAOD_HIGG8D1.e6671_e5984_s3126_r10201_r10210_p4133
 mc16_13TeV.410644.PowhegPythia8EvtGen_A14_singletop_schan_lept_top.deriv.DAOD_HIGG8D1.e6527_e5984_s3126_r10201_r10210_p4133
 mc16_13TeV.410645.PowhegPythia8EvtGen_A14_singletop_schan_lept_antitop.deriv.DAOD_HIGG8D1.e6527_s3126_r10201_r10210_p4133
 mc16_13TeV.304014.MadGraphPythia8EvtGen_A14NNPDF23_3top_SM.deriv.DAOD_HIGG8D1.e4324_e5984_s3126_r10201_r10210_p4133
 mc16_13TeV.410080.MadGraphPythia8EvtGen_A14NNPDF23_4topSM.deriv.DAOD_HIGG8D1.e4111_e5984_s3126_r10201_r10210_p4133
 mc16_13TeV.410081.MadGraphPythia8EvtGen_A14NNPDF23_ttbarWW.deriv.DAOD_HIGG8D1.e4111_e5984_s3126_r10201_r10210_p4133
 mc16_13TeV.364100.Sherpa_221_NNPDF30NNLO_Zmumu_MAXHTPTV0_70_CVetoBVeto.deriv.DAOD_HIGG8D1.e5271_s3126_r10201_r10210_p4133
 mc16_13TeV.364101.Sherpa_221_NNPDF30NNLO_Zmumu_MAXHTPTV0_70_CFilterBVeto.deriv.DAOD_HIGG8D1.e5271_s3126_r10201_r10210_p4133
 mc16_13TeV.364101.Sherpa_221_NNPDF30NNLO_Zmumu_MAXHTPTV0_70_CFilterBVeto.deriv.DAOD_HIGG8D1.e5271_e5984_s3126_r10201_r10210_p4133
 mc16_13TeV.364102.Sherpa_221_NNPDF30NNLO_Zmumu_MAXHTPTV0_70_BFilter.deriv.DAOD_HIGG8D1.e5271_s3126_r10201_r10210_p4133
 mc16_13TeV.364103.Sherpa_221_NNPDF30NNLO_Zmumu_MAXHTPTV70_140_CVetoBVeto.deriv.DAOD_HIGG8D1.e5271_s3126_r10201_r10210_p4133
 mc16_13TeV.364104.Sherpa_221_NNPDF30NNLO_Zmumu_MAXHTPTV70_140_CFilterBVeto.deriv.DAOD_HIGG8D1.e5271_s3126_r10201_r10210_p4133
 mc16_13TeV.364106.Sherpa_221_NNPDF30NNLO_Zmumu_MAXHTPTV140_280_CVetoBVeto.deriv.DAOD_HIGG8D1.e5271_s3126_r10201_r10210_p4133
 mc16_13TeV.364107.Sherpa_221_NNPDF30NNLO_Zmumu_MAXHTPTV140_280_CFilterBVeto.deriv.DAOD_HIGG8D1.e5271_s3126_r10201_r10210_p4133
 mc16_13TeV.364108.Sherpa_221_NNPDF30NNLO_Zmumu_MAXHTPTV140_280_BFilter.deriv.DAOD_HIGG8D1.e5271_e5984_s3126_r10201_r10210_p4133
 mc16_13TeV.364108.Sherpa_221_NNPDF30NNLO_Zmumu_MAXHTPTV140_280_BFilter.deriv.DAOD_HIGG8D1.e5271_s3126_r10201_r10210_p4133
 mc16_13TeV.364109.Sherpa_221_NNPDF30NNLO_Zmumu_MAXHTPTV280_500_CVetoBVeto.deriv.DAOD_HIGG8D1.e5271_e5984_s3126_r10201_r10210_p4133
 mc16_13TeV.364109.Sherpa_221_NNPDF30NNLO_Zmumu_MAXHTPTV280_500_CFilterBVeto.deriv.DAOD_HIGG8D1.e5271_s3126_r10201_r10210_p4133
 mc16_13TeV.364110.Sherpa_221_NNPDF30NNLO_Zmumu_MAXHTPTV280_500_CFilterBVeto.deriv.DAOD_HIGG8D1.e5271_s3126_r10201_r10210_p4133
 mc16_13TeV.364111.Sherpa_221_NNPDF30NNLO_Zmumu_MAXHTPTV280_500_BFilter.deriv.DAOD_HIGG8D1.e5271_e5984_s3126_r10201_r10210_p4133

mc16_13TeV.364111.Sherpa_221_NNPDF30NNLO_Zmumu_MAXHTPTV280_500_BFilter.deriv.DAOD_HIGG8D1.e5271_s3126_r10201_r10210_p4133
 mc16_13TeV.364112.Sherpa_221_NNPDF30NNLO_Zmumu_MAXHTPTV500_1000.deriv.DAOD_HIGG8D1.e5271_e5984_s3126_r10201_r10210_p4133
 mc16_13TeV.364112.Sherpa_221_NNPDF30NNLO_Zmumu_MAXHTPTV500_1000.deriv.DAOD_HIGG8D1.e5271_s3126_r10201_r10210_p4133
 mc16_13TeV.364113.Sherpa_221_NNPDF30NNLO_Zmumu_MAXHTPTV1000_E_CMS.deriv.DAOD_HIGG8D1.e5271_s3126_r10201_r10210_p4133
 mc16_13TeV.364114.Sherpa_221_NNPDF30NNLO_Zee_MAXHTPTV0_70_CVetoBVeto.deriv.DAOD_HIGG8D1.e5299_s3126_r10201_r10210_p4133
 mc16_13TeV.364115.Sherpa_221_NNPDF30NNLO_Zee_MAXHTPTV0_70_CFilterBVeto.deriv.DAOD_HIGG8D1.e5299_e5984_s3126_r10201_r10210_p4133
 mc16_13TeV.364116.Sherpa_221_NNPDF30NNLO_Zee_MAXHTPTV0_70_BFilter.deriv.DAOD_HIGG8D1.e5299_e5984_s3126_r10201_r10210_p4133
 mc16_13TeV.364117.Sherpa_221_NNPDF30NNLO_Zee_MAXHTPTV70_140_CVetoBVeto.deriv.DAOD_HIGG8D1.e5299_e5984_s3126_r10201_r10210_p4133
 mc16_13TeV.364118.Sherpa_221_NNPDF30NNLO_Zee_MAXHTPTV70_140_CFilterBVeto.deriv.DAOD_HIGG8D1.e5299_e5984_s3126_r10201_r10210_p4133
 mc16_13TeV.364119.Sherpa_221_NNPDF30NNLO_Zee_MAXHTPTV70_140_BFilter.deriv.DAOD_HIGG8D1.e5299_e5984_s3126_r10201_r10210_p4133
 mc16_13TeV.364120.Sherpa_221_NNPDF30NNLO_Zee_MAXHTPTV140_280_CVetoBVeto.deriv.DAOD_HIGG8D1.e5299_e5984_s3126_r10201_r10210_p4133
 mc16_13TeV.364121.Sherpa_221_NNPDF30NNLO_Zee_MAXHTPTV140_280_CFilterBVeto.deriv.DAOD_HIGG8D1.e5299_e5984_s3126_r10201_r10210_p4133
 mc16_13TeV.364122.Sherpa_221_NNPDF30NNLO_Zee_MAXHTPTV140_280_BFilter.deriv.DAOD_HIGG8D1.e5299_e5984_s3126_r10201_r10210_p4133
 mc16_13TeV.364123.Sherpa_221_NNPDF30NNLO_Zee_MAXHTPTV280_500_CVetoBVeto.deriv.DAOD_HIGG8D1.e5299_e5984_s3126_r10201_r10210_p4133
 mc16_13TeV.364124.Sherpa_221_NNPDF30NNLO_Zee_MAXHTPTV280_500_CFilterBVeto.deriv.DAOD_HIGG8D1.e5299_e5984_s3126_r10201_r10210_p4133
 mc16_13TeV.364125.Sherpa_221_NNPDF30NNLO_Zee_MAXHTPTV280_500_BFilter.deriv.DAOD_HIGG8D1.e5299_e5984_s3126_r10201_r10210_p4133
 mc16_13TeV.364126.Sherpa_221_NNPDF30NNLO_Zee_MAXHTPTV500_1000.deriv.DAOD_HIGG8D1.e5299_e5984_s3126_r10201_r10210_p4133
 mc16_13TeV.364127.Sherpa_221_NNPDF30NNLO_Zee_MAXHTPTV1000_E_CMS.deriv.DAOD_HIGG8D1.e5299_e5984_s3126_r10201_r10210_p4133
 mc16_13TeV.364128.Sherpa_221_NNPDF30NNLO_Ztautau_MAXHTPTV0_70_CVetoBVeto.deriv.DAOD_HIGG8D1.e5307_e5984_s3126_r10201_r10210_p4133
 mc16_13TeV.364129.Sherpa_221_NNPDF30NNLO_Ztautau_MAXHTPTV0_70_CFilterBVeto.deriv.DAOD_HIGG8D1.e5307_e5984_s3126_r10201_r10210_p4133
 mc16_13TeV.364130.Sherpa_221_NNPDF30NNLO_Ztautau_MAXHTPTV0_70_BFilter.deriv.DAOD_HIGG8D1.e5307_e5984_s3126_r10201_r10210_p4133
 mc16_13TeV.364131.Sherpa_221_NNPDF30NNLO_Ztautau_MAXHTPTV70_140_CVetoBVeto.deriv.DAOD_HIGG8D1.e5307_e5984_s3126_r10201_r10210_p4133
 mc16_13TeV.364132.Sherpa_221_NNPDF30NNLO_Ztautau_MAXHTPTV70_140_CFilterBVeto.deriv.DAOD_HIGG8D1.e5307_e5984_s3126_r10201_r10210_p4133
 mc16_13TeV.364133.Sherpa_221_NNPDF30NNLO_Ztautau_MAXHTPTV70_140_BFilter.deriv.DAOD_HIGG8D1.e5307_e5984_s3126_r10201_r10210_p4133
 mc16_13TeV.364134.Sherpa_221_NNPDF30NNLO_Ztautau_MAXHTPTV140_280_CVetoBVeto.deriv.DAOD_HIGG8D1.e5307_e5984_s3126_r10201_r10210_p4133
 mc16_13TeV.364135.Sherpa_221_NNPDF30NNLO_Ztautau_MAXHTPTV140_280_CFilterBVeto.deriv.DAOD_HIGG8D1.e5307_e5984_s3126_r10201_r10210_p4133
 mc16_13TeV.364136.Sherpa_221_NNPDF30NNLO_Ztautau_MAXHTPTV140_280_BFilter.deriv.DAOD_HIGG8D1.e5307_e5984_s3126_r10201_r10210_p4133
 mc16_13TeV.364137.Sherpa_221_NNPDF30NNLO_Ztautau_MAXHTPTV280_500_CVetoBVeto.deriv.DAOD_HIGG8D1.e5307_e5984_s3126_r10201_r10210_p4133
 mc16_13TeV.364138.Sherpa_221_NNPDF30NNLO_Ztautau_MAXHTPTV280_500_CFilterBVeto.deriv.DAOD_HIGG8D1.e5313_e5984_s3126_r10201_r10210_p4133
 mc16_13TeV.364139.Sherpa_221_NNPDF30NNLO_Ztautau_MAXHTPTV280_500_BFilter.deriv.DAOD_HIGG8D1.e5313_e5984_s3126_r10201_r10210_p4133
 mc16_13TeV.364140.Sherpa_221_NNPDF30NNLO_Ztautau_MAXHTPTV500_1000.deriv.DAOD_HIGG8D1.e5307_e5984_s3126_r10201_r10210_p4133

mc16_13TeV.364141.Sherpa_221_NNPDF30NNLO_Ztautau_MAXHTPTV1000_E_CMS.deriv.DAOD_HIGG8D1.e5307_e5984_s3126_r10201_r10210_p4133
 mc16_13TeV.364198.Sherpa_221_NN30NNLO_Zmm_Mll10_40_MAXHTPTV0_70_BVeto.deriv.DAOD_HIGG8D1.e5421_e5984_s3126_r10201_r10210_p4133
 mc16_13TeV.364199.Sherpa_221_NN30NNLO_Zmm_Mll10_40_MAXHTPTV0_70_BFilter.deriv.DAOD_HIGG8D1.e5421_e5984_s3126_r10201_r10210_p4133
 mc16_13TeV.364200.Sherpa_221_NN30NNLO_Zmm_Mll10_40_MAXHTPTV70_280_BVeto.deriv.DAOD_HIGG8D1.e5421_e5984_s3126_r10201_r10210_p4133
 mc16_13TeV.364201.Sherpa_221_NN30NNLO_Zmm_Mll10_40_MAXHTPTV70_280_BFilter.deriv.DAOD_HIGG8D1.e5421_e5984_s3126_r10201_r10210_p4133
 mc16_13TeV.364202.Sherpa_221_NN30NNLO_Zmm_Mll10_40_MAXHTPTV280_E_CMS_BVeto.deriv.DAOD_HIGG8D1.e5421_e5984_s3126_r10201_r10210_p4133
 mc16_13TeV.364203.Sherpa_221_NN30NNLO_Zmm_Mll10_40_MAXHTPTV280_E_CMS_BFilter.deriv.DAOD_HIGG8D1.e5421_e5984_s3126_r10201_r10210_p4133
 mc16_13TeV.364204.Sherpa_221_NN30NNLO_Zee_Mll10_40_MAXHTPTV0_70_BVeto.deriv.DAOD_HIGG8D1.e5421_e5984_s3126_r10201_r10210_p4133
 mc16_13TeV.364205.Sherpa_221_NN30NNLO_Zee_Mll10_40_MAXHTPTV0_70_BFilter.deriv.DAOD_HIGG8D1.e5421_e5984_s3126_r10201_r10210_p4133
 mc16_13TeV.364206.Sherpa_221_NN30NNLO_Zee_Mll10_40_MAXHTPTV70_280_BVeto.deriv.DAOD_HIGG8D1.e5421_e5984_s3126_r10201_r10210_p4133
 mc16_13TeV.364207.Sherpa_221_NN30NNLO_Zee_Mll10_40_MAXHTPTV70_280_BFilter.deriv.DAOD_HIGG8D1.e5421_e5984_s3126_r10201_r10210_p4133
 mc16_13TeV.364208.Sherpa_221_NN30NNLO_Zee_Mll10_40_MAXHTPTV280_E_CMS_BVeto.deriv.DAOD_HIGG8D1.e5421_e5984_s3126_r10201_r10210_p4133
 mc16_13TeV.364209.Sherpa_221_NN30NNLO_Zee_Mll10_40_MAXHTPTV280_E_CMS_BFilter.deriv.DAOD_HIGG8D1.e5421_e5984_s3126_r10201_r10210_p4133
 mc16_13TeV.364210.Sherpa_221_NN30NNLO_Ztt_Mll10_40_MAXHTPTV0_70_BVeto.deriv.DAOD_HIGG8D1.e5421_e5984_s3126_r10201_r10210_p4133
 mc16_13TeV.364211.Sherpa_221_NN30NNLO_Ztt_Mll10_40_MAXHTPTV0_70_BFilter.deriv.DAOD_HIGG8D1.e5421_e5984_s3126_r10201_r10210_p4133
 mc16_13TeV.364212.Sherpa_221_NN30NNLO_Ztt_Mll10_40_MAXHTPTV70_280_BVeto.deriv.DAOD_HIGG8D1.e5421_e5984_s3126_r10201_r10210_p4133
 mc16_13TeV.364213.Sherpa_221_NN30NNLO_Ztt_Mll10_40_MAXHTPTV70_280_BFilter.deriv.DAOD_HIGG8D1.e5421_e5984_s3126_r10201_r10210_p4133
 mc16_13TeV.364214.Sherpa_221_NN30NNLO_Ztt_Mll10_40_MAXHTPTV280_E_CMS_BVeto.deriv.DAOD_HIGG8D1.e5421_e5984_s3126_r10201_r10210_p4133
 mc16_13TeV.364215.Sherpa_221_NN30NNLO_Ztt_Mll10_40_MAXHTPTV280_E_CMS_BFilter.deriv.DAOD_HIGG8D1.e5421_e5984_s3126_r10201_r10210_p4133
 mc16_13TeV.364156.Sherpa_221_NNPDF30NNLO_Wmunu_MAXHTPTV0_70_CVetoBVeto.deriv.DAOD_HIGG8D1.e5340_s3126_r10201_r10210_p4133
 mc16_13TeV.364156.Sherpa_221_NNPDF30NNLO_Wmunu_MAXHTPTV0_70_CVetoBVeto.deriv.DAOD_HIGG8D1.e5340_e5984_s3126_s3136_r10201_r10210_p4133
 mc16_13TeV.364157.Sherpa_221_NNPDF30NNLO_Wmunu_MAXHTPTV0_70_CFilterBVeto.deriv.DAOD_HIGG8D1.e5340_e5984_s3126_s3136_r10201_r10210_p4133
 mc16_13TeV.364157.Sherpa_221_NNPDF30NNLO_Wmunu_MAXHTPTV0_70_CFilterBVeto.deriv.DAOD_HIGG8D1.e5340_s3126_r10201_r10210_p4133
 mc16_13TeV.364157.Sherpa_221_NNPDF30NNLO_Wmunu_MAXHTPTV0_70_CFilterBVeto.deriv.DAOD_HIGG8D1.e5340_e5984_s3126_r10201_r10210_p4133
 mc16_13TeV.364158.Sherpa_221_NNPDF30NNLO_Wmunu_MAXHTPTV0_70_BFilter.deriv.DAOD_HIGG8D1.e5340_e5984_s3126_s3136_r10201_r10210_p4133
 mc16_13TeV.364158.Sherpa_221_NNPDF30NNLO_Wmunu_MAXHTPTV0_70_BFilter.deriv.DAOD_HIGG8D1.e5340_s3126_r10201_r10210_p4133
 mc16_13TeV.364159.Sherpa_221_NNPDF30NNLO_Wmunu_MAXHTPTV70_140_CVetoBVeto.deriv.DAOD_HIGG8D1.e5340_s3126_r10201_r10210_p4133
 mc16_13TeV.364159.Sherpa_221_NNPDF30NNLO_Wmunu_MAXHTPTV70_140_CVetoBVeto.deriv.DAOD_HIGG8D1.e5340_e5984_s3126_r10201_r10210_p4133
 mc16_13TeV.364159.Sherpa_221_NNPDF30NNLO_Wmunu_MAXHTPTV70_140_CVetoBVeto.deriv.DAOD_HIGG8D1.e5340_e5984_s3126_s3136_r10201_r10210_p4133
 mc16_13TeV.364160.Sherpa_221_NNPDF30NNLO_Wmunu_MAXHTPTV70_140_CFilterBVeto.deriv.DAOD_HIGG8D1.e5340_e5984_s3126_r10201_r10210_p4133
 mc16_13TeV.364160.Sherpa_221_NNPDF30NNLO_Wmunu_MAXHTPTV70_140_CFilterBVeto.deriv.DAOD_HIGG8D1.e5340_s3126_r10201_r10210_p4133

mc16_13TeV.364161.Sherpa_221_NNPDF30NNLO_Wmunu_MAXHTPTV70_140_BFilter.deriv.DAOD_HIGG8D1.e5340_s3126_r10201_r10210_p4133
 mc16_13TeV.364161.Sherpa_221_NNPDF30NNLO_Wmunu_MAXHTPTV70_140_BFilter.deriv.DAOD_HIGG8D1.e5340_e5984_s3126_s3136_r10201_r10210_p4133
 mc16_13TeV.364162.Sherpa_221_NNPDF30NNLO_Wmunu_MAXHTPTV140_280_CVetoBVeto.deriv.DAOD_HIGG8D1.e5340_s3126_r10201_r10210_p4133
 mc16_13TeV.364162.Sherpa_221_NNPDF30NNLO_Wmunu_MAXHTPTV140_280_CVetoBVeto.deriv.DAOD_HIGG8D1.e5340_e5984_s3126_s3136_r10201_r10210_p4133
 mc16_13TeV.364163.Sherpa_221_NNPDF30NNLO_Wmunu_MAXHTPTV140_280_CFilterBVeto.deriv.DAOD_HIGG8D1.e5340_s3126_r10201_r10210_p4133
 mc16_13TeV.364163.Sherpa_221_NNPDF30NNLO_Wmunu_MAXHTPTV140_280_CFilterBVeto.deriv.DAOD_HIGG8D1.e5340_e5984_s3126_s3136_r10201_r10210_p4133
 mc16_13TeV.364163.Sherpa_221_NNPDF30NNLO_Wmunu_MAXHTPTV140_280_CFilterBVeto.deriv.DAOD_HIGG8D1.e5340_e5984_s3126_r10201_r10210_p4133
 mc16_13TeV.364164.Sherpa_221_NNPDF30NNLO_Wmunu_MAXHTPTV140_280_BFilter.deriv.DAOD_HIGG8D1.e5340_s3126_r10201_r10210_p4133
 mc16_13TeV.364164.Sherpa_221_NNPDF30NNLO_Wmunu_MAXHTPTV140_280_BFilter.deriv.DAOD_HIGG8D1.e5340_e5984_s3126_s3136_r10201_r10210_p4133
 mc16_13TeV.364165.Sherpa_221_NNPDF30NNLO_Wmunu_MAXHTPTV280_500_CVetoBVeto.deriv.DAOD_HIGG8D1.e5340_e5984_s3126_s3136_r10201_r10210_p4133
 mc16_13TeV.364165.Sherpa_221_NNPDF30NNLO_Wmunu_MAXHTPTV280_500_CVetoBVeto.deriv.DAOD_HIGG8D1.e5340_s3126_r10201_r10210_p4133
 mc16_13TeV.364166.Sherpa_221_NNPDF30NNLO_Wmunu_MAXHTPTV280_500_CFilterBVeto.deriv.DAOD_HIGG8D1.e5340_s3126_r10201_r10210_p4133
 mc16_13TeV.364166.Sherpa_221_NNPDF30NNLO_Wmunu_MAXHTPTV280_500_CFilterBVeto.deriv.DAOD_HIGG8D1.e5340_e5984_s3126_s3136_r10201_r10210_p4133
 mc16_13TeV.364167.Sherpa_221_NNPDF30NNLO_Wmunu_MAXHTPTV280_500_BFilter.deriv.DAOD_HIGG8D1.e5340_e5984_s3126_r10201_r10210_p4133
 mc16_13TeV.364167.Sherpa_221_NNPDF30NNLO_Wmunu_MAXHTPTV280_500_BFilter.deriv.DAOD_HIGG8D1.e5340_s3126_r10201_r10210_p4133
 mc16_13TeV.364168.Sherpa_221_NNPDF30NNLO_Wmunu_MAXHTPTV500_1000.deriv.DAOD_HIGG8D1.e5340_s3126_r10201_r10210_p4133
 mc16_13TeV.364168.Sherpa_221_NNPDF30NNLO_Wmunu_MAXHTPTV500_1000.deriv.DAOD_HIGG8D1.e5340_e5984_s3126_s3136_r10201_r10210_p4133
 mc16_13TeV.364169.Sherpa_221_NNPDF30NNLO_Wmunu_MAXHTPTV1000_E_CMS.deriv.DAOD_HIGG8D1.e5340_s3126_r10201_r10210_p4133
 mc16_13TeV.364169.Sherpa_221_NNPDF30NNLO_Wmunu_MAXHTPTV1000_E_CMS.deriv.DAOD_HIGG8D1.e5340_e5984_s3126_s3136_r10201_r10210_p4133
 mc16_13TeV.364170.Sherpa_221_NNPDF30NNLO_Wenu_MAXHTPTV0_70_CVetoBVeto.deriv.DAOD_HIGG8D1.e5340_e5984_s3126_s3136_r10201_r10210_p4133
 mc16_13TeV.364170.Sherpa_221_NNPDF30NNLO_Wenu_MAXHTPTV0_70_CVetoBVeto.deriv.DAOD_HIGG8D1.e5340_s3126_r10201_r10210_p4133
 mc16_13TeV.364171.Sherpa_221_NNPDF30NNLO_Wenu_MAXHTPTV0_70_CFilterBVeto.deriv.DAOD_HIGG8D1.e5340_e5984_s3126_r10201_r10210_p4133
 mc16_13TeV.364171.Sherpa_221_NNPDF30NNLO_Wenu_MAXHTPTV0_70_CFilterBVeto.deriv.DAOD_HIGG8D1.e5340_s3126_r10201_r10210_p4133
 mc16_13TeV.364171.Sherpa_221_NNPDF30NNLO_Wenu_MAXHTPTV0_70_CFilterBVeto.deriv.DAOD_HIGG8D1.e5340_e5984_s3126_s3136_r10201_r10210_p4133
 mc16_13TeV.364172.Sherpa_221_NNPDF30NNLO_Wenu_MAXHTPTV0_70_BFilter.deriv.DAOD_HIGG8D1.e5340_e5984_s3126_s3136_r10201_r10210_p4133
 mc16_13TeV.364172.Sherpa_221_NNPDF30NNLO_Wenu_MAXHTPTV0_70_BFilter.deriv.DAOD_HIGG8D1.e5340_s3126_r10201_r10210_p4133
 mc16_13TeV.364173.Sherpa_221_NNPDF30NNLO_Wenu_MAXHTPTV70_140_CVetoBVeto.deriv.DAOD_HIGG8D1.e5340_s3126_r10201_r10210_p4133
 mc16_13TeV.364173.Sherpa_221_NNPDF30NNLO_Wenu_MAXHTPTV70_140_CVetoBVeto.deriv.DAOD_HIGG8D1.e5340_e5984_s3126_r10201_r10210_p4133
 mc16_13TeV.364174.Sherpa_221_NNPDF30NNLO_Wenu_MAXHTPTV70_140_CFilterBVeto.deriv.DAOD_HIGG8D1.e5340_s3126_r10201_r10210_p4133
 mc16_13TeV.364174.Sherpa_221_NNPDF30NNLO_Wenu_MAXHTPTV70_140_CFilterBVeto.deriv.DAOD_HIGG8D1.e5340_e5984_s3126_r10201_r10210_p4133

mc16_13TeV.364175.Sherpa_221_NNPDF30NNLO_Wenu_MAXHTPTV70_140_BFilter.deriv.DAOD_HIGG8D1.e5340_e5984_s3126_r10201_r10210_p4133
 mc16_13TeV.364175.Sherpa_221_NNPDF30NNLO_Wenu_MAXHTPTV70_140_BFilter.deriv.DAOD_HIGG8D1.e5340_e5984_s3126_s3136_r10201_r10210_p4133
 mc16_13TeV.364175.Sherpa_221_NNPDF30NNLO_Wenu_MAXHTPTV70_140_BFilter.deriv.DAOD_HIGG8D1.e5340_s3126_r10201_r10210_p4133
 mc16_13TeV.364176.Sherpa_221_NNPDF30NNLO_Wenu_MAXHTPTV140_280_CVetoBVeto.deriv.DAOD_HIGG8D1.e5340_e5984_s3126_s3136_r10201_r10210_p4133
 mc16_13TeV.364176.Sherpa_221_NNPDF30NNLO_Wenu_MAXHTPTV140_280_CVetoBVeto.deriv.DAOD_HIGG8D1.e5340_s3126_r10201_r10210_p4133
 mc16_13TeV.364177.Sherpa_221_NNPDF30NNLO_Wenu_MAXHTPTV140_280_CFilterBVeto.deriv.DAOD_HIGG8D1.e5340_s3126_r10201_r10210_p4133
 mc16_13TeV.364177.Sherpa_221_NNPDF30NNLO_Wenu_MAXHTPTV140_280_CFilterBVeto.deriv.DAOD_HIGG8D1.e5340_e5984_s3126_s3136_r10201_r10210_p4133
 mc16_13TeV.364177.Sherpa_221_NNPDF30NNLO_Wenu_MAXHTPTV140_280_CFilterBVeto.deriv.DAOD_HIGG8D1.e5340_e5984_s3126_r10201_r10210_p4133
 mc16_13TeV.364178.Sherpa_221_NNPDF30NNLO_Wenu_MAXHTPTV140_280_BFilter.deriv.DAOD_HIGG8D1.e5340_e5984_s3126_r10201_r10210_p4133
 mc16_13TeV.364178.Sherpa_221_NNPDF30NNLO_Wenu_MAXHTPTV140_280_BFilter.deriv.DAOD_HIGG8D1.e5340_s3126_r10201_r10210_p4133
 mc16_13TeV.364179.Sherpa_221_NNPDF30NNLO_Wenu_MAXHTPTV280_500_CVetoBVeto.deriv.DAOD_HIGG8D1.e5340_s3126_r10201_r10210_p4133
 mc16_13TeV.364179.Sherpa_221_NNPDF30NNLO_Wenu_MAXHTPTV280_500_CVetoBVeto.deriv.DAOD_HIGG8D1.e5340_e5984_s3126_r10201_r10210_p4133
 mc16_13TeV.364180.Sherpa_221_NNPDF30NNLO_Wenu_MAXHTPTV280_500_CFilterBVeto.deriv.DAOD_HIGG8D1.e5340_e5984_s3126_s3136_r10201_r10210_p4133
 mc16_13TeV.364180.Sherpa_221_NNPDF30NNLO_Wenu_MAXHTPTV280_500_CFilterBVeto.deriv.DAOD_HIGG8D1.e5340_s3126_r10201_r10210_p4133
 mc16_13TeV.364181.Sherpa_221_NNPDF30NNLO_Wenu_MAXHTPTV280_500_BFilter.deriv.DAOD_HIGG8D1.e5340_e5984_s3126_r10201_r10210_p4133
 mc16_13TeV.364181.Sherpa_221_NNPDF30NNLO_Wenu_MAXHTPTV280_500_BFilter.deriv.DAOD_HIGG8D1.e5340_s3126_r10201_r10210_p4133
 mc16_13TeV.364182.Sherpa_221_NNPDF30NNLO_Wenu_MAXHTPTV500_1000.deriv.DAOD_HIGG8D1.e5340_s3126_r10201_r10210_p4133
 mc16_13TeV.364182.Sherpa_221_NNPDF30NNLO_Wenu_MAXHTPTV500_1000.deriv.DAOD_HIGG8D1.e5340_e5984_s3126_s3136_r10201_r10210_p4133
 mc16_13TeV.364183.Sherpa_221_NNPDF30NNLO_Wenu_MAXHTPTV1000_E_CMS.deriv.DAOD_HIGG8D1.e5340_e5984_s3126_r10201_r10210_p4133
 mc16_13TeV.364184.Sherpa_221_NNPDF30NNLO_Wtaunu_MAXHTPTV0_70_CVetoBVeto.deriv.DAOD_HIGG8D1.e5340_e5984_s3126_r10201_r10210_p4133
 mc16_13TeV.364184.Sherpa_221_NNPDF30NNLO_Wtaunu_MAXHTPTV0_70_CVetoBVeto.deriv.DAOD_HIGG8D1.e5340_s3126_r10201_r10210_p4133
 mc16_13TeV.364185.Sherpa_221_NNPDF30NNLO_Wtaunu_MAXHTPTV0_70_CFilterBVeto.deriv.DAOD_HIGG8D1.e5340_e5984_s3126_r10201_r10210_p4133
 mc16_13TeV.364186.Sherpa_221_NNPDF30NNLO_Wtaunu_MAXHTPTV0_70_BFilter.deriv.DAOD_HIGG8D1.e5340_e5984_s3126_r10201_r10210_p4133
 mc16_13TeV.364187.Sherpa_221_NNPDF30NNLO_Wtaunu_MAXHTPTV70_140_CVetoBVeto.deriv.DAOD_HIGG8D1.e5340_e5984_s3126_r10201_r10210_p4133
 mc16_13TeV.364188.Sherpa_221_NNPDF30NNLO_Wtaunu_MAXHTPTV70_140_CFilterBVeto.deriv.DAOD_HIGG8D1.e5340_e5984_s3126_r10201_r10210_p4133
 mc16_13TeV.364189.Sherpa_221_NNPDF30NNLO_Wtaunu_MAXHTPTV70_140_BFilter.deriv.DAOD_HIGG8D1.e5340_s3126_r10201_r10210_p4133
 mc16_13TeV.364189.Sherpa_221_NNPDF30NNLO_Wtaunu_MAXHTPTV70_140_BFilter.deriv.DAOD_HIGG8D1.e5340_e5984_s3126_r10201_r10210_p4133
 mc16_13TeV.364190.Sherpa_221_NNPDF30NNLO_Wtaunu_MAXHTPTV140_280_CVetoBVeto.deriv.DAOD_HIGG8D1.e5340_s3126_r10201_r10210_p4133
 mc16_13TeV.364190.Sherpa_221_NNPDF30NNLO_Wtaunu_MAXHTPTV140_280_CVetoBVeto.deriv.DAOD_HIGG8D1.e5340_e5984_s3126_s3136_r10201_r10210_p4133
 mc16_13TeV.364191.Sherpa_221_NNPDF30NNLO_Wtaunu_MAXHTPTV140_280_CFilterBVeto.deriv.DAOD_HIGG8D1.e5340_e5984_s3126_s3136_r10201_r10210_p4133
 mc16_13TeV.364191.Sherpa_221_NNPDF30NNLO_Wtaunu_MAXHTPTV140_280_CFilterBVeto.deriv.DAOD_HIGG8D1.e5340_s3126_r10201_r10210_p4133

mc16_13TeV.364192.Sherpa_221_NNPDF30NNLO_Wtaunu_MAXHTPTV140_280_BFilter.deriv.DAOD_HIGG8D1.e5340_e5984_s3126_r10201_r10210_p4133
 mc16_13TeV.364193.Sherpa_221_NNPDF30NNLO_Wtaunu_MAXHTPTV280_500_CVetoBVeto.deriv.DAOD_HIGG8D1.e5340_e5984_s3126_r10201_r10210_p4133
 mc16_13TeV.364193.Sherpa_221_NNPDF30NNLO_Wtaunu_MAXHTPTV280_500_CVetoBVeto.deriv.DAOD_HIGG8D1.e5340_e5984_s3126_s3136_r10201_r10210_p4133
 mc16_13TeV.364194.Sherpa_221_NNPDF30NNLO_Wtaunu_MAXHTPTV280_500_CFilterBVeto.deriv.DAOD_HIGG8D1.e5340_e5984_s3126_r10201_r10210_p4133
 mc16_13TeV.364194.Sherpa_221_NNPDF30NNLO_Wtaunu_MAXHTPTV280_500_CFilterBVeto.deriv.DAOD_HIGG8D1.e5340_s3126_r10201_r10210_p4133
 mc16_13TeV.364194.Sherpa_221_NNPDF30NNLO_Wtaunu_MAXHTPTV280_500_CFilterBVeto.deriv.DAOD_HIGG8D1.e5340_e5984_s3126_s3136_r10201_r10210_p4133
 mc16_13TeV.364195.Sherpa_221_NNPDF30NNLO_Wtaunu_MAXHTPTV280_500_BFilter.deriv.DAOD_HIGG8D1.e5340_e5984_s3126_r10201_r10210_p4133
 mc16_13TeV.364195.Sherpa_221_NNPDF30NNLO_Wtaunu_MAXHTPTV280_500_BFilter.deriv.DAOD_HIGG8D1.e5340_s3126_r10201_r10210_p4133
 mc16_13TeV.364196.Sherpa_221_NNPDF30NNLO_Wtaunu_MAXHTPTV500_1000.deriv.DAOD_HIGG8D1.e5340_e5984_s3126_s3136_r10201_r10210_p4133
 mc16_13TeV.364196.Sherpa_221_NNPDF30NNLO_Wtaunu_MAXHTPTV500_1000.deriv.DAOD_HIGG8D1.e5340_s3126_r10201_r10210_p4133
 mc16_13TeV.364197.Sherpa_221_NNPDF30NNLO_Wtaunu_MAXHTPTV1000_E_CMS.deriv.DAOD_HIGG8D1.e5340_e5984_s3126_r10201_r10210_p4133
 mc16_13TeV.364500.Sherpa_222_NNPDF30NNLO_eegamma_pty_7_15.deriv.DAOD_HIGG8D1.e5928_e5984_s3126_r10201_r10210_p4133
 mc16_13TeV.364501.Sherpa_222_NNPDF30NNLO_eegamma_pty_15_35.deriv.DAOD_HIGG8D1.e5928_e5984_s3126_r10201_r10210_p4133
 mc16_13TeV.364502.Sherpa_222_NNPDF30NNLO_eegamma_pty_35_70.deriv.DAOD_HIGG8D1.e5928_e5984_s3126_r10201_r10210_p4133
 mc16_13TeV.364503.Sherpa_222_NNPDF30NNLO_eegamma_pty_70_140.deriv.DAOD_HIGG8D1.e5928_e5984_s3126_r10201_r10210_p4133
 mc16_13TeV.364504.Sherpa_222_NNPDF30NNLO_eegamma_pty_140_E_CMS.deriv.DAOD_HIGG8D1.e5928_e5984_s3126_r10201_r10210_p4133
 mc16_13TeV.364505.Sherpa_222_NNPDF30NNLO_mumugamma_pty_7_15.deriv.DAOD_HIGG8D1.e5928_e5984_s3126_r10201_r10210_p4133
 mc16_13TeV.364506.Sherpa_222_NNPDF30NNLO_mumugamma_pty_15_35.deriv.DAOD_HIGG8D1.e5928_e5984_s3126_r10201_r10210_p4133
 mc16_13TeV.364507.Sherpa_222_NNPDF30NNLO_mumugamma_pty_35_70.deriv.DAOD_HIGG8D1.e5928_e5984_s3126_r10201_r10210_p4133
 mc16_13TeV.364508.Sherpa_222_NNPDF30NNLO_mumugamma_pty_70_140.deriv.DAOD_HIGG8D1.e5928_e5984_s3126_r10201_r10210_p4133
 mc16_13TeV.364509.Sherpa_222_NNPDF30NNLO_mumugamma_pty_140_E_CMS.deriv.DAOD_HIGG8D1.e5928_e5984_s3126_r10201_r10210_p4133
 mc16_13TeV.364510.Sherpa_222_NNPDF30NNLO_tautaugamma_pty_7_15.deriv.DAOD_HIGG8D1.e5928_e5984_s3126_r10201_r10210_p4133
 mc16_13TeV.364511.Sherpa_222_NNPDF30NNLO_tautaugamma_pty_15_35.deriv.DAOD_HIGG8D1.e5928_e5984_s3126_r10201_r10210_p4133
 mc16_13TeV.364512.Sherpa_222_NNPDF30NNLO_tautaugamma_pty_35_70.deriv.DAOD_HIGG8D1.e5928_e5984_s3126_r10201_r10210_p4133
 mc16_13TeV.364513.Sherpa_222_NNPDF30NNLO_tautaugamma_pty_70_140.deriv.DAOD_HIGG8D1.e5982_e5984_s3126_r10201_r10210_p4133
 mc16_13TeV.364513.Sherpa_222_NNPDF30NNLO_tautaugamma_pty_70_140.deriv.DAOD_HIGG8D1.e5928_e5984_s3126_r10201_r10210_p4133
 mc16_13TeV.364514.Sherpa_222_NNPDF30NNLO_tautaugamma_pty_140_E_CMS.deriv.DAOD_HIGG8D1.e5928_e5984_s3126_r10201_r10210_p4133
 mc16_13TeV.364521.Sherpa_222_NNPDF30NNLO_enugamma_pty_7_15.deriv.DAOD_HIGG8D1.e5928_e5984_s3126_r10201_r10210_p4133
 mc16_13TeV.364522.Sherpa_222_NNPDF30NNLO_enugamma_pty_15_35.deriv.DAOD_HIGG8D1.e5928_e5984_s3126_r10201_r10210_p4133
 mc16_13TeV.364523.Sherpa_222_NNPDF30NNLO_enugamma_pty_35_70.deriv.DAOD_HIGG8D1.e5928_e5984_s3126_r10201_r10210_p4133
 mc16_13TeV.364524.Sherpa_222_NNPDF30NNLO_enugamma_pty_70_140.deriv.DAOD_HIGG8D1.e5928_e5984_s3126_r10201_r10210_p4133

mc16_13TeV.364525.Sherpa_222_NNPDF30NNLO_enugamma_pty_140_E_CMS.deriv.DAOD_HIGG8D1.e5928_e5984_s3126_r10201_r10210_p4133
 mc16_13TeV.364526.Sherpa_222_NNPDF30NNLO_munugamma_pty_7_15.deriv.DAOD_HIGG8D1.e5928_e5984_s3126_r10201_r10210_p4133
 mc16_13TeV.364527.Sherpa_222_NNPDF30NNLO_munugamma_pty_15_35.deriv.DAOD_HIGG8D1.e5928_e5984_s3126_r10201_r10210_p4133
 mc16_13TeV.364528.Sherpa_222_NNPDF30NNLO_munugamma_pty_35_70.deriv.DAOD_HIGG8D1.e5928_e5984_s3126_r10201_r10210_p4133
 mc16_13TeV.364529.Sherpa_222_NNPDF30NNLO_munugamma_pty_70_140.deriv.DAOD_HIGG8D1.e5928_e5984_s3126_r10201_r10210_p4133
 mc16_13TeV.364530.Sherpa_222_NNPDF30NNLO_munugamma_pty_140_E_CMS.deriv.DAOD_HIGG8D1.e5928_e5984_s3126_r10201_r10210_p4133
 mc16_13TeV.364531.Sherpa_222_NNPDF30NNLO_taunugamma_pty_7_15.deriv.DAOD_HIGG8D1.e5928_e5984_s3126_r10201_r10210_p4133
 mc16_13TeV.364532.Sherpa_222_NNPDF30NNLO_taunugamma_pty_15_35.deriv.DAOD_HIGG8D1.e5928_e5984_s3126_r10201_r10210_p4133
 mc16_13TeV.364533.Sherpa_222_NNPDF30NNLO_taunugamma_pty_35_70.deriv.DAOD_HIGG8D1.e5928_e5984_s3126_r10201_r10210_p4133
 mc16_13TeV.364534.Sherpa_222_NNPDF30NNLO_taunugamma_pty_70_140.deriv.DAOD_HIGG8D1.e5928_e5984_s3126_r10201_r10210_p4133
 mc16_13TeV.364535.Sherpa_222_NNPDF30NNLO_taunugamma_pty_140_E_CMS.deriv.DAOD_HIGG8D1.e5928_e5984_s3126_r10201_r10210_p4133
 mc16_13TeV.410560.MadGraphPythia8EvtGen_A14_tZ_4fl_tchan_noAllHad.deriv.DAOD_HIGG8D1.e5803_e5984_s3126_r10201_r10210_p4133
 mc16_13TeV.410013.PowhegPythiaEvtGen_P2012_Wt_inclusive_top.deriv.DAOD_HIGG8D1.e3753_s3126_r10201_r10210_p4133
 mc16_13TeV.410014.PowhegPythiaEvtGen_P2012_Wt_inclusive_antitop.deriv.DAOD_HIGG8D1.e3753_s3126_r10201_r10210_p4133
 mc16_13TeV.410408.aMcAtNloPythia8EvtGen_tWZ_Ztoll_minDR1.deriv.DAOD_HIGG8D1.e6423_e5984_s3126_r10201_r10210_p4133
 mc16_13TeV.364242.Sherpa_222_NNPDF30NNLO_WWW_3l3v_EW6.deriv.DAOD_HIGG8D1.e5887_e5984_s3126_r10201_r10210_p4133
 mc16_13TeV.364243.Sherpa_222_NNPDF30NNLO_WWZ_4l2v_EW6.deriv.DAOD_HIGG8D1.e5887_e5984_s3126_r10201_r10210_p4133
 mc16_13TeV.364244.Sherpa_222_NNPDF30NNLO_WWZ_2l4v_EW6.deriv.DAOD_HIGG8D1.e5887_e5984_s3126_r10201_r10210_p4133
 mc16_13TeV.364245.Sherpa_222_NNPDF30NNLO_WZZ_5l1v_EW6.deriv.DAOD_HIGG8D1.e5887_e5984_s3126_r10201_r10210_p4133
 mc16_13TeV.364246.Sherpa_222_NNPDF30NNLO_WZZ_3l3v_EW6.deriv.DAOD_HIGG8D1.e5887_e5984_s3126_r10201_r10210_p4133
 mc16_13TeV.364247.Sherpa_222_NNPDF30NNLO_ZZZ_6l0v_EW6.deriv.DAOD_HIGG8D1.e5887_e5984_s3126_r10201_r10210_p4133
 mc16_13TeV.364248.Sherpa_222_NNPDF30NNLO_ZZZ_4l2v_EW6.deriv.DAOD_HIGG8D1.e5887_e5984_s3126_r10201_r10210_p4133
 mc16_13TeV.364249.Sherpa_222_NNPDF30NNLO_ZZZ_2l4v_EW6.deriv.DAOD_HIGG8D1.e5887_e5984_s3126_r10201_r10210_p4133
 mc16_13TeV.342284.Pythia8EvtGen_A14NNPDF23LO_WH125_inc.deriv.DAOD_HIGG8D1.e4246_e5984_s3126_r10201_r10210_p4133
 mc16_13TeV.342285.Pythia8EvtGen_A14NNPDF23LO_ZH125_inc.deriv.DAOD_HIGG8D1.e4246_e5984_s3126_r10201_r10210_p4133
 mc16_13TeV.341998.aMcAtNloHppEG_UEEE5_CTEQ6L1_CT10ME_tWH125_gamgam_yt_plus1.deriv.DAOD_HIGG8D1.e4394_e5984_s3126_r10201_r10210_p4133
 mc16_13TeV.410470.PhPy8EG_A14_ttbar_hdamp258p75_nonallhad.deriv.DAOD_HIGG8D1.e6337_e5984_s3126_r10201_r10210_p4133
 mc16_13TeV.410472.PhPy8EG_A14_ttbar_hdamp258p75_dil.deriv.DAOD_HIGG8D1.e6348_e5984_s3126_r10201_r10210_p4133
 mc16_13TeV.346343.PhPy8EG_A14NNPDF23_NNPDF30ME_ttH125_allhad.deriv.DAOD_HIGG8D1.e7148_e5984_s3126_r10201_r10210_p4133
 mc16_13TeV.346344.PhPy8EG_A14NNPDF23_NNPDF30ME_ttH125_semilep.deriv.DAOD_HIGG8D1.e7148_e5984_a875_r10201_r10210_p4133
 mc16_13TeV.346345.PhPy8EG_A14NNPDF23_NNPDF30ME_ttH125_dilep.deriv.DAOD_HIGG8D1.e7148_e5984_a875_r10201_r10210_p4133

mc16e:

mc16_13TeV.361605.PowhegPy8EG_CT10nloME_AZNLOCTEQ6L1_ZZvvvv_mll4.deriv.DAOD_HIGG8D1.e4054_e5984_s3126_r10724_r10726_p4133
 mc16_13TeV.361602.PowhegPy8EG_CT10nloME_AZNLOCTEQ6L1_WZlvvv_mll4.deriv.DAOD_HIGG8D1.e4054_e5984_s3126_r10724_r10726_p4133
 mc16_13TeV.361601.PowhegPy8EG_CT10nloME_AZNLOCTEQ6L1_WZlvl_lml4.deriv.DAOD_HIGG8D1.e4475_e5984_s3126_r10724_r10726_p4133
 mc16_13TeV.361600.PowhegPy8EG_CT10nloME_AZNLOCTEQ6L1_WWlvlv.deriv.DAOD_HIGG8D1.e4616_e5984_s3126_r10724_r10726_p4133
 mc16_13TeV.361603.PowhegPy8EG_CT10nloME_AZNLOCTEQ6L1_ZZllll_mll4.deriv.DAOD_HIGG8D1.e4475_e5984_s3126_r10724_r10726_p4133
 mc16_13TeV.361604.PowhegPy8EG_CT10nloME_AZNLOCTEQ6L1_ZZvvll_mll4.deriv.DAOD_HIGG8D1.e4475_e5984_s3126_r10724_r10726_p4133
 mc16_13TeV.364288.Sherpa_222_NNPDF30NNLO_llll_lowMllPtComplement.deriv.DAOD_HIGG8D1.e6096_s3126_r10724_p3983 mc16_13TeV.364287.Sherpa_222_NNPDF30NNLO_llvvjj_EW6.deriv.DAOD_HIGG8D1.e6055_e5984_s3126_r10724_r10726_p3983
 mc16_13TeV.364285.Sherpa_222_NNPDF30NNLO_llvjjj_EW6.deriv.DAOD_HIGG8D1.e4475_e5984_s3126_r10724_r10726_p4133
 mc16_13TeV.364284.Sherpa_222_NNPDF30NNLO_lllljj_EW6.deriv.DAOD_HIGG8D1.e6055_s3126_r10724_p3983
 mc16_13TeV.364283.Sherpa_222_NNPDF30NNLO_lllljjj_EW6.deriv.DAOD_HIGG8D1.e6055_s3126_r10724_p3983
 mc16_13TeV.364739.MGPy8EG_NNPDF30NLO_A14NNPDF23LO_lvlljjEW6_OFMinus.deriv.DAOD_HIGG8D1.e7421_e5984_s3126_r10724_r10726_p4133
 mc16_13TeV.364742.MGPy8EG_NNPDF30NLO_A14NNPDF23LO_lvlljjEW6_SFPlus.deriv.DAOD_HIGG8D1.e7421_e5984_s3126_r10724_r10726_p4133
 mc16_13TeV.364740.MGPy8EG_NNPDF30NLO_A14NNPDF23LO_lvlljjEW6_OFPlus.deriv.DAOD_HIGG8D1.e7421_e5984_s3126_r10724_r10726_p4133
 mc16_13TeV.364741.MGPy8EG_NNPDF30NLO_A14NNPDF23LO_lvlljjEW6_SFMinus.deriv.DAOD_HIGG8D1.e7421_e5984_s3126_r10724_r10726_p4133
 mc16_13TeV.364253.Sherpa_222_NNPDF30NNLO_llv.deriv.DAOD_HIGG8D1.e5916_e5984_s3126_r10724_r10726_p4133
 mc16_13TeV.364250.Sherpa_222_NNPDF30NNLO_llll.deriv.DAOD_HIGG8D1.e5894_e5984_s3126_r10724_r10726_p4133
 mc16_13TeV.364254.Sherpa_222_NNPDF30NNLO_llv.deriv.DAOD_HIGG8D1.e5916_e5984_s3126_r10724_r10726_p4133
 mc16_13TeV.364255.Sherpa_222_NNPDF30NNLO_lvvv.deriv.DAOD_HIGG8D1.e5916_e5984_s3126_r10724_r10726_p4133
 mc16_13TeV.410155.aMcAtNloPythia8EvtGen_MEN30NLO_A14N23LO_ttW.deriv.DAOD_HIGG8D1.e5070_e5984_s3126_r10724_r10726_p4133
 mc16_13TeV.410156.aMcAtNloPythia8EvtGen_MEN30NLO_A14N23LO_ttZnunu.deriv.DAOD_HIGG8D1.e5070_e5984_s3126_r10724_r10726_p4133
 mc16_13TeV.410157.aMcAtNloPythia8EvtGen_MEN30NLO_A14N23LO_ttZqq.deriv.DAOD_HIGG8D1.e5070_e5984_s3126_r10724_r10726_p4133
 mc16_13TeV.410218.aMcAtNloPythia8EvtGen_MEN30NLO_A14N23LO_ttee.deriv.DAOD_HIGG8D1.e5070_e5984_s3126_r10724_r10726_p4133
 mc16_13TeV.410219.aMcAtNloPythia8EvtGen_MEN30NLO_A14N23LO_ttmumu.deriv.DAOD_HIGG8D1.e5070_e5984_s3126_r10724_r10726_p4133
 mc16_13TeV.410220.aMcAtNloPythia8EvtGen_MEN30NLO_A14N23LO_ttautau.deriv.DAOD_HIGG8D1.e5070_e5984_s3126_r10724_r10726_p4133
 mc16_13TeV.410276.aMcAtNloPythia8EvtGen_MEN30NLO_A14N23LO_ttee_mll_1_5.deriv.DAOD_HIGG8D1.e6087_e5984_s3126_r10724_r10726_p4133
 mc16_13TeV.410277.aMcAtNloPythia8EvtGen_MEN30NLO_A14N23LO_ttmumu_mll_1_5.deriv.DAOD_HIGG8D1.e6087_e5984_s3126_r10724_r10726_p4133
 mc16_13TeV.410278.aMcAtNloPythia8EvtGen_MEN30NLO_A14N23LO_ttautau_mll_1_5.deriv.DAOD_HIGG8D1.e6087_e5984_s3126_r10724_r10726_p4133
 mc16_13TeV.410397.MadGraphPythia8EvtGen_ttbar_wbee_MEN30LO_A14N23LO.deriv.DAOD_HIGG8D1.e6086_e5984_s3126_r10724_r10726_p4133
 mc16_13TeV.410398.MadGraphPythia8EvtGen_ttbar_wbmumu_MEN30LO_A14N23LO.deriv.DAOD_HIGG8D1.e6086_e5984_s3126_r10724_r10726_p4133

mc16_13TeV.410399.MadGraphPythia8EvtGen_ttbar_wbtautau_MEN30LO_A14N23LO.deriv.DAOD_HIGG8D1.e6086_e5984_s3126_r10724_r10726_p4133
 mc16_13TeV.410658.PhPy8EG_A14_tchan_BW50_lept_top.deriv.DAOD_HIGG8D1.e6671_e5984_s3126_s3136_r10724_r10726_p4133
 mc16_13TeV.410659.PhPy8EG_A14_tchan_BW50_lept_antitop.deriv.DAOD_HIGG8D1.e6671_e5984_s3126_s3136_r10724_r10726_p4133
 mc16_13TeV.410644.PowhegPythia8EvtGen_A14_singletop_schan_lept_top.deriv.DAOD_HIGG8D1.e6527_e5984_s3126_r10724_r10726_p4133
 mc16_13TeV.410645.PowhegPythia8EvtGen_A14_singletop_schan_lept_antitop.deriv.DAOD_HIGG8D1.e6527_e5984_s3126_r10724_r10726_p4133
 mc16_13TeV.304014.MadGraphPythia8EvtGen_A14NNPDF23_3top_SM.deriv.DAOD_HIGG8D1.e4324_e5984_s3126_r10724_r10726_p4133
 mc16_13TeV.410080.MadGraphPythia8EvtGen_A14NNPDF23_4topSM.deriv.DAOD_HIGG8D1.e4111_e5984_s3126_r10724_r10726_p4133
 mc16_13TeV.410081.MadGraphPythia8EvtGen_A14NNPDF23_ttbarWW.deriv.DAOD_HIGG8D1.e4111_e5984_s3126_r10724_r10726_p4133
 mc16_13TeV.364100.Sherpa_221_NNPDF30NNLO_Zmumu_MAXHTPTV0_70_CVetoBVeto.deriv.DAOD_HIGG8D1.e5271_e5984_s3126_s3136_r10724_r10726_p4133
 mc16_13TeV.364100.Sherpa_221_NNPDF30NNLO_Zmumu_MAXHTPTV0_70_CVetoBVeto.deriv.DAOD_HIGG8D1.e5271_e5984_s3126_r10724_r10726_p4133
 mc16_13TeV.364101.Sherpa_221_NNPDF30NNLO_Zmumu_MAXHTPTV0_70_CFilterBVeto.deriv.DAOD_HIGG8D1.e5271_e5984_s3126_r10724_r10726_p4133
 mc16_13TeV.364102.Sherpa_221_NNPDF30NNLO_Zmumu_MAXHTPTV0_70_BFilter.deriv.DAOD_HIGG8D1.e5271_e5984_s3126_s3136_r10724_r10726_p4133
 mc16_13TeV.364102.Sherpa_221_NNPDF30NNLO_Zmumu_MAXHTPTV0_70_BFilter.deriv.DAOD_HIGG8D1.e5271_e5984_s3126_r10724_r10726_p4133
 mc16_13TeV.364103.Sherpa_221_NNPDF30NNLO_Zmumu_MAXHTPTV70_140_CVetoBVeto.deriv.DAOD_HIGG8D1.e5271_e5984_s3126_r10724_r10726_p4133
 mc16_13TeV.364103.Sherpa_221_NNPDF30NNLO_Zmumu_MAXHTPTV70_140_CVetoBVeto.deriv.DAOD_HIGG8D1.e5271_e5984_s3126_s3136_r10724_r10726_p4133
 mc16_13TeV.364104.Sherpa_221_NNPDF30NNLO_Zmumu_MAXHTPTV70_140_CFilterBVeto.deriv.DAOD_HIGG8D1.e5271_e5984_s3126_r10724_r10726_p4133
 mc16_13TeV.364106.Sherpa_221_NNPDF30NNLO_Zmumu_MAXHTPTV140_280_CVetoBVeto.deriv.DAOD_HIGG8D1.e5271_e5984_s3126_s3136_r10724_r10726_p4133
 mc16_13TeV.364106.Sherpa_221_NNPDF30NNLO_Zmumu_MAXHTPTV140_280_CVetoBVeto.deriv.DAOD_HIGG8D1.e5271_e5984_s3126_r10724_r10726_p4133
 mc16_13TeV.364107.Sherpa_221_NNPDF30NNLO_Zmumu_MAXHTPTV140_280_CFilterBVeto.deriv.DAOD_HIGG8D1.e5271_e5984_s3126_r10724_r10726_p4133
 mc16_13TeV.364107.Sherpa_221_NNPDF30NNLO_Zmumu_MAXHTPTV140_280_CFilterBVeto.deriv.DAOD_HIGG8D1.e5271_e5984_s3126_s3136_r10724_r10726_p4133
 mc16_13TeV.364108.Sherpa_221_NNPDF30NNLO_Zmumu_MAXHTPTV140_280_BFilter.deriv.DAOD_HIGG8D1.e5271_e5984_s3126_r10724_r10726_p4133
 mc16_13TeV.364109.Sherpa_221_NNPDF30NNLO_Zmumu_MAXHTPTV280_500_CVetoBVeto.deriv.DAOD_HIGG8D1.e5271_e5984_s3126_r10724_r10726_p4133
 mc16_13TeV.364110.Sherpa_221_NNPDF30NNLO_Zmumu_MAXHTPTV280_500_CFilterBVeto.deriv.DAOD_HIGG8D1.e5271_e5984_s3126_r10724_r10726_p4133
 mc16_13TeV.364110.Sherpa_221_NNPDF30NNLO_Zmumu_MAXHTPTV280_500_CFilterBVeto.deriv.DAOD_HIGG8D1.e5271_e5984_s3126_s3136_r10724_r10726_p4133
 mc16_13TeV.364111.Sherpa_221_NNPDF30NNLO_Zmumu_MAXHTPTV280_500_BFilter.deriv.DAOD_HIGG8D1.e5271_e5984_s3126_s3136_r10724_r10726_p4133
 mc16_13TeV.364111.Sherpa_221_NNPDF30NNLO_Zmumu_MAXHTPTV280_500_BFilter.deriv.DAOD_HIGG8D1.e5271_e5984_s3126_r10724_r10726_p4133
 mc16_13TeV.364112.Sherpa_221_NNPDF30NNLO_Zmumu_MAXHTPTV500_1000.deriv.DAOD_HIGG8D1.e5271_e5984_s3126_r10724_r10726_p4133
 mc16_13TeV.364113.Sherpa_221_NNPDF30NNLO_Zmumu_MAXHTPTV1000_E_CMS.deriv.DAOD_HIGG8D1.e5271_e5984_s3126_r10724_r10726_p4133
 mc16_13TeV.364113.Sherpa_221_NNPDF30NNLO_Zmumu_MAXHTPTV1000_E_CMS.deriv.DAOD_HIGG8D1.e5271_e5984_s3126_s3136_r10724_r10726_p4133
 mc16_13TeV.364114.Sherpa_221_NNPDF30NNLO_Zee_MAXHTPTV0_70_CVetoBVeto.deriv.DAOD_HIGG8D1.e5299_e5984_s3126_s3136_r10724_r10726_p4133

mc16_13TeV.364114.Sherpa_221_NNPDF30NNLO_Zee_MAXHTPTV0_70_CVetoBVeto.deriv.DAOD_HIGG8D1.e5299_e5984_s3126_r10724_r10726_p4133
 mc16_13TeV.364115.Sherpa_221_NNPDF30NNLO_Zee_MAXHTPTV0_70_CFilterBVeto.deriv.DAOD_HIGG8D1.e5299_e5984_s3126_s3136_r10724_r10726_p4133
 mc16_13TeV.364115.Sherpa_221_NNPDF30NNLO_Zee_MAXHTPTV0_70_CFilterBVeto.deriv.DAOD_HIGG8D1.e5299_e5984_s3126_r10724_r10726_p4133
 mc16_13TeV.364116.Sherpa_221_NNPDF30NNLO_Zee_MAXHTPTV0_70_BFilter.deriv.DAOD_HIGG8D1.e5299_e5984_s3126_r10724_r10726_p4133
 mc16_13TeV.364117.Sherpa_221_NNPDF30NNLO_Zee_MAXHTPTV70_140_CVetoBVeto.deriv.DAOD_HIGG8D1.e5299_e5984_s3126_s3136_r10724_r10726_p4133
 mc16_13TeV.364117.Sherpa_221_NNPDF30NNLO_Zee_MAXHTPTV70_140_CFilterBVeto.deriv.DAOD_HIGG8D1.e5299_e5984_s3126_r10724_r10726_p4133
 mc16_13TeV.364118.Sherpa_221_NNPDF30NNLO_Zee_MAXHTPTV70_140_CFilterBVeto.deriv.DAOD_HIGG8D1.e5299_e5984_s3126_s3136_r10724_r10726_p4133
 mc16_13TeV.364118.Sherpa_221_NNPDF30NNLO_Zee_MAXHTPTV70_140_CFilterBVeto.deriv.DAOD_HIGG8D1.e5299_e5984_s3126_r10724_r10726_p4133
 mc16_13TeV.364119.Sherpa_221_NNPDF30NNLO_Zee_MAXHTPTV70_140_BFilter.deriv.DAOD_HIGG8D1.e5299_e5984_s3126_r10724_r10726_p4133
 mc16_13TeV.364120.Sherpa_221_NNPDF30NNLO_Zee_MAXHTPTV140_280_CVetoBVeto.deriv.DAOD_HIGG8D1.e5299_e5984_s3126_r10724_r10726_p4133
 mc16_13TeV.364121.Sherpa_221_NNPDF30NNLO_Zee_MAXHTPTV140_280_CFilterBVeto.deriv.DAOD_HIGG8D1.e5299_e5984_s3126_r10724_r10726_p4133
 mc16_13TeV.364122.Sherpa_221_NNPDF30NNLO_Zee_MAXHTPTV140_280_BFilter.deriv.DAOD_HIGG8D1.e5299_e5984_s3126_s3136_r10724_r10726_p4133
 mc16_13TeV.364122.Sherpa_221_NNPDF30NNLO_Zee_MAXHTPTV140_280_BFilter.deriv.DAOD_HIGG8D1.e5299_e5984_s3126_r10724_r10726_p4133
 mc16_13TeV.364123.Sherpa_221_NNPDF30NNLO_Zee_MAXHTPTV280_500_CVetoBVeto.deriv.DAOD_HIGG8D1.e5299_e5984_s3126_r10724_r10726_p4133
 mc16_13TeV.364124.Sherpa_221_NNPDF30NNLO_Zee_MAXHTPTV280_500_CFilterBVeto.deriv.DAOD_HIGG8D1.e5299_e5984_s3126_r10724_r10726_p4133
 mc16_13TeV.364125.Sherpa_221_NNPDF30NNLO_Zee_MAXHTPTV280_500_BFilter.deriv.DAOD_HIGG8D1.e5299_e5984_s3126_s3136_r10724_r10726_p4133
 mc16_13TeV.364125.Sherpa_221_NNPDF30NNLO_Zee_MAXHTPTV280_500_BFilter.deriv.DAOD_HIGG8D1.e5299_e5984_s3126_r10724_r10726_p4133
 mc16_13TeV.364126.Sherpa_221_NNPDF30NNLO_Zee_MAXHTPTV500_1000.deriv.DAOD_HIGG8D1.e5299_e5984_s3126_r10724_r10726_p4133
 mc16_13TeV.364126.Sherpa_221_NNPDF30NNLO_Zee_MAXHTPTV500_1000.deriv.DAOD_HIGG8D1.e5299_e5984_s3126_s3136_r10724_r10726_p4133
 mc16_13TeV.364127.Sherpa_221_NNPDF30NNLO_Zee_MAXHTPTV1000_E_CMS.deriv.DAOD_HIGG8D1.e5299_e5984_s3126_s3136_r10724_r10726_p4133
 mc16_13TeV.364127.Sherpa_221_NNPDF30NNLO_Zee_MAXHTPTV1000_E_CMS.deriv.DAOD_HIGG8D1.e5299_e5984_s3126_r10724_r10726_p4133
 mc16_13TeV.364128.Sherpa_221_NNPDF30NNLO_Ztautau_MAXHTPTV0_70_CVetoBVeto.deriv.DAOD_HIGG8D1.e5307_e5984_s3126_s3136_r10724_r10726_p4133
 mc16_13TeV.364128.Sherpa_221_NNPDF30NNLO_Ztautau_MAXHTPTV0_70_CVetoBVeto.deriv.DAOD_HIGG8D1.e5307_e5984_s3126_r10724_r10726_p4133
 mc16_13TeV.364129.Sherpa_221_NNPDF30NNLO_Ztautau_MAXHTPTV0_70_CFilterBVeto.deriv.DAOD_HIGG8D1.e5307_e5984_s3126_r10724_r10726_p4133
 mc16_13TeV.364129.Sherpa_221_NNPDF30NNLO_Ztautau_MAXHTPTV0_70_CFilterBVeto.deriv.DAOD_HIGG8D1.e5307_e5984_s3126_s3136_r10724_r10726_p4133
 mc16_13TeV.364130.Sherpa_221_NNPDF30NNLO_Ztautau_MAXHTPTV0_70_BFilter.deriv.DAOD_HIGG8D1.e5307_e5984_s3126_s3136_r10724_r10726_p4133
 mc16_13TeV.364130.Sherpa_221_NNPDF30NNLO_Ztautau_MAXHTPTV0_70_BFilter.deriv.DAOD_HIGG8D1.e5307_e5984_s3126_r10724_r10726_p4133
 mc16_13TeV.364131.Sherpa_221_NNPDF30NNLO_Ztautau_MAXHTPTV70_140_CVetoBVeto.deriv.DAOD_HIGG8D1.e5307_e5984_s3126_r10724_r10726_p4133
 mc16_13TeV.364132.Sherpa_221_NNPDF30NNLO_Ztautau_MAXHTPTV70_140_CFilterBVeto.deriv.DAOD_HIGG8D1.e5307_e5984_s3126_r10724_r10726_p4133
 mc16_13TeV.364132.Sherpa_221_NNPDF30NNLO_Ztautau_MAXHTPTV70_140_CFilterBVeto.deriv.DAOD_HIGG8D1.e5307_e5984_s3126_s3136_r10724_r10726_p4133
 mc16_13TeV.364133.Sherpa_221_NNPDF30NNLO_Ztautau_MAXHTPTV70_140_BFilter.deriv.DAOD_HIGG8D1.e5307_e5984_s3126_r10724_r10726_p4133

mc16_13TeV.364134.Sherpa_221_NNPDF30NNLO_Ztautau_MAXHTPTV140_280_CVetoBVeto.deriv.DAOD_HIGG8D1.e5307_e5984_s3126_r10724_r10726_p4133
 mc16_13TeV.364135.Sherpa_221_NNPDF30NNLO_Ztautau_MAXHTPTV140_280_CFilterBVeto.deriv.DAOD_HIGG8D1.e5307_e5984_s3126_r10724_r10726_p4133
 mc16_13TeV.364135.Sherpa_221_NNPDF30NNLO_Ztautau_MAXHTPTV140_280_CFilterBVeto.deriv.DAOD_HIGG8D1.e5307_e5984_s3126_s3136_r10724_r10726_p4133
 mc16_13TeV.364136.Sherpa_221_NNPDF30NNLO_Ztautau_MAXHTPTV140_280_BFilter.deriv.DAOD_HIGG8D1.e5307_e5984_s3126_r10724_r10726_p4133
 mc16_13TeV.364137.Sherpa_221_NNPDF30NNLO_Ztautau_MAXHTPTV280_500_CVetoBVeto.deriv.DAOD_HIGG8D1.e5307_e5984_s3126_r10724_r10726_p4133
 mc16_13TeV.364138.Sherpa_221_NNPDF30NNLO_Ztautau_MAXHTPTV280_500_CFilterBVeto.deriv.DAOD_HIGG8D1.e5313_e5984_s3126_s3136_r10724_r10726_p4133
 mc16_13TeV.364138.Sherpa_221_NNPDF30NNLO_Ztautau_MAXHTPTV280_500_CFilterBVeto.deriv.DAOD_HIGG8D1.e5313_e5984_s3126_r10724_r10726_p4133
 mc16_13TeV.364139.Sherpa_221_NNPDF30NNLO_Ztautau_MAXHTPTV280_500_BFilter.deriv.DAOD_HIGG8D1.e5313_e5984_s3126_r10724_r10726_p4133
 mc16_13TeV.364139.Sherpa_221_NNPDF30NNLO_Ztautau_MAXHTPTV280_500_BFilter.deriv.DAOD_HIGG8D1.e5313_e5984_s3126_s3136_r10724_r10726_p4133
 mc16_13TeV.364140.Sherpa_221_NNPDF30NNLO_Ztautau_MAXHTPTV500_1000.deriv.DAOD_HIGG8D1.e5307_e5984_s3126_r10724_r10726_p4133
 mc16_13TeV.364140.Sherpa_221_NNPDF30NNLO_Ztautau_MAXHTPTV500_1000.deriv.DAOD_HIGG8D1.e5307_e5984_s3126_s3136_r10724_r10726_p4133
 mc16_13TeV.364141.Sherpa_221_NNPDF30NNLO_Ztautau_MAXHTPTV1000_E_CMS.deriv.DAOD_HIGG8D1.e5307_e5984_s3126_s3136_r10724_r10726_p4133
 mc16_13TeV.364141.Sherpa_221_NNPDF30NNLO_Ztautau_MAXHTPTV1000_E_CMS.deriv.DAOD_HIGG8D1.e5307_e5984_s3126_r10724_r10726_p4133
 mc16_13TeV.364198.Sherpa_221_NN30NNLO_Zmm_Mll10_40_MAXHTPTV0_70_BVeto.deriv.DAOD_HIGG8D1.e5421_e5984_s3126_r10724_r10726_p4133
 mc16_13TeV.364199.Sherpa_221_NN30NNLO_Zmm_Mll10_40_MAXHTPTV0_70_BFilter.deriv.DAOD_HIGG8D1.e5421_e5984_s3126_r10724_r10726_p4133
 mc16_13TeV.364200.Sherpa_221_NN30NNLO_Zmm_Mll10_40_MAXHTPTV70_280_BVeto.deriv.DAOD_HIGG8D1.e5421_e5984_s3126_r10724_r10726_p4133
 mc16_13TeV.364201.Sherpa_221_NN30NNLO_Zmm_Mll10_40_MAXHTPTV70_280_BFilter.deriv.DAOD_HIGG8D1.e5421_e5984_s3126_r10724_r10726_p4133
 mc16_13TeV.364202.Sherpa_221_NN30NNLO_Zmm_Mll10_40_MAXHTPTV280_E_CMS_BVeto.deriv.DAOD_HIGG8D1.e5421_e5984_s3126_r10724_r10726_p4133
 mc16_13TeV.364203.Sherpa_221_NN30NNLO_Zmm_Mll10_40_MAXHTPTV280_E_CMS_BFilter.deriv.DAOD_HIGG8D1.e5421_e5984_s3126_r10724_r10726_p4133
 mc16_13TeV.364204.Sherpa_221_NN30NNLO_Zee_Mll10_40_MAXHTPTV0_70_BVeto.deriv.DAOD_HIGG8D1.e5421_e5984_s3126_r10724_r10726_p4133
 mc16_13TeV.364205.Sherpa_221_NN30NNLO_Zee_Mll10_40_MAXHTPTV0_70_BFilter.deriv.DAOD_HIGG8D1.e5421_e5984_s3126_r10724_r10726_p4133
 mc16_13TeV.364206.Sherpa_221_NN30NNLO_Zee_Mll10_40_MAXHTPTV70_280_BVeto.deriv.DAOD_HIGG8D1.e5421_e5984_s3126_r10724_r10726_p4133
 mc16_13TeV.364207.Sherpa_221_NN30NNLO_Zee_Mll10_40_MAXHTPTV70_280_BFilter.deriv.DAOD_HIGG8D1.e5421_e5984_s3126_r10724_r10726_p4133
 mc16_13TeV.364208.Sherpa_221_NN30NNLO_Zee_Mll10_40_MAXHTPTV280_E_CMS_BVeto.deriv.DAOD_HIGG8D1.e5421_e5984_s3126_r10724_r10726_p4133
 mc16_13TeV.364209.Sherpa_221_NN30NNLO_Zee_Mll10_40_MAXHTPTV280_E_CMS_BFilter.deriv.DAOD_HIGG8D1.e5421_e5984_s3126_r10724_r10726_p4133
 mc16_13TeV.364210.Sherpa_221_NN30NNLO_Ztt_Mll10_40_MAXHTPTV0_70_BVeto.deriv.DAOD_HIGG8D1.e5421_e5984_s3126_r10724_r10726_p4133
 mc16_13TeV.364211.Sherpa_221_NN30NNLO_Ztt_Mll10_40_MAXHTPTV0_70_BFilter.deriv.DAOD_HIGG8D1.e5421_e5984_s3126_r10724_r10726_p4133
 mc16_13TeV.364212.Sherpa_221_NN30NNLO_Ztt_Mll10_40_MAXHTPTV70_280_BVeto.deriv.DAOD_HIGG8D1.e5421_e5984_s3126_r10724_r10726_p4133
 mc16_13TeV.364213.Sherpa_221_NN30NNLO_Ztt_Mll10_40_MAXHTPTV70_280_BFilter.deriv.DAOD_HIGG8D1.e5421_e5984_s3126_r10724_r10726_p4133
 mc16_13TeV.364214.Sherpa_221_NN30NNLO_Ztt_Mll10_40_MAXHTPTV280_E_CMS_BVeto.deriv.DAOD_HIGG8D1.e5421_e5984_s3126_r10724_r10726_p4133
 mc16_13TeV.364215.Sherpa_221_NN30NNLO_Ztt_Mll10_40_MAXHTPTV280_E_CMS_BFilter.deriv.DAOD_HIGG8D1.e5421_e5984_s3126_r10724_r10726_p4133

mc16_13TeV.364156.Sherpa_221_NNPDF30NNLO_Wmunu_MAXHTPTV0_70_CVetoBVeto.deriv.DAOD_HIGG8D1.e5340_e5984_s3126_r10724_r10726_p4133
 mc16_13TeV.364157.Sherpa_221_NNPDF30NNLO_Wmunu_MAXHTPTV0_70_CFilterBVeto.deriv.DAOD_HIGG8D1.e5340_e5984_s3126_r10724_r10726_p4133
 mc16_13TeV.364158.Sherpa_221_NNPDF30NNLO_Wmunu_MAXHTPTV0_70_BFilter.deriv.DAOD_HIGG8D1.e5340_e5984_s3126_s3136_r10724_r10726_p4133
 mc16_13TeV.364158.Sherpa_221_NNPDF30NNLO_Wmunu_MAXHTPTV0_70_BFilter.deriv.DAOD_HIGG8D1.e5340_e5984_s3126_r10724_r10726_p4133
 mc16_13TeV.364159.Sherpa_221_NNPDF30NNLO_Wmunu_MAXHTPTV70_140_CVetoBVeto.deriv.DAOD_HIGG8D1.e5340_e5984_s3126_s3136_r10724_r10726_p4133
 mc16_13TeV.364160.Sherpa_221_NNPDF30NNLO_Wmunu_MAXHTPTV70_140_CFilterBVeto.deriv.DAOD_HIGG8D1.e5340_e5984_s3126_s3136_r10724_r10726_p4133
 mc16_13TeV.364160.Sherpa_221_NNPDF30NNLO_Wmunu_MAXHTPTV70_140_CFilterBVeto.deriv.DAOD_HIGG8D1.e5340_e5984_s3126_r10724_r10726_p4133
 mc16_13TeV.364161.Sherpa_221_NNPDF30NNLO_Wmunu_MAXHTPTV70_140_BFilter.deriv.DAOD_HIGG8D1.e5340_e5984_s3126_r10724_r10726_p4133
 mc16_13TeV.364162.Sherpa_221_NNPDF30NNLO_Wmunu_MAXHTPTV140_280_CVetoBVeto.deriv.DAOD_HIGG8D1.e5340_e5984_s3126_r10724_r10726_p4133
 mc16_13TeV.364163.Sherpa_221_NNPDF30NNLO_Wmunu_MAXHTPTV140_280_CFilterBVeto.deriv.DAOD_HIGG8D1.e5340_e5984_s3126_s3136_r10724_r10726_p4133
 mc16_13TeV.364163.Sherpa_221_NNPDF30NNLO_Wmunu_MAXHTPTV140_280_CFilterBVeto.deriv.DAOD_HIGG8D1.e5340_e5984_s3126_r10724_r10726_p4133
 mc16_13TeV.364164.Sherpa_221_NNPDF30NNLO_Wmunu_MAXHTPTV140_280_BFilter.deriv.DAOD_HIGG8D1.e5340_e5984_s3126_r10724_r10726_p4133
 mc16_13TeV.364165.Sherpa_221_NNPDF30NNLO_Wmunu_MAXHTPTV280_500_CVetoBVeto.deriv.DAOD_HIGG8D1.e5340_e5984_s3126_r10724_r10726_p4133
 mc16_13TeV.364165.Sherpa_221_NNPDF30NNLO_Wmunu_MAXHTPTV280_500_CVetoBVeto.deriv.DAOD_HIGG8D1.e5340_e5984_s3126_s3136_r10724_r10726_p4133
 mc16_13TeV.364166.Sherpa_221_NNPDF30NNLO_Wmunu_MAXHTPTV280_500_CFilterBVeto.deriv.DAOD_HIGG8D1.e5340_e5984_s3126_s3136_r10724_r10726_p4133
 mc16_13TeV.364166.Sherpa_221_NNPDF30NNLO_Wmunu_MAXHTPTV280_500_CFilterBVeto.deriv.DAOD_HIGG8D1.e5340_e5984_s3126_r10724_r10726_p4133
 mc16_13TeV.364167.Sherpa_221_NNPDF30NNLO_Wmunu_MAXHTPTV280_500_BFilter.deriv.DAOD_HIGG8D1.e5340_e5984_s3126_r10724_r10726_p4133
 mc16_13TeV.364167.Sherpa_221_NNPDF30NNLO_Wmunu_MAXHTPTV280_500_BFilter.deriv.DAOD_HIGG8D1.e5340_e5984_s3126_s3136_r10724_r10726_p4133
 mc16_13TeV.364168.Sherpa_221_NNPDF30NNLO_Wmunu_MAXHTPTV500_1000.deriv.DAOD_HIGG8D1.e5340_e5984_s3126_r10724_r10726_p4133
 mc16_13TeV.364168.Sherpa_221_NNPDF30NNLO_Wmunu_MAXHTPTV500_1000.deriv.DAOD_HIGG8D1.e5340_e5984_s3126_s3136_r10724_r10726_p4133
 mc16_13TeV.364169.Sherpa_221_NNPDF30NNLO_Wmunu_MAXHTPTV1000_E_CMS.deriv.DAOD_HIGG8D1.e5340_e5984_s3126_s3136_r10724_r10726_p4133
 mc16_13TeV.364169.Sherpa_221_NNPDF30NNLO_Wmunu_MAXHTPTV1000_E_CMS.deriv.DAOD_HIGG8D1.e5340_e5984_s3126_r10724_r10726_p4133
 mc16_13TeV.364170.Sherpa_221_NNPDF30NNLO_Wenu_MAXHTPTV0_70_CVetoBVeto.deriv.DAOD_HIGG8D1.e5340_e5984_s3126_r10724_r10726_p4133
 mc16_13TeV.364171.Sherpa_221_NNPDF30NNLO_Wenu_MAXHTPTV0_70_CFilterBVeto.deriv.DAOD_HIGG8D1.e5340_e5984_s3126_r10724_r10726_p4133
 mc16_13TeV.364172.Sherpa_221_NNPDF30NNLO_Wenu_MAXHTPTV0_70_BFilter.deriv.DAOD_HIGG8D1.e5340_e5984_s3126_r10724_r10726_p4133
 mc16_13TeV.364173.Sherpa_221_NNPDF30NNLO_Wenu_MAXHTPTV70_140_CVetoBVeto.deriv.DAOD_HIGG8D1.e5340_e5984_s3126_s3136_r10724_r10726_p4133
 mc16_13TeV.364174.Sherpa_221_NNPDF30NNLO_Wenu_MAXHTPTV70_140_CFilterBVeto.deriv.DAOD_HIGG8D1.e5340_e5984_s3126_r10724_r10726_p4133
 mc16_13TeV.364175.Sherpa_221_NNPDF30NNLO_Wenu_MAXHTPTV70_140_BFilter.deriv.DAOD_HIGG8D1.e5340_e5984_s3126_s3136_r10724_r10726_p4133
 mc16_13TeV.364176.Sherpa_221_NNPDF30NNLO_Wenu_MAXHTPTV140_280_CVetoBVeto.deriv.DAOD_HIGG8D1.e5340_e5984_s3126_r10724_r10726_p4133
 mc16_13TeV.364177.Sherpa_221_NNPDF30NNLO_Wenu_MAXHTPTV140_280_CFilterBVeto.deriv.DAOD_HIGG8D1.e5340_e5984_s3126_r10724_r10726_p4133
 mc16_13TeV.364177.Sherpa_221_NNPDF30NNLO_Wenu_MAXHTPTV140_280_CFilterBVeto.deriv.DAOD_HIGG8D1.e5340_e5984_s3126_s3136_r10724_r10726_p4133

mc16_13TeV.364178.Sherpa_221_NNPDF30NNLO_Wenu_MAXHTPTV140_280_BFilter.deriv.DAOD_HIGG8D1.e5340_e5984_s3126_r10724_r10726_p4133
 mc16_13TeV.364179.Sherpa_221_NNPDF30NNLO_Wenu_MAXHTPTV280_500_CVetoBVeto.deriv.DAOD_HIGG8D1.e5340_e5984_s3126_r10724_r10726_p4133
 mc16_13TeV.364179.Sherpa_221_NNPDF30NNLO_Wenu_MAXHTPTV280_500_CVetoBVeto.deriv.DAOD_HIGG8D1.e5340_e5984_s3126_s3136_r10724_r10726_p4133
 mc16_13TeV.364180.Sherpa_221_NNPDF30NNLO_Wenu_MAXHTPTV280_500_CFilterBVeto.deriv.DAOD_HIGG8D1.e5340_e5984_s3126_s3136_r10724_r10726_p4133
 mc16_13TeV.364180.Sherpa_221_NNPDF30NNLO_Wenu_MAXHTPTV280_500_CFilterBVeto.deriv.DAOD_HIGG8D1.e5340_e5984_s3126_r10724_r10726_p4133
 mc16_13TeV.364181.Sherpa_221_NNPDF30NNLO_Wenu_MAXHTPTV280_500_BFilter.deriv.DAOD_HIGG8D1.e5340_e5984_s3126_s3136_r10724_r10726_p4133
 mc16_13TeV.364181.Sherpa_221_NNPDF30NNLO_Wenu_MAXHTPTV280_500_BFilter.deriv.DAOD_HIGG8D1.e5340_e5984_s3126_r10724_r10726_p4133
 mc16_13TeV.364182.Sherpa_221_NNPDF30NNLO_Wenu_MAXHTPTV500_1000.deriv.DAOD_HIGG8D1.e5340_e5984_s3126_s3136_r10724_r10726_p4133
 mc16_13TeV.364182.Sherpa_221_NNPDF30NNLO_Wenu_MAXHTPTV500_1000.deriv.DAOD_HIGG8D1.e5340_e5984_s3126_r10724_r10726_p4133
 mc16_13TeV.364183.Sherpa_221_NNPDF30NNLO_Wenu_MAXHTPTV1000_E_CMS.deriv.DAOD_HIGG8D1.e5340_e5984_s3126_r10724_r10726_p4133
 mc16_13TeV.364183.Sherpa_221_NNPDF30NNLO_Wenu_MAXHTPTV1000_E_CMS.deriv.DAOD_HIGG8D1.e5340_e5984_s3126_s3136_r10724_r10726_p4133
 mc16_13TeV.364184.Sherpa_221_NNPDF30NNLO_Wtaunu_MAXHTPTV0_70_CVetoBVeto.deriv.DAOD_HIGG8D1.e5340_e5984_s3126_r10724_r10726_p4133
 mc16_13TeV.364185.Sherpa_221_NNPDF30NNLO_Wtaunu_MAXHTPTV0_70_CFilterBVeto.deriv.DAOD_HIGG8D1.e5340_e5984_s3126_r10724_r10726_p4133
 mc16_13TeV.364186.Sherpa_221_NNPDF30NNLO_Wtaunu_MAXHTPTV0_70_BFilter.deriv.DAOD_HIGG8D1.e5340_e5984_s3126_s3136_r10724_r10726_p4133
 mc16_13TeV.364186.Sherpa_221_NNPDF30NNLO_Wtaunu_MAXHTPTV0_70_BFilter.deriv.DAOD_HIGG8D1.e5340_e5984_s3126_r10724_r10726_p4133
 mc16_13TeV.364187.Sherpa_221_NNPDF30NNLO_Wtaunu_MAXHTPTV70_140_CVetoBVeto.deriv.DAOD_HIGG8D1.e5340_e5984_s3126_r10724_r10726_p4133
 mc16_13TeV.364188.Sherpa_221_NNPDF30NNLO_Wtaunu_MAXHTPTV70_140_CFilterBVeto.deriv.DAOD_HIGG8D1.e5340_e5984_s3126_r10724_r10726_p4133
 mc16_13TeV.364189.Sherpa_221_NNPDF30NNLO_Wtaunu_MAXHTPTV70_140_BFilter.deriv.DAOD_HIGG8D1.e5340_e5984_s3126_r10724_r10726_p4133
 mc16_13TeV.364189.Sherpa_221_NNPDF30NNLO_Wtaunu_MAXHTPTV70_140_BFilter.deriv.DAOD_HIGG8D1.e5340_e5984_s3126_s3136_r10724_r10726_p4133
 mc16_13TeV.364190.Sherpa_221_NNPDF30NNLO_Wtaunu_MAXHTPTV140_280_CVetoBVeto.deriv.DAOD_HIGG8D1.e5340_e5984_s3126_r10724_r10726_p4133
 mc16_13TeV.364190.Sherpa_221_NNPDF30NNLO_Wtaunu_MAXHTPTV140_280_CVetoBVeto.deriv.DAOD_HIGG8D1.e5340_e5984_s3126_s3136_r10724_r10726_p4133
 mc16_13TeV.364191.Sherpa_221_NNPDF30NNLO_Wtaunu_MAXHTPTV140_280_CFilterBVeto.deriv.DAOD_HIGG8D1.e5340_e5984_s3126_r10724_r10726_p4133
 mc16_13TeV.364191.Sherpa_221_NNPDF30NNLO_Wtaunu_MAXHTPTV140_280_CFilterBVeto.deriv.DAOD_HIGG8D1.e5340_e5984_s3126_s3136_r10724_r10726_p4133
 mc16_13TeV.364192.Sherpa_221_NNPDF30NNLO_Wtaunu_MAXHTPTV140_280_BFilter.deriv.DAOD_HIGG8D1.e5340_e5984_s3126_s3136_r10724_r10726_p4133
 mc16_13TeV.364192.Sherpa_221_NNPDF30NNLO_Wtaunu_MAXHTPTV140_280_BFilter.deriv.DAOD_HIGG8D1.e5340_e5984_s3126_r10724_r10726_p4133
 mc16_13TeV.364193.Sherpa_221_NNPDF30NNLO_Wtaunu_MAXHTPTV280_500_CVetoBVeto.deriv.DAOD_HIGG8D1.e5340_e5984_s3126_s3136_r10724_r10726_p4133
 mc16_13TeV.364193.Sherpa_221_NNPDF30NNLO_Wtaunu_MAXHTPTV280_500_CVetoBVeto.deriv.DAOD_HIGG8D1.e5340_e5984_s3126_s3136_r10724_r10726_p4133
 mc16_13TeV.364194.Sherpa_221_NNPDF30NNLO_Wtaunu_MAXHTPTV280_500_CFilterBVeto.deriv.DAOD_HIGG8D1.e5340_e5984_s3126_s3136_r10724_r10726_p4133
 mc16_13TeV.364194.Sherpa_221_NNPDF30NNLO_Wtaunu_MAXHTPTV280_500_CFilterBVeto.deriv.DAOD_HIGG8D1.e5340_e5984_s3126_r10724_r10726_p4133
 mc16_13TeV.364195.Sherpa_221_NNPDF30NNLO_Wtaunu_MAXHTPTV280_500_BFilter.deriv.DAOD_HIGG8D1.e5340_e5984_s3126_s3136_r10724_r10726_p4133
 mc16_13TeV.364195.Sherpa_221_NNPDF30NNLO_Wtaunu_MAXHTPTV280_500_BFilter.deriv.DAOD_HIGG8D1.e5340_e5984_s3126_r10724_r10726_p4133

mc16_13TeV.364196.Sherpa_221_NNPDF30NNLO_Wtaunu_MAXHTPTV500_1000.deriv.DAOD_HIGG8D1.e5340_e5984_s3126_s3136_r10724_r10726_p4133
 mc16_13TeV.364196.Sherpa_221_NNPDF30NNLO_Wtaunu_MAXHTPTV500_1000.deriv.DAOD_HIGG8D1.e5340_e5984_s3126_r10724_r10726_p4133
 mc16_13TeV.364197.Sherpa_221_NNPDF30NNLO_Wtaunu_MAXHTPTV1000_E_CMS.deriv.DAOD_HIGG8D1.e5340_e5984_s3126_s3136_r10724_r10726_p4133
 mc16_13TeV.364197.Sherpa_221_NNPDF30NNLO_Wtaunu_MAXHTPTV1000_E_CMS.deriv.DAOD_HIGG8D1.e5340_e5984_s3126_r10724_r10726_p4133
 mc16_13TeV.364500.Sherpa_222_NNPDF30NNLO_eegamma_pty_7_15.deriv.DAOD_HIGG8D1.e5928_e5984_s3126_r10724_r10726_p4133
 mc16_13TeV.364501.Sherpa_222_NNPDF30NNLO_eegamma_pty_15_35.deriv.DAOD_HIGG8D1.e5928_e5984_s3126_r10724_r10726_p4133
 mc16_13TeV.364502.Sherpa_222_NNPDF30NNLO_eegamma_pty_35_70.deriv.DAOD_HIGG8D1.e5928_e5984_s3126_r10724_r10726_p4133
 mc16_13TeV.364503.Sherpa_222_NNPDF30NNLO_eegamma_pty_70_140.deriv.DAOD_HIGG8D1.e5928_e5984_s3126_r10724_r10726_p4133
 mc16_13TeV.364504.Sherpa_222_NNPDF30NNLO_eegamma_pty_140_E_CMS.deriv.DAOD_HIGG8D1.e5928_e5984_s3126_r10724_r10726_p4133
 mc16_13TeV.364505.Sherpa_222_NNPDF30NNLO_mumugamma_pty_7_15.deriv.DAOD_HIGG8D1.e5928_e5984_s3126_r10724_r10726_p4133
 mc16_13TeV.364506.Sherpa_222_NNPDF30NNLO_mumugamma_pty_15_35.deriv.DAOD_HIGG8D1.e5928_e5984_s3126_r10724_r10726_p4133
 mc16_13TeV.364507.Sherpa_222_NNPDF30NNLO_mumugamma_pty_35_70.deriv.DAOD_HIGG8D1.e5928_e5984_s3126_r10724_r10726_p4133
 mc16_13TeV.364508.Sherpa_222_NNPDF30NNLO_mumugamma_pty_70_140.deriv.DAOD_HIGG8D1.e5928_e5984_s3126_r10724_r10726_p4133
 mc16_13TeV.364509.Sherpa_222_NNPDF30NNLO_mumugamma_pty_140_E_CMS.deriv.DAOD_HIGG8D1.e5928_e5984_s3126_r10724_r10726_p4133
 mc16_13TeV.364511.Sherpa_222_NNPDF30NNLO_tautaugamma_pty_15_35.deriv.DAOD_HIGG8D1.e5928_e5984_s3126_r10724_r10726_p4133
 mc16_13TeV.364512.Sherpa_222_NNPDF30NNLO_tautaugamma_pty_35_70.deriv.DAOD_HIGG8D1.e5928_e5984_s3126_r10724_r10726_p4133
 mc16_13TeV.364513.Sherpa_222_NNPDF30NNLO_tautaugamma_pty_70_140.deriv.DAOD_HIGG8D1.e5982_e5984_s3126_r10724_r10726_p4133
 mc16_13TeV.364514.Sherpa_222_NNPDF30NNLO_tautaugamma_pty_140_E_CMS.deriv.DAOD_HIGG8D1.e5928_e5984_s3126_r10724_r10726_p4133
 mc16_13TeV.364522.Sherpa_222_NNPDF30NNLO_enugamma_pty_15_35.deriv.DAOD_HIGG8D1.e5928_e5984_s3126_r10724_r10726_p4133
 mc16_13TeV.364523.Sherpa_222_NNPDF30NNLO_enugamma_pty_35_70.deriv.DAOD_HIGG8D1.e5928_e5984_s3126_r10724_r10726_p4133
 mc16_13TeV.364524.Sherpa_222_NNPDF30NNLO_enugamma_pty_70_140.deriv.DAOD_HIGG8D1.e5928_e5984_s3126_r10724_r10726_p4133
 mc16_13TeV.364525.Sherpa_222_NNPDF30NNLO_enugamma_pty_140_E_CMS.deriv.DAOD_HIGG8D1.e5928_e5984_s3126_r10724_r10726_p4133
 mc16_13TeV.364527.Sherpa_222_NNPDF30NNLO_munugamma_pty_15_35.deriv.DAOD_HIGG8D1.e5928_e5984_s3126_r10724_r10726_p4133
 mc16_13TeV.364528.Sherpa_222_NNPDF30NNLO_munugamma_pty_35_70.deriv.DAOD_HIGG8D1.e5928_e5984_s3126_r10724_r10726_p4133
 mc16_13TeV.364529.Sherpa_222_NNPDF30NNLO_munugamma_pty_70_140.deriv.DAOD_HIGG8D1.e5928_e5984_s3126_r10724_r10726_p4133
 mc16_13TeV.364530.Sherpa_222_NNPDF30NNLO_munugamma_pty_140_E_CMS.deriv.DAOD_HIGG8D1.e5928_e5984_s3126_r10724_r10726_p4133
 mc16_13TeV.364532.Sherpa_222_NNPDF30NNLO_taunugamma_pty_15_35.deriv.DAOD_HIGG8D1.e5928_e5984_s3126_r10724_r10726_p4133
 mc16_13TeV.364533.Sherpa_222_NNPDF30NNLO_taunugamma_pty_35_70.deriv.DAOD_HIGG8D1.e5928_e5984_s3126_r10724_r10726_p4133
 mc16_13TeV.364534.Sherpa_222_NNPDF30NNLO_taunugamma_pty_70_140.deriv.DAOD_HIGG8D1.e5928_e5984_s3126_r10724_r10726_p4133
 mc16_13TeV.364535.Sherpa_222_NNPDF30NNLO_taunugamma_pty_140_E_CMS.deriv.DAOD_HIGG8D1.e5928_e5984_s3126_r10724_r10726_p4133
 mc16_13TeV.410560.MadGraphPythia8EvtGen_A14_tZ_4fl_tchan_noAllHad.deriv.DAOD_HIGG8D1.e5803_e5984_s3126_r10724_r10726_p4133

mc16_13TeV.410408.aMcAtNloPythia8EvtGen_tWZ_Ztoll_minDR1.deriv.DAOD_HIGG8D1.e6423_e5984_s3126_r10724_r10726_p4133
mc16_13TeV.364242.Sherpa_222_NNPDF30NNLO_WWW_3l3v_EW6.deriv.DAOD_HIGG8D1.e5887_e5984_s3126_r10724_r10726_p4133
mc16_13TeV.364243.Sherpa_222_NNPDF30NNLO_WWZ_4l2v_EW6.deriv.DAOD_HIGG8D1.e5887_e5984_s3126_r10724_r10726_p4133
mc16_13TeV.364244.Sherpa_222_NNPDF30NNLO_WWZ_2l4v_EW6.deriv.DAOD_HIGG8D1.e5887_e5984_s3126_r10724_r10726_p4133
mc16_13TeV.364245.Sherpa_222_NNPDF30NNLO_WZZ_5l1v_EW6.deriv.DAOD_HIGG8D1.e5887_e5984_s3126_r10724_r10726_p4133
mc16_13TeV.364246.Sherpa_222_NNPDF30NNLO_WZZ_3l3v_EW6.deriv.DAOD_HIGG8D1.e5887_e5984_s3126_r10724_r10726_p4133
mc16_13TeV.364247.Sherpa_222_NNPDF30NNLO_ZZZ_6l0v_EW6.deriv.DAOD_HIGG8D1.e5887_e5984_s3126_r10724_r10726_p4133
mc16_13TeV.364248.Sherpa_222_NNPDF30NNLO_ZZZ_4l2v_EW6.deriv.DAOD_HIGG8D1.e5887_e5984_s3126_r10724_r10726_p4133
mc16_13TeV.364249.Sherpa_222_NNPDF30NNLO_ZZZ_2l4v_EW6.deriv.DAOD_HIGG8D1.e5887_e5984_s3126_r10724_r10726_p4133
mc16_13TeV.342284.Pythia8EvtGen_A14NNPDF23LO_WH125_inc.deriv.DAOD_HIGG8D1.e4246_e5984_s3126_r10724_r10726_p4133
mc16_13TeV.342285.Pythia8EvtGen_A14NNPDF23LO_ZH125_inc.deriv.DAOD_HIGG8D1.e4246_e5984_s3126_r10724_r10726_p4133
mc16_13TeV.341998.aMcAtNloHppEG_UEEE5_CTEQ6L1_CT10ME_tWH125_gamgam_yt_plus1.deriv.DAOD_HIGG8D1.e4394_e5984_s3126_r10724_r10726_p4133
mc16_13TeV.410389.MadGraphPythia8EvtGen_A14NNPDF23_ttgamma_nonallhadronic.deriv.DAOD_HIGG8D1.e6155_e5984_s3126_r10724_r10726_p4133
mc16_13TeV.410470.PhPy8EG_A14_ttbar_hdamp258p75_nonallhad.deriv.DAOD_HIGG8D1.e6337_e5984_s3126_r10724_r10726_p4133
mc16_13TeV.410472.PhPy8EG_A14_ttbar_hdamp258p75_dil.deriv.DAOD_HIGG8D1.e6348_e5984_s3126_r10724_r10726_p4133
mc16_13TeV.346343.PhPy8EG_A14NNPDF23_NNPDF30ME_ttH125_allhad.deriv.DAOD_HIGG8D1.e7148_e5984_s3126_r10724_r10726_p4133
mc16_13TeV.346343.PhPy8EG_A14NNPDF23_NNPDF30ME_ttH125_allhad.deriv.DAOD_HIGG8D1.e7148_e5984_a875_r10724_r10726_p4133
mc16_13TeV.346344.PhPy8EG_A14NNPDF23_NNPDF30ME_ttH125_semilep.deriv.DAOD_HIGG8D1.e7148_e5984_a875_r10724_r10726_p4133
mc16_13TeV.346344.PhPy8EG_A14NNPDF23_NNPDF30ME_ttH125_semilep.deriv.DAOD_HIGG8D1.e7148_e5984_s3126_r10724_r10726_p4133
mc16_13TeV.346345.PhPy8EG_A14NNPDF23_NNPDF30ME_ttH125_dilep.deriv.DAOD_HIGG8D1.e7148_e5984_a875_r10724_r10726_p4133
mc16_13TeV.346345.PhPy8EG_A14NNPDF23_NNPDF30ME_ttH125_dilep.deriv.DAOD_HIGG8D1.e7148_e5984_s3126_r10724_r10726_p4133

¹⁷⁴⁷ **A Machine Learning Models**

¹⁷⁴⁸ The following section provides details of the various MVAs as well as a few studies performed
¹⁷⁴⁹ in support of this analysis, exploring alternate decisions and strategies.

¹⁷⁵⁰ **A.1 Higgs Reconstruction Models**

¹⁷⁵¹ **A.1.1 b-jet Identification Features - 2lSS**

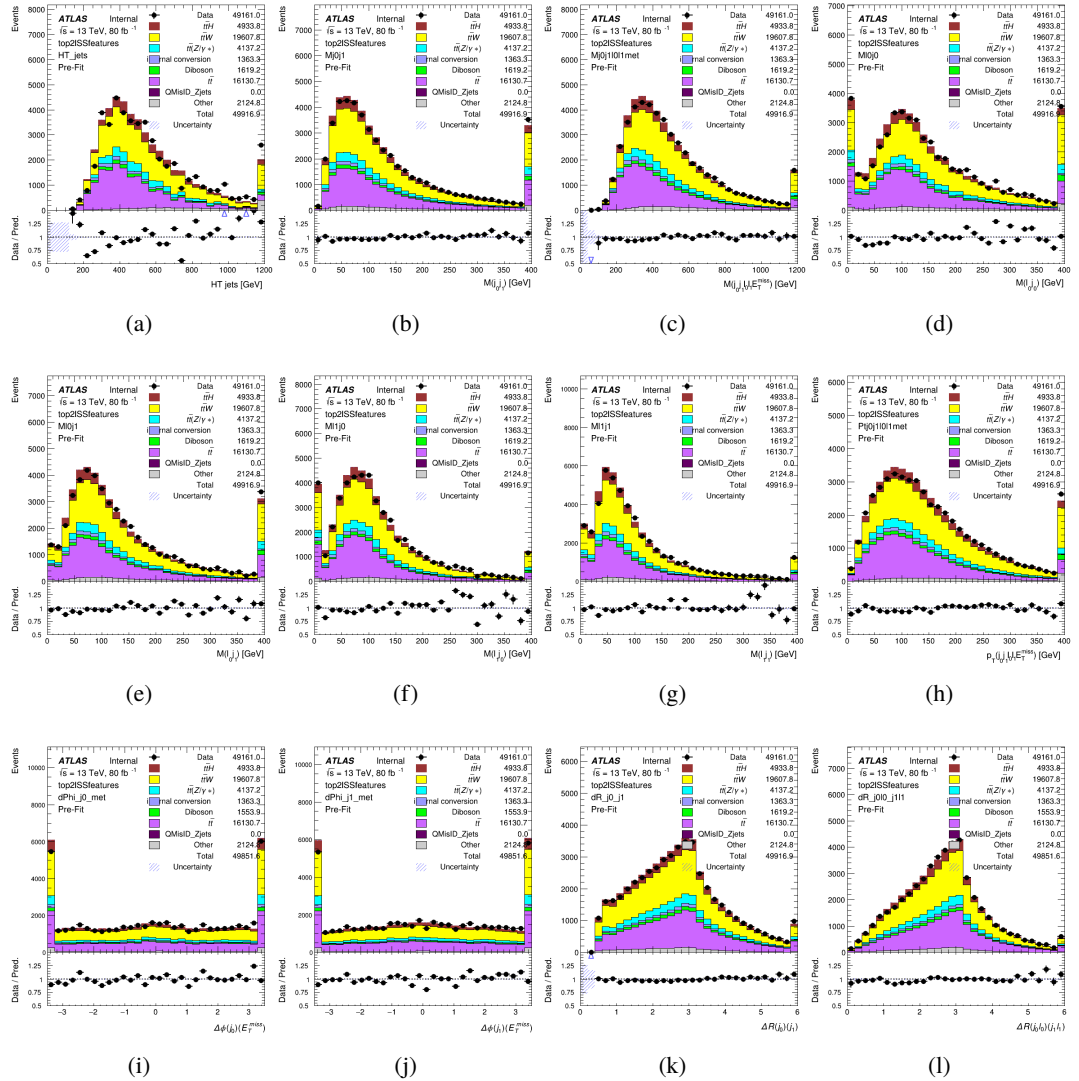


Figure A.1: Input features for top2lSS

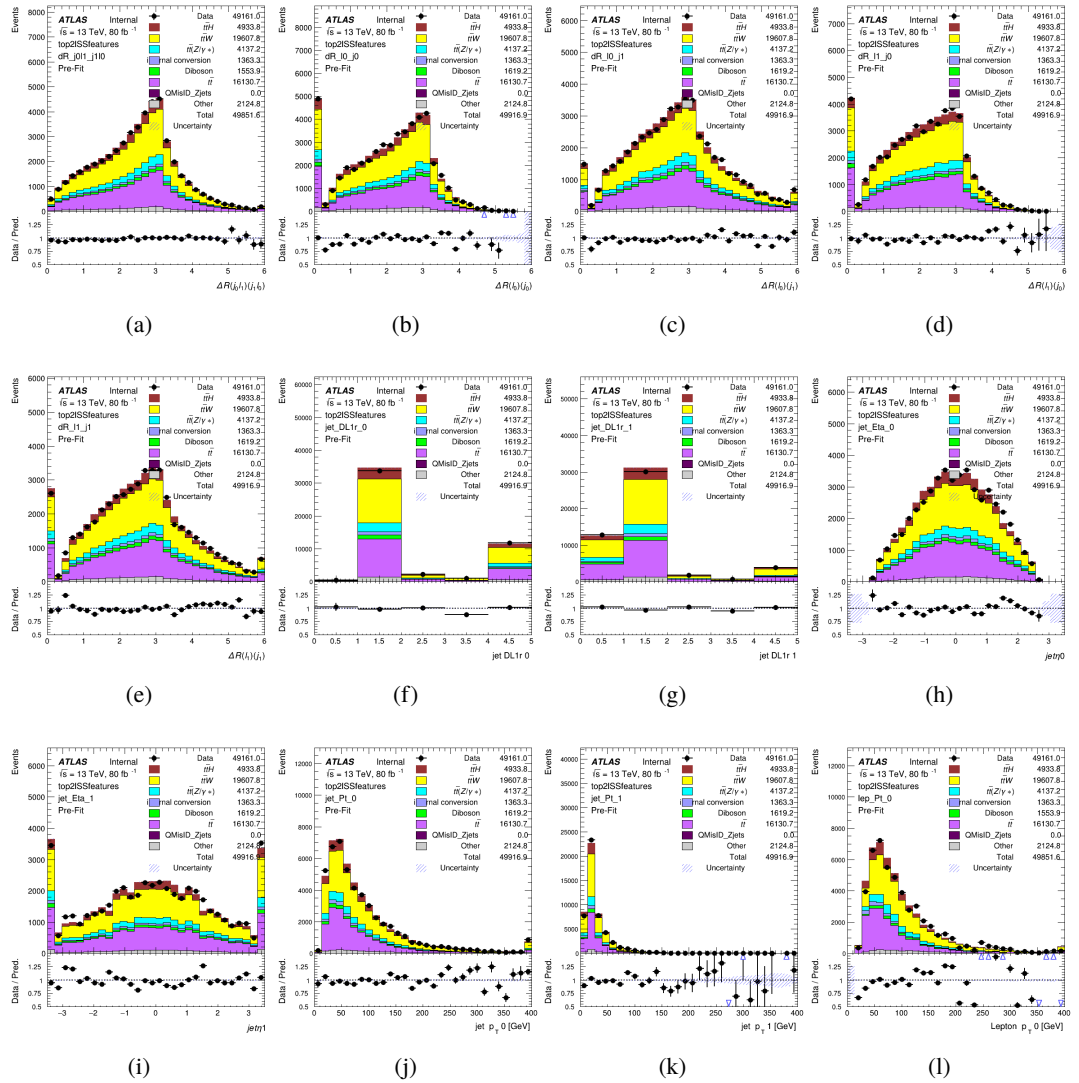


Figure A.2: Input features for top2lSS

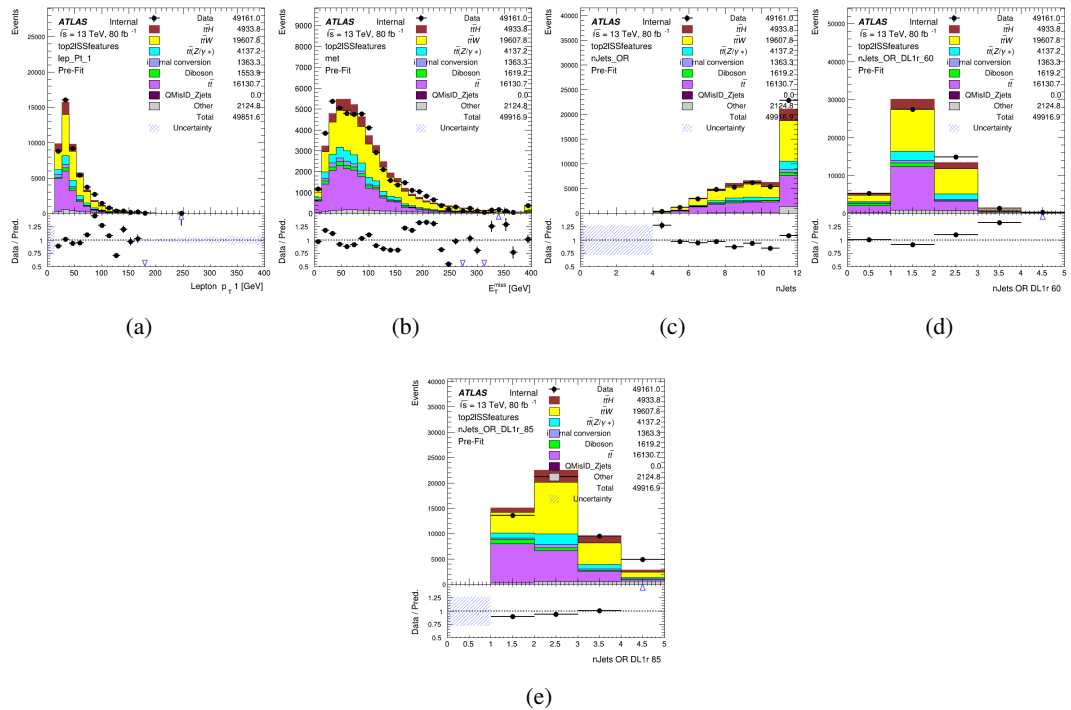


Figure A.3: Input features for top2lSS

1752 **A.1.2 b-jet Identification Features - 3l**

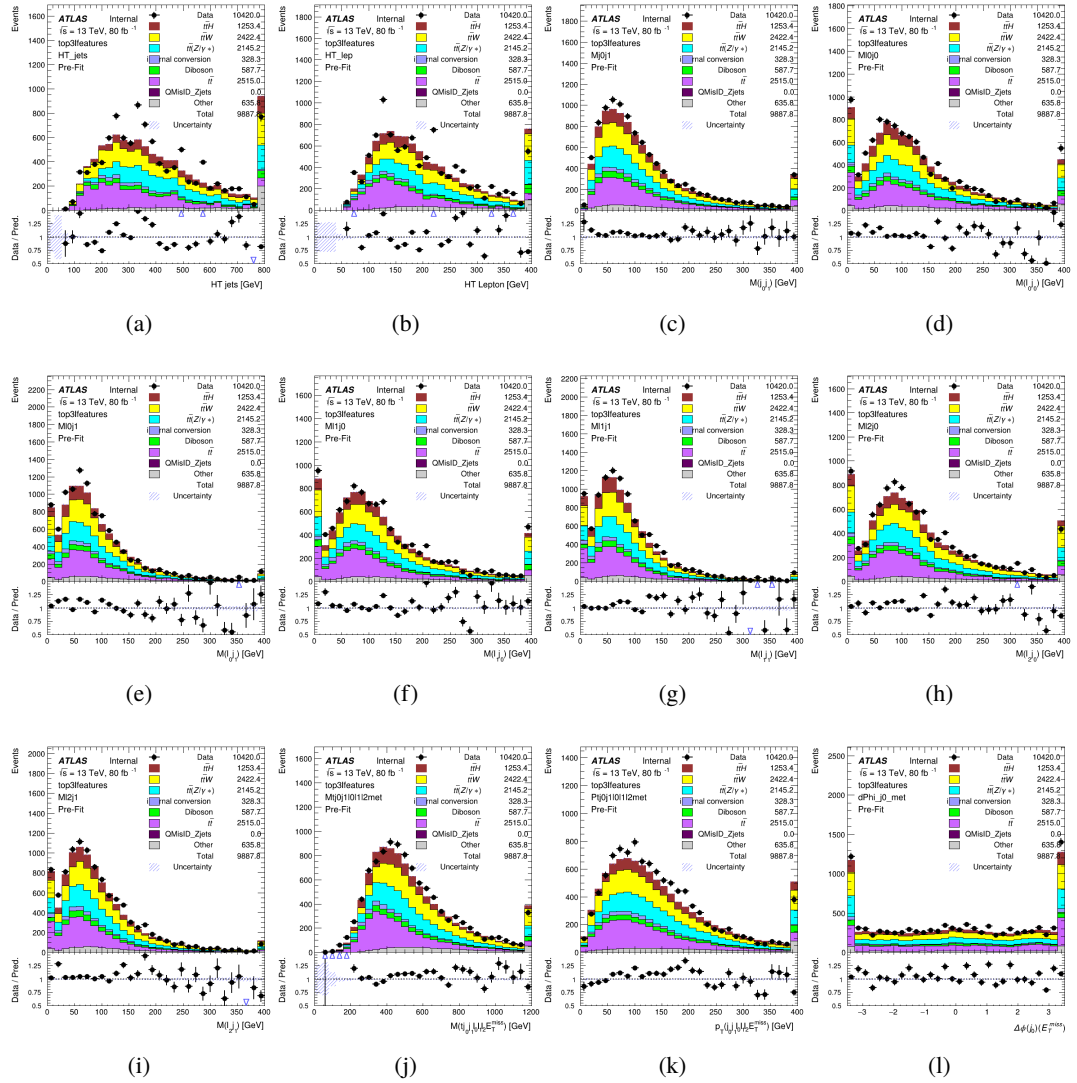


Figure A.4: Input features for top31

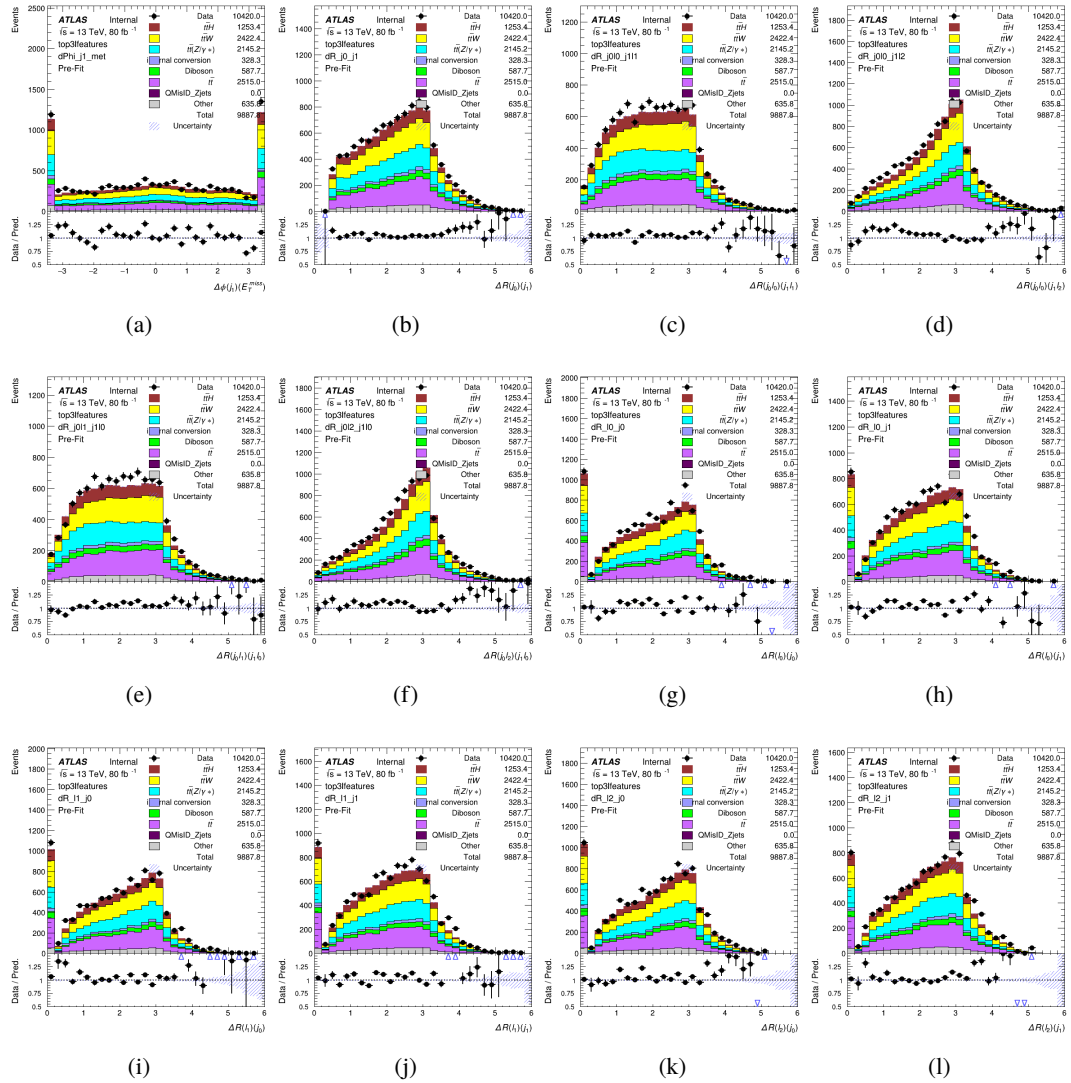


Figure A.5: Input features for top31

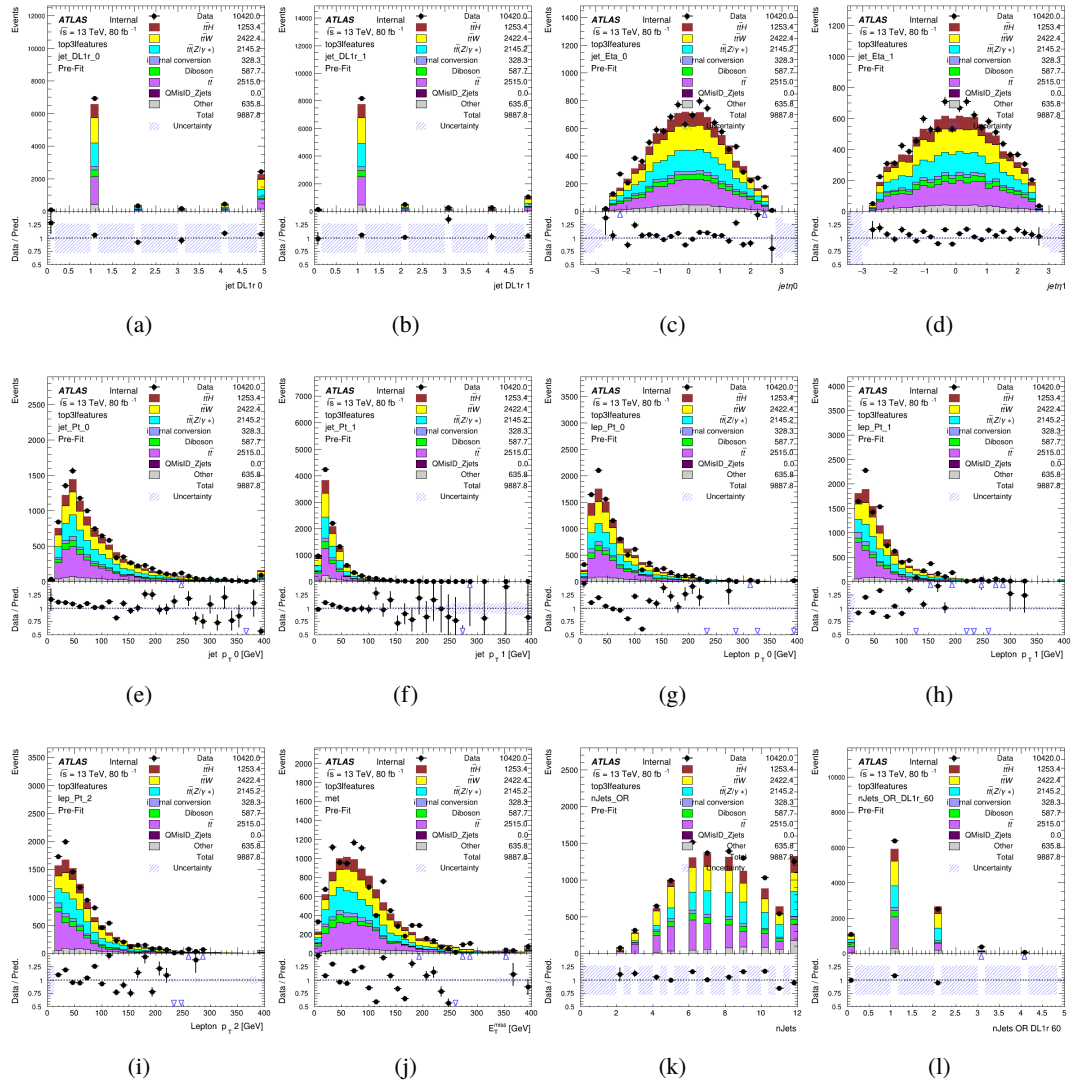
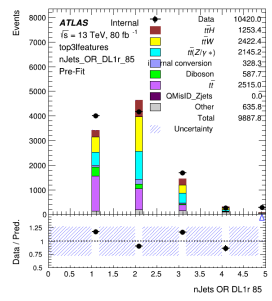


Figure A.6: Input features for top31



(a)

Figure A.7: Input features for top3l

1753 **A.1.3 Higgs Reconstruction Features - 2lSS**

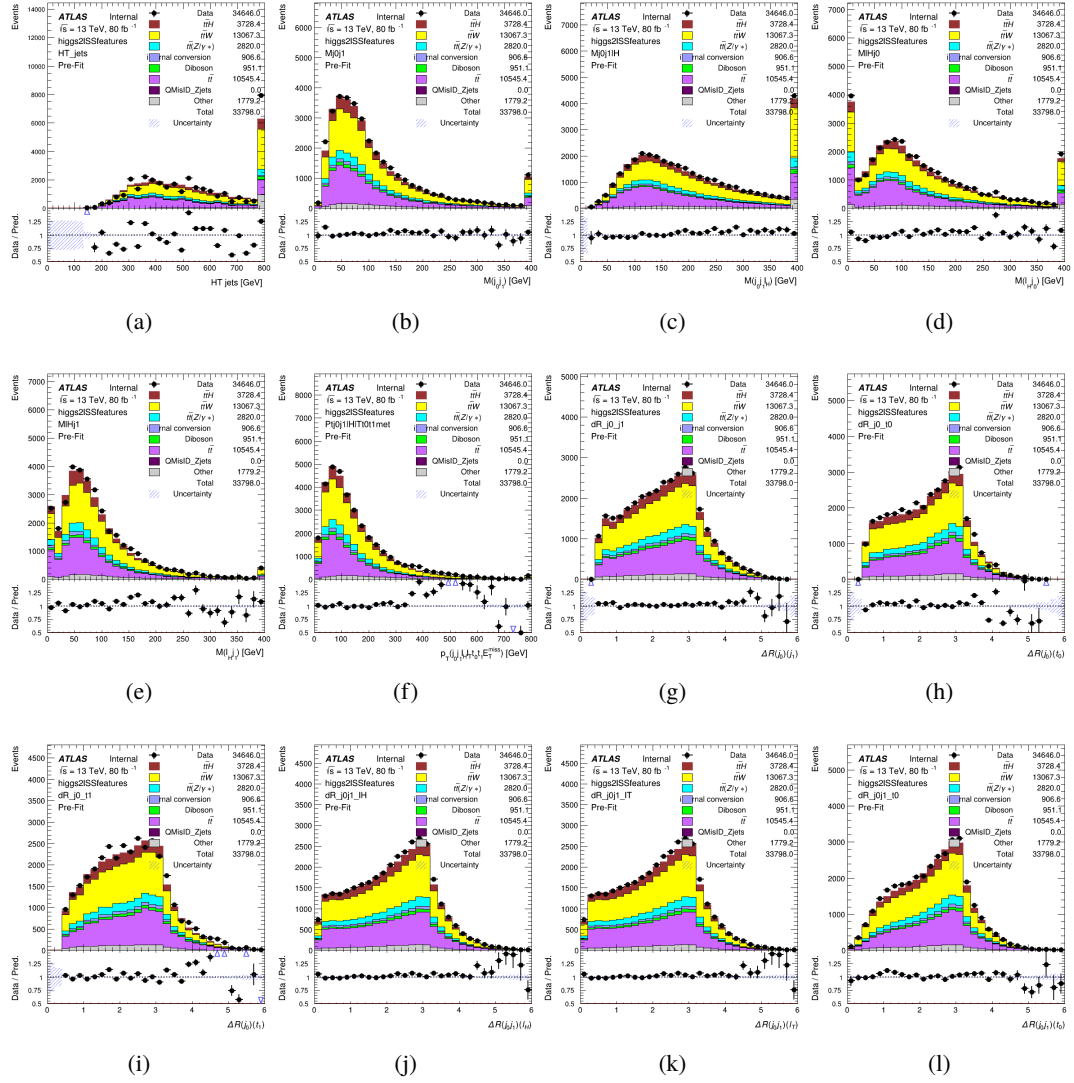


Figure A.8: Input features for higgs2lSS

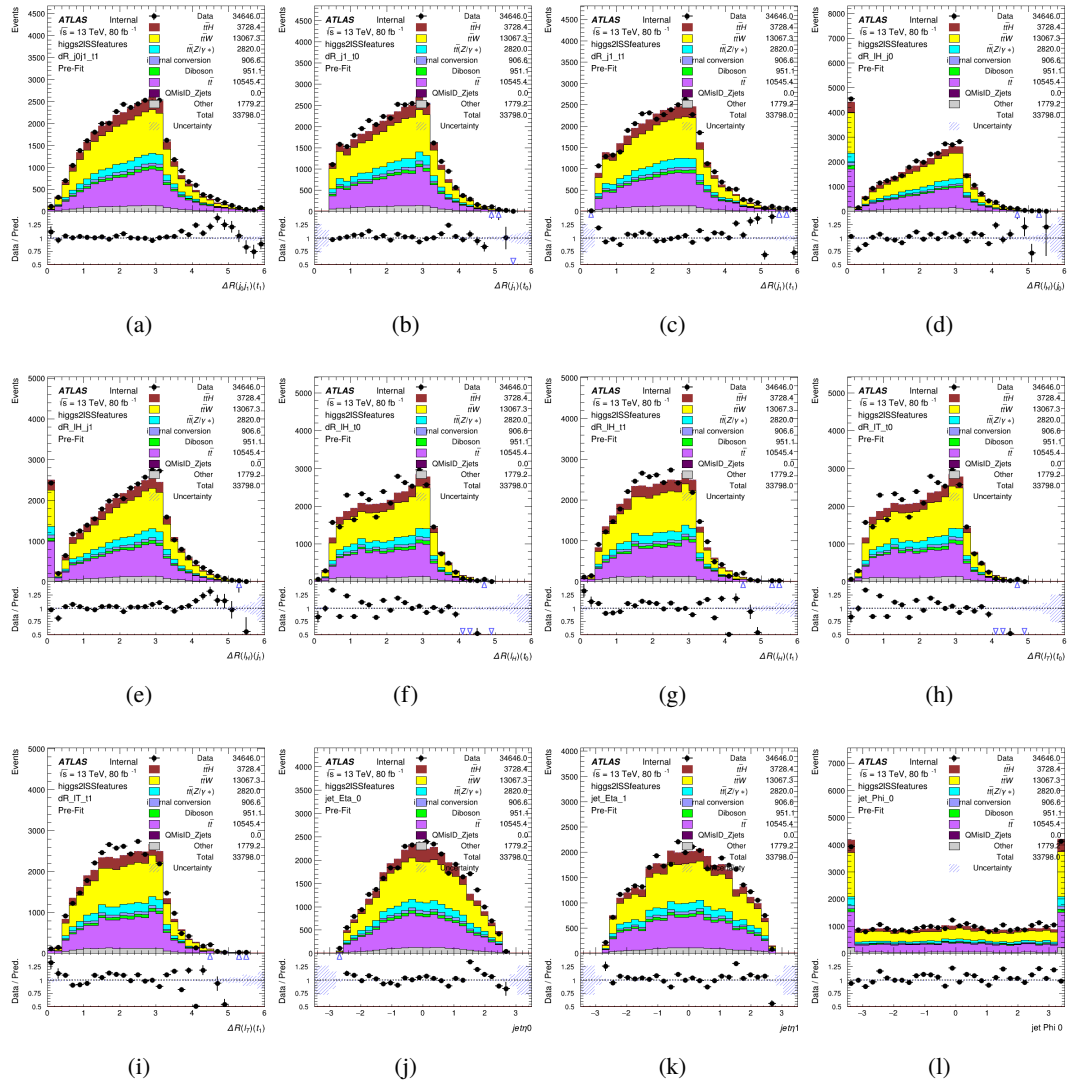


Figure A.9: Input features for higgs2lSS

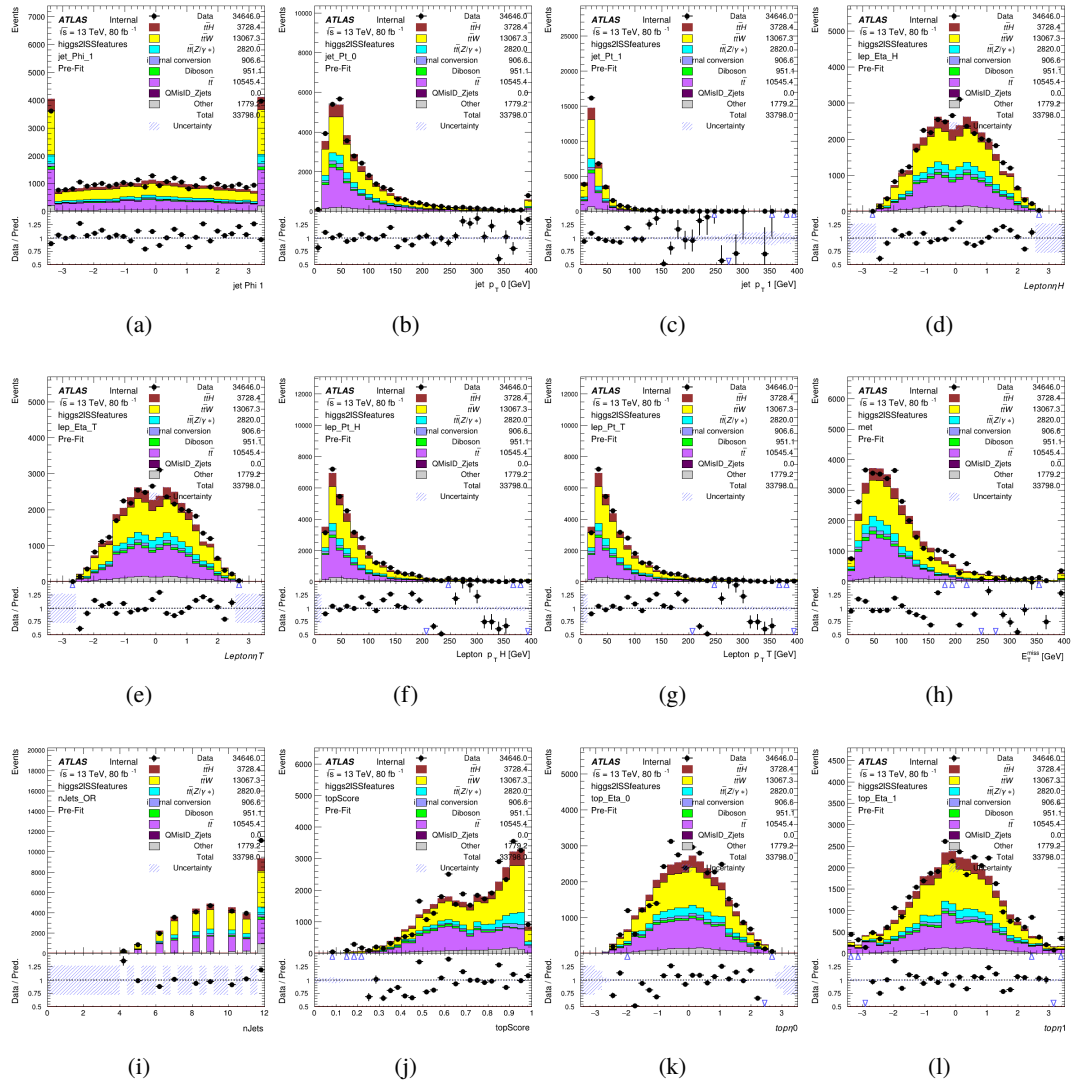


Figure A.10: Input features for higgs2ISS

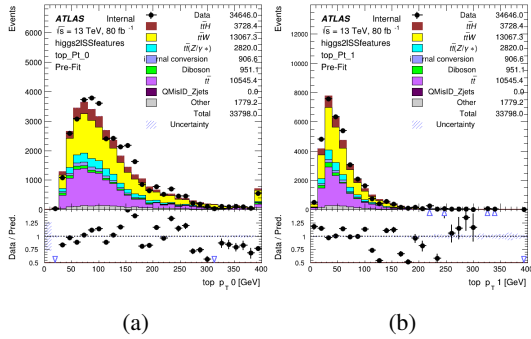


Figure A.11: Input features for higgs2lSS

1754 **A.1.4 Higgs Reconstruction Features - 3lS**

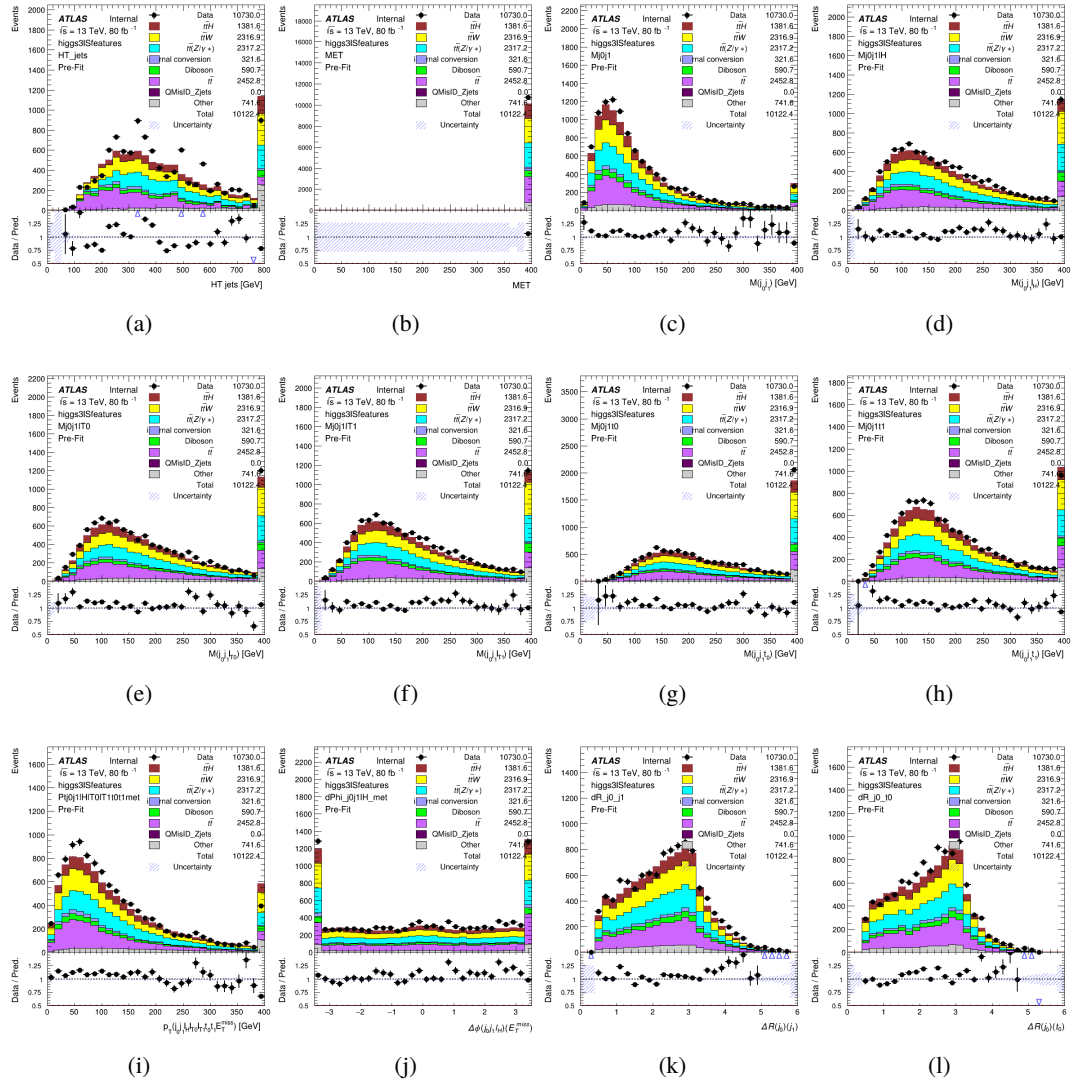


Figure A.12: Input features for higgs3IS

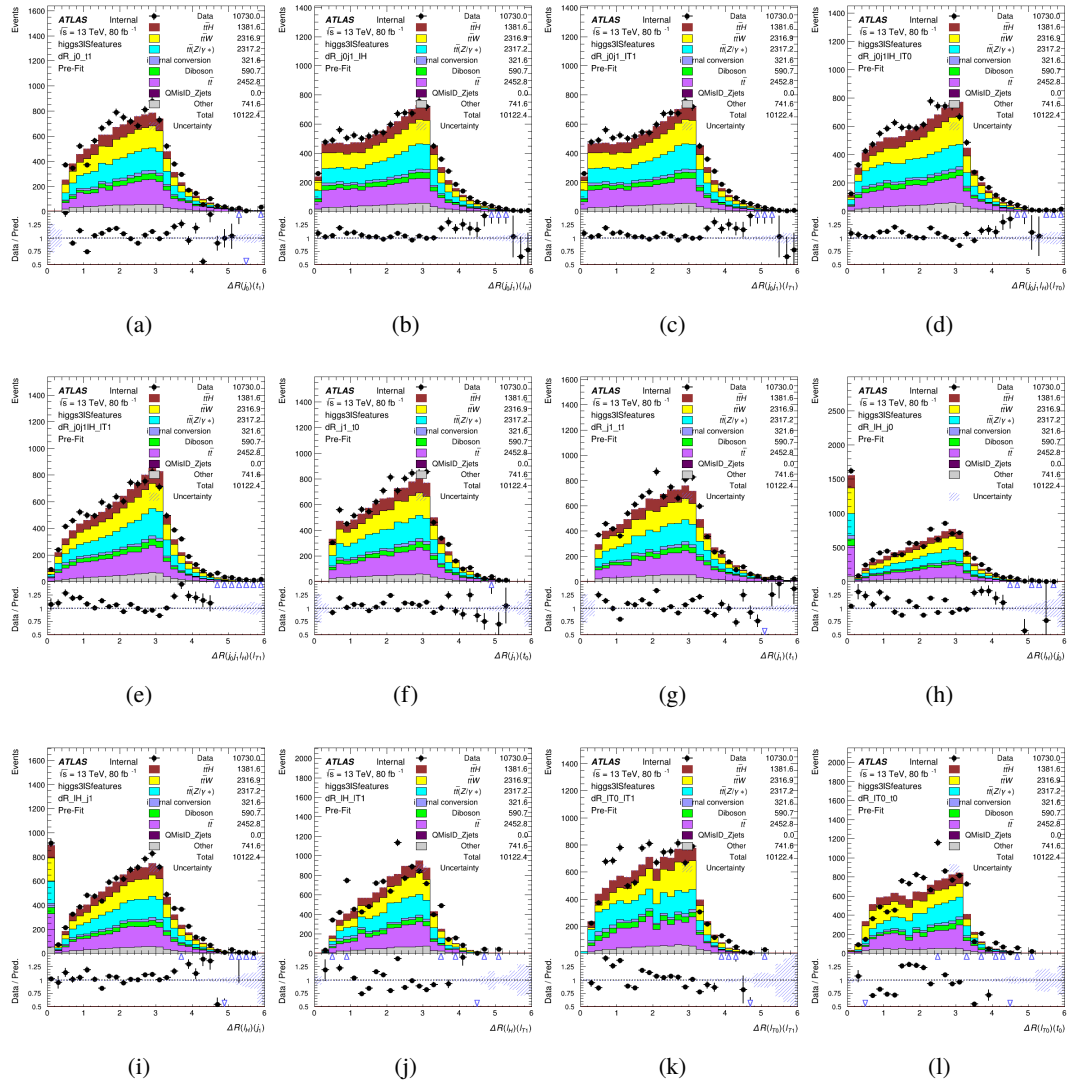


Figure A.13: Input features for higgs3lS

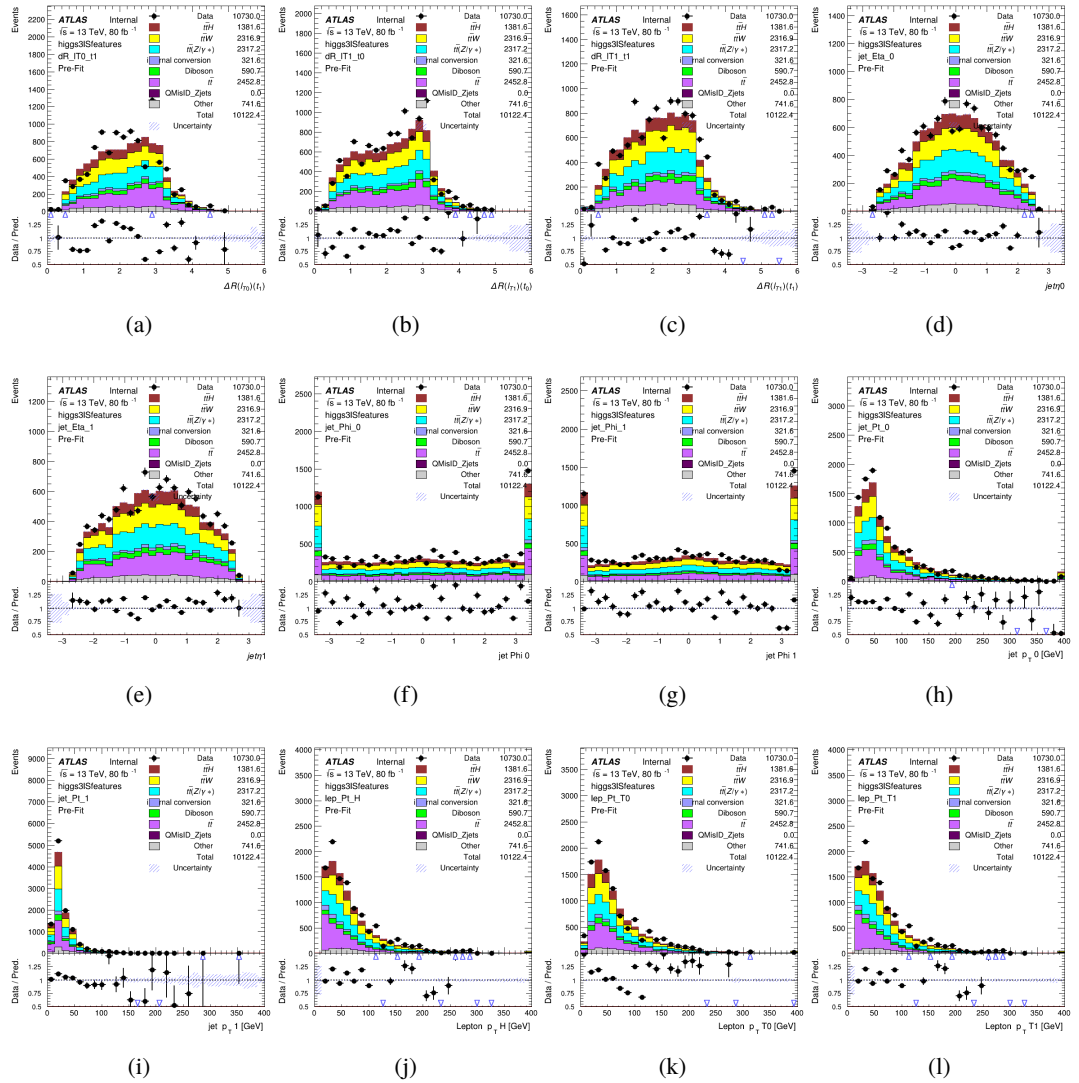


Figure A.14: Input features for higgs3lS

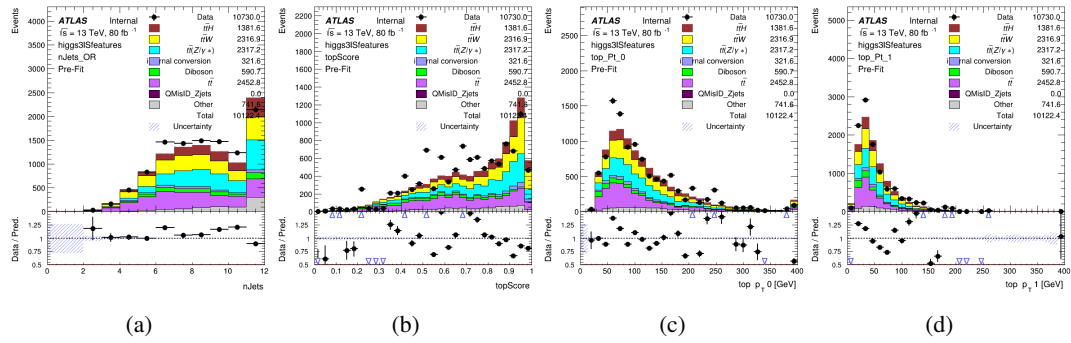


Figure A.15: Input features for higgs3lS

1755 **A.1.5 Higgs Reconstruction Features - 3lF**

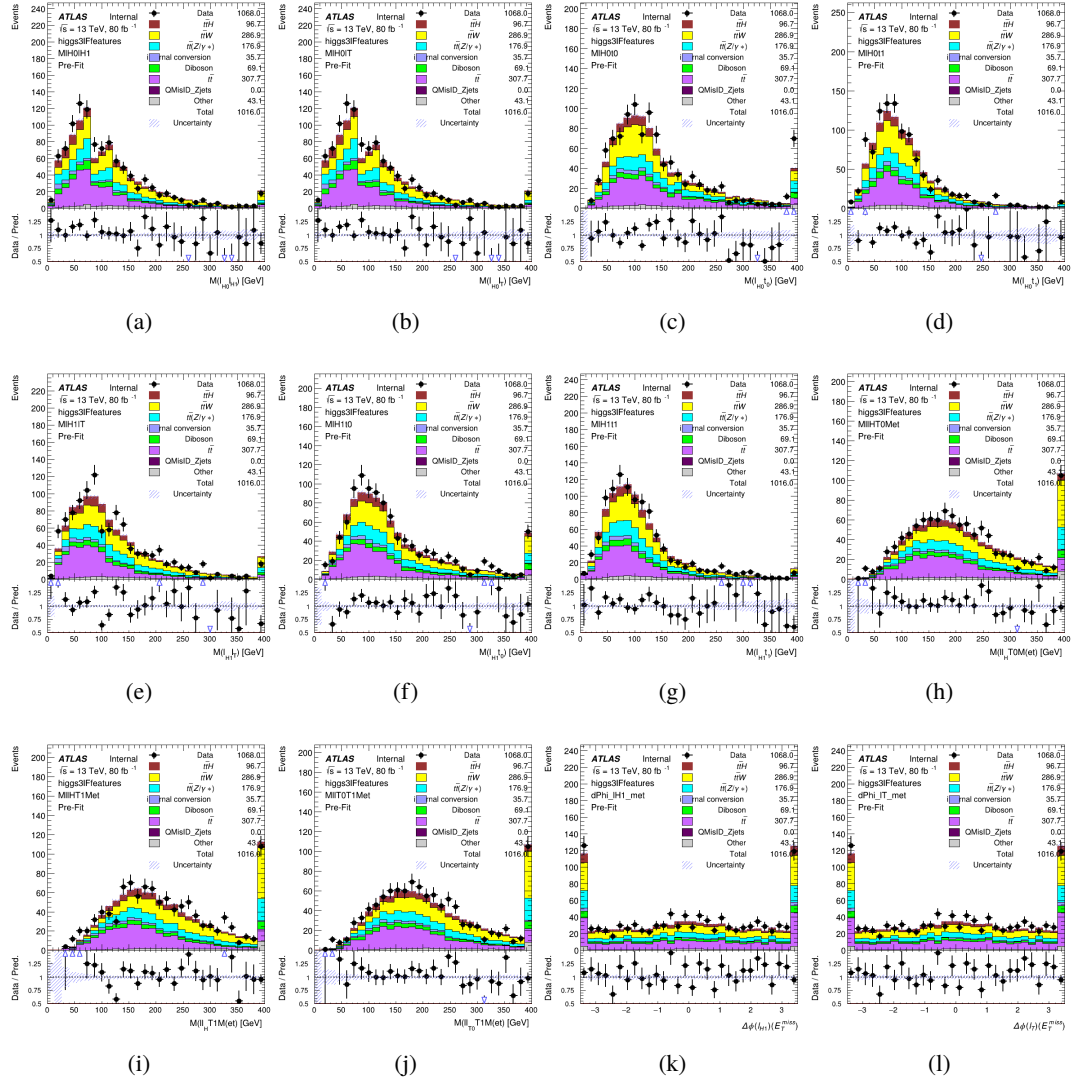


Figure A.16: Input features for higgs3IF

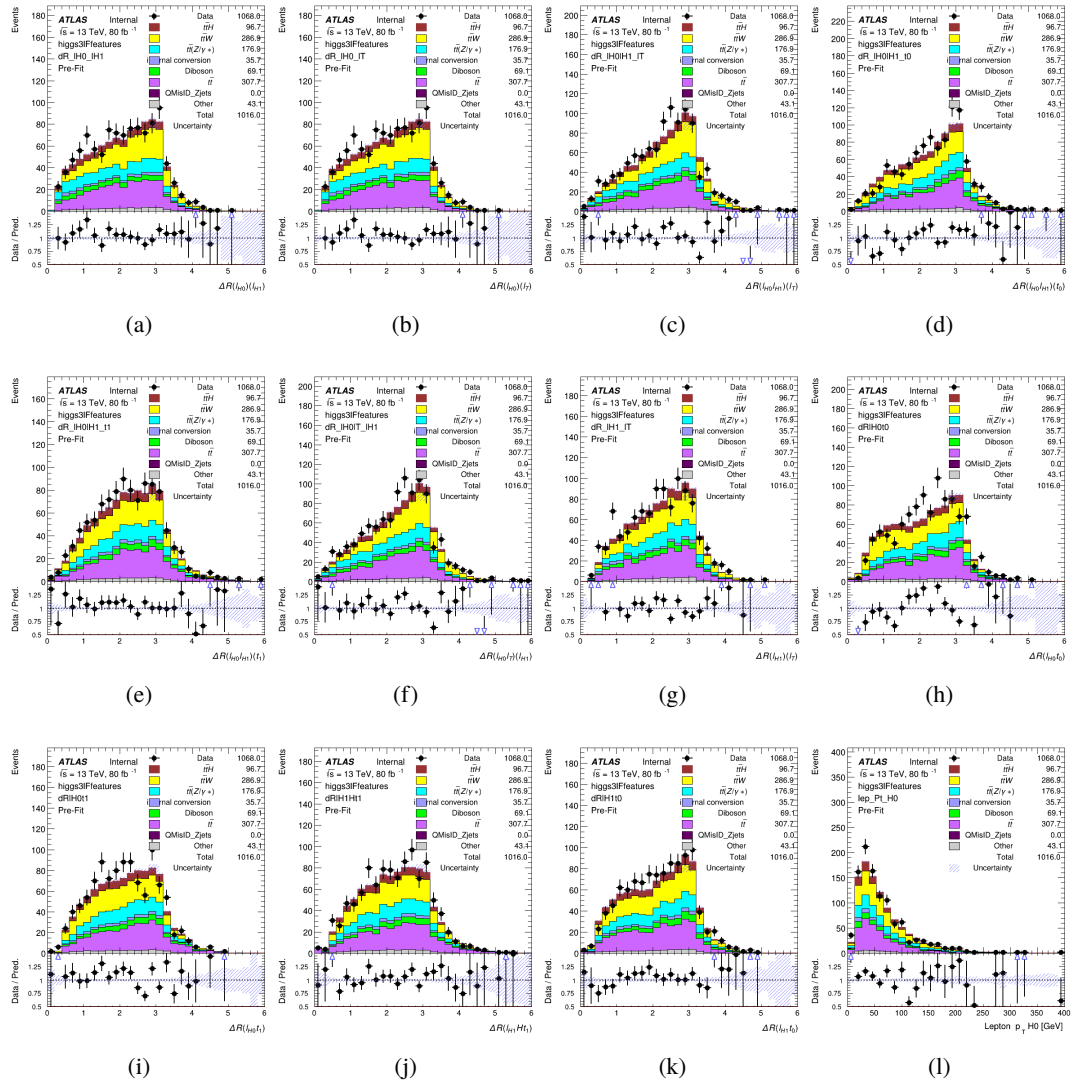


Figure A.17: Input features for higgs3lF

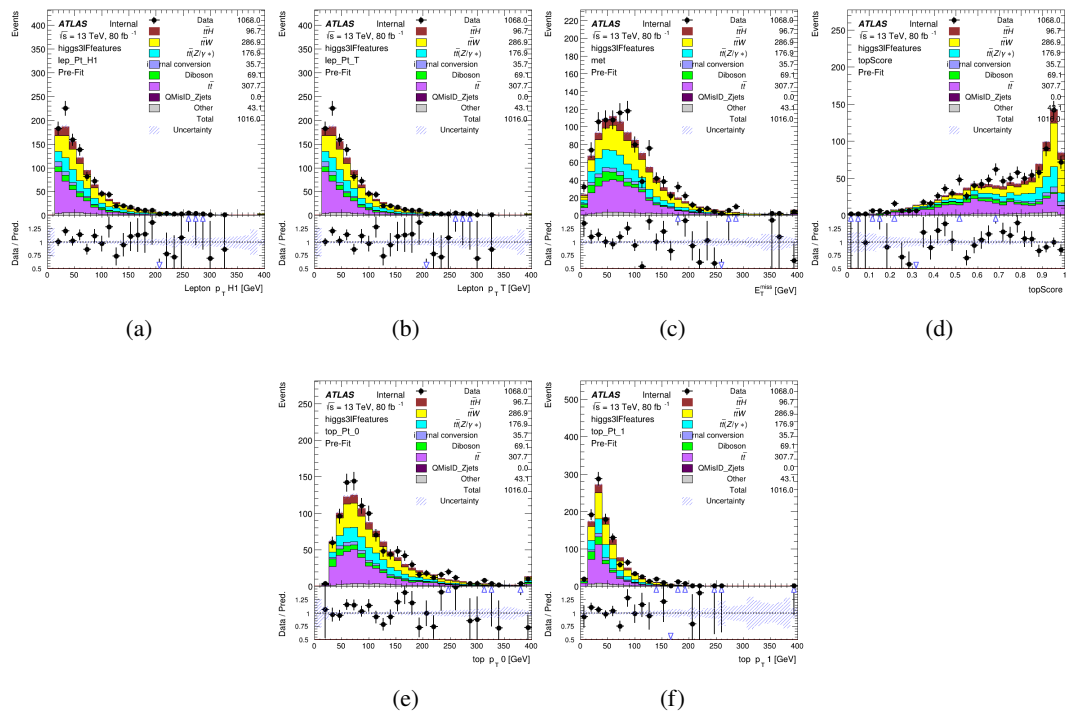


Figure A.18: Input features for higgs3IF

¹⁷⁵⁶ **A.2 Background Rejection MVAs**

¹⁷⁵⁷ **A.2.1 Background Rejection MVA Features - 2lSS**

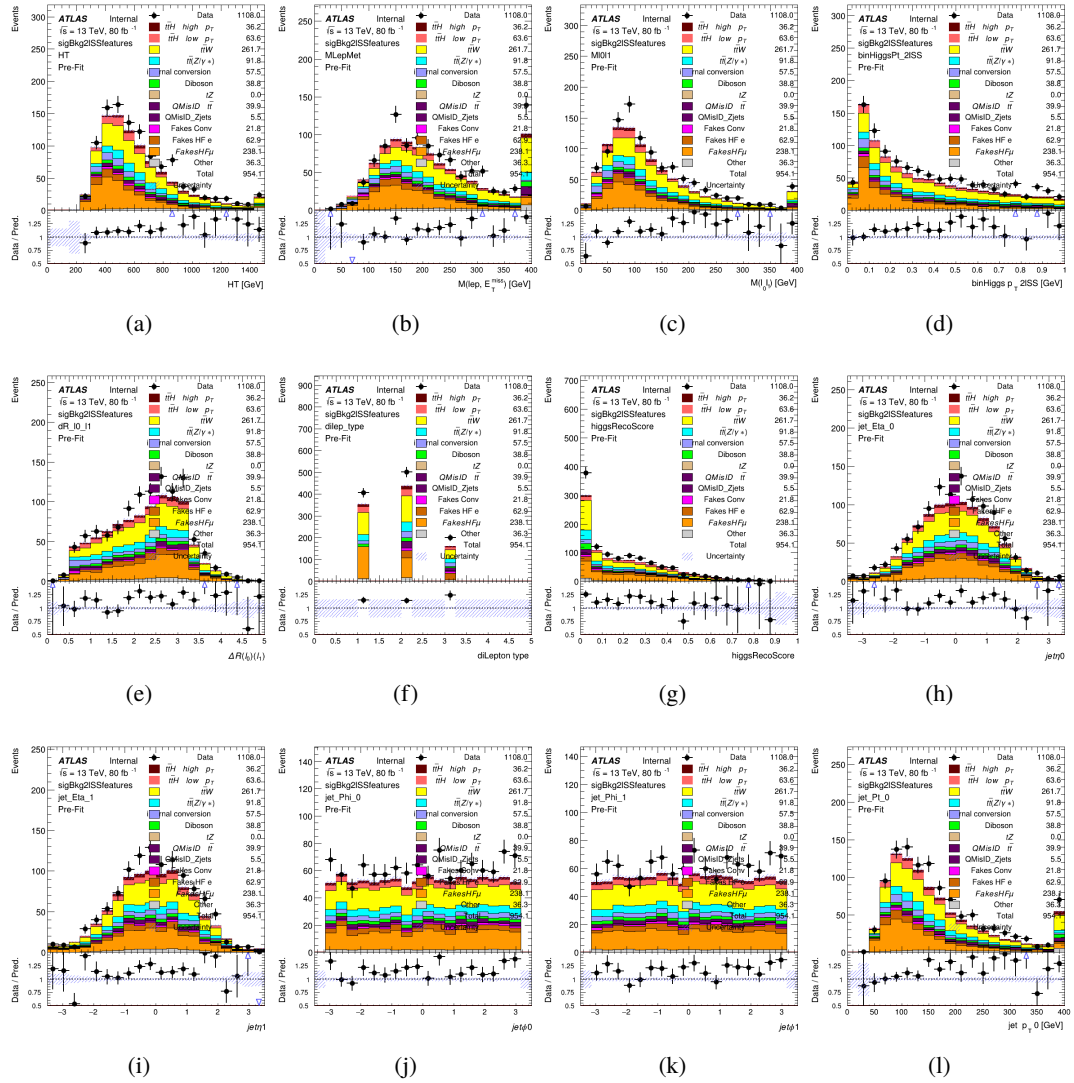


Figure A.19: Input features for sigBkg2lSS

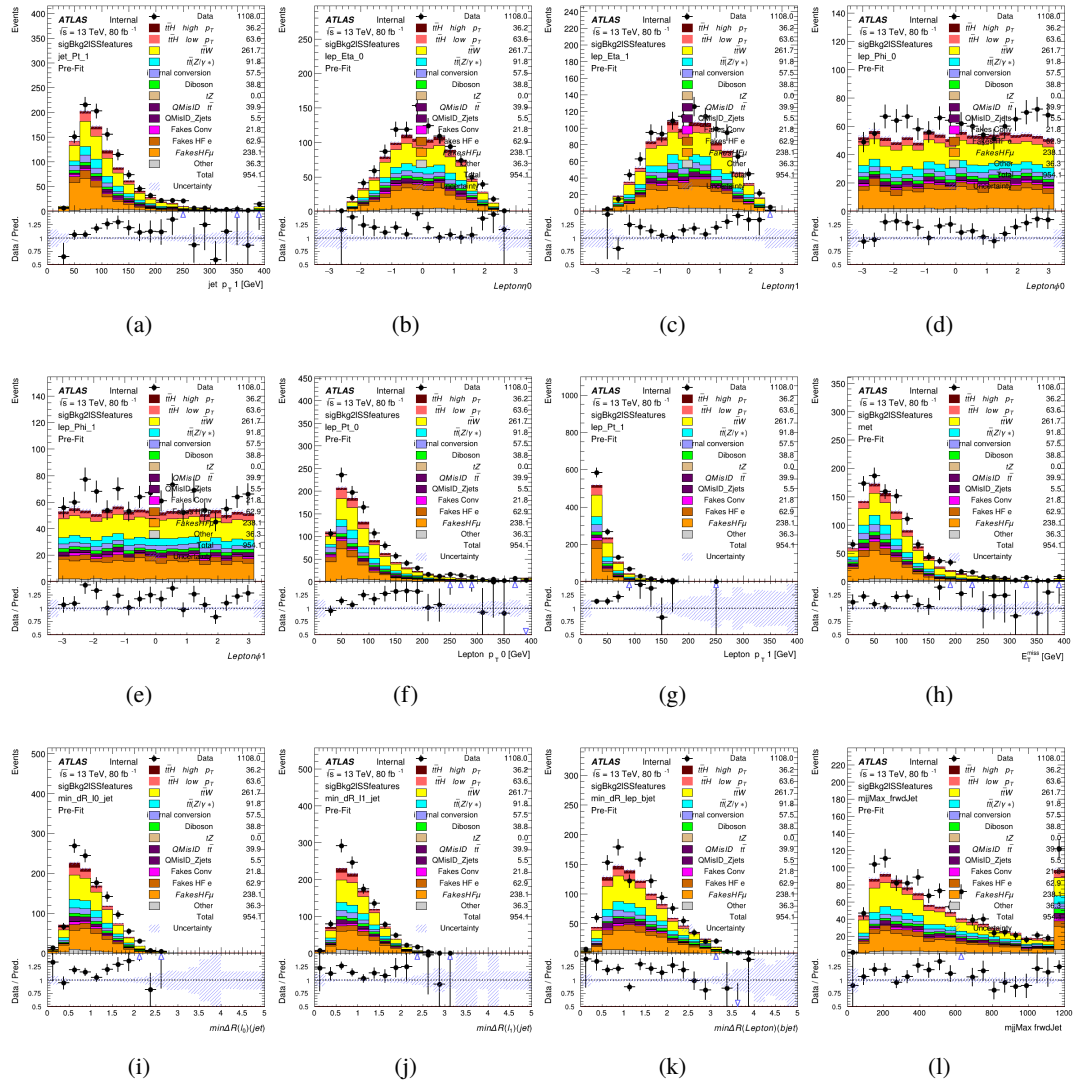


Figure A.20: Input features for sigBkg2lSS

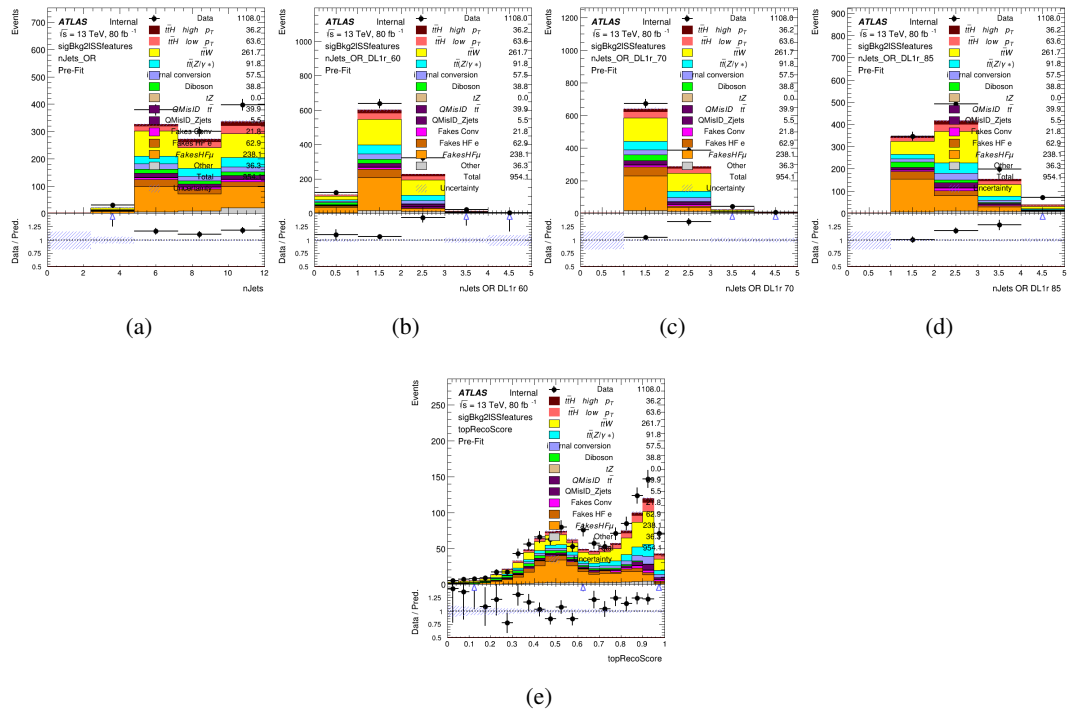
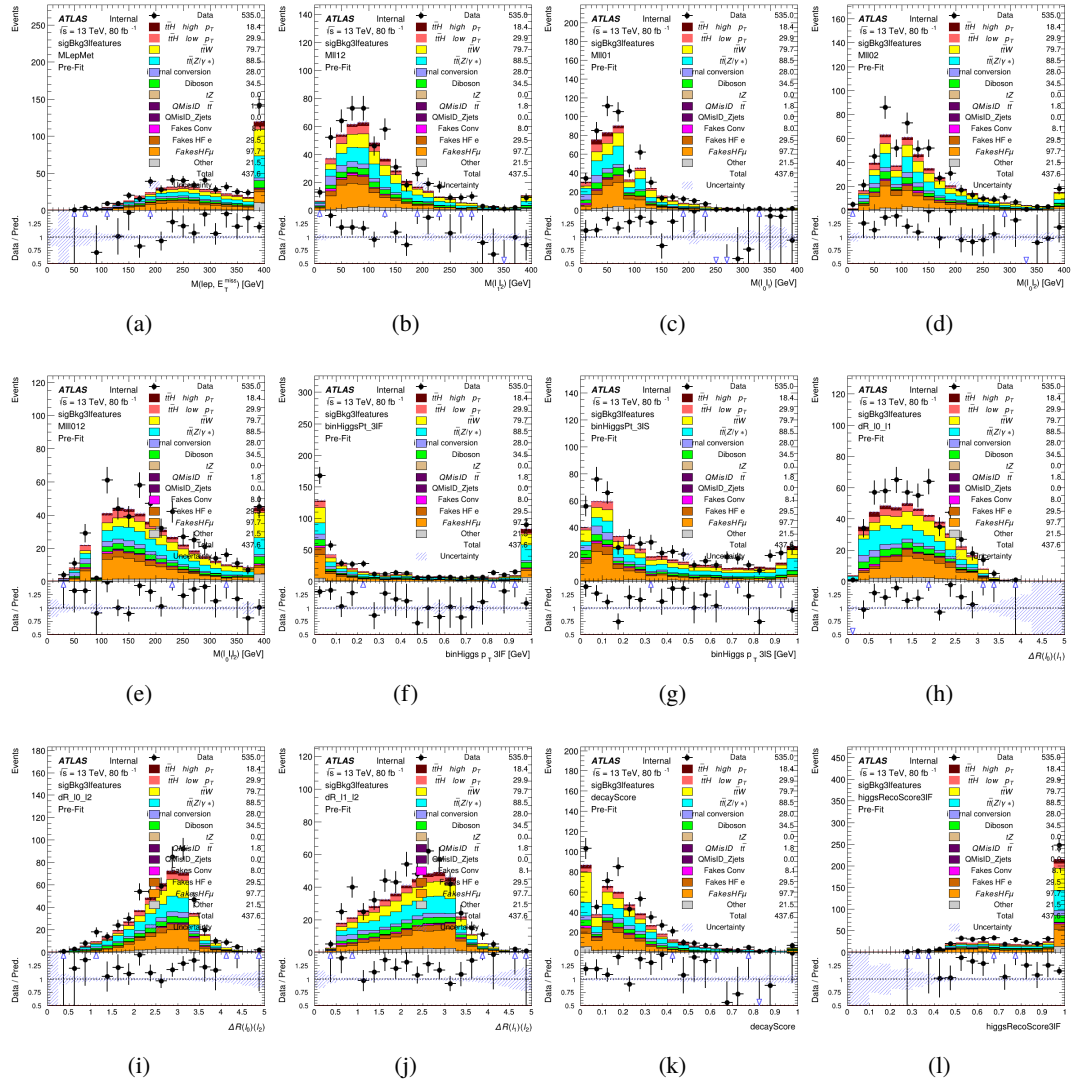


Figure A.21: Input features for sigBkg2ISS

¹⁷⁵⁸ **A.2.2 Background Rejection MVA Features - 31**

Figure A.22: Input features for `sigBkg3l`

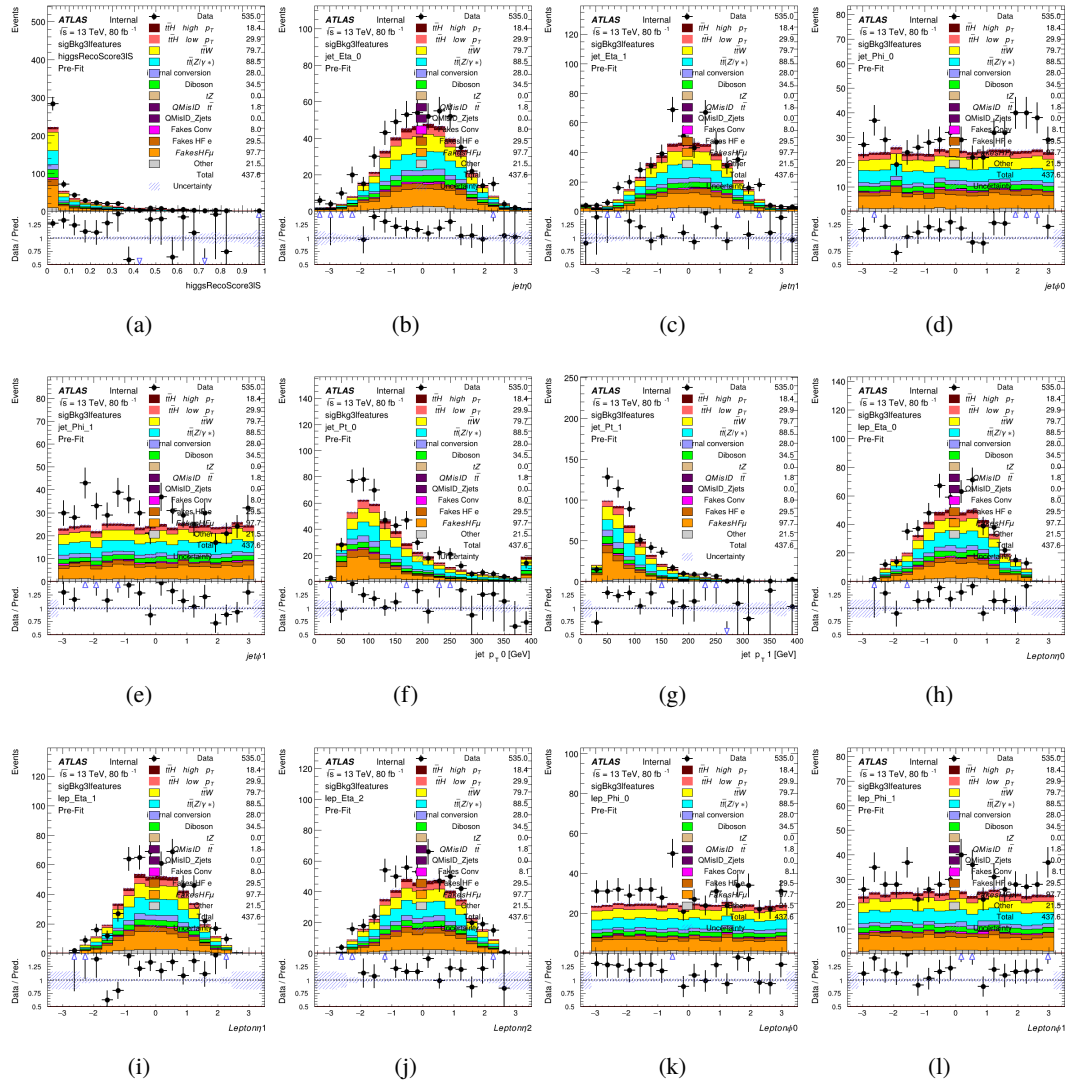


Figure A.23: Input features for sigBkg3l

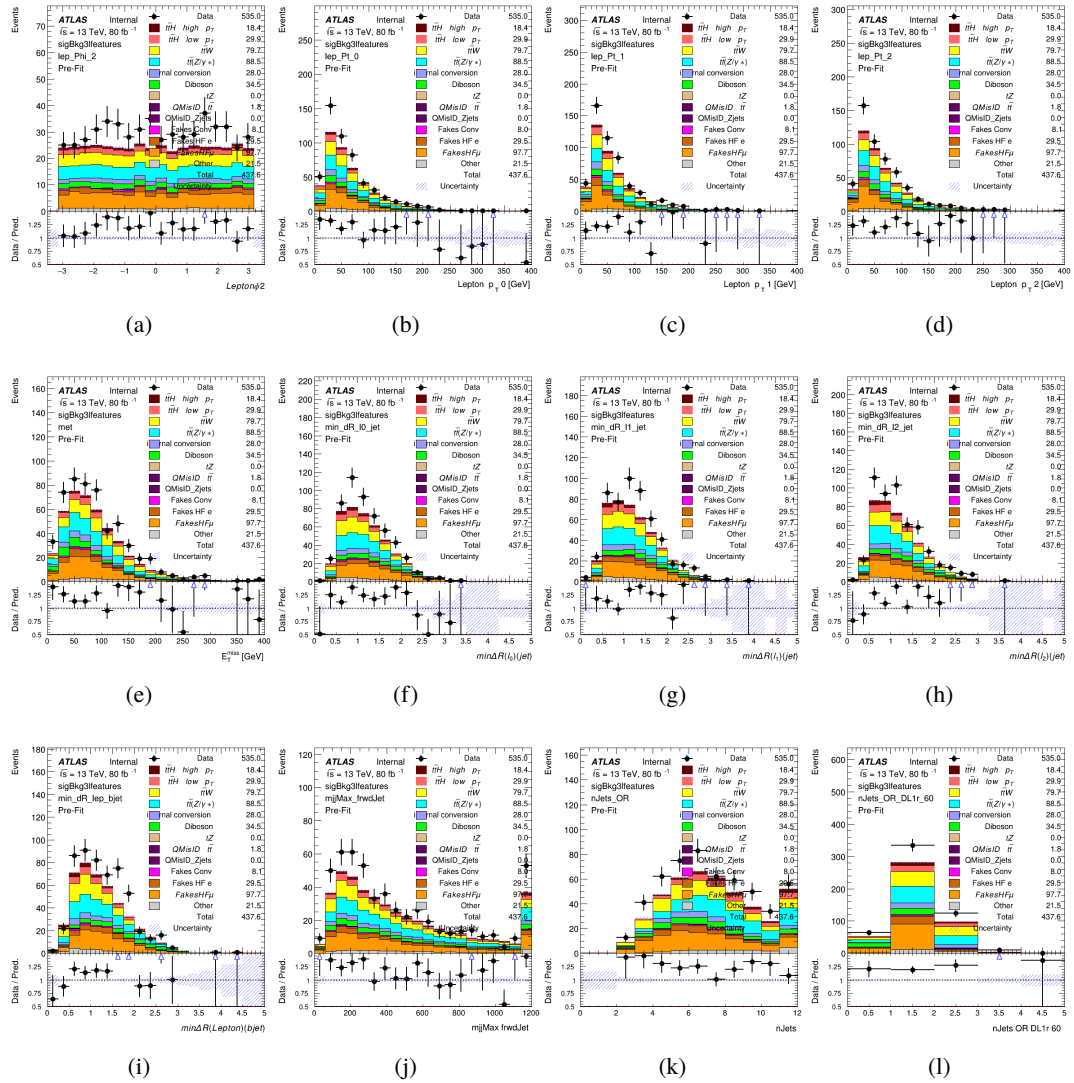


Figure A.24: Input features for sigBkg3l

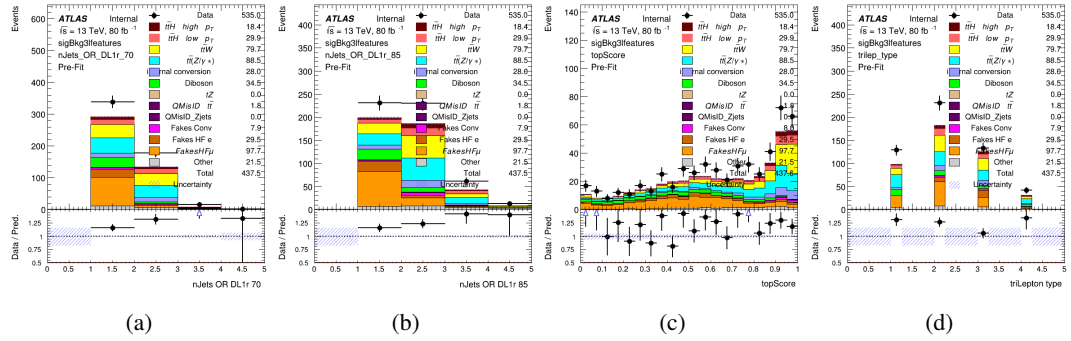


Figure A.25: Input features for sigBkg3l

1759 **A.3 Alternate b-jet Identification Algorithm**

1760 The nominal analysis reconstructs the b-jets by considering different combinations of jets, and
 1761 asking a neural network to determine whether each combination consists of b-jets from top quark
 1762 decays. An alternate approach would be to give the neural network about all of the jets in an event
 1763 at once, and train it to select which two are most likely to be the b-jets from top decay. It was
 1764 hypothesized that this could perform better than considering each combination independently, as
 1765 the neural network could consider the event as a whole. While this is not found to be the case,
 1766 these studies are documented here as a point of interest and comparison.

1767 For these studies, the kinematics of the 10 highest p_T jets in each event are used for
 1768 training. This includes the vast majority of truth b-jets. Specifically the p_T , η , ϕ , E , and DL1r
 1769 score of each jet are used. For events with fewer than 10 jets, these values are substituted with 0.
 1770 The p_T , η , ϕ , and E of the leptons and E_T^{miss} are included as well. Categorical cross entropy is
 1771 used as the loss function.

Table 56: Accuracy of the NN in identifying b-jets from tops in 2lSS events for the alternate categorical method compared to the nominal method.

Channel	Categorical	Nominal
2lSS	70.6%	73.9%
3l	76.1%	79.8%

1772 **A.4 Binary Classification of the Higgs p_T**

1773 A two bin fit of the Higgs momentum is used because statistics are insufficient for any finer
 1774 resolution. This means separating high and low p_T events is sufficient for this analysis. As

1775 such, rather than attempting the reconstruct the full Higgs p_T spectrum, a binary classification
 1776 approach is explored.

1777 A model is built to determine whether $t\bar{t}H$ events include a high p_T (>150 GeV) or low
 1778 p_T (<150 GeV) Higgs Boson. While this is now a classification model, it uses the same input
 1779 features described in section 18.4. Binary crossentropy is used as the loss function.

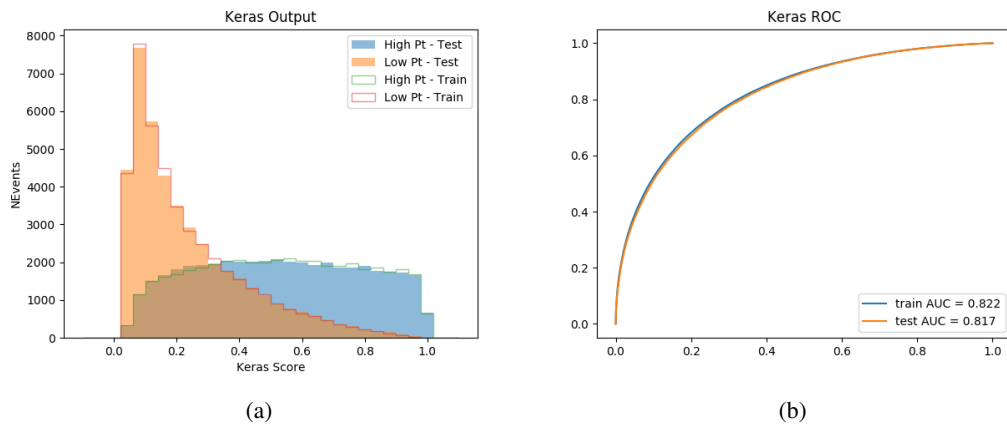


Figure A.26:

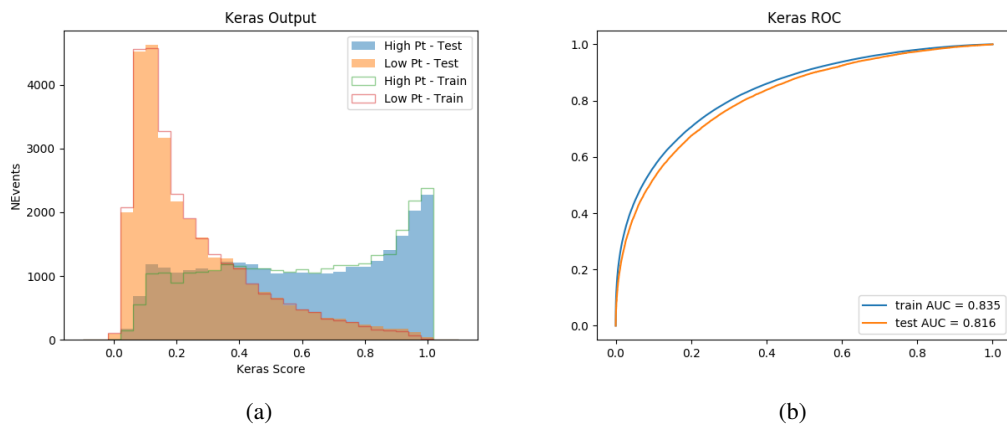


Figure A.27:

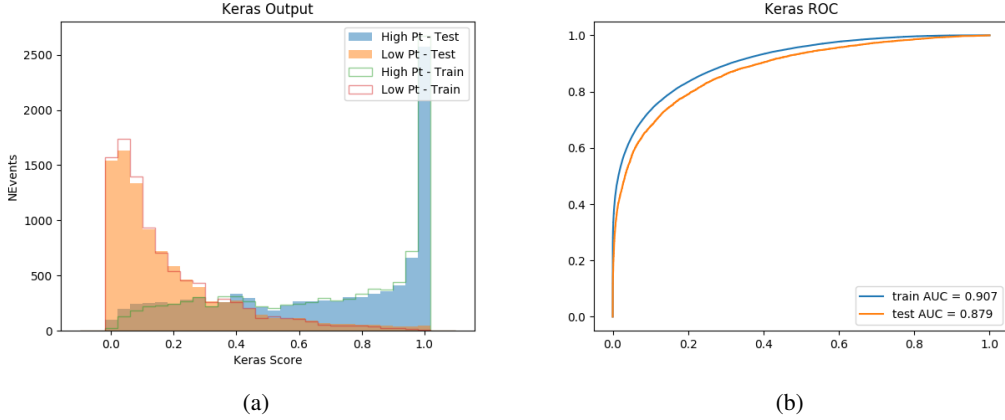


Figure A.28:

1780 A.5 Impact of Alternative Jet Selection

1781 A relatively low p_T threshold of 15 GeV is used to determine jet candidates, as the jets originating
 1782 from the Higgs decay are found to fall between 15 and 25 GeV a large fraction of the time. The
 1783 impact of different jet p_T cuts on our ability to reconstruct the Higgs p_T is explored here. The
 1784 performance of the Higgs p_T prediction models is evaluated for jet p_T cuts of 10, 15, 20, and 25
 1785 GeV.

1786 **B**

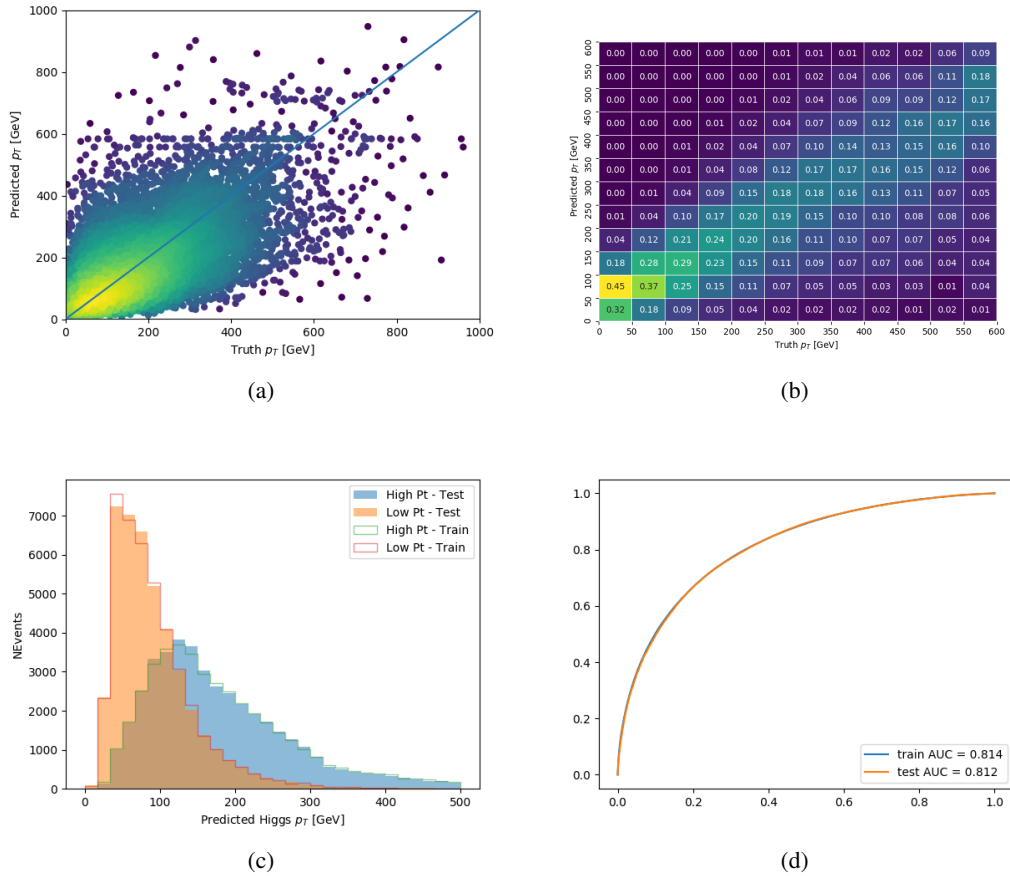


Figure A.29: